BRNO UNIVERSITY OF TECHNOLOGY
VYSOKÉ UČENÍ TECHNICKÉ V BRNĚ

FACULTY OF MECHANICAL ENGINEERING
FAKULTA STROJNÍHO INŽENÝRSTVÍ

HEAT TRANSFER AND FLUID FLOW LABORATORY
LABORATOŘ PŘENOSU TEPLA A PROUDĚNÍ

LIMIT MODES OF PARTICULATE MATERIALS CLASSIFIERS
LIMITNÍ REŽIMY TŘÍDIČŮ PARTIKULÁRNÍCH LÁTEK

DOCTORAL THESIS
DIZERTAČNÍ PRÁCE

AUTHOR — Ing. Martin Adamčík
AUTOR PRÁCE

SUPERVISOR — doc. Ing. Tomáš Svěrák, CSc.
VEDOUCÍ PRÁCE

BRNO 2017

Abstract

With material science demands on ever smaller particle sizes, new approaches and effective methods of their classification are needed. Turbulent flow field patterns and particle trajectories inside of a dynamic air classifier are investigated. Increasing computing power together with new turbulence models and approaches to simulate complex fully turbulent problems by solving Navier-Stokes equations allows studying and capturing smaller flow structures and properties more accurately. Particles below 10 microns are more susceptible to smaller local vortexes and particle fates are therefore more dependent on these local structures. Area of focus are the conditions required for classification of particles with sizes below 10 microns as this size is at the limit of air classification method possibilities. CFD software and the latest knowledge in turbulence modelling are used to numerically simulate flow field inside a dynamic air classifier. Effects of varying operating parameters on flow patterns and discrete phase classification outputs are investigated. Experimental verification of the simulated flow fields includes advanced imaging method (PIV) measurement of flow velocity and is used to visualize flow field structures in the classifier rotor blade passageway region. Predicted particle trajectories and their fates are experimentally verified by classification trials carried out on dynamic air classifier and the particle distribution curves are established by laser diffraction method. Tromp curves and efficiency of classification process are studied.

Keywords

Rotor air classifier, fine particle classification, Tromp curve, particle image velocimetry (PIV), laser diffraction method, numerical simulation CFD

Abstrakt

S požadavky materiálových věd na stále menší částice jsou potřebné i nové přístupy a metody jejich klasifikace. V disertační práci jsou zkoumány struktury turbulentního proudění a trajektorie částic uvnitř dynamického větrného třídiče. Zvyšující se výpočtový výkon a nové modely turbulence a přístupy modelování komplexních plně turbulentních problémů řešením Navier-Stokesových rovnic umožňují zkoumání stále menších lokálních proudových struktur a vlastností proudění s větší přesností. Částice menší než 10 mikronů jsou více ovlivnitelné a jejich klasifikace do hrubé nebo jemné frakce závisí na malých vírových strukturách. Práce se zaměřuje na podmínky nutné ke klasifikaci částic pod 10 mikronů, což je současná hranice možností metody větrné separace. CFD software a poslední poznatky modelování turbulence jsou použity v numerické simulaci proudových polí dynamického větrného třídiče a jsou zkoumány efekty měnících se operačních parametrů na proudová pole a klasifikaci diskrétní fáze. Experimentální verifikace numerických predikcí je realizovaná prostřednictvím částicové anemometrie na základě statistického zpracování obrazu (PIV) a proudění lopatkami rotoru je vizualizováno. Predikované trajektorie částic jsou experimentálně ověřeny třídícími testy na větrném třídiči a granulometrie je určená pomocí laserové difrakční metody. Zkoumány jsou Trompovy křivky a efektivita třídění.

Klíčová slova

Větrný třídič s rotorem, třídění velmi jemných partikulárních látek, Trompova křivka, měření PIV, laserová difrakční granulometrie, numerická simulace CFD

Bibliografická citace

ADAMČÍK, M. *Limitní režimy třídičů partikulárních látek.* Brno: Vysoké učení technické v Brně, Fakulta strojního inženýrství, 2017. 219s. Vedoucí dizertační práce doc. Ing. Tomáš Svěrák, CSc.

Declaration

I declare that the doctoral thesis submitted hereby is my own work under supervision of doc. Ing. Tomáš Svěrák, CSc. and that all literature sources were quoted completely and correctly.

In Brno Ing. Martin Adamčík

Acknowledgements

Herein, I would like to express my sincere gratitude to my supervisor doc. Ing. Tomáš Svěrák, CSc. for his support, motivation and valuable advice during my Ph.D studies. Also, I would like to thank to doc. Ing. Pavel Rudolf Ph.D and M.S. Alexandrina Untaroiu Ph.D. for their advice and support with numerical simulations. I would like to thank the staff at Bradley Pulverizer Co. for their support and for allowing me to combine my work and study duties. A very special gratitude goes to my wife for her endless support, help and understanding in difficult times. Finally, I would like to thank my family and my friends for being in my life and making me the person I am.

Contents

1 INTRODUCTION

Material comminution and classification is a process as old as humanity itself. Whether it is separation of rye from husk, grinding wheat to flour or state of the art industrial micronization and classification of minerals to obtain core elements for materials with superior properties, requirements on these processes have been continuously increasing. It is the continual research, knowledge and understanding of mineral materials that allows for this advancement in the field. Bradley Pulverizer Company has been established almost some 140 years ago in the USA to serve phosphate fertilizer industry and since has developed and supplied pulverizing, classifying and process equipment worldwide. My employment with this company at its London office has inspired me into research focused on fine powder classification.

It is a process where the initial feed material is divided into fractions differing by some physical property like for example size or density. Size classification is the subject of this work and the size is represented by equivalent particle diameter. The feed material is divided into two or more fractions with different particle size distributions in order to achieve a desired level of uniformity of fractions. Particle classification based on size can be realized by several methods, where each of them has advantages and disadvantages. Air classification realized by dynamic air classifiers is one of the most widespread methods due to its attributes that satisfy industrial requirements, particularly high throughputs and low achievable cut sizes. Cut size of classifier under given operating parameters is a particle with unique size which has 50% chance to be classified into fine or coarse fraction. Its value can be established as balance of forces present in the classifier and acting on a particle with specific diameter. The dominant forces are centrifugal force introduced by rotation of classifier rotor cage and swirling flow pattern, further it is a drag force acting on particle introduced by forced air flow in the classifier and gravitational force acting on particle. Cut size of classifier is further influenced by material feed rate, degree of dispersion of particles in the classifier, geometrical design of the classifier and properties of the feed material like particle density, moisture content and capability to agglomerate. Varying operating parameters directly influence flow patterns and eddy formations, their time and size scales which consequentially effect classifier performance. Effects of varying operating parameters on cut size are studied together with effects on the flow field and flow patterns in the classifier.

In the experimental part, flow patterns and velocity vector maps in the near rotor region and in the blade passageway are studied and visualized by particle image velocimetry PIV method. Series of readings are taken and evaluated for combination of different fan and classifier rotor settings. In the second stage of the experimental part, classification trials with barite feed material are carried out. These trials are realized with operating parameters selected for finest cut size and an additional parameter, the feed rate is added to the experiment. Particle size distributions for fine and coarse fraction are established by laser diffraction method. Performance of the classifier, split ratios and Tromp curves are analysed for different operating parameters. Velocity readings at the inlet to the classifier and particle size distribution of the feed material are measured and used as input boundary conditions in the numerical simulations.

Numerical model representing simplified dimensional and geometrical copy of the classifier used in the experiment is created in commercial CFD software Ansys Fluent. Measured physical variables for different operating parameters are used as boundary conditions in several numerical

simulations. Results are then compared with data collected in experimental section. Furthermore, particle trajectories are calculated in these simulations and effect of flow field is generalized.

Classifiers are often used in the close circuit milling systems (Figure 1) so that the particles which comply required cut size can be extracted timely and the over grinding phenomenon is avoided. Reduced rejection rate improves efficiency of the milling system and it reduces wear and energy consumption. In today's material processing, ultrafine powder classification techniques play an important role in exploiting the advanced materials. Ultrafine powders possess many special properties and effects which are closely related to their particle size. Rapid development in materials science introduces new and demanding product requirements. To meet the needs of industries such as chemical industry, ceramics or bioengineering, which work with ultrafine powders, it is very important to research on ultrafine pulverising and classification theories and their applications.

Classification of particulate materials with sizes below 10 microns is commonly considered as a borderline for effective application of air classifiers across various industries. For the given mass flow rate the number of particles increases exponentially with decreasing particle size. High tangential velocity of rotor blades, also called tip velocity is required for ultrafine particle classification. It however also has a negative effect of increasing particle residence time and therefore increasing chances of particle agglomeration. Aim of this work is study of air classification method for applications with particle sizes below 10 microns with special focus on turbulent flow field structures and their effects on particle trajectories and final termination points.

Figure 1 Close-circuit milling system[1]

[1]Martin Adamčík for Bradley Pulverizer Company, 2016

2 AIR CLASSIFIERS

The various types of size classifiers fall into two general categories: those that separate by forces of fluid dynamics and those involving the possibility of passing through an aperture. The former is density dependent, whereas particle density considerations do not enter the latter scenario. Fluid dynamic size separation takes advantage of the differences in rates of travel of particles in a fluid arising from differences in particle size. If the rates of travel are also influenced by differences in densities, the separation is terminal sorting. Air classifiers belong to this category [28].

Numerous air classifier designs are described in the literature [22, 27, 28]. This paper will use the systematization of air classifiers which uses the separation zones as presented by Shapiro el al. [28].Four basic separation zones are known:

1. *Gravitational – counter flow*
2. *Gravitational – crossflow*
3. *Centrifugal – counter flow*
4. *Centrifugal – crossflow*

Gravitational – counter flow

The gravitational – counterflow zone exists in an air stream rising up with velocity u inside a vertical chamber with parallel walls (Figure 2). Particles experience gravity G and drag forces F_d acting in the opposite directions. Coarse particles, having terminal settling velocity V_{TS} larger than air flow velocity, move downwards, against the air stream, and fines rise with the stream [5, 28].

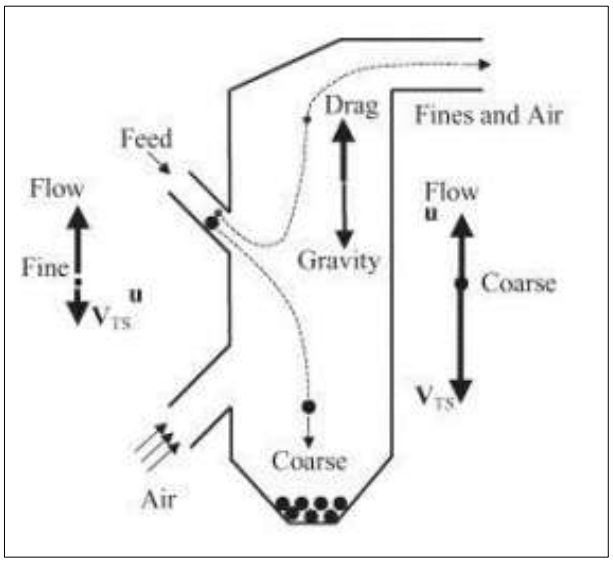

Figure 2 Gravitational – counterflow zone [28]

Gravitational – crossflow zone

A horizontal air stream entering this zone expands within a chamber and converges towards the outlet (Figure 3). Particles fed in the chamber with zero velocity accelerate horizontally by drag force F_d and also fall down. Separation occurs due to particle's vertical motion through the air stream. Each particle falls at its own terminal settling velocity. Accordingly, due to the horizontal motion they land on the bottom at different chamber locations: coarse fraction is gathered on the bottom of the chamber and fines do not reach the bottom and are carried away by the air flow through the outlet [28].

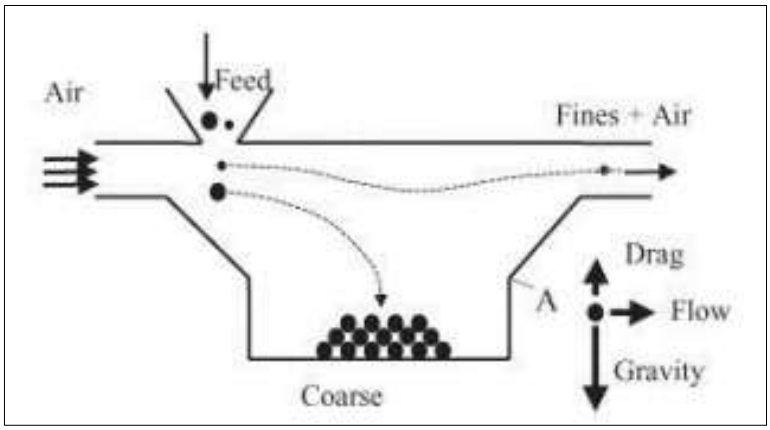

Figure 3 Gravitational – crossflow zone [28]

Centrifugal – counter flow zone

This separation zone is characterized by a flat air vortex prevailing in a cylindrical chamber with tangential inlet and central outlet (Figure 4). In this vortex air rotates and flows radially towards the chamber centre. This radial air movement serves as the particles separation track. Particles fed tangentially with air stream are involved in rotation. Due to the centrifugal force $F_{c,}$ their trajectories gradually deviate from the air streamlines. Separation is determined by the balance between F_c and the drag force component F_d induced by the radial air movement. Coarse particles drift towards the chamber walls, where they fall down to the outlet. Fines move towards the chamber axis where they are carried out by the air stream [28].

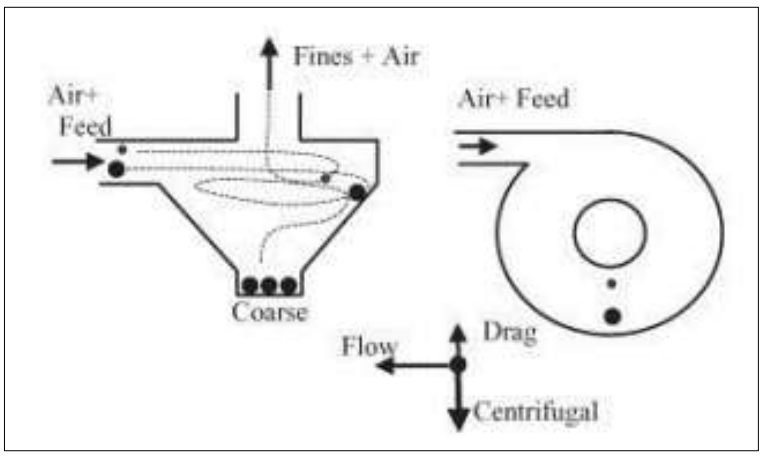

Figure 4 Centrifugal – counterflow zone [28]

Centrifugal – crossflow zone

This zone can be created in an air vortex for example in a cylindrical chamber with inlet and outlet placed on the opposite sides of the chamber axis (Figure 5). The fed particles enter with the air stream through whirl blades, which create a screw-type flow. Particles rotate while drifting radially towards the chamber walls with size dependent velocities. As they simultaneously proceed along the chamber axis they reach the wall in different locations. Larger particles arrive to the wall faster; smaller ones make it farther along the axial direction. The chamber is designed in such a way that the cut size particles reach the periphery at its edge [28].

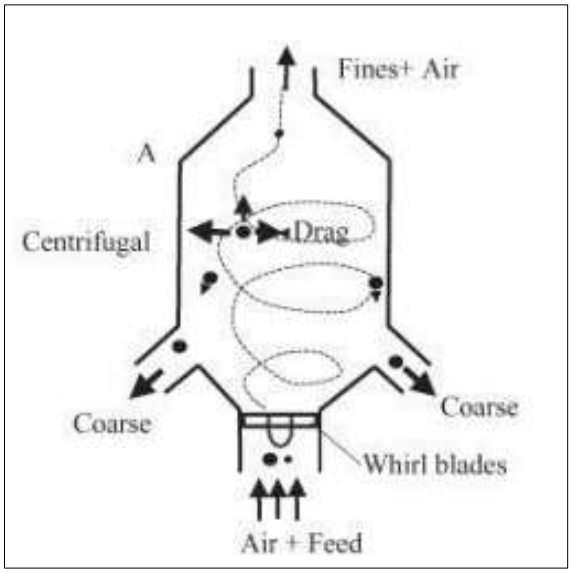

Figure 5 Centrifugal –crossflow zone [28]

3 ROTOR AIR CLASSIFIER

Guo et al. [12] described the dynamic state air classifiers development through three generations, with centrifugal and cyclone classifiers as the first and second-generation classifiers, respectively. The third generation is rotor air classifier. Compared to its predecessors, the advantage of the rotor air classifier is the employment of the rotor cage as the classifier component which can exert a radial forced centrifugal field (Figure 6). Rotor cage composed of upper base plate, lower base plate and rotor blades. As a third generation, this classifier has high classification precision and good classification performance [7, 12].

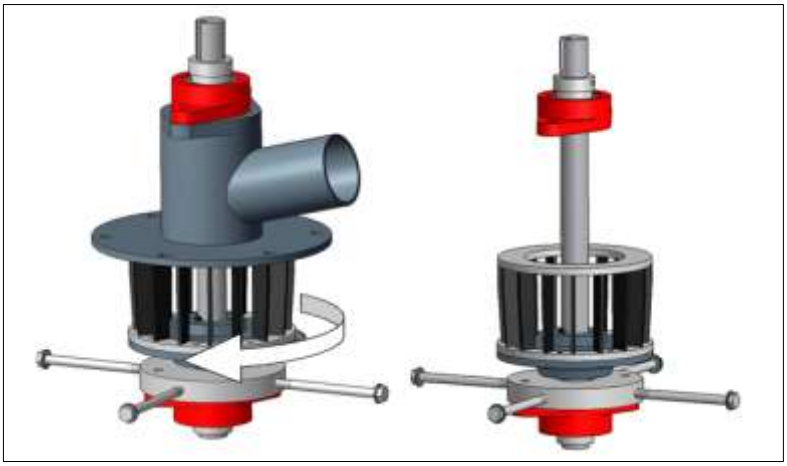

Figure 6 The air classifier rotor [34]

Numerous rotor air classifier designs are described in the literature. The main differences include the outer and inner radius of rotor cage and its position (vertical/horizontal, Figure 7), the rotor blades designs (more in 4.2.2. Structural parameters), the utilisation and design of guide vanes (more in 4.2.2.Structural parameters), the cross-sectional areas of feeding inlets, fine powder outlets and air inlets and volute height [31, 28].

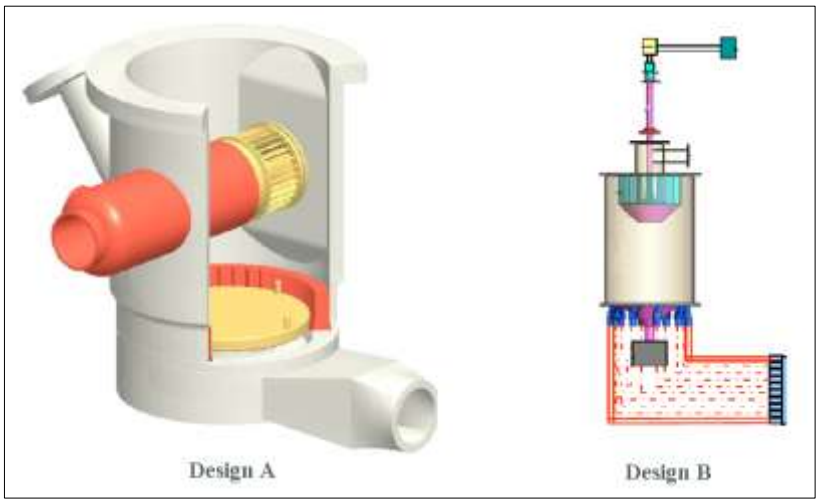

Figure 7 Horizontal (design A) and vertical (design B) position of rotor cage [42, 45]

In case of this dissertation a rotor air classifier with vertically installed rotor cage, radial blades and no guide vanes installed is used. In such classifier particles enter from the top or particle laden air enters from below and rises upwards into a conical vessel, containing a drive-activated rotor with a cone and rotating blades. These blades whirl the air to create a centrifugal – counter flow separation zone in the upper part of the vessel. These devices are used for separation of fine quartz powder, cement, ground limestone, etc. The space around the blades is arranged to form a centrifugal – crossflow zone. In this zone particle separation occurs as described previously [12, 28].

Due to a minimum of momentum exchange between air and solid phases, the centrifugal counter flow air classifier has a high sharpness of cut. Optimized design and high centrifugal acceleration enables centrifugal counter flow air classifier to work in the submicron range which is not possible for the gravity counter flow systems due to their small settling rates [8, 24].

4 ROTOR AIR CLASSIFIER PERFORMANCE

4.1 PERFORMANCE MEASURES

Performance of a rotor air classifier can be measured in terms of three major parameters [20]:

1. *The size selectivity increment (ΔS)*
2. *The sharpness of the separation (β)*
3. *The cut size (d_{50})*

4.1.1 Size selectivity increment and sharpness of the separation

In the ideal classification, it would be possible to divide the mixture of sizes into two fractions, such that one lay wholly below a predetermined cut size (called fine, Figure 8) and that the other lay wholly above it (called coarse, Figure 8). Particles with the size equal to the predetermined cut size would have 50% probability of being collected together with either fine or coarse powders [27, 31].

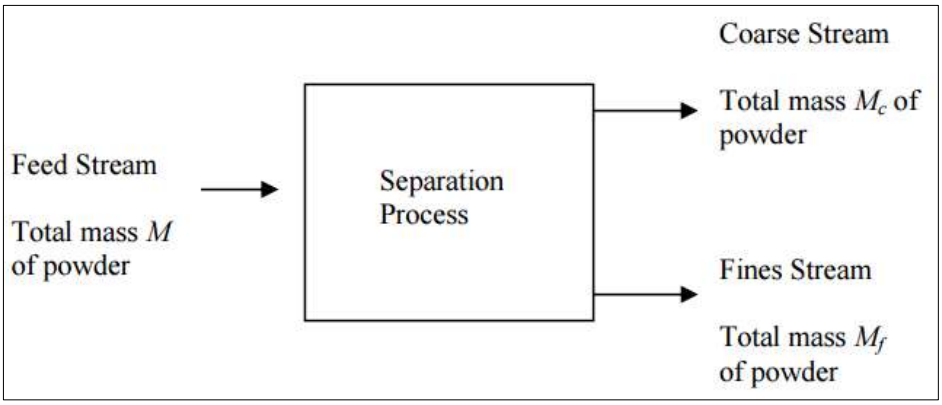

Figure 8 Separation of coarse particles from fine particles [17]

However, such ideal process does not exist due to various stochastic factors such as particle collisions during which the coarse particles can capture the fine particles or fine particles can get into the aerodynamic wake formed behind other particles, and thus some fines get into the coarse product and vice versa [15, 20, 28]. The actual classification would generally be represented by typical S-shaped grade efficiency curve, which is related to the size distribution function:

$$G(x) = \frac{M_c f_{cx}}{M f_x} \tag{4.1}$$

Where G(x) is the grade efficiency and f_{cx} and f_x are the relative frequencies of particles of the size x.

A typical plot of the grade efficiency versus the particle size is shown in Figure 9. The size selectivity S_d is defined as the ratio of the quantity of particles of size *d* in the coarse fraction to

that in the feed. For proper classification, S_d should be low for small particles and high for large particles. With reference to Figure 9, the particle size that has 50% probability of getting into the coarse fraction is called cut size – d_{cut} or d_{50}. For an ideal classifier, the S_d= 0for $d<d_{50}$ and S_d= 1 for $d>d_{50}$. The size selective coefficient (ΔS) characterizes the quantity of feed material that goes directly into the coarse fraction without classification and is given by the intercept on the abscissa of the extrapolated grade efficiency curve. The sharpness of separation (β) describes the effectiveness of a given classification. It is defined as d_{25}/d_{75}, which is the ratio of particle size with a grade efficiency of 25% to the particle size at 75% grade efficiency. For a perfect classification, it has a value of unity. The smaller the value of β is, the poorer the sharpness of classification [20].

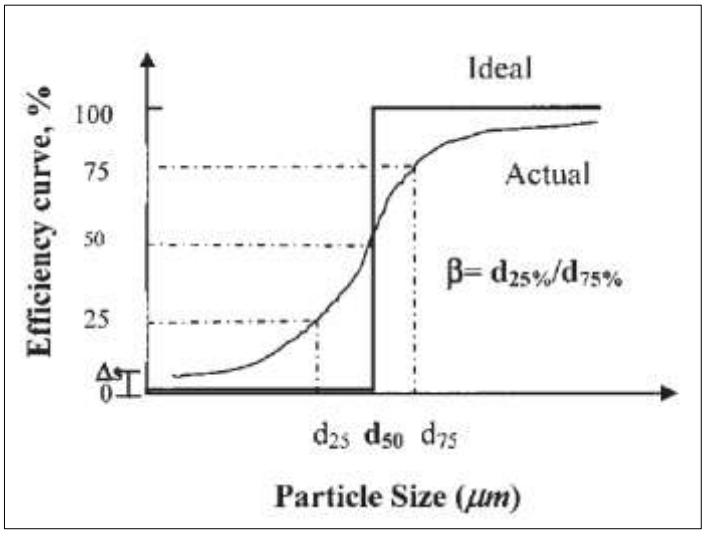

Figure 9 Ideal and actual efficiency curve in a size classifier [20]

4.1.2 Cut size

The generic mechanism for air classifier is following – the feed material to be classified is suspended in an air stream and the coarse fraction is separated from the fine fraction by the air stream by aerodynamic drag force (F_d), which usually overcomes another force, such as gravitational (F_g), Coriolis (F_{Cor}), or centrifugal (F_c), or their combination [20] (Figure 10).

The dominant forces can be considered as: the centrifugal force and the air drag force. A classifier rotor generates centrifugal forces, when particles are accelerated to the peripheral velocity of the rotor. The air drag forces result from the exposure of the particles to the gas flow which is additionally used for pneumatic transport of materials. The centrifugal force (F_c) is defined by.

$$F_c = \frac{mv^2}{r} = \frac{V_p \rho_p v^2}{r} = \frac{4\pi r_p^3 \rho_p v^2}{3r} \quad (4.2)$$

Where the V_p is the volume of the particle, ρ_p is the density of the particle, m is the mass of the particle, v is the peripheral velocity of the rotor, r is the rotor radius and r_p is the particle radius.

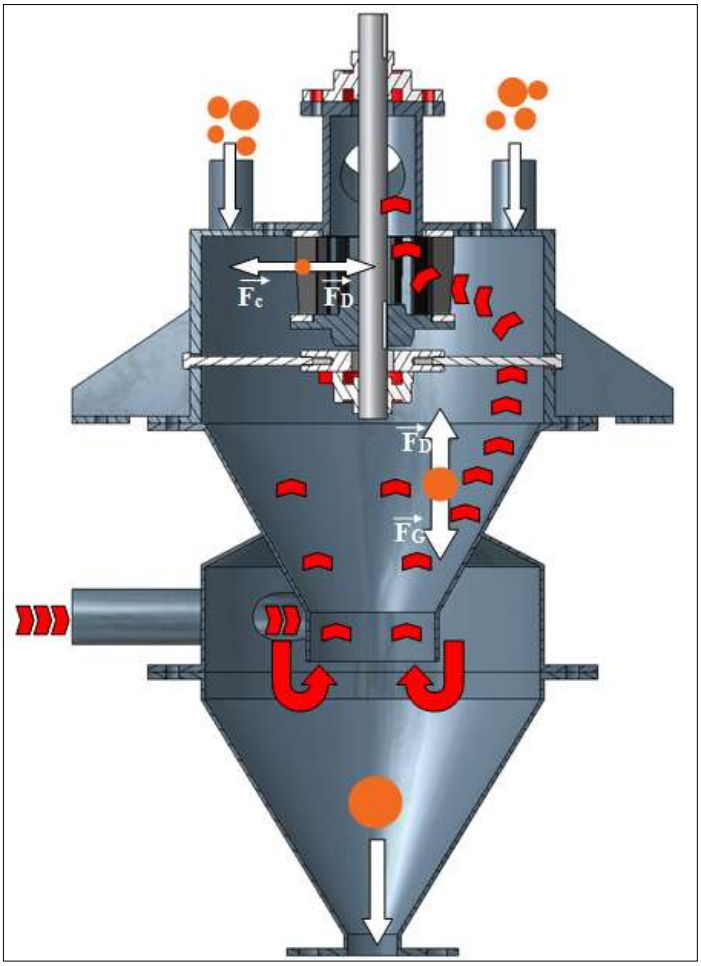

Figure 10 Rotor air classifier with flow direction and action of the forces highlighted [34]

The air drag force (F_d) for the spherical shape can be defined from the formula

$$F_d = \frac{c_d \rho A v_a^2}{2} = \frac{c_d \rho \pi r_p^2 v_a^2}{2} \quad (4.3)$$

Where c_d is the drag coefficient, ρ is the gas density, A is the cross – sectional area of the particle, v_a is the relative velocity between the fluid and the particle and r_p is the particle radius. Considering a spherical particle which is in the balance when exposed to these forces, the derived particle size will be

$$D_p = \frac{3 c_d r \rho v_a^2}{4 \rho_p v^2} \quad (4.4)$$

As it can be seen, the particle size is primarily dependent on the air and rotor peripheral velocities, which are square in function. Other factors, like drag coefficient or particle and gas density, have less effect on the separation forces. Only when very heavy or very light materials are involved or particle shape varies would there be a significant factor to consider [13, 19, 23].If the particle is small, the drag force will predominate and the particle will move with the air stream into

the fine fraction. If the centrifugal force is greater than the drag force, the particles will be deflected into the coarse fraction. The particle size for which the centrifugal force equals the drag force is called cut size. In principle, if the two forces are equal, the particles will be held in equilibrium. This equilibrium determines the cut size of an ideal classifier [20]. The centrifugal force tends to push the material towards the classifier outer walls. The drag force tends to pull the particles to the rotating cage blades. So, it is the sum of these forces which determines the trajectory of the particles to the coarse outlet or to the fine outlet. The trajectory of the particles is calculated by the integration of the momentum balance of a particle. The equation of motion of a discrete particle is formulated as:

$$\frac{\pi D_p^3}{6}\rho_p \frac{d\overrightarrow{u_p}}{dt} = \frac{\pi}{8} C_d \rho D_p^2 |\overrightarrow{v_{rel}}| \overrightarrow{v_{rel}} + \frac{\pi}{6} D_p^3 \rho_p \vec{g} + m_p\left(-2\vec{\Omega} \times \overrightarrow{u_p}\right) +$$

$$+ m_p(-\vec{\Omega} \times (\vec{\Omega} \times \vec{r})) \qquad (4.5)$$

The first term on the right-hand side represents the drag force ($\overrightarrow{F_d}$). C_d is the drag coefficient, ρ_p is the particle density, *Dp* denotes the particle diameter and the $\overrightarrow{v_{rel}}$ is the relative velocity between the fluid and the particle. The second term on the right-hand side represents the gravity force ($\overrightarrow{F_g}$) where $\vec{g}$ is the gravity vector. Since the classifier rotor rotates, the Coriolisforce and the centrifugal force ($\overrightarrow{F_{Cor}}$; $\overrightarrow{F_c}$) are taken into account. These are expressed by the two last terms on the right-hand side of the equation, where m_p is the particle mass, $\vec{\Omega}$ is the angular velocity, $\overrightarrow{u_p}$ is the particle velocity and $\vec{r}$ denotes the position vector [11, 29].

4.2 PERFORMANCE PARAMETERS

The factors that affect classification via rotor air classifier are [31]:

1. *Operational parameters*- feeding speed, rotor cage rotary speed and air inlet velocity.
2. *Structural parameters* - different structural designs
3. *Characteristics parameters of raw materials and fluid media* - the characteristic parameters of raw material and fluid media are the density of raw material, air density and air viscosity.

4.2.1 Operational parameters

To obtain theoretical formula of cut size, researches often assume minimal solid concentration and synergy among particles in the annular classification region. Based on these assumptions, the forces applied to a single particle in the annular classification region are then analysed [31]. Guo et al.[12] deduced the theoretical model of cut size in accordance with the analysis of the inner flow of the rotor air classifier, as per (4.4).

Based on the systematic analysis of calculation formulas obtained under different assumptions for findings of the cut size of the rotor air classifiers, Liu et al. [25] obtained a simplified equation as follows:

$$d_{50} = k\frac{Q^{\varepsilon}}{n^{\delta}} \tag{4.6}$$

Where Q is airflow rate and n is, rotor cage rotary speed, ε, δ and k are the parameters related to the property of materials, the temperature, humidity, and pressure of air, and the structure of the classifier. However, the authors of the theoretical model themselves admit that this method suffers from a serious deficiency as the theoretical results deviate from the actual values. For example, Zhang et al. [33] showed that theoretical values of cut size (d_{50}) are larger than the actual ones under different rotor cage rotary speeds. They concluded that maybe the theoretical air flow is greater than the actual air flow [9]. During the actual classification, particle motion in the annular classification region is complicated. Particle collision, agglomeration, and other interactions among particles influence the cut size. Researchers usually disregard these factors or fail to simplify them as coefficients in theoretical functions, which cause large discrepancies between theoretical and experimental results. In view of this shortcoming, new methods with sufficient accuracy and precision are highly desirable to determine the cut size of classifiers [9, 31].

Yu et al. [31] modelled the relationship between the cut size and the operational parameters of rotor air classifier and developed a method for establishing a prediction model for the cut size of the rotor air classifier. This method is developed on the basis of a dimensionless equation. The operational parameters are subjected to the dimensionless analysis and structural parameters of the classifier, as well as the characteristic parameters of a representative raw material and fluid medium, are used to determine similarity parameters. All these parameters are independent variables (Table 1).

Table 1 Symbols and dimension of the factors effecting classification via the rotor air classifier [31]

Factor and index	Symbol	Dimension
Gravity acceleration	g	$[LT^{-2}]$
Cross-sectional area of air inlet	A_e	$[L^2]$
Cross-sectional area of fine powder outlet	A_f	$[L^2]$
Cross-sectional area of feeding inlet	A_g	$[L^2]$
Volute height	H	[L]
Inner radius of rotor cage	R_{zn}	[L]
Outer radius of rotor cage	R_{zw}	[L]
Outer radius of guide blades	R_{dw}	[L]
Inner radius of guide blades	R_{dn}	[L]
Installation angle of the guide blades	β	
Air density	ρ_a	$[ML^{-3}]$
Raw material density	ρ	$[ML^{-3}]$
Air viscosity	μ	$[ML^{-1}T^{-1}]$
Air inlet velocity	v	$[LT^{-1}]$
Rotor cage rotary speed	n	$[T^{-1}]$
Feeding speed	Q	$[MT^{-1}]$
Cut size	d_{50}	[L]
Pressure difference	$\triangle P$	$[ML^{-1}T^{-2}]$

Using all the parameters effecting the classification via the rotor air classifier Yu et al. [31] formulated equations for group of similarity parameters. Dimensionless numbers for cut sizes are calculated by 4.7 which describes relation between force ratios expressed by common

dimensionless criteria of viscous, aerodynamical and gravitational forces together with relative dimensionless geometrical simplexes of air classifier.

$$Dr = kGr^{n1}Ld^{n2}Re^{n3}Rn^{n4}Ar^{n5}Er^{n6}Ad^{n7}Gd^{n8}Fd^{n9}Hd^{n10}Fe^{n11}Ge^{n12}\beta^{n13} \quad (4.7)$$

In examining the influence of operation parameters on cut size, Yu et al. (2014) study uses a certain structure of a rotor air classifier. Similarity parameters Ar, Er, Ad, Gd, Fd, Hd, Fe, Ge and β can be considered constants, and the dimensionless equation (4.7) can be simplified into:

$$Dr = kGr^{n1}Ld^{n2}Re^{n3}R_n{}^{n4} \quad (4.8)$$

The prediction model using the dimensionless equation considers more factors that influence the cut size of rotor air classifier than the theoretical model. Compared with the cut sizes calculated according to the theoretical model, the predicted values more strongly correspond with the experimental values as the below Figure 11 represent [31].

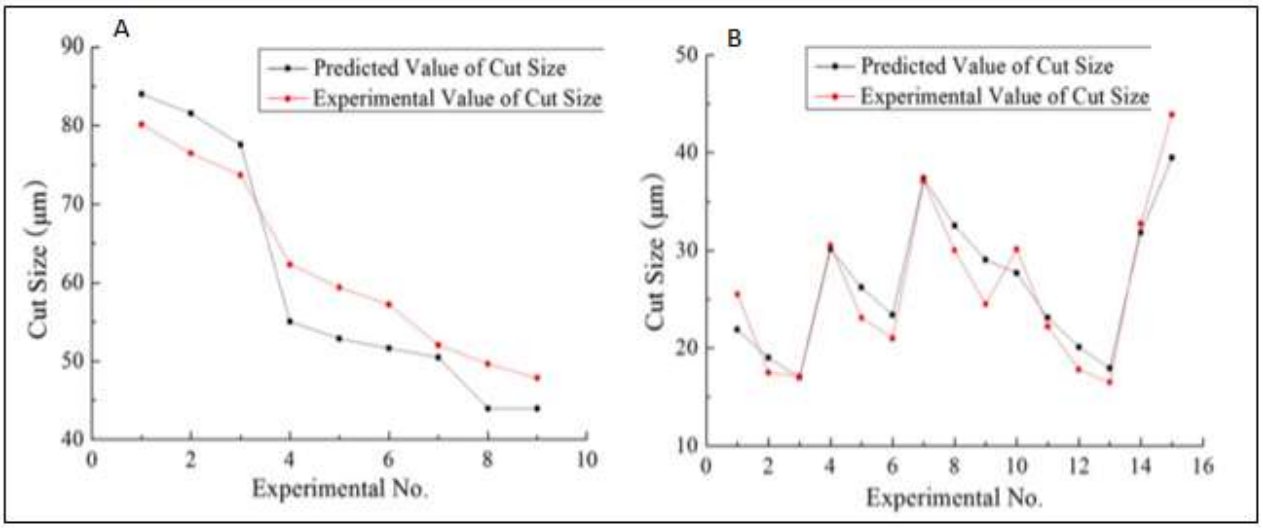

Figure 11 Comparison of experimental and predicted cut sizes for the calcium carbonate testing samples (Fig A) and for the talc powder testing samples (Fig B)[31]

Yu et al. [31] conclusions regarding the relationship between the cut size and the operational parameters of rotor air classifier are following -cut size decreases with increasing rotor cage rotary speed (Table 2, Table 3) and increases with rising air inlet velocity (Table 3). A high feeding speed increases the probability of particle aggregation as solid concentration increases. This occurrence decreases cut size (Table 2, Table 3).

Table 2 Experimental and predicted cut sizes for the calcium carbonate test samples [31]

Sample no.	Air inlet velocity v/m/s	Rotor cage rotary speed n/r/min	Feeding speed Q/kg/h	Exp d_{50}/μm	Predicted d_{50}/μm with Eq. (11)	Deviation between exp d_{50} and predicted d_{50}/%	Calculated d_{50}/μm with Eq. (1)
2–1	18	600	56.69	84	80.15	4.8	195.8
2–2	18	600	86.54	81.55	76.46	−6.6	195.8
2–3	18	600	120.81	77.55	73.67	−5.3	195.8
2–4	18	900	56.69	55.02	62.25	11.6	114.1
2–5	18	900	86.54	52.87	59.38	10.9	114.1
2–6	18	900	120.81	51.65	57.22	9.7	114.1
2–7	18	1200	56.69	50.43	52.03	3.1	77.7
2–8	18	1200	86.54	43.93	49.63	11.5	77.7
2–9	18	1200	120.81	43.93	47.83	8.1	77.7

Table 3 Experimental and predicted cut sizes in talc powder classification experiments [31]

Sample no.	Air inlet velocity v/m/s	Rotor cage rotary speed n/r/min	Feeding speed Q/kg/h	Exp d_{50}/μm	Predicted d_{50}/μm with Eq. (11)	Deviation between exp d_{50} and predicted d_{50}/%	Calculated d_{50}/μm with Eq. (1)
1	5	800	66	25.5	21.88	−14.2	35.3
2	5	1000	66	17.5	19.04	8.8	26.2
3	5	1200	66	17.1	16.99	−0.6	20.5
4	8	800	66	30.5	30.12	−1.2	56.4
5	8	1000	66	23.1	26.21	13.4	41.9
6	8	1200	66	21	23.39	11.4	32.9
7	11	800	66	37.1	37.40	0.8	77.6
8	11	1000	66	30	32.54	8.4	57.7
9	11	1200	66	24.5	29.04	18.5	45.2
10	5	600	40.2	30.1	27.66	−8.1	51.8
11	5	800	40.2	22.2	23.12	4.1	35.3
12	5	1000	40.2	17.8	20.12	13	26.2
13	5	1200	40.2	16.5	17.96	8.8	20.5
14	8	800	40.2	32.7	31.83	−2.7	56.5
15	11	800	40.2	43.9	39.52	−10	77.6

The theoretical model of calculation cut size for rotor air classifier presented by Yu et al. [31] analyses geometrically structural parameters and uses a certain structure of a rotor air classifier. Therefore, the prediction model can be applied to the rotor air classifier with similar structure as the one used during the experiment. If the structure and shape of the rotor air classifier is different, the model should be constructed according to the method Yu et al. [31] proposed.

Karunakumari et al. [20] in line with Yu el al. [31] findings concluded that cut size typically increases as the air inlet velocity increases for a constant flow rate. This can be attributed to the stronger secondary flow that is created at higher air inlet velocity within the classifier. Because the flow field scales linearly with the fan tip speed, the higher the rotational speed, the stronger will be the secondary circulation and the higher will be axial velocity. Stronger recirculation enables even larger particles to be carried away into the fine fraction. This results in an increase in the cut size. Figure 12 shows how the cut size increases with increasing fan speed.

The measured effect of feed rate on cut size is opposite to that of increasing air inlet velocity: increasing feed rate decreases the cut size. This can be attributed to the momentum coupling between the disperse phase (the particles) and the continuous phase (the circulating air). The air loses momentum in accelerating the particles from their initially small velocity to nearly the tip

speed. This momentum loss is proportional to the particle flow rate. Also, the higher this momentum loss, the less strong will be the secondary circulation. As the secondary circulation diminishes, its ability to carry away particles also decreases, resulting in increased collection efficiencies for particles in the borderline, that is, those that are just able to be carried away by the air stream. This is resulting into decreasing cut size (Figure 12) [31].

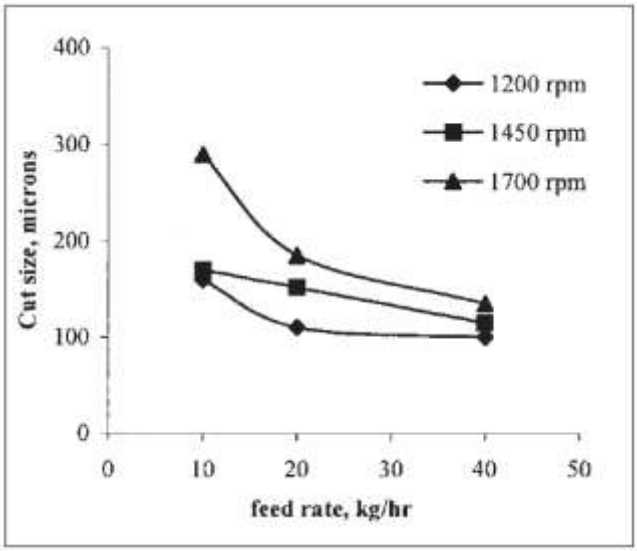

Figure 12 Effect of feed rate and fan speed on the cut size [20]

Within the scope of study of Altun&Benzer [1] was to find out correlations between the efficiency of a rotor air classifier and the operational parameters. Their findings support other experiments mentioned in this chapter. Figure 13 shows variations of rotor speed with the cut size parameter. It implies that as the rotor speed increases the cut size decreases. When the rotor speed is normalized with the air speed, steady upward trend is obtained between the air speed-rotor speed ration and the cut size [1].

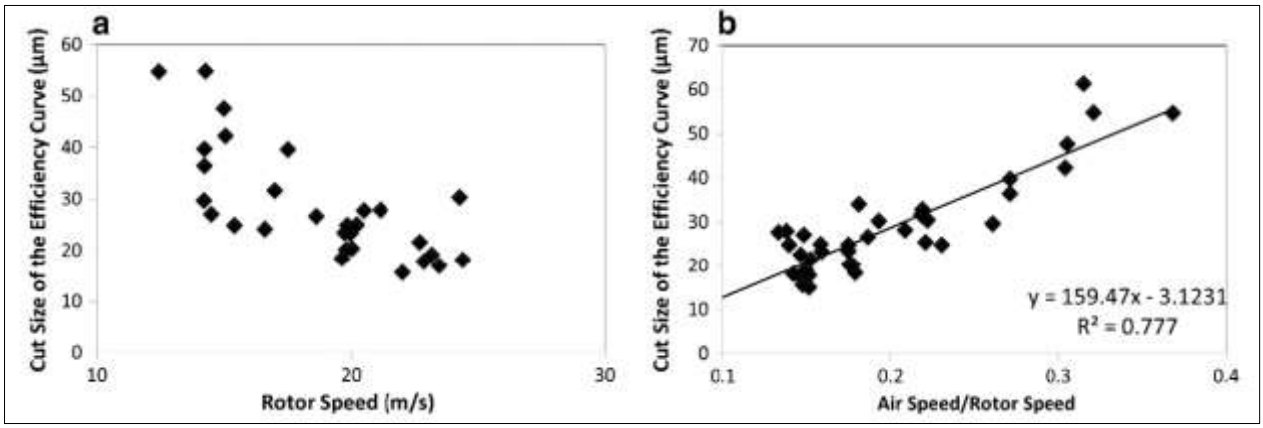

Figure 13 Trends between rotor speed-cut size (Fig a) and air/rotor speed-cut size (Fig b) [1]

Similar studies focusing on classification performance have been conducted for rotor classifiers operating in different environments, for example in water. Xia et al. **[**46] based on the analysis of the liquid-solid two-phase flow studied the trajectories of each particle by using discrete phase

model. Simulation results shows that when the inlet velocity of two-phase flow is 2m/s and the volume fraction of the particle is set as 0.1, the cut size is close to 1 μm when the classification wheel speed is 1000rpm, the cut size is close to 0.5 μm and when the classification wheel speed is 2000rpm and the cut size is smaller than 0.5 μm when the classification wheel speed is 3000rpm (Table 4).

Table 4 Comparison of the cut sizes between simulation results and experimental results [46]

Rotary speed (N)	d_{50} of simulation results	d_{50} of experiment results
1000rpm	≈1μm	1.27μm
2000rpm	≈0.5μm	0.62μm
3000rpm	<0.5μm	0.38μm

Through adjusting the operational parameters of the rotor air classifier many researchers have been devoted to the improvement of the classification performance in terms of decreasing cut size. Industrial applications require cut sizes between 100 μm and 5 μm with a tendency towards fine particles. The largest field of application is the classification of mineral products. In the mineral industry, the fine fraction is often used as product (e.g. as filler or additive). The availability of classifiers with cut sizes down to or even below 1μm would allow the production of materials with superior properties. But the production of such particle sizes is one of the most difficult tasks in the mechanical processing of powders [8, 12, 24].

Leschonski [24] summarizes the operational parameters necessary for classifications with lower cut size limit of approximately 1 μm to 2 μm for mineral particles as follows:

1. *High circumferential velocity, v_{φ}, of the air and of the particles, respectively*
2. *Reduction of the volume flow rate of air, or the size of the classifier*
3. *Operating the classifier at reduced air pressure using the so-called slip between the particles and the gas molecules*

The optimal operational parameters presented by Leschonski [24] agree with the previously presented research studies. The high circumferential velocity is achieved by high rotor cage rotary speed and reduction of the volume flow rate is related to the reduction of air inlet velocity.

Galk et al.[8] designed a new impeller wheel classifier MikroCut MC, which classifies particles from 10 μm down to the submicrone range. Galk et al. [8] as well highlighted the importance of the high rotor cage rotary speed resulting in high centrifugal acceleration for obtaining the finest fractions. Due to high centrifugal acceleration of over 15,000 x g, very fine particle size distributions with a top size below 1-2 μm can be achieved.

Yu et al. [30] pointed out that most of the current methods of optimizing operational parameters and improving the classification performance of a rotor air classifier are almost single objective decisions only for one, maximally two, of the classification performance indices (mainly cut size), like the above presented researches. Based on these findings Yu et al. [30] established multi-objective programming (MOP) model for classification performance of rotor air classifier to evaluate performance indices comprehensively and achieve optimal classification performance. They determined following classification evaluation criteria:

1. *Newton classification efficiency (η_N)* – represents resolution of qualified fine particles and non-qualified coarse particles. The meaning of Newton classification efficiency is to reflect mass-ratio of ideal classification to the total powders to be classified.
2. *Classification sharpness* – described above in 4.1.1 Size selectivity increment and sharpness of the separation
3. *Cut size* – described above in 4.1.2 Cut size
4. *Yield* – refers to the mass-ratio of finished products (fine powders or coarse powders) to raw material.
5. *Particle fineness* – it can be represented by D_{50}, D_{90}, D_{95} or D_{98}, which is the equivalent diameter of the maximum particle corresponding to 50%, 90%, 95% or 98% in cumulative distribution curve.
6. *Degree of dispersion (S)* – The degree of dispersion is expressed as $S = (D_{90} – D_{10}) / D_{50,}$ S is small and the particle-size distribution range is narrow, which means that the big particles and small particles are little in collected fine powder and there is a highly-concentrated particle-size distribution.

Discussed classification operational parameters are following: feeding speed, rotor cage rotary speed and air inlet velocity.

In the classification experiments, which Yu et al. [30] conducted for talc powders and calcium carbonate powders the optimal operational parameters from rotor air classifier were established. In both material cases, they concluded that high rotor cage rotary speed (in this case 1200 r/min) is an optimal parameter for the most efficient classification, taking into account all six above mentioned evaluation criteria. In case of feeding speed and air inlet velocity the situation is more complicated when considering all criteria.

For talc powders the optimal feeding speed is 40 kg/h and air inlet velocity 5 m/s (Table 5). In the case of calcium carbonate the optimal feeding speed is 92 kg/h and air inlet velocity 12 m/s (Table 6).

Table 5 Operational parameters and classification evaluation indexes in the talc experiment [30]

No.	Feeding speed/ kg · h^{-1}	Wind speed/ m · s^{-1}	Rotor cage's rotary speed/ min^{-1}	d_{50}/μm	K	η_N/%	Y/%	D90/μm	S
1	66	5	600	26.5	0.43	40	60	30.2	2.26
2	66	5	1000	17.5	0.47	55	45	19.8	2.52
3	66	5	1200	17.1	0.51	65	44	19.4	2.66
4	66	8	800	30.5	0.63	55	75	31.5	2.23
5	66	8	1000	23.1	0.6	60	63	28.4	2.29
6	66	8	1200	21	0.6	61	57	26.0	2.31
7	66	11	800	37.1	0.63	60	87	33.0	2.14
8	66	11	1000	30	0.64	63	78	30.7	2.18
9	66	11	1200	24.5	0.63	58	68	28.9	2.14
10	40	5	600	30.1	0.6	44	71	31.1	2.17
11	40	5	800	22.2	0.64	49	57	27.5	2.05
12	40	5	1000	17.8	0.55	52	45	20.1	2.13
13	40	5	1200	16.5	0.59	57	41	18.8	2.13
14	40	8	800	32.7	0.8	51	80	31.9	2.19
15	40	11	800	43.9	0.7	20	89	35.1	2.07

Table 6 Operational parameters and classification evaluation indexes in the calcium carbonate experiments [30]

No.	Feeding speed/ kg · h⁻¹	Wind speed/ m · s⁻¹	Rotor cage's rotary speed/ min⁻¹	d_{50}/μm	K	η_N/%	Y/%	D90/μm	S
1	48	6	600	30.5	0.24	0.39	43	80.9	1.99
2	92	6	600	32.2	0.34	0.44	33	91.4	1.79
3	120	6	600	33.2	0.17	0.44	35	95.7	1.80
4	48	6	900	30.9	0.64	0.68	35	100.4	1.46
5	92	6	900	27.2	0.51	0.62	28	94.4	1.66
6	120	6	900	26.5	0.67	0.65	29	97.1	1.58
7	48	6	1200	26.9	0.63	0.70	26	100.0	1.58
8	92	6	1200	23.1	0.56	0.76	24	92.9	1.65
9	120	6	1200	30.9	0.63	0.69	24	93.5	1.57
10	48	12	600	73.8	0.57	0.49	76	144.4	1.05
11	92	12	600	64.7	0.61	0.37	73	131.7	1.04
12	120	12	600	59.6	0.57	0.50	71	129.4	1.20
13	48	12	900	50.6	0.66	0.55	58	128.3	1.18
14	92	12	900	47.5	0.64	0.58	54	117.9	1.19
15	120	12	900	40.0	0.60	0.65	66	116.2	1.31
16	48	12	1200	36.1	0.68	0.72	47	110.1	1.25
17	92	12	1200	31.4	0.74	0.74	45	99.5	1.27
18	120	12	1200	31.8	0.64	0.76	43	104.8	1.33
19	48	20	600	84.0	0.70	0.25	82	144.2	1.04
20	92	20	600	81.5	0.68	0.21	82	141.7	1.02
21	120	20	600	77.5	0.65	0.43	78	138.8	1.05
22	48	20	900	55.0	0.63	0.44	68	121.6	1.06
23	92	20	900	52.9	0.73	0.45	64	122.5	1.07
24	120	20	900	51.6	0.75	0.63	63	124.5	1.15
25	48	20	1200	50.4	0.66	0.57	58	108.0	1.10
26	92	20	1200	43.9	0.66	0.68	53	111.4	1.19
27	120	20	1200	43.9	0.67	0.57	54	105.9	1.14

Interesting comparison is between Yu et al. [30] findings and Yu et al. [31] findings in case of cut size for rotor cage rotary speed of 600 r/min, air inlet velocity 6 m/s and increasing feeding speed. Under these experimental condition results are the exact opposites (Table 7). But as under all other experimental conditions the results are in line, it is assumed that this is a typing error.

Table 7 Yu et al. [31] and Yu et al. [30] experimental results

Sample no.	Air inlet velocity v/m/s	Rotor cage rotary speed n/r/min	Feeding speed Q/kg/h	Experimental cut size d_{50}/μm
1	6	600	56.69	33.23
2	6	600	86.54	32.22
3	6	600	120.81	30.52

No.	Feeding speed/ kg · h⁻¹	Wind speed/ m · s⁻¹	Rotor cage's rotary speed/ min⁻¹	d_{50}/μm
1	48	6	600	30.5
2	92	6	600	32.2
3	120	6	600	33.2

Based on presented experimental studies it is obvious that all three operational parameters, rotor cage rotary speed, air inlet velocity and feeding speed, should be in certain balance to obtain the most effective classification process. It is essentially the balance between the centrifugal and air drag force that determine the cut size of the classification. As observed, typically, if the air drag force is constant (constant air flow rate), a higher centrifugal force (higher rotor speed) will

provide finer classification and vice versa. However, if forces are altered to the same extent (both increase or decrease), the fineness will remain unchanged, but the classification efficiency will be different (Table 2, Table 3, Table 5, Table 6) [23].

4.2.2 Structural parameters

A reasonable structure design can improve the classification performance of a rotor air classifier. Therefore, many studies have been conducted on the structure of an air classifier, especially on the structure of rotor cage [8, 16, 26].

Structural parameters include the outer and inner radii of rotor cage and its position, the installation angles of rotor cage blades and, if present, the outer and inner radii of guide vanes and their installation angles, the cross-sectional areas of feeding inlets, fine powder outlets and air inlets, as well as volute height [31]. There are multiple studies focusing on different structural adjustments, mainly of the rotor cage area, and their relations to the rotor air classifier performance.

For example, in recent studies, the guide vanes are identified as an important functional unit in a turbo air classifier, which maintains the uniform of the annular region flow field. Liu et al [26] analysed the upward axial velocity in the annular region of a rotor air classifier and confirmed that it was responsible for a change of the airflow velocity direction and decreasing stability of the flow field. Based on the findings they introduced new classifier guide vanes which incline along the rotating axis and confirmed that the axial inclined guide vanes can decrease the upward axial velocity in the annular region and keep the flow field more uniform. The calcium carbonate classification experiment results showed that the cut size decreased by 0.97–8.42 μm and the accuracy increased by 6%–9% (Table 8).

Table 8 Comparison of D_{50} and K between the structures T-0 (traditional guide vanes) and T-2.5 (axial inclined guide vanes) [26]

Operating parameters	D_{50}/μm		K/%	
	T-0	T-2.5	T-0	T-2.5
6–800	23.6	19.9	46	54
9–800	28.0	25.4	72	78
12–800	42.6	34.2	59	66
9–1100	26.3	24.5	70	79
12–1100	30.2	29.0	65	73

Huang et al.[16], as well, focused in their study on the guide vanes of the rotor air classifier as an important functional unit of the classifier. They introduced new curved guide vanes which should realize an ideal flow field wherein air velocity is kept uniform in the annular region. The researchers found out that in the air classifier with positively bowed guide vanes, the velocity deviation is significantly decreased along circle lines of different radii in the annular region. The tangential and radial velocity distributions are also uniform. The guide vanes structural variations dramatically influence the flow field in the passageway of the two rotor cage blades. For the bowed guide vanes, the air flow tangential velocity is approximately equal to the tangential

velocity of the rotor cage blade exterior edge. Consequently, the intensity of the inertia rotating vortex in the passageway of the two rotor cage blades is evidently decreased. And decreased vortex intensity is apparently advantageous for material classification (Figure 14) [16].

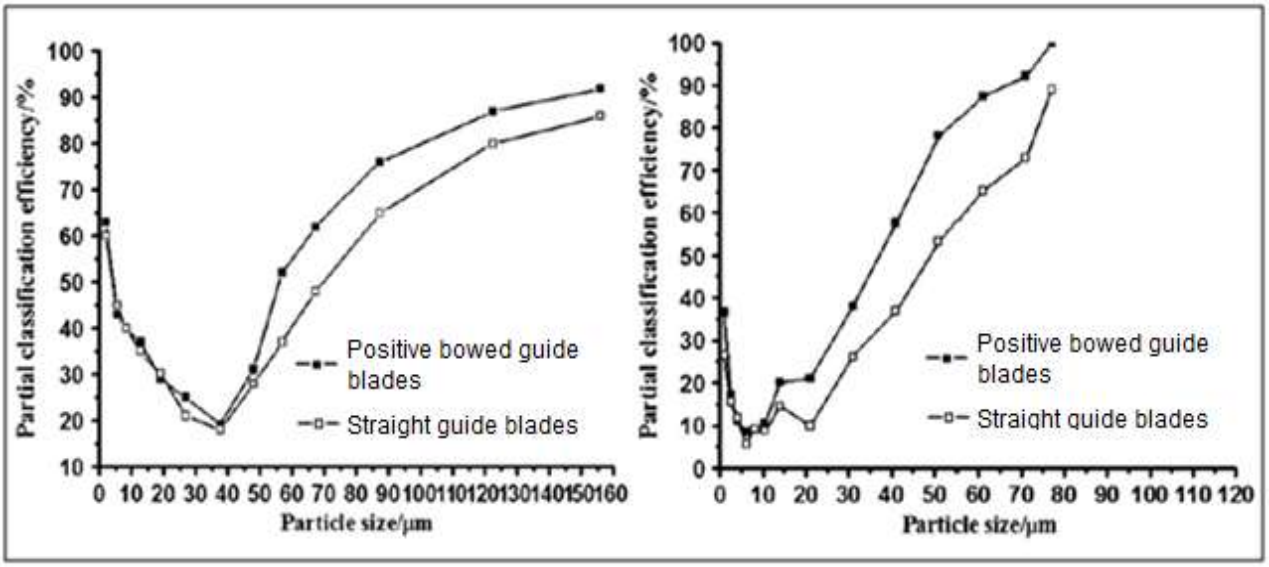

Figure 14 Tromp curve for rotor speed 600 r/min and 1200 r/min

These are two examples of studies focusing on the effect of guide vanes on the rotor air classifier performance. As the classifier used in the experimental study does not incorporate guide vanes, this was not further analysed. Next chapter focuses on the rotor cage blades themselves and their role in the classification process.

Rotor cage blades

The rotor air classifier can have different rotor blade arrangement angle. Depending on that the rotor can be divided into three groups (Figure 15) [47]:

1. *Forward-blade, where y>0*
2. *Radial-blade, where y=0*
3. *Backward-blade, where y<0*

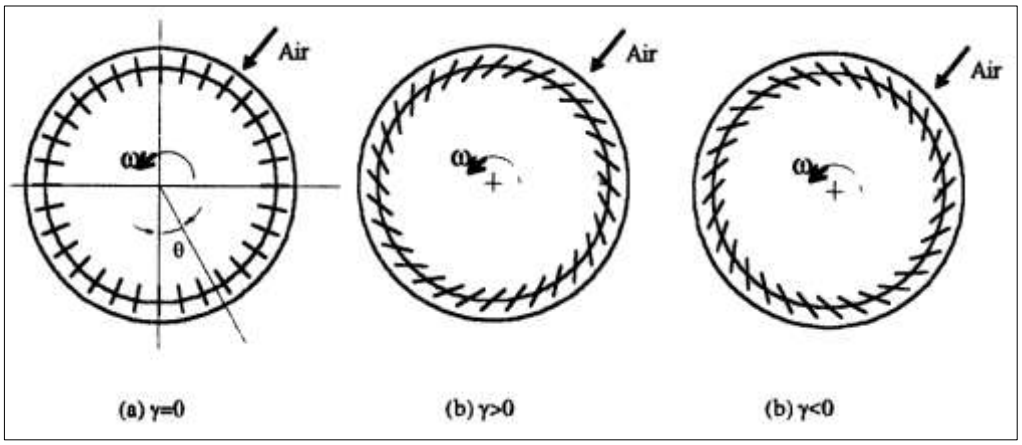

Figure 15Air classifier rotor types depending on the rotor blade arrangement angle [47]

Main attention will be focused on the radial-blade rotor air classifier and its comparison with the forward-blade and backward-blade, as this is the type of rotor which will be used during the experiment.

The flow in the radial-blade rotor air classifier can be divided into three characteristics regions. The first region is the one between the classifier blades, where a forced vortex is observed (Figure 16, region I). This vortex is characterised by increasing tangential velocity. Two regions with opposite dependences of the circumferential velocity on the classifier radius can be distinguished between the blades and the centre of the classifier (Figure 16, region II). In the region where the tangential velocity increases with decreasing radius the particles reach a radius where equilibrium between the centrifugal and the drag force exists. In this case the particles are not transported further to the interior of the classifier and remain at this trajectory. In the centre of the classifier the flow exhibits characteristics similar to the forced vortex (Figure 16, region III) [45].

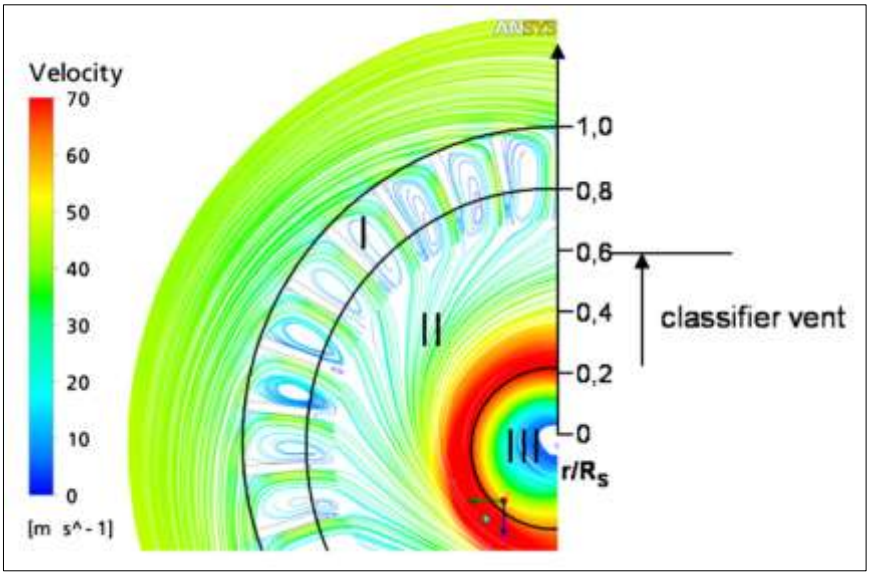

Figure 16 Calculated flow pattern at the rotor air classifier [45]

Toneva et al. [45] focused on experimental and numerical investigations of the single-phase flow in an air classifier mill. Using 2D-PIV[2] and CFD[3] solver they studied the flow between the radial blades of the rotor. The forced vortex formation which they identified between each neighbouring classifier blades influenced the separation behaviour. Even though this vortex should be favourable for the separation process, because it is characterised by increasing tangential velocity and the cut size decreases with increasing tangential velocity, the total separation efficiency strongly decreased. The vortex led to a confinement of the cross-section area available for the particles-laden flow to enter the wheel. Therefore, the mean radial velocity increased which shifted the grade efficiency curve to coarse particle sizes.

Similar results presented Feng et al. [7], who focused in their research on analysing the reasons for the poor performance of the classifier. In line with Yu et al. [31], Karunakurami et al. [20] and Altun et al. [1] findings they obtained high classification precision by adjusting the operating

[2] Two-dimensional Particle Imagine Velocimetry (more in 4.3.2 Online measurement techniques)
[3] Computational Fluid Dynamics (more in 4.3.1 Software modelling)

parameters – the air inlet velocity and rotation speed of the rotor. To assess different operating parameters that contribute to classification performance they conducted flow field velocity measurements by laser Doppler velocimetry (LDV) and carried out experiments of raw material to testify the results of the flow field measurements (Figure 17).

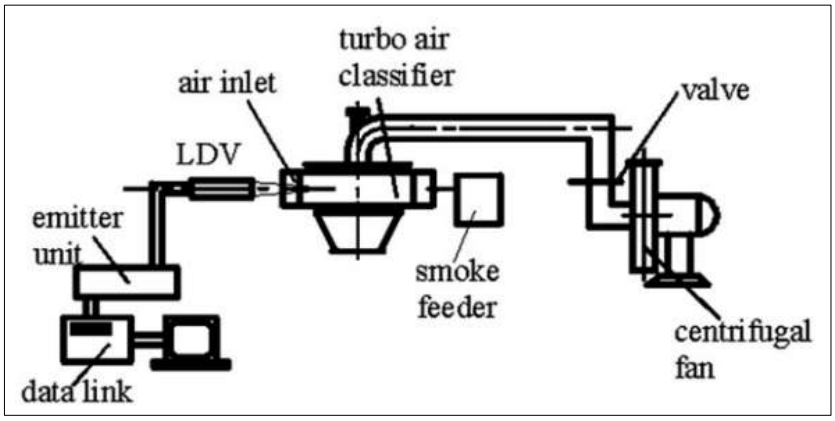

Figure 17 Schematic diagram of the measurement systems of flow field [7]

Feng et al. [7] obtained 2D vector graphs of the revolving flow field based on the tangential and radial velocity in the passageway of rotor blades. Figure 18 shows the revolving flow field characteristics at an inlet velocity of 8m/s and at rotor rotating speeds of 100, 600 and 1200 r/min.

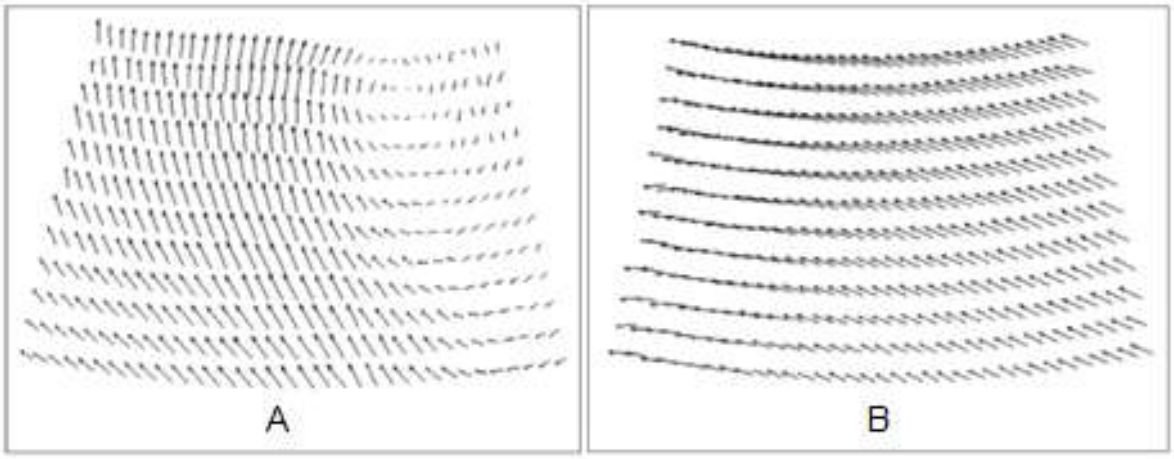

Figure 18 2D vector graphs of the revolving flow fields for A (100r/min; 8 m/s) and B (1200r/min; 8 m/s) [7]

The vortex is present under all three operating parameters. However, the intensity, position and rotation direction of the vortex is different with the difference in operating parameters. Feng et al. [7] are taking vortex as disadvantageous element for the classification because it makes the air velocity unequal in the same arc line of the revolving flow field. Furthermore, the presence of vortex may result in coarse powder getting into fine powder and vice versa, decreasing the classification precision. Authors concluded that in the classification process, vortex should be

avoided if possible[4]. It is impossible to eliminate vortex completely because of the structure effect of the rotor. Therefore, Feng et al. [7] derived the measures to decrease the intensity of the vortex by changing the operating parameters. Figure 18 shows that the effect of vortex is the least at rotor rotation speed of 600 rpm.

From Figure 19 it is obvious that if we are taking into account only cut size, same as above presented studies [20, 31, 45], the best situation for achieving the finest particles is high rotor cage rotary speed and low inlet air velocity. But for achieving high classification sharpness the rotor cage rotary speed and inlet air velocity must be in certain balance. Feng et al. [7] calculated that when the tangential velocity of the rotor blade exterior edge and the tangential velocity of the air flow in the rotor exterior edge are approximately equal, the intensity of the vortex is the least under the experimental operating parameters. They obtained high classification precision by carrying out the experiment of ground calcium carbonate for an air inlet velocity of 18 m/s and a rotation speed of 1200 r/min, and for and air inlet velocity of 14.5 m/s and a rotation speed of 900 r/min [7].

Classification experiment results

Inlet air velocity (m/s)	Rotation speed (r/min)			
	1200		900	
	Classification sharpness index	Classification particle cut size (μm)	Classification sharpness index	Classification particle cut size (μm)
26	0.61	65.51	0.65	91.24
20	0.64	58.85	0.63	75.38
14	0.64	43.94	0.69	55.65
8	0.51	25.7	0.55	37.47

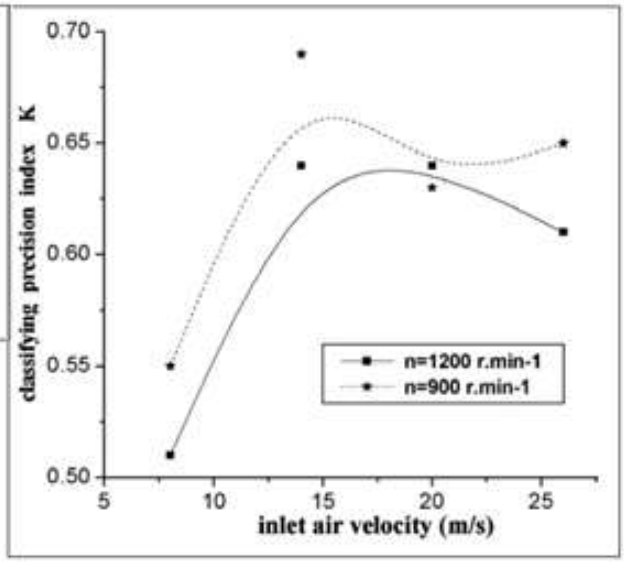

Figure 19 Calculation experiment results and relation between classification sharpness index k and air inlet velocity [7]

Equivalent results presented Xu et al. [48]. For radial blades at low rotor speed (n=2000 r.min $^{-1}$), the observed flow field between the blades was fairly uniform, with only minor fluctuation at the outlet. With increasing rotor speed (n=4000 r.min $^{-1}$), the flow field begun to be unsteady and reverse whirling appeared. When the speed reached n=6000 r.min $^{-1}$, strong reverse whirling took place because of increased turbulence, resulting in marked change in the velocity vector (Figure

[4]Guizani et al. [11] developed a detailed study of vortex in the rotor air classifier. Based on their findings it is not the vortex itself what is causing the decreasing of the classification performance, but the vortex breakdown. There are two types of vortex breakdown: 1) bubble type and 2) spiral type. In the dynamic classifier, the first type is dominant. The bubble-type vortex breakdown can be described as an abrupt change of flow structure forming free stagnation points or recirculation zones having the shape of bubbles. These bubbles appeared in the vortex axis of the flow consisting of asymmetric double recirculation zones. These recirculation flows are the most responsible factors for the entrainment of the fine particles in the coarse fraction that we have called the fish-hook effect. The vortex breakdown is disadvantageous for the classification. In general, the vortex breakdown and these secondary recirculation flows decrease the classification efficiency and should be avoided if possible [11].

20). Reverse whirling fluid made part of the separated fine particles rebound to the classifier district, therefore lowering both the grade efficiency and grade precision.

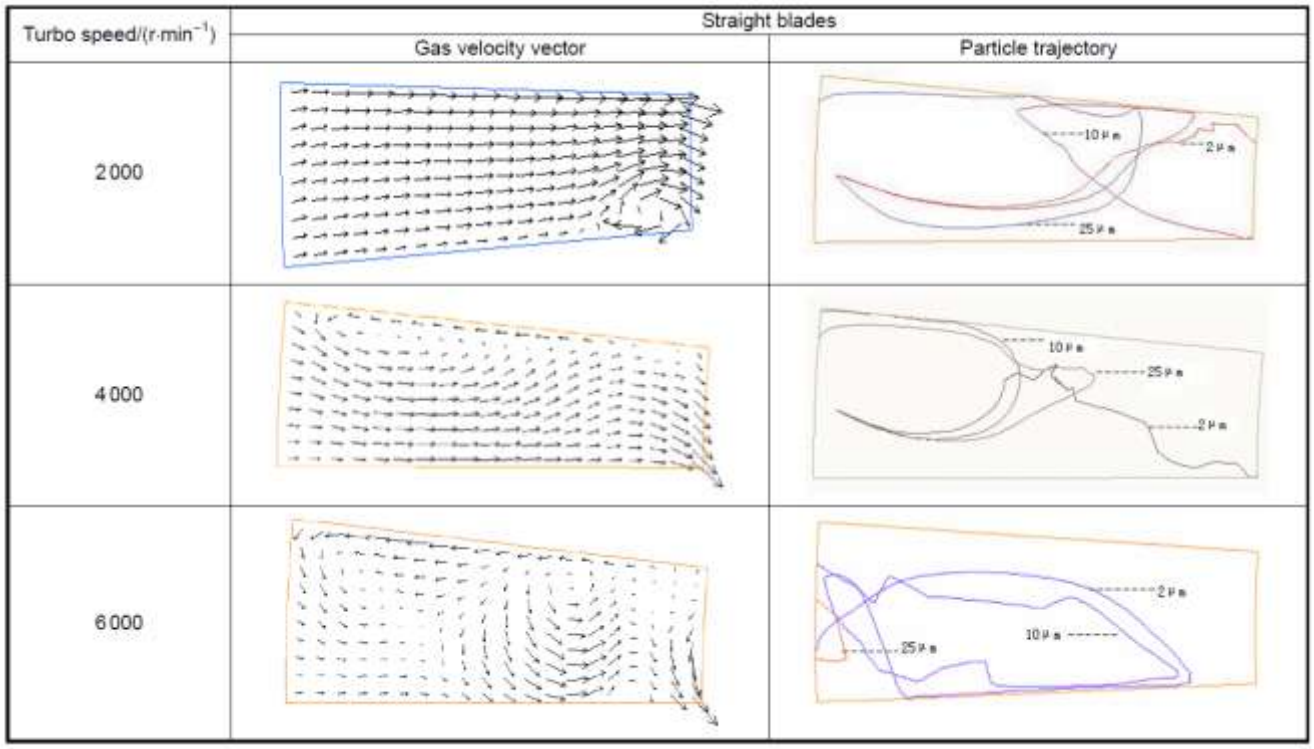

Figure 20 Simulated velocity vectors and particle trajectories for straight blades.

Ren et al. [49] analysed the influence of rotor blade configuration on flow field and were comparing the flow field of rotor cage with radial and non-radial arc blades using CFD simulations. They confirmed that between radial blades the flow was not well-distributed. Large radial velocity gradient caused back-mixing of both coarse and fine particles. Some coarse particles were dragged into the rotor cage by airflow with the action of the large radial velocity near the pressure side of the rotor blade. These coarse particles were then collected as fine powder. However, some fine particles that were dragged into the channels of the rotor cage returned to the annular region and mixed with the coarse powder by airflow with the positive radial velocity near the suction side of the rotor blade. As result, the classification accuracy decreased (Figure 21).

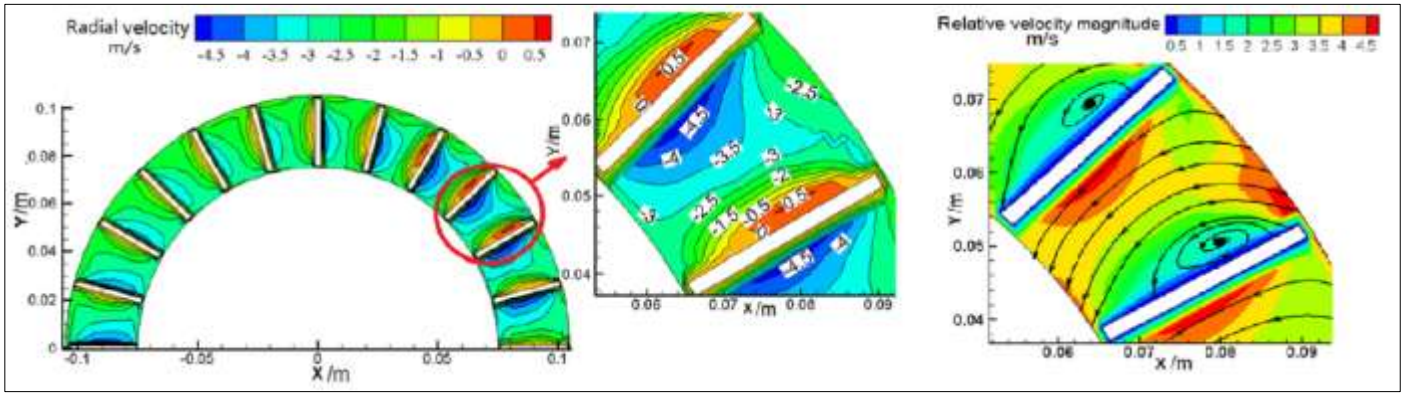

Figure 21 Radial velocity distribution and streamlines between radial blades

The classification performance of the rotor air classifier may be improved by modifying the blades shape and arrangement angle.

Xu et al. [48] as well as Ren et al. [49] observed significant improvement in grade efficiency and grade precision by installing non-radial arc blades (Figure 22, Figure 23). The flow with arc or crooked blades is reported as steadier compared to the radial blades. Ren et al. [49] results indicated that the classification accuracy of classifier with arc blades compared to radial blades increased by 10.6% - 40.8% and the fine powder yield is increased by 12.5% - 40.1%. This happened due to the arc rotor blade with concave pressure side which decreased the velocity gradient and probability of air vortex in the rotor cage. When the relative velocity angle was equal to the rotor blade installed angle, the incidence angle between the airflow and rotor blades was zero. This situation avoided the impact of airflow and particles on the rotor blades and the well-distributed flow field in the rotor cage improved greatly.

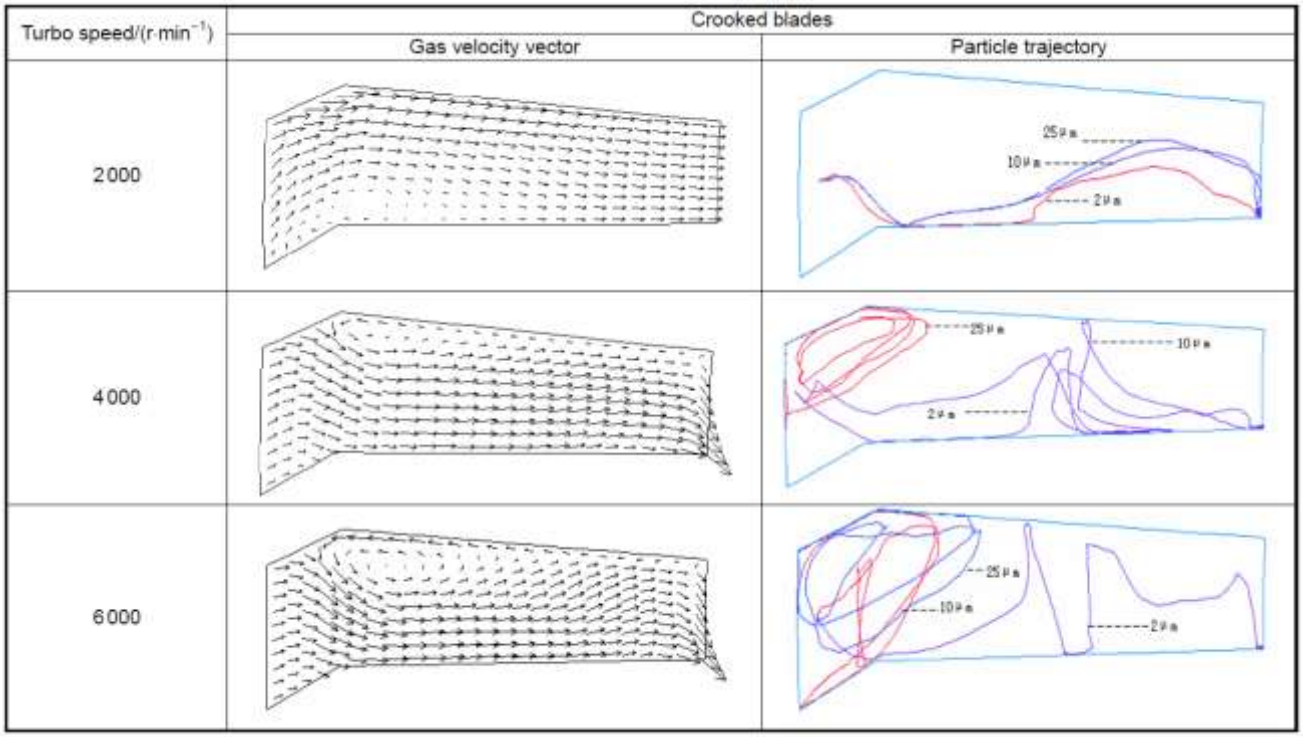

Figure 22 Simulated velocity vectors and particle trajectories for crooked blades [48]

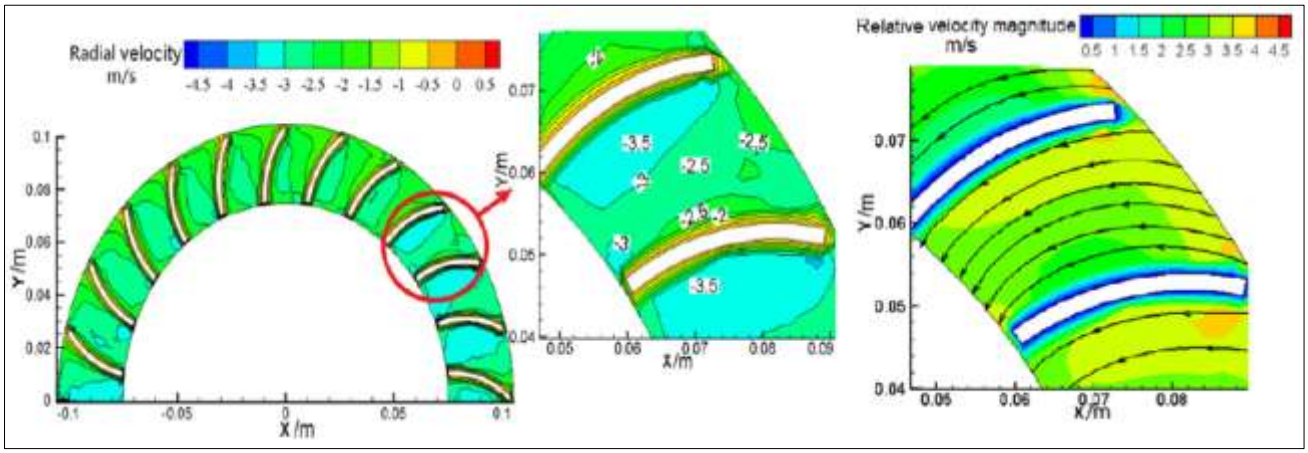

Figure 23 Radial velocity distribution and streamlines between arc blades [49]

Similar studies were conducted for hydro rotor classifier by Xia et al. [46] with alike results confirming that the classification performance is better for the arc rotor blades when compared to the radial blades. By using Eulerian multiphase flow model, RNG k−ε turbulence model and multiple reference frame (MRF) method, they studied the influence of different blade angles on the classification performance. When the blade angle is 15-30 degrees, the classification performance was the best and the classification efficiency was highest (Figure 24).

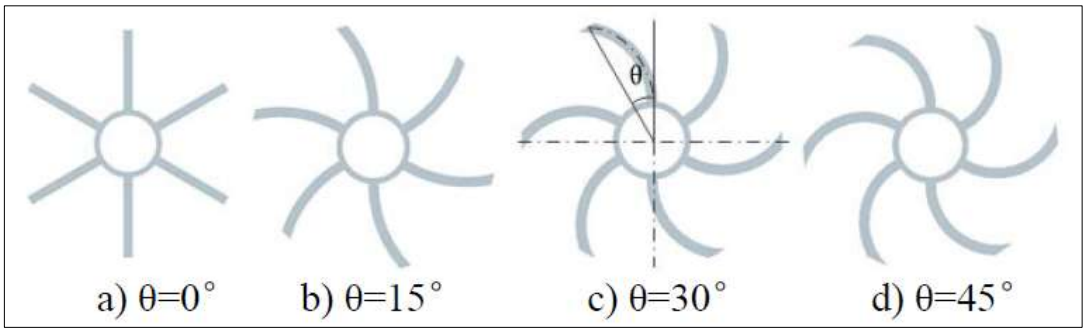

Figure 24 Geometric model of rotor air classification wheel

Xing et al [42] analysed the flow field formation in rotor air classifier with blades installed in an angle of 45 degrees using 2D-PIV and CFD modelling. In contradiction to Xu et al. [48] and Ren et al. [49] they measured strong vortex which formed between the two adjacent blades, pushing back the flow out of the channel. The results showed that vortex swirling flow existed between the two blades or in the near annular region. Within a certain range of impeller rotation speed, the vortex centre located in the middle of the blade channel and when the speed further increased it departed from the middle location toward the downstream blades (Figure 25). The swirling intensity increased with the total air flow rate, while the cortex centre barely changed. The classification performance experiments showed that the overall classification efficiency firstly increased with increasing rotation speed, but then decreased with the further increase of the speed.

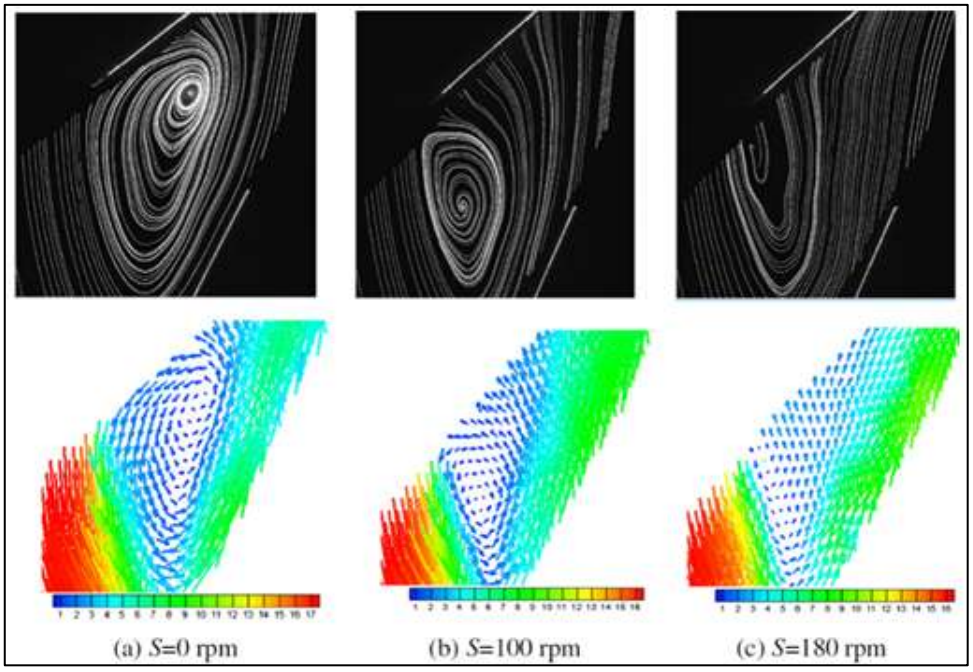

Figure 25 Streamlines and velocity vector contour between two adjacent blades under different rotor rotary speed [42]

Even though the performance results of air classifiers with arc rotor blades designs are very promising, mainly the most recent ones [48, 49], there are also studies which are suggesting that the classifier with radial blades offer optimal performance results when classification particle cut size as well as classification precision are considered [50].

For example, Wang et al. [47, 50] were comparing the performance of classifiers with radial rotor blades and those with inclining blades angle equal to -30 degrees and +30 degrees. Based on the performance results they agreed that the inclining angle of the rotor blades should be 0 degrees if both particle cut size and classification precision are considered (Table 9). When the inclining angle of the blades increased, the fluid flow gradually became turbulent flow and the resistance to the particles in the classification zone decreased, so the large particles more easily passed through the rotor and become fine particles. As the result, classified particle cut size became larger.

Table 9 Classification precision and efficiency for radial blades and inclining blades with +30 and -30 degrees' angle (D_{50} = cut size, E_T = deviation, η = classification sharpness index, η_N = Newton's classification efficiency)

Classification precision and efficiency			
Inclining angle of turbine blades	+30°	0°	−30°
D_{50}	9.4	8.2	7.2
E_T	1.45	2.05	2.98
η	1.34	1.79	2.70
η_N	0.73	0.72	0.59

From the Table 9 it is obvious that for achieving the best classification particle cut size the rotor with inclining blades with -30 degrees' angle was ideal, but the classification precision was

affected. On the other hand, taking into account only the classification precision, the rotor with inclining blades with +30 degrees' angle was optimal as with the increasing in inclining angle of the blades the fish-hook effect decreased and the classification precision increased. The radial blades seemed as optimal solution [47, 50].

To clearly determine the ideal rotor blades configurations for the air classifier, more studies are needed to reveal the solid-gas interactions in the blades region under different conditions.

4.3 PERFORMANCE ANALYSIS

Until the beginning of 1970s for testing of air classifiers a so called black box method had been used, where the input and output streams of solids were analysed for their particle size distributions. Hereby no detailed information about the process inside the classifier could be obtained. This theory could explain the phenomena only for low particle concentrations. At higher concentrations, direct observation and measurement of the motions of solid particles and gas became essential [38].

In 1973 Bernotatet al. [38] published air classifier performance study using spark tracing method as described by Bomelburg et al. in 1959 [39]. Bomelburg et al. [39] showed that it is possible to photograph patters of flow of air currents by means of spark traces. For this purpose, a limited sequence of high frequency pulses is fed to a spark gap, which is arranged in the air current under examination. The plasma of the first spark is carried away by the air current, so that the subsequent spark paths trace the further development of the moving plasma, which can then be photographically recorded.

Bernotat et al. [38] used the spark tracing method and high-speed photography to investigate the flow conditions inside a cross stream air classifier. The photographs obtained during the experiment clearly demonstrated the increasing mutual interplay between gas flow and particle stream with increasing concentration of the solid (Figure 26). The results showed that in fluid-solids systems the method can generally be used up to volume concentrations of approximately 1 x 10^{-2}.

Figure 26 Spark tracing photograph, limestone particles being injected [38]

Today, more sophisticated methods are used to analyse the rotor air classifier performance. These can be divided into three groups:

1) Numerical modelling – numerical models of the air classifier performance using available software, for example ANSYS CFD(FLUENT, CFX),OpenFOAM, and similar

2) On-line measurement techniques – methods of data collection during the classification process, for example Particle Image Velocimetry (PIV) 2D, Stereoscopic PIV, Tomographic PIV, Digital Manometer, and similar

3) Output analysis – particle size analysis (laser diffraction method[5], sieve method [32,49]), weight fraction analysis, moisture analysis, morphology, and similar

Next chapters will predominantly focus on the methods used in the experimental part of this dissertation

4.3.1 Numerical modelling

In view of the theoretical models of air classification performance shortcomings, new methods with sufficient accuracy and precision are highly desirable to determine the performance of the rotor air classifiers. While there has been a continuous evolution of the design of air classifiers, systematic theoretical and modelling studies are of recent origin. Software modelling, in case of this dissertation Computational Fluid Dynamics (CFD) technology, has become a promising tool to solve these complex calculation problems [6, 9].

Researchers, equipment designers and process engineers are increasingly using CFD to analyse the flow and performance of process equipment such as rotor air classifiers. CFD allows in depth analysis of fluid mechanisms and local effects in these types of equipment by solving mathematical equations that govern processes such as fluid flow, mass transfer, heat transfer, etc., using a numerical algorithm. In many cases this results in improved performance, better reliability, more confident scale-up, improved product consistency, and higher plant productivity. Introduction of CFD made it possible to investigate far more parameters than before and provided new possibilities for the rotor air classifier performance monitoring. The application of CFD to air classifiers and other types of gas-solid separators is well documented in the literature. In case of rotor air classifier FLUENT is particularly very useful, which is a dedicated CFD software for fluid flow problems in complex geometric regions. FLUENT is widely used to analyse flow field characteristics and particle trajectories [2, 9, 23].

Since the first CFD calculation of the flow field in an industrial cyclone was done by Boysan et al. [3], extensive studies have been conducted to improve computational capabilities and model qualities. In the field of modelling confined swirling flow, an important issue is the accurate description of the turbulent behaviour of flow. A number of turbulence models are available, such as the standard k-ε model, the RNG k-ε model, realizable k-ε model and the Reynolds stress model [18].

The first CFD simulations used in the air classification field were simulations of cyclone. Griffiths et al. [10] carried out an investigation to examine the usefulness of a CFD package to

[5]For example: HELOS-laser method [32], LS-POP laser particle sizer [7, 12, 16], EasySizer20 laser particle sizer [26, 49], Analysette 22 laser particle sizer [18], BT-9300S laser particle sizer [52].

model the collection performance of a range of small sampling cyclones. CFD package FLUENT has been used to model the performance of three types of small cyclone aerosol samplers. The CFD predicted pressure drops for the sampling cyclones were shown to be in excellent agreement with the measured data. This modelling approach was also able to predict the features of the cyclone flow field in great detail, thus provided a better understanding of the fluid dynamics of these devices. Performance curves were also derived for the three types of cyclone samplers from the application of CFD and three semi-empirical theories. CFD engineered performance curves, for example for a type of cyclone considered by Kim et al. [21] have been shown to be a more accurate reflection of experimental results than performance curves derived from three semi-empirical theories (Figure 27).

Overall the authors concluded that the results obtained from the computer modelling exercise have demonstrated that CFD is a reliable and relatively inexpensive method of examining what effects had a number of design changes on the performance of three types of relatively small cyclone sampler. They agreed that this method of analysis is almost certainly less expensive than experiment, and represents a cost-effective route for design optimization [10].

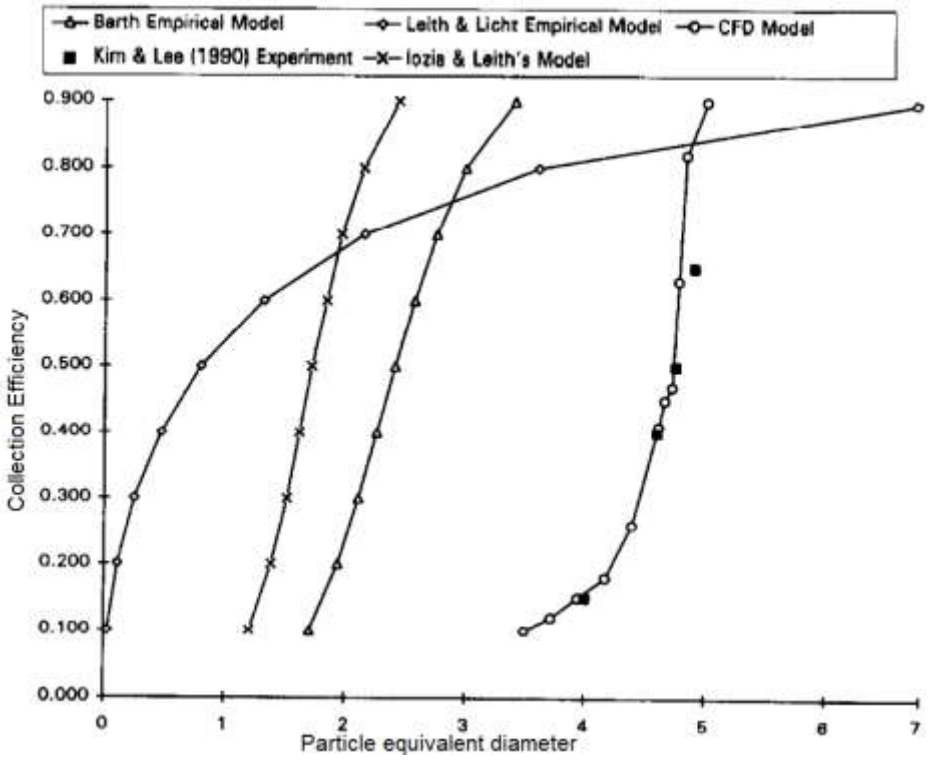

Figure 27 Calculated and measured collection efficiencies for Kim and Lee (1990) cyclone [10]

One of the first comparisons of three CFD turbulence models - standard k-ε model, the RNG k-ε model, and the Reynolds stress model in terms of the ability to predict the strongly swirling flow in cyclone was carried out by Hoekstra et al [14]. Both the k-ε model and the RNG k-ε model predicted an unrealistic distribution of axial and tangential velocities, and therefore the authors concluded that these are unsuitable for calculation of the cyclonic flow. Results obtained with the Reynolds stress model were in reasonable agreement with the experimental data, although still some discrepancies existed which plead for further improvement. They recommended future

extensions of this work including the numerical prediction of the cyclone collection performance. They suggested that for a specifics geometrical layout of a cyclone, this may be done by (1) solving the gas flow filed using the Reynolds stress model, and (2) Lagrangian tracking of a number of particle size classes to obtain complete grade-efficiency curves. In this way, the performance of a specific cyclone design could be determined in terms of pressure drop and particle cut-size [14].

Wang et al. [32] research objectives were to find the reasons for poorer performance than expected, and to identify measures to improve sharpness of cut for cross-flow air classifier using computer simulations in FLUENT, particularly standard k-ε model. The model predictions for the flow field were compared with the experimental results and good agreement was observed when using the structural grid. The model predictions for sharpness of cut were much higher than the measurements because only the turbulence and vortex could be included in the simulation, while inter-particle effects could not be allowed. The predictions of cut size, however, were in a good agreement with the experimental data (Figure 28) [32].

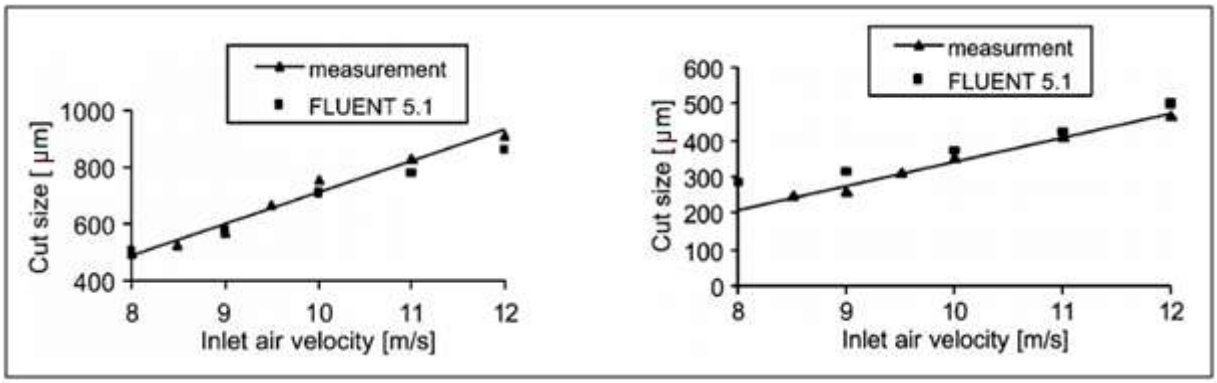

Figure 28 Cut size as a function of inlet air velocity – comparison of simulated and measured data [32]

Johansen et al. [19] used FLUENT to simulate flow field, particle dispersion and grade efficiency of a rotor air classifier and through the simulations they confirmed that both the flow field and the particle trajectories were more complicated than what one obtained using simple theories. But the predicted grade efficiency was lower that the measured one even for the smallest particles (Figure 29). This was probably evidence of agglomeration, which was not accounted for in the model. The predictions were in better agreement with experiments for the larger sizes [19].

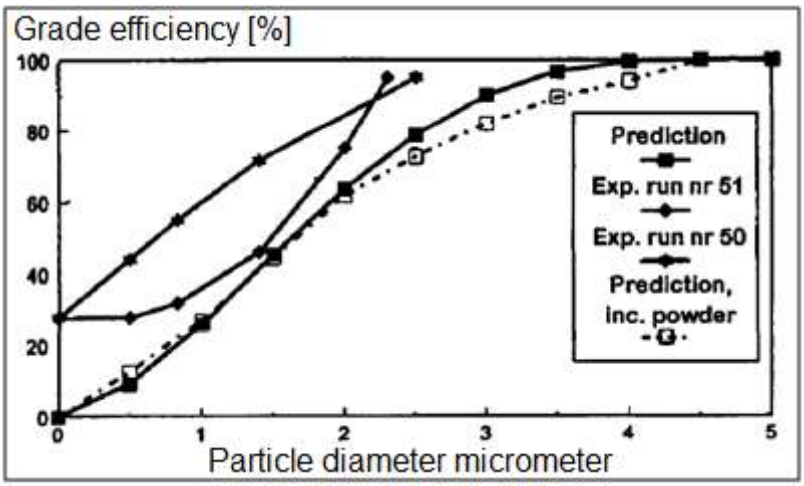

Figure 29 A comparison of two experimental grade efficiencies and two predicted efficiencies [19]

Karunakumari et al. [20] used CFD in their study of rotor air classifier, particularly standard k-ε model, RNG k-ε model and Reynolds stress model, to calculate the flow field. The flow rate measurements were carried out over a range of fan speeds and the results obtained from CFD were in good agreement with the two experimental techniques (flow meter and Pitot tube) used in their study (Figure 30) [20].

Jiao et al. [18] simulated the flow field of newly developed dynamic cyclone for fine particles separation in CFD. They introduced a rotor air classifier to replace the vortex finder in conventional cyclone. The separation was achieved by leading the dusty air stream through two stage separation – in the first stage the large particles were separated by cyclone and in the second stage smaller particles were separated by the rotor air classifier.

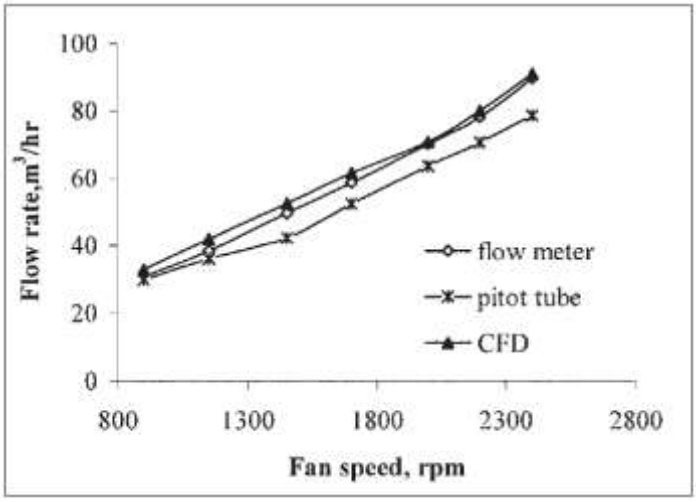

Figure 30 Comparison of calculated and measured air flow rates at the air outlet with angular vanes [20]

The measured results and simulation predictions on the tangential velocity agreed well, which proves that Reynolds stress model used in this study truly described the highly swirling gas flow in the dynamic cyclone (Figure 31) [18].

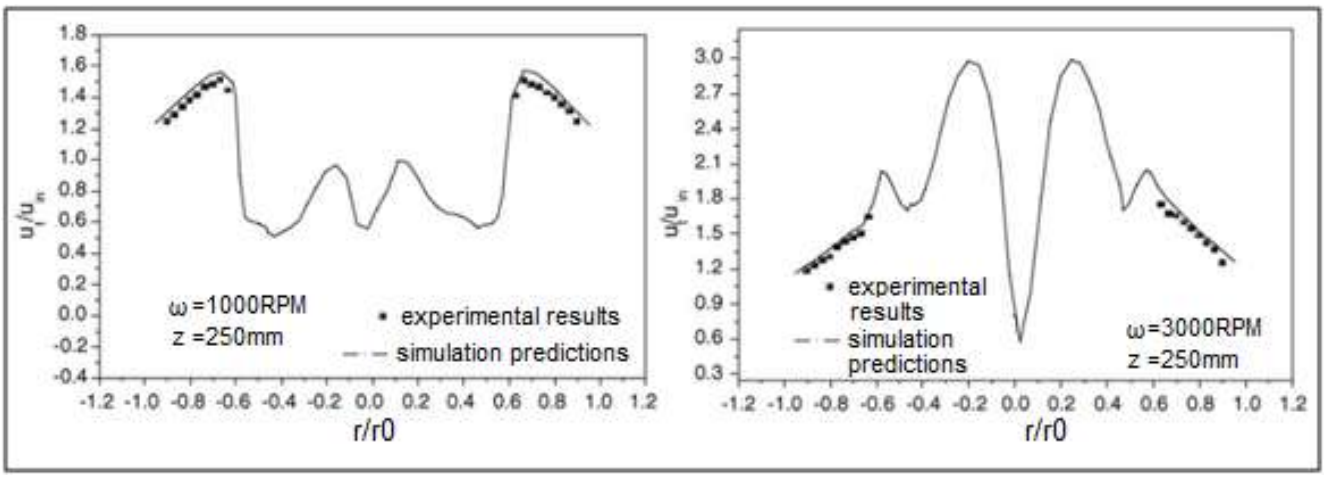

Figure 31 Comparison of the simulation predictions and measurements of the tangential velocity [18]

Gao et al. [9] in their study on cut size of a rotor air classifier developed a new strategy for calculation cut size using a FLUENT-based simulation of particle trajectories in the classifier. This proposed strategy was the first example of using the simulation of particle trajectories to determine cut size. Simulation and material experimental results revealed that the developed method held great potential as a convenient and precise platform for determining the cut size of classifiers.

Flows within the rotor air classifiers are usually turbulence of moderate strength. The research team utilize the RNG k-ε turbulence model, which is mostly used for the treatment of strong swirling flows or high-strain rate flows, to accurately describe the flow field in the classifier. Through the Discrete Phase Model of FLUENT, the trajectory of a discrete phase particle can be calculated in a Lagrangian reference frame by integrating the force balance on the particle.

By establishing the model the research team observed the trajectories of the particles in the classifier. The trajectories were different when different size particles were fed at the same position. Smaller diameter particles moved into the annular region while larger diameter particles rotated in the annular region, and eventually were gathered into the coarse fraction at the base (Figure 32) [9].

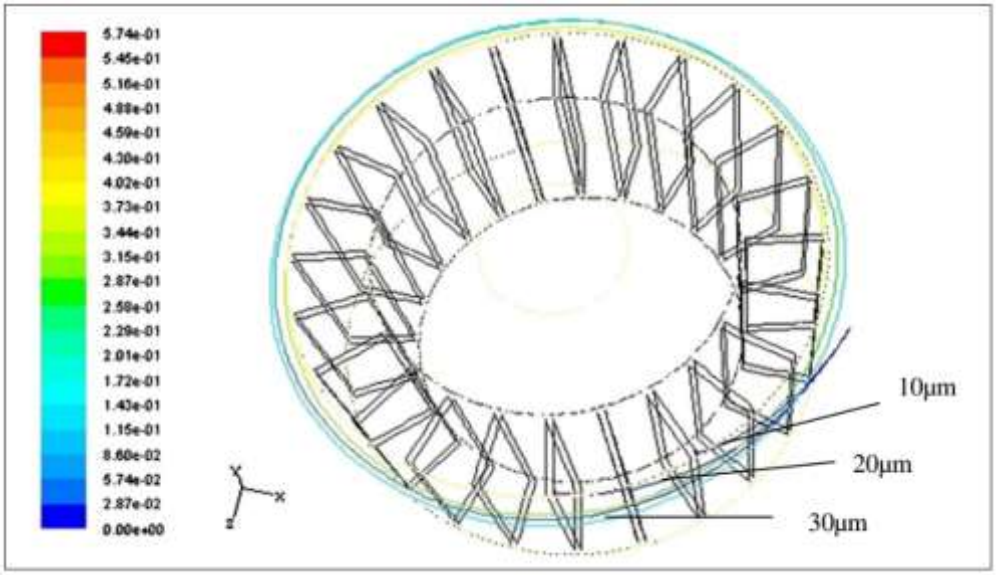

Figure 32 Particle trajectories of different talcum particle sizes [9]

The simulation results of cut size and the results obtained from experiments under the same operational conditions were in line as per the Table 10 below.

Table 10 Simulated and experimental cut size values for quartz sand and talcum powder [9]

The ratio of air inlet velocity and rotor cage rotary speed (m/s-r/min)	Simulated cut size for quartz sand (μm)	Experimental cut size for quartz sand (μm)	Simulated cut size for talcum powder (μm)	Experimental cut size for talcum powder (μm)
8-800	40-50	47	30-40	37
8-1200	30-40	32	20-30	25

Liu et al. [26] used FLUENT software to simulate flow field and particle trajectories in order to determine new design of air classifier guide vanes which incline along rotating axis. To simulate the turbulent flow, they used RNG k-ε model and Discrete Random Walk model to track particles trajectories. Discrete Random Walk model is suitable for calculation of particle trajectories in turbulent flow field, which consider the effect of instantaneous turbulent velocity on particle orbit by using the stochastic method. The interaction of the particle with a succession of discrete stylized fluid phase turbulent eddies is simulated.

Model correctly simulated that particles of different sizes have different trajectories. The larger diameter particles rapidly run into the guide vane (Figure 32, C) after injecting because of a large inertial centrifugal force. The smaller ones quickly enter the rotor cage under the air drag force (Figure 33, A) [26].

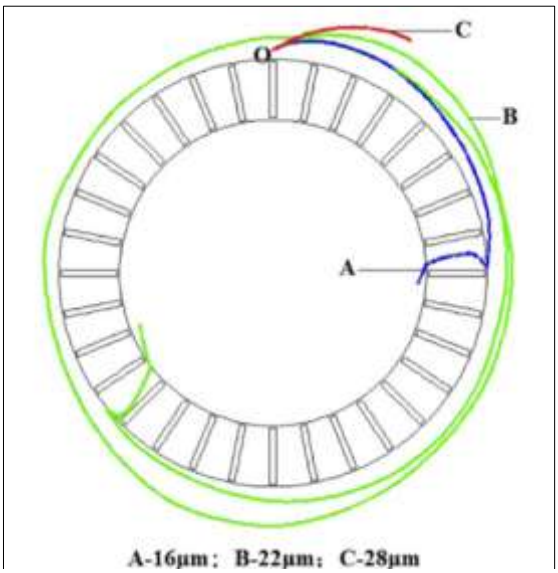

Figure 33 Particle trajectories of different sizes fed at point O [26]

Huang et al. [16] focused in their study on guide vanes as an important functional unit of the classifier. The flow conditions were simulated using the FLUENT software and confirmed by actual material experiments. The Reynolds stress model was used to model the rotating turbulent flow. The simulation same as the actual experiments indicate that a rotor air classifier with

positively bowed guide vanes produces smaller cut size and higher classification precision index than with straight guide vanes [16].

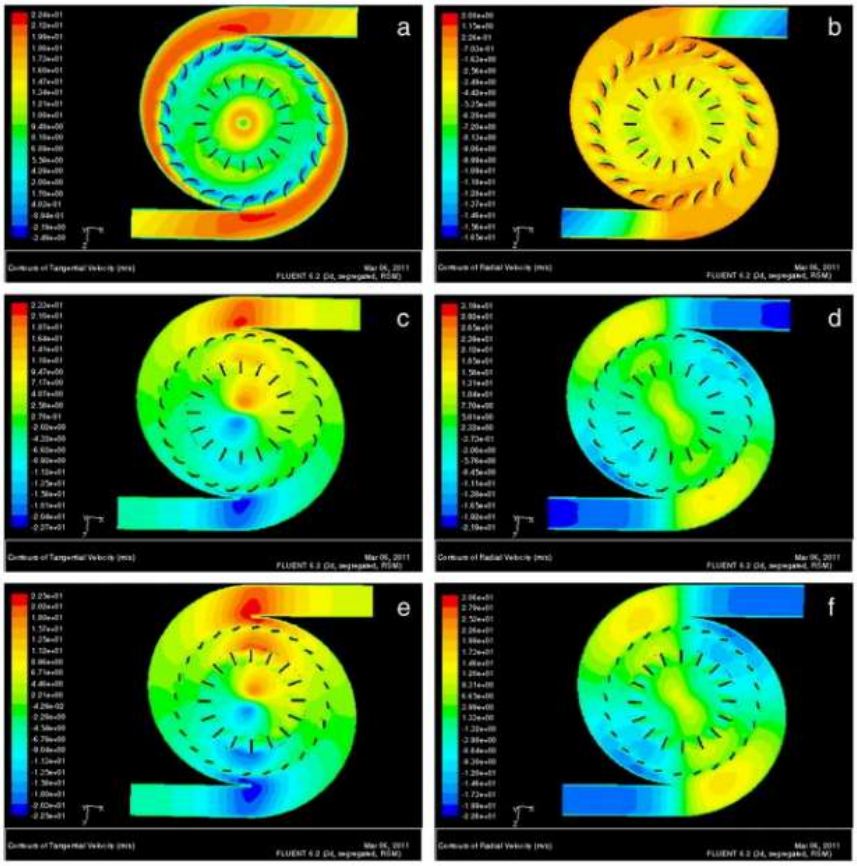

Figure 34 FLUENT simulations (a) Tangential velocity distribution in a rotor air classifier equipped with a positively bowed guide blade. (b) Radial velocity distribution in a rotor air classifier equipped with a positively bowed guide blade. (c) Tangential velocity distribution in a rotor air classifier equipped with a negatively bowed guide blade. (d) Radial velocity distribution in a rotor air classifier equipped with a negatively bowed guide blade. (e) Tangential velocity distribution in a rotor air classifier equipped with a straight guide blade. (f) Radial velocity distribution in a rotor air classifier equipped with a straight guide blade [16]

Guizani et al. [11] simulated the flow field in a rotor air classifier using the FLUENT software. The moving rotor has a defined definite position and the Multiple Reference Frame model (MRF) was selected to simulate the interaction between the moving rotor and the stationary surroundings particles. To predict the flow pattern and the performance of the dynamic separator, they tried to model the turbulence by use of the standard two-equation k-ε model, the RNG k-ε model and the Reynolds stress model (RSM) available in the FLUENT code. In the steady case, it was found that convergence was possible using the RNG k-ε model, but it was more difficult than using the standard k-ε model.

With the RSM model, the solution diverged, although they tried to get convergence such as reducing under relaxation factors, starting with the k-ε model. Convergence with the RSM model was possible except when they used unsteady CFD simulations with time step sizes ranging from 0.1 to 0.0001 s. It was found that the smaller the time step size, the more accurate the stability of results. So, they have chosen a time step size of 0.0005s in all calculations. Due to the Reynolds stress turbulence model being very suitable for high swirling flows in air classifiers, they adopted

it to make the equations in all calculations. The results of this study proved that the turbulence RSM model can correctly predict the flow pattern and better captured the essential features of the swirling flow in the third-generation rotor air classifier. The research team also proved the ability of the stochastic Lagrangian DPM model to accurately predict the selectivity curve of the classifier (Figure 35). The calculated selectivity curve was compared to the industrial results. The maximum deviation between the industrial and numerical efficiency curves was observed in the fish-hook effect for finer size particles. Particle-particle collisions need to be taken into account. Therefore, the use of a different multiphase model as the Euler-Euler model can improve the predicted selectivity curve [11].

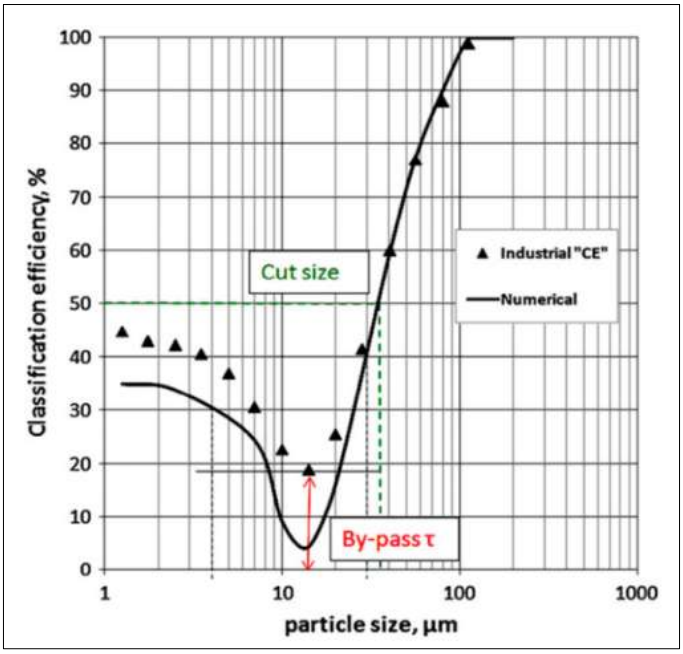

Figure 35 Industrial and predicted selectivity curves of the studied air classifier [11]

Secondary recirculation flows and the bubble-type vortex breakdown phenomenon are the most pronounced effects that lead to the reporting of fine particles to the coarse fraction and the appearance of the fish-hook shape of selectivity curve (Figure 35). These physical phenomena can be observed by CFD simulation and locating these flows can be an important factor for the improvement of the high efficiency separator conception and modelling (Figure 36) [11].

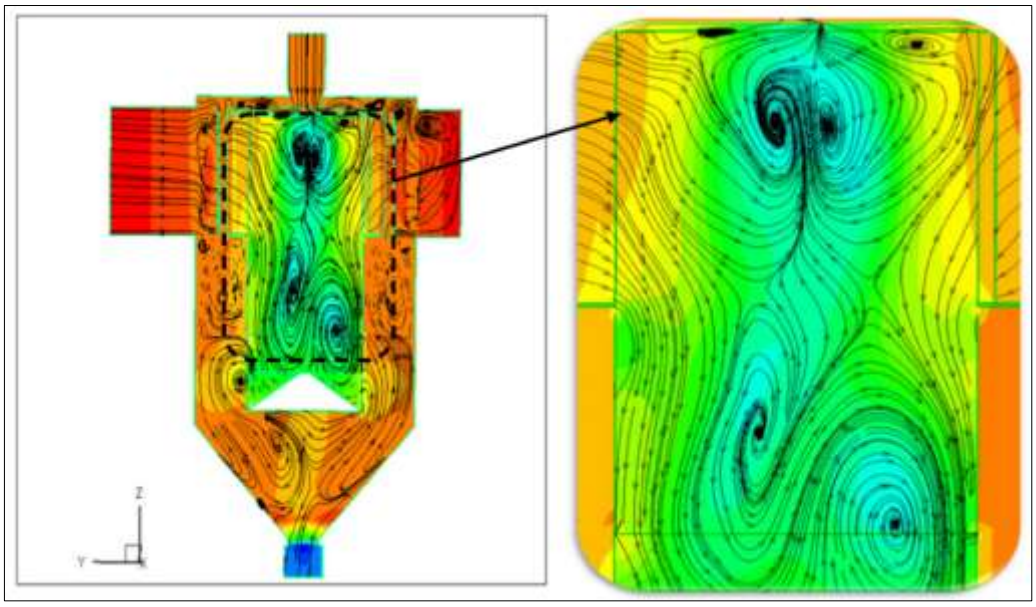

Figure 36 Path lines and secondary flow inside rotor air classifier, detail of bubble-type vortex breakdown [11]

One of the most recently published studies is from Yu et al. [40], who as well simulated the particle's trajectory using CFD. The cut size was determined from differences in trajectory of particles with different size in the same air flow field. (Figure 37).

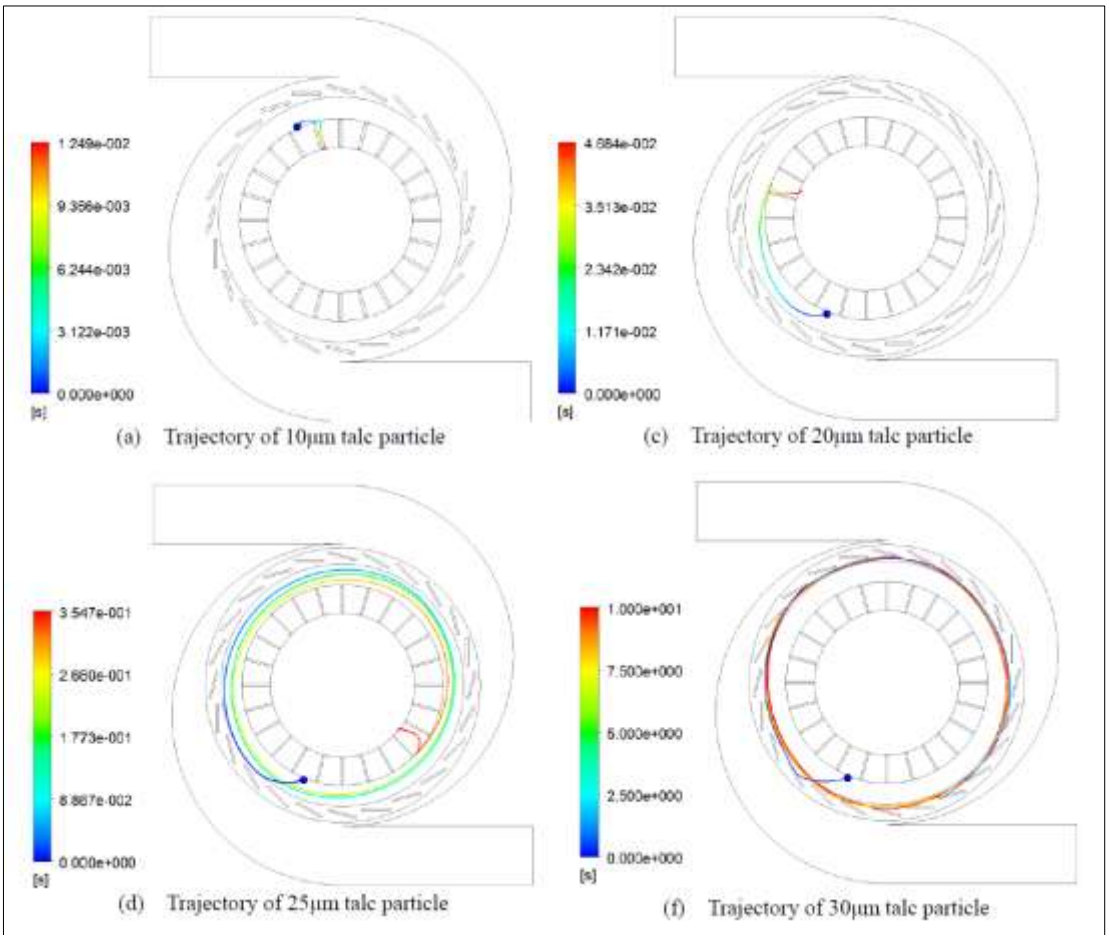

Figure 37 Talc particle trajectory (10-30 μm) [40]

The effects of rotation speed of the rotor cage and material selection were established based on analysis of the trajectory changes. The simulation results were validated against experimental data (Table 11).

Table 11 Comparison of simulated and experimental cut sizes for talc classification [40]

No.	Simulated d_{50} /µm in CFX	Experimental d_{50} /µm	Deviation between simulated d_{50} and experimental d_{50} /%
1	29	30.1	3.6
2	24	22.2	-8.1
3	26	30.5	14.7
4	24	23.1	-3.9
5	21	21.1	0.5
6	25	30.0	16.7
7	23	24.5	6.1

Since there were several factors, which could cause a deviation between simulated and experimental cut size, the maximum deviation less than 20% was classified as accepted. Therefore, numerical simulation to predict the cut size of the turbo air classifier may be considered a useful and reliable tool and new reference method to study performance of various other types of classifier [40]. From the above-mentioned studies and their comparisons of simulation and experimental results it is obvious that CFD modelling provides an accurate and convenient method to predict classifier performance and a sufficient reference for classifier operating parameter selection.

4.3.2 On-line measurement techniques

The growing trend toward automation in industry has resulted in many studies of rapid procedures for generating air classification performance information so that feedback loops can be instituted as an integral part of a process. Many of these techniques are modifications of more traditional methods [51].Main on-line measurement technique used in this dissertation is Particle image velocimetry (PIV). It is a non-intrusive visualization technique used to measure instantaneous velocity vector fields from slow flows to supersonic flows. In contrast to other methods for one-point measurements (Pitot tube or laser Doppler velocimeter), PIV is able to carry out two-dimensional and three-dimensional instantaneous velocity measurement. Physical information, such as pressure field and vorticity field, can be extracted based on the velocity vector map obtained from PIV. This method has been rapidly advanced in its fundamentals and applications to multiphase flows, thermal flows, turbulence structures, and other [43].

When there is no out-of-plane (perpendicular to the illumination light sheet plane) motion, planar flows can be accurately observed with two-dimensional 2D-PIV technique, consisting of only one camera. However, contamination will be introduced into the experimental results when the out-of-plane velocity is considerable. With 2D-PIV, the axial and radial velocities in rotor air classifier can be observed simultaneously, but contamination is registered on them due to the prominent tangential velocity in classifier. To make the PIV results applicable, the contamination should be removed efficiently [41].

For example, Liu et al. [44] introduced two methods used for eliminating the contamination with very promising results. They measure the axial velocity of the gas flow in a gas cyclone by 2D-PIV and 3D-PIV (which consist of two cameras). It is shown that the axial velocity measured by 2D-PIV can be distorted by the tangential velocity. This distortion is due to the intrinsic weakness of 2D-PIV. But corrected profiles of the axial velocity were compared with those obtained by 3D-PIV, and good agreements were obtained. The 2D-PIV has been successfully used in multiple studies of rotor air classifiers. For example, Xing et al. [42] measured the velocity field between two adjacent rotary blades in a rotor air classifier using the 2D-PIV technique equipped with a self-developed synchronizer (Figure 38) to reveal insight of classification mechanism and to provide some data for CFD modelling.

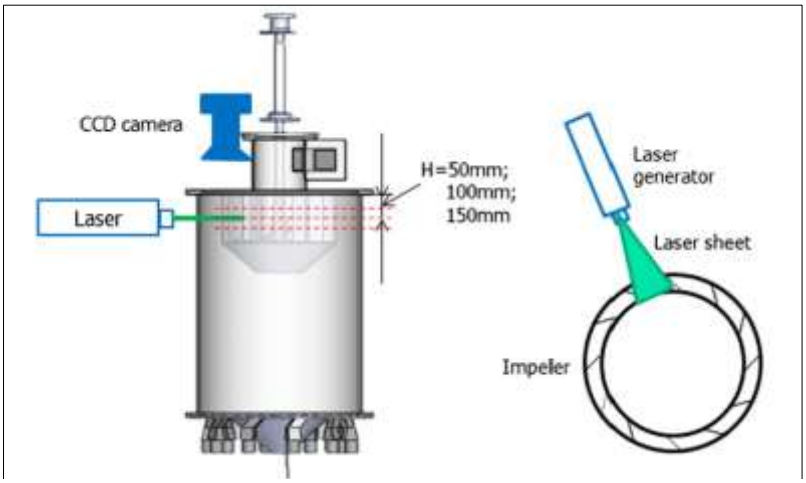

Figure 38 Set up for PIV measurement [42]

Toneva et al. [29,45] used the 2D-PIV to obtain the time-dependent 2D-velocity distributions of the single-phase flow and two-phase flow in the regions of the impact element and the classifier. The 2D-PIV set up for the classifier zone is demonstrated below (Figure 39).

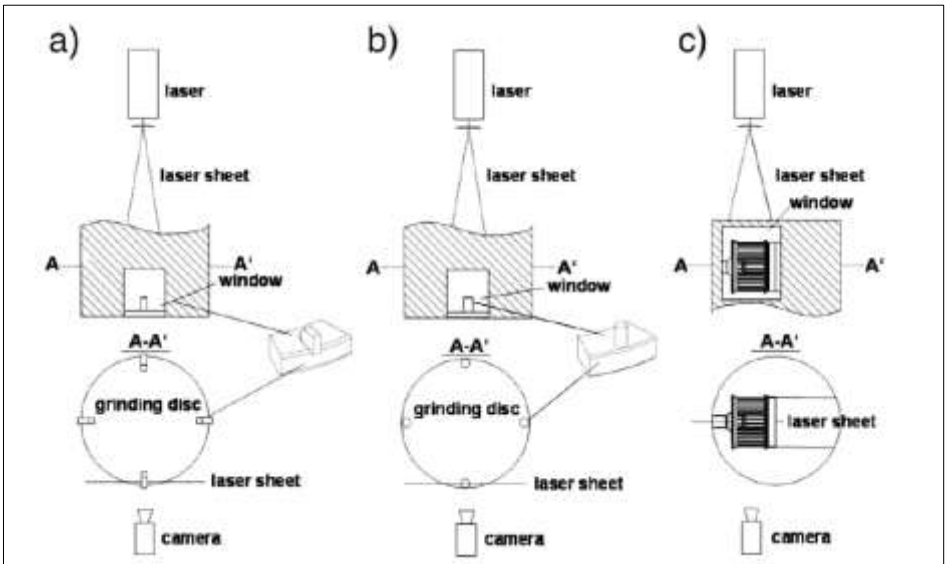

Figure 39 Exemplary PIV arrangement for the flow measurements at the grinding disk and at the classifier a) grinding disk with prismatic pins; b) grinding disk with cylindrical pins; c) classifier zone [45]

The 2D-PIV results were compared with numerical calculations based on the absolute tangential velocity profile were in good qualitative agreement as demonstrated on Figure 40. Both methods confirmed the formation of forced vortex.

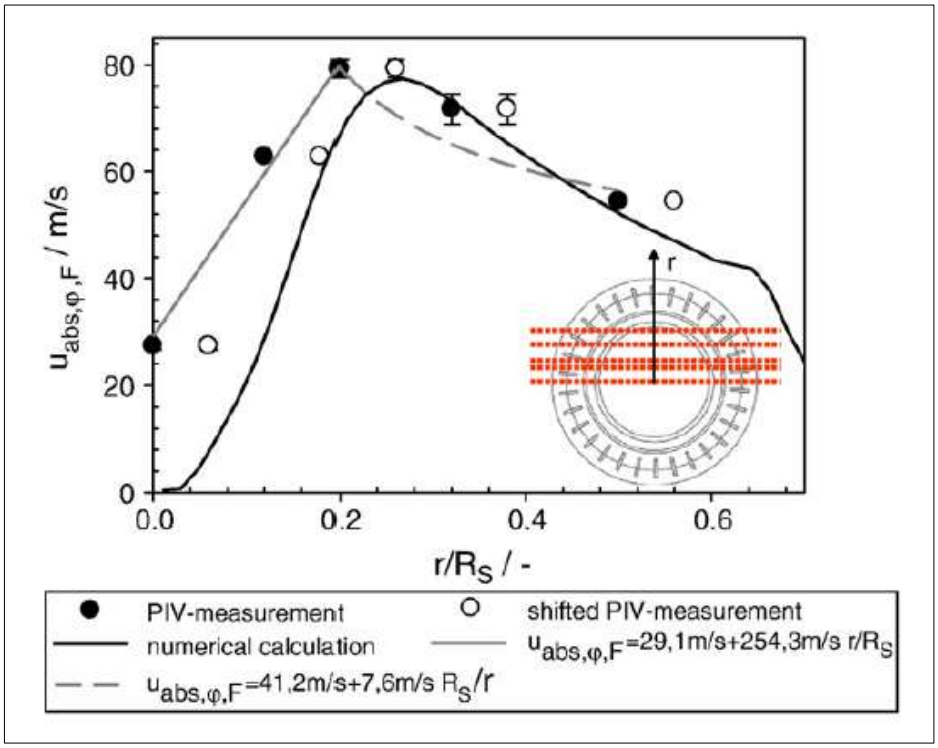

Figure 40 Vortex formation within the classifier core. Comparison between experimental method (2D-PIV) and numerical calculations [45]

Similarly, as 2D-PIV, widely used in-line measurement techniques are pitot tube and digital manometer, utilised for measuring air inlet velocity and total and static pressure. These methods used for example by Karunakumari et al. [20], who installed a traversing pitot tube connected to a micro manometer to measure air flow rates at different rotational speeds. The measurements were carried out at several points by traversing the pitot tube along the diameter horizontally in two mutually orthogonal directions. The resulting velocity profiles were integrated to give the overall volumetric flow rate. Each profile measurement was carried out three times to verify repeatability. These were found to match closely and an average value was taken to calculate the flow rate.

Sun et al. [52] utilised pitot tube to measure primary and secondary air velocities and the pressure drop between the feed inlet and the air outlet of the classifier was measured by an inclined tube manometer. Guizani et al. [11] successfully used pitot tube measure air inlet velocity in the cross section of the pipe's air inlet.

5 SUMMARY OF LITERATURE REVIEW

With respect to reviewed literature it can be observed that most of the researches focus on the rotor air classification when compared to other air classification methods. This is in agreement with personal experience from within the process industry. This focus can be attributed to its versatile applicability and supreme performance over described static classifiers. Few advantages of this type of classification are efficient performance (with respect to grade efficiency curve), finer and sharper cut size and cut size controllability by adjustment of operational parameters.

Main operational parameters used to adjust classifier performance are identified as rotational speed of the rotor, air inlet velocity and feed rate. Researchers developed several analytical prediction models for cut size, with different involvement of parameters affecting classification process and with varying level of prediction accuracy. Described models include also some structural parameters nevertheless significant simplification of classifier geometry, which has a crucial influence on the process, is carried out. These models are mainly trying to optimize above mentioned three operational conditions in order to achieve desired cut size of classifier. In private sector however, the fine fraction is commonly the desired product. By increasing the feed rate of material, air in the classifying chamber becomes dust loaded and particle-particle interactions become more frequent. Particles tend to agglomerate therefore increasing their mass and as a result are rejected into coarse outlet. This may be decreasing cut size of the classifier but is also decreasing the yield of fine particles. Classifiers are very often designed for a certain range of throughputs and they operate most efficiently whilst maintaining these levels. Feed rate is a very important operational parameter, however altering it as a measure of achieving desired cut size in industrial operation should be one of the last resources. Rotational speed of the rotor is operational parameter that is adjusted most frequently. This has a direct impact on the peripheral velocity of the rotor exterior edge, or tip velocity. Higher tip velocity can be achieved either by increasing rotational speed or by increasing diameter of the rotor. One should consider implications of excessively high rotational speed and its impact on blades wear, machine vibrations, bearing life, energy consumption, etc. Another implication of high rotational speeds is creation of forced vortex.

Rapid development of computing power of processors allows new techniques to be used for flow field analysis. Number of researchers carried out simulations using computational fluid dynamics approach with varying levels accuracy. This can be partially attributed to selection of turbulence models and current stage of their advancement. K-epsilon realizable model is the latest addition to family of 2 equation turbulence modelling and it has improved accuracy for simulations involving swirling flows.

Feng et al. [7] displays a 2D vector graph of the rotating flow field in his study. He finds out that vortex is not convenient for the classification as the fine particles can get into coarse and vice versa. Therefore, he seeks the most convenient rotational speed to minimize the vortex. He calculated that the intensity of the vortex is the least when tangential velocity of the exterior of

rotor blade and tangential velocity of the air flow in the rotor exterior edge are approximately equal.

Guizani et al. [11] also focused on the vortex in the classifier. He identified that it is not the vortex which has a negative impact on classification performance but it is its breakdown. He further describes two types of vortex breakdown, namely bubble and spiral breakdown. In the air classifiers the occurrence of bubble type breakdown is dominant and it is the main factor responsible for creation of recirculation areas. These recirculation flows are further responsible for the entrainment of fine particles in the coarse fraction. This phenomenon is called fish-hook effect.

Galk et al.[8] studies the importance of forced vortex and its influence on fine particle separation. Research displays size and position of the vortex in the passageway between blades depending on rotational speed and radial velocity. One of the results of his research is a finding that to achieve very fine cut size, high circumferential velocities together with low radial velocities are required.

From the experience and from the observation of wear locations on the rotor blades, these findings are in good agreement with technical practise. There is however only a small number of researches which describe flow field in rotor region by use of direct vector measurements. This may be partially attributed to difficulties related to implementation of PIV measuring technique into rotor air classifier. To name a few, environment in rotor air classifier needs to be controlled strictly for PIV and thus eliminating the possibility of applying PIV to industrial installations. This leaves us with smaller laboratory versions of rotor air classifiers whose geometrical aspects make it very difficult to implement PIV equipment due to its dimensional size. Also, the cost of equipment needed to realize PIV measurements is significant and thus preventing from its wider use. PIV measurement and its results give us however an invaluable insight into flow physics and form a great data set for validation of numerical model.

6 DISSERTATION WORK OBJECTIVES

6.1 DEFINITION OF OBJECTIVES

- Design and realization of trajectories measurement and granulometry analysis of major flows of very fine particulate materials in the latest generation of dynamic air classifiers
- Modelling of particle motion of very fine particulate materials in dynamic air classifiers by means of latest available numerical model apparatus
- Opportunities of process and mechanical design modifications of dynamic air classifiers which would help overcome current granulometric limits of classification processes

Synopsis:

- Literature review of dynamic air classification of very fine particulate materials process
- Design and modification of current dynamic air classifier allowing nonintrusive flow field velocity measurement and flow pattern visualization in active classification zones
- Testing of measuring systems of the experimental setup
- Measurements of separation efficiency in relation to rotor speed, feed rate and flow rate
- Elaboration of experimental results by use of available mathematical models
- Evaluation of data obtained experimentally and prediction of possibilities of overcoming current granulometric limits of dynamic air classifiers

6.2 PROPOSAL OF RESEARCH METHODOLOGY

Methods used during elaboration of the dissertation work can be subdivided as follows:

a) Logical methods involve principles of logic and logical thinking and can be further described as three pairs:

- abstraction and concretization
- analysis and synthesis
- induction and deduction

Kolb's learning cycle describes connection between induction and deduction method, which are very closely related [35].

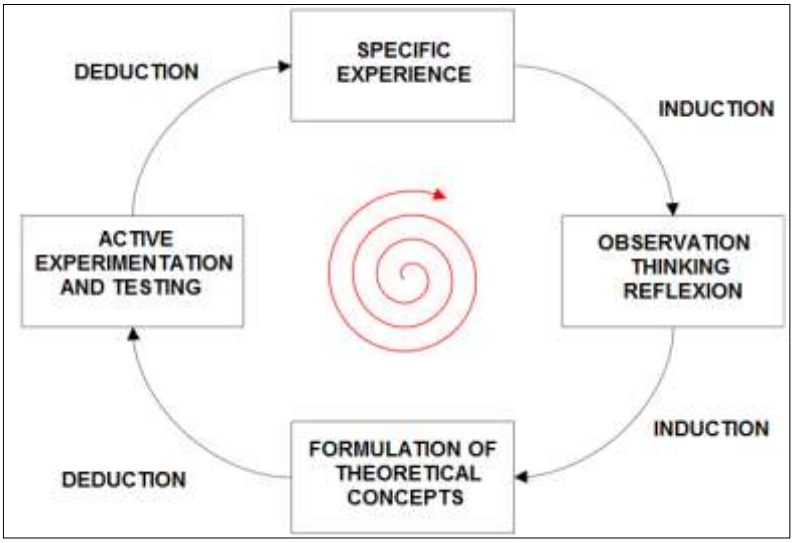

Figure 41Kolb's learning cycle [35]

b) Empirical methods are methods which allow us to determine a specific and unique property of some object or phenomena in reality. This is one of the core scientific methods which require all evidence to be empirical which means that data is produced by experiment and observation. It can be subdivided further as:

- observation
- measurement
- experiment

7 EXPERIMENTAL SETUP AND DESCRIPTION OF TRIALS

Main objective of this chapter is to introduce classifier pilot plant and its components. Individual devices of the system are presented together with their parameters and characteristics. Classifier testing unit is being currently used for classification trials at Bradley Pulverizer Company Incorporated. The unit was overhauled and modifications were carried out prior to classification trials due to increased operational requirements.

7.1 AIR & PARTICULATE MATERIAL FLOW DIAGRAM

Classifier testing unit is set up in a closed circuit. Air is used as a particle transportation medium and it circulates within the system. Feed material with given particle size distribution enters the classification process through top face of the classifier. Coarse particles are separated from the air flow through combined effects of classifier‘s rotor action and cyclonic separation in the body of the classifier. Coarse product fraction then exits system at the bottom section of classifier. Figure 42 shows functional flow diagram of rotor air classifier installed in closed circuit.

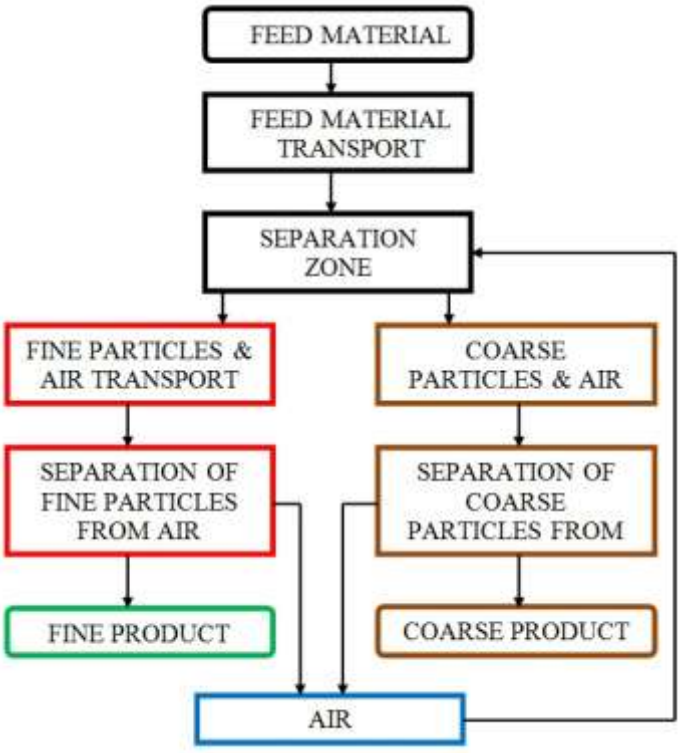

Figure 42 Flow diagram of rotor air classifier in closed circuit

Fine particles are carried away from the classifier into cyclone which is the next device in circuit. Here the fines are separated from the air flow through the effects of cyclonic separation and electrostatic energy and they exit the system in the bottom section of the cyclone, as indicated in Figure 43. Purified air then leaves cyclone through the vortex finder in the top section of the cyclone and continues to centrifugal fan. Here the air is accelerated again by action of the fan and it enters classifier again.

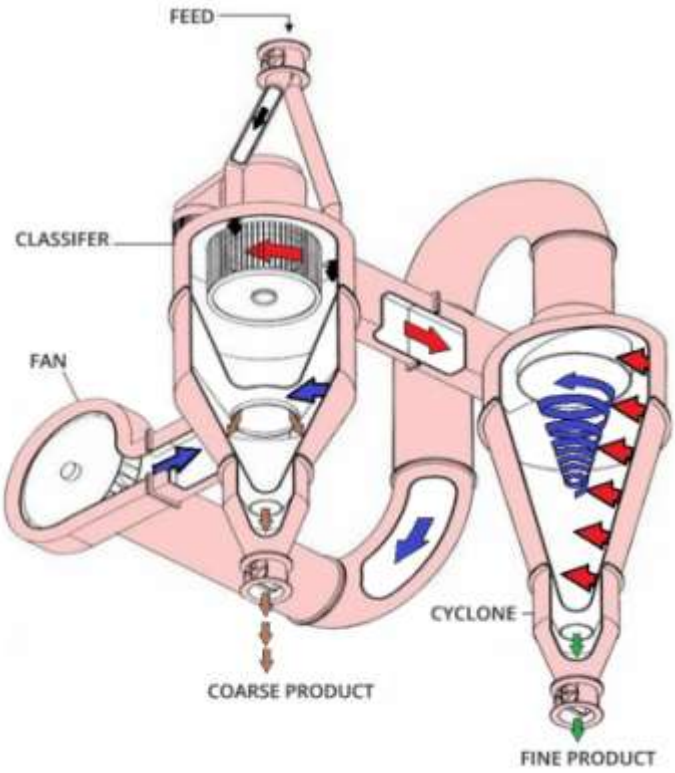

Figure 43 Indication of flow pattern. Black colour indicates feed material. Red colour indicates air flow saturated by fine particles. Brown colour indicates coarse particles. Blue colour indicates purified air. [34]

7.2 PARTICULATE MATERIAL FEED ARRANGEMENT

Material to be classified is kept in a feed bin above the classifier and each classification trial is carried out with 25 kg of powder material. Feed hopper is under suction by industrial vacuum unit to provide dust free operation. Material is being fed into the classifier at a constant rate by rotary valve feeder, as is shown in Figure 44. Feed rate is controlled by adjusting rotational speed of the valve.

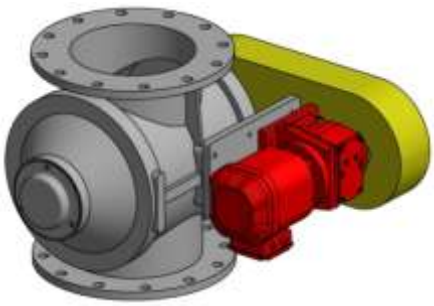

Figure 44 Rotary valve used in the experiment

7.3 ROTOR AIR CLASSIFIER DESIGN

Main parts of the classifier are shown in Figure 45. Classifier is of a metal construction with the main body parts being lower chamber, upper chamber and rotor housing. Internal parts are rotor, bearing and shaft housing and the inner cone. Depending on particular application, these parts can be lined with different abrasion resistant materials to form a wear protecting layer. Testing unit

however has no protection lining. Lower chamber outer faces are designed in particular conical fashion. Clean air enters cylindrical chamber via tangential inlet and therefore creates vortex flow pattern. This cyclonic phenomenon is commonly used in applications where separation of discrete phase from fluid is required. In this application it is used to separate coarse particles from air flow. Coarse particles then exit lower chamber through flanged outlet which is connected air tightly to plastic bucket. Inner cone is used to separate lower chamber separation zone from upper chamber separation zone. Air velocity between lower and upper chamber can be adjusted by changing cross sectional area of the inner cone throat.

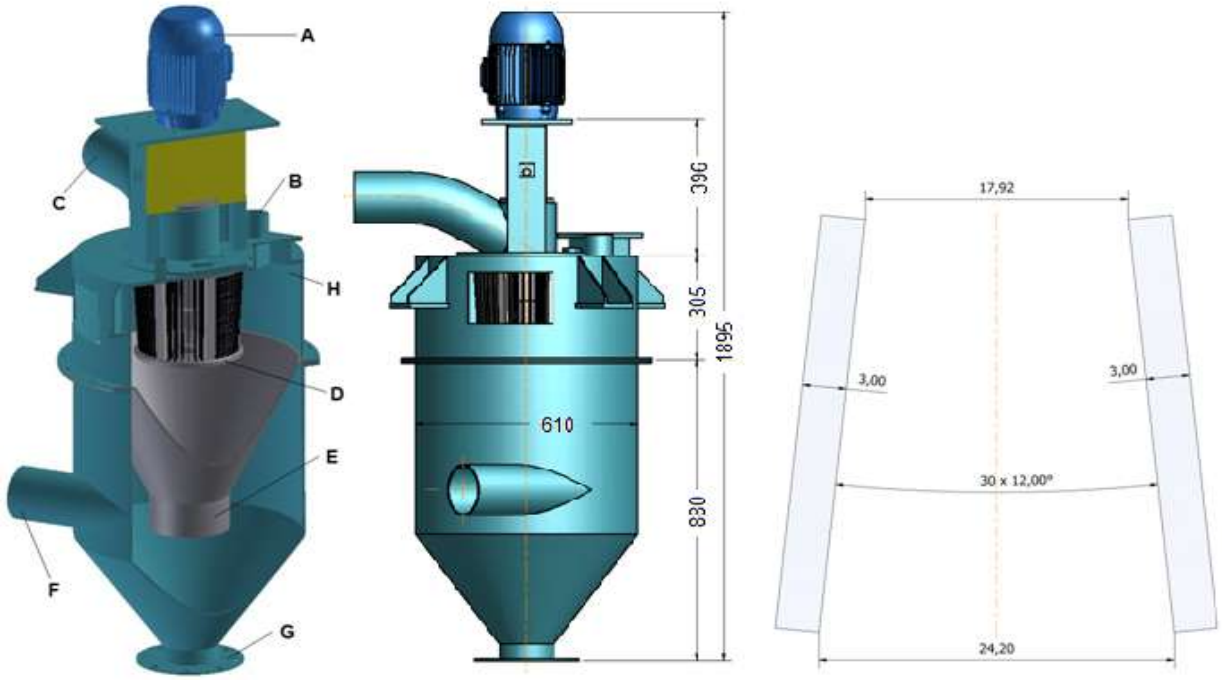

Figure 45 Outline and blade arrangement dimensions in mm & main parts: A- motor; B- feed inlet; C- fine particles outlet; D- rotor cage; E- inner cone; F-lower chamber; G- coarse particle outlet; H- upper chamber

Upper chamber together with inner cone form a cylindrical housing for the centrifugal cross flow separation zone. Feed material enters this separation zone through feed inlet in top face of the chamber. It is then mixed with air and different particles are accelerated to their individual terminal velocities through the airflow. Fine particles satisfying classifier cut size parameter are carried into the internal area of rotor whilst coarse particles are rejected and are accelerated towards outer wall. Coarse particles then slide down in the near wall region into lower chamber. Rotor housing is located on top face of the upper chamber. It supports electric motor and bearing housing with the rotor attached to its end.

Rotor cage is designed as a hanging rotor with 30 abrasion resistant blades. These are arranged in a straight radial pattern. Rotor is direct driven and rotational speed can by controlled by changing frequency and voltage by using variable frequency drive. Rotor blades which are 3mm thick are tapered and thus the rotor is arranged as a conical frustum with larger diameter at the top. Diameter of the rotor at the centre is 275mm and its height is 250mm. Fine particles are carried away from internal area of the rotor vertically up through the exit in the rotor housing.

7.3.1 Classifier modifications

Particle image velocimetry method (PIV) is used to visualize vector field and flow pattern in the selected region of interest. Details of equipment used for this measurement are described in separate chapter of this paper. In order to allow this equipment to capture flow in the near rotor blades region, modifications to the classifier are carried out. These involve creation of opening in the top face of the classifier to allow the sCMOS camera to gain field of view at the selected region of interest. Camera window opening is then sealed with treated glass to create air tight seal.

Inspection opening on the side of the cylindrical body of the classifier is extended in order to allow double laser head to illuminate the plane intersecting field of interest. Inspection door is modified to provide air tight seal for extended opening in the classifier and a flat surface is created for laser sheet window. Again, this window is sealed with treated glass to provide air tight seal whilst allowing laser illumination. Support frame for laser head and camera has been designed and fabricated as an independent steel structure in order to isolate machine vibrations from optical equipment. Laser frame then further allows two angular and three linear adjustments.

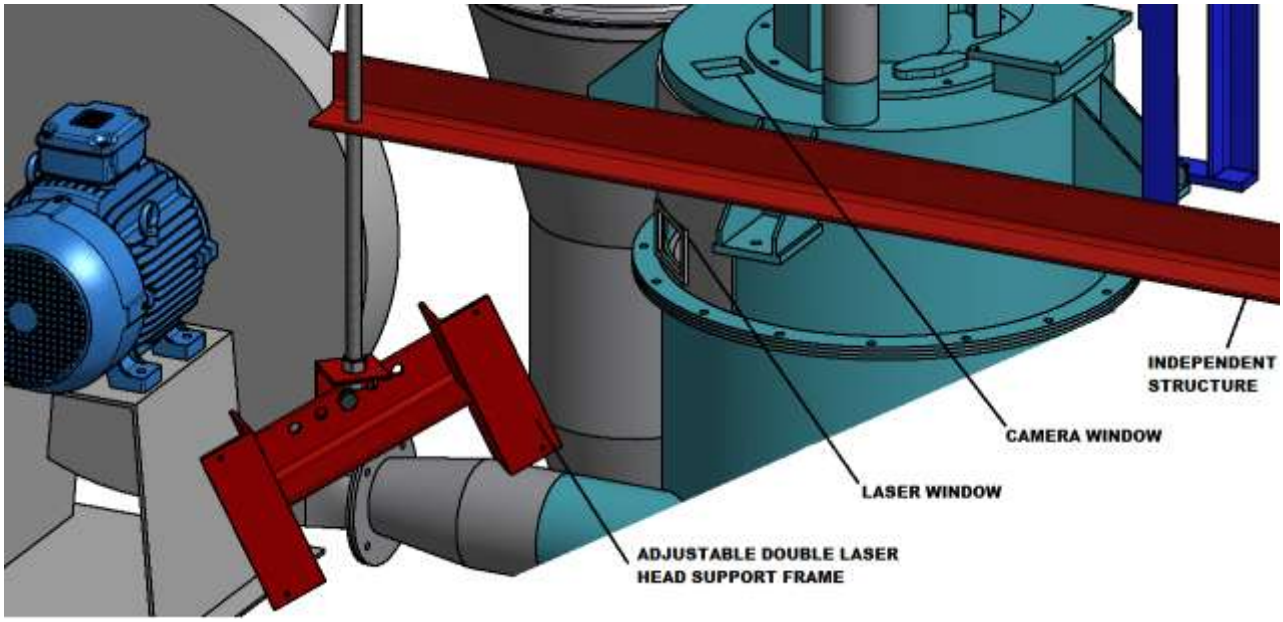

Figure 46 Double laser head support frame and windows in the classifier

Figure 46 shows support arrangement for PIV measuring equipment. Physical installation of PIV devices is carried out with respect to spatial constraints and optical assembly limitations. Extra effort was taken in order to minimize these limitations to ensure sufficient quality of collected data for post processing. Main rules followed are as follows:

- Distance between laser lenses and region of interest is to be 300 mm.
- Flat glass windows are used to limit light refraction and material deterioration due to wear.
- Classifier was thoroughly cleaned and vacuumed of all the particles deposited inside from the previous classification trials.

- Angle between laser sheet plane and axis coming through centre of camera lenses is optimized to be approaching perpendicular values. Ninety-degree angle however is not achievable due to geometrical limitations imposed by construction of the classifier. Special Scheimpglug lens was used to compensate for this distortion of perspective.
- Vibrations are minimized by supporting the measuring assembly off the independent frame.
- Blankets are used in order to minimize amount of natural light coming into classifier due to windows.

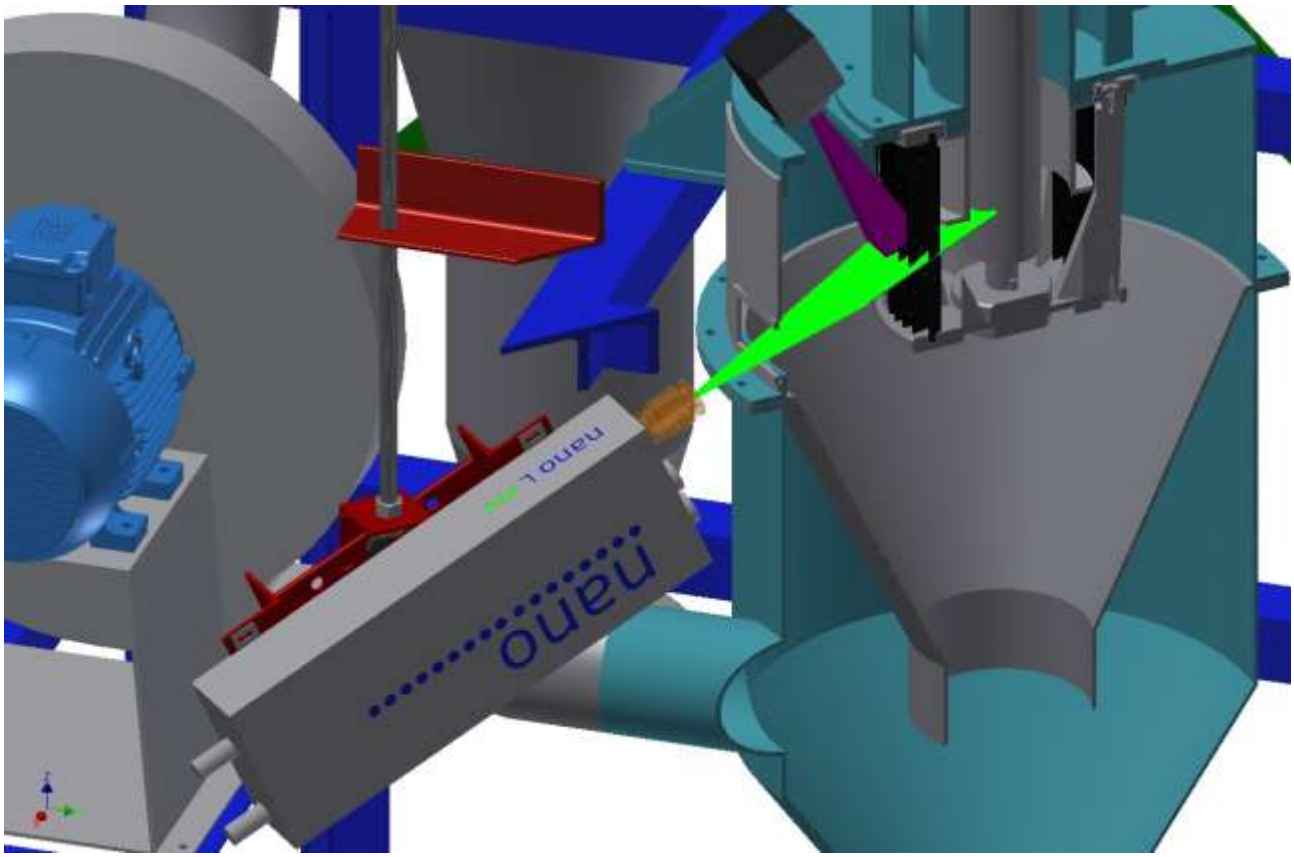

Figure 47 Assembly of classifier and PIV devices

Figure 48 Double head laser, sCMOS camera, aerosol generator and classifier setup

7.4 CYCLONE

Cyclone is a centrifugal device which separates particles from the stream of fluid. Typical geometrical arrangement of cyclone body is with cylindrical section located on top of the conical section. Cylindrical section further has a tangential inlet and axial outlet which is also called a vortex finder. Usually it is arranged as an axial pipe protruding inside of the cyclone. It acts as an inner vortex stabilizer and it also reduces pressure drop across the cyclone by separating zone with high inlet velocity from inner vortex core. Main forces responsible for particle separation are centrifugal force, gravitational force and friction on the wall. Swirling motion of the fluid saturated with particles in the cyclone is induced by tangential inlet. Swirling fluid propagates axially downwards with high tangential velocity component and low radial component which gives particles resident time so that they can be separated from the flow. Solid particles with certain size and density higher than density of fluid are forced towards wall of the cyclone and they continue axially downwards on swirling trajectory towards exit from the cyclone in the wall region.

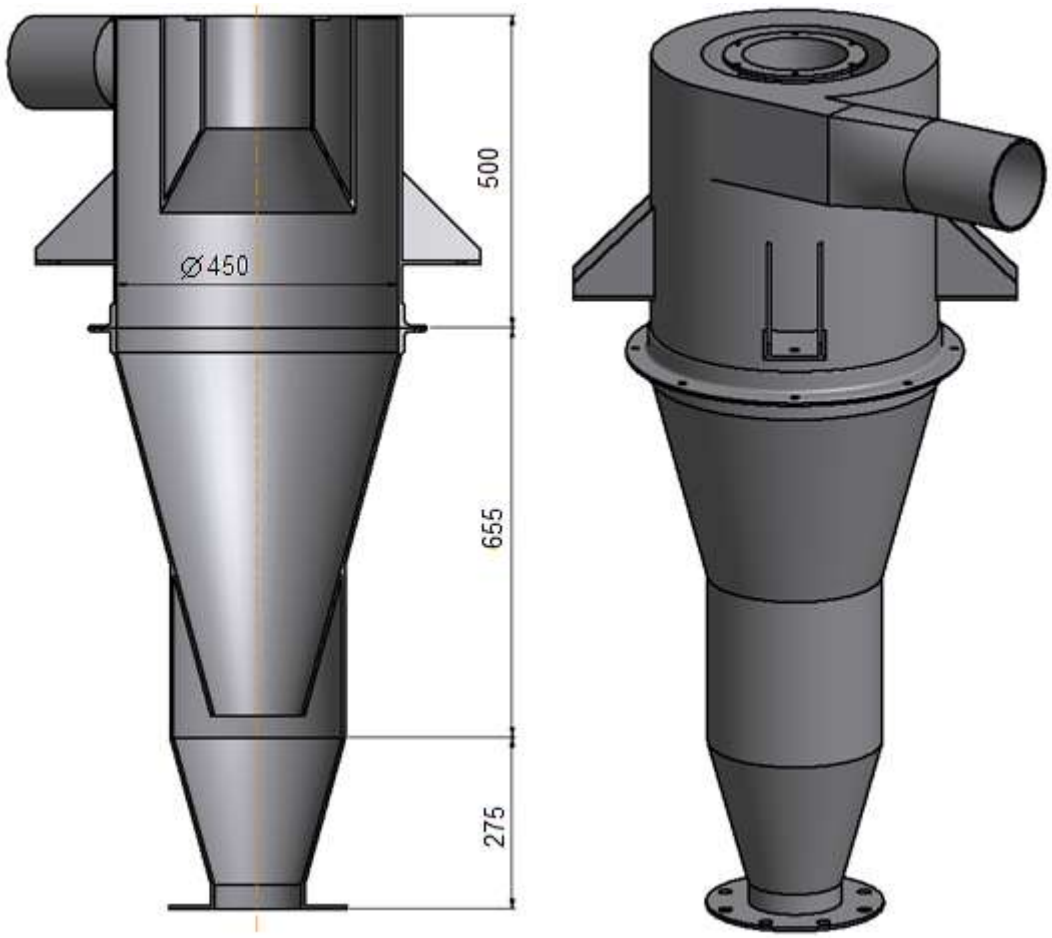

Figure 49 Outline dimensions of cyclone

Conical section of the cyclone increases radial velocity component of the fluid and together with swirling flow give rise to a low-pressure zone along the vertical axis, creating the inner vortex with opposite axial propagation direction. Fluid then exits cyclone through the vortex finder. Outline dimensions of cyclone used in the experimental part are shown in Figure 49.

7.5 CONTROL PANEL

Rotor air classifier experimental setup is an assembly which includes devices with dynamic elements. These devices are actuated by electric motors and their controllability allows operational parameters to be optimized in order to achieve desired results. Parameters are adjusted independently and it is operator's responsibility to select suitable values. Electric motors are controlled by use of frequency inverters located in the control panel. Motor list is shown in Table 12 and control panel is shown in Figure 50.

Table 12 List of asynchronous electric motors

	MOTOR POWER	POLES	SUPPLY
ROTOR CLASSIFIER	3 kW	2	3PH/400V
CENTRIFUGAL FAN	5.5 kW	2	3PH/400V
FEED AIRLOCK	0.37kW	4	3PH/400V

Figure 50 Control panel

7.6 CENTRIFUGAL FAN

Centrifugal fan is a mechanical device with rotating impeller which increases velocity of an air stream. In the particular case, air from the cyclone enters the fan axially and then it passes through the impeller where the kinetic energy of the impeller is used to displace air radially towards volute casing of the fan. It is then discharged at right angle to the inlet flow. Rotational speed of the impeller is controlled via variable frequency drive.

Figure 51 Centrifugal fan

7.6.1 Fan performance curve

Relationship between static pressure, total pressure and volumetric flow rate of the fan is expressed by the fan performance curve. Some of the important parameters used for fan selection are maximum developed pressure at required volumetric flow rate and particle loading for a certain system resistance curve. Figure 52 shows fan performance curve and the designed operating point.

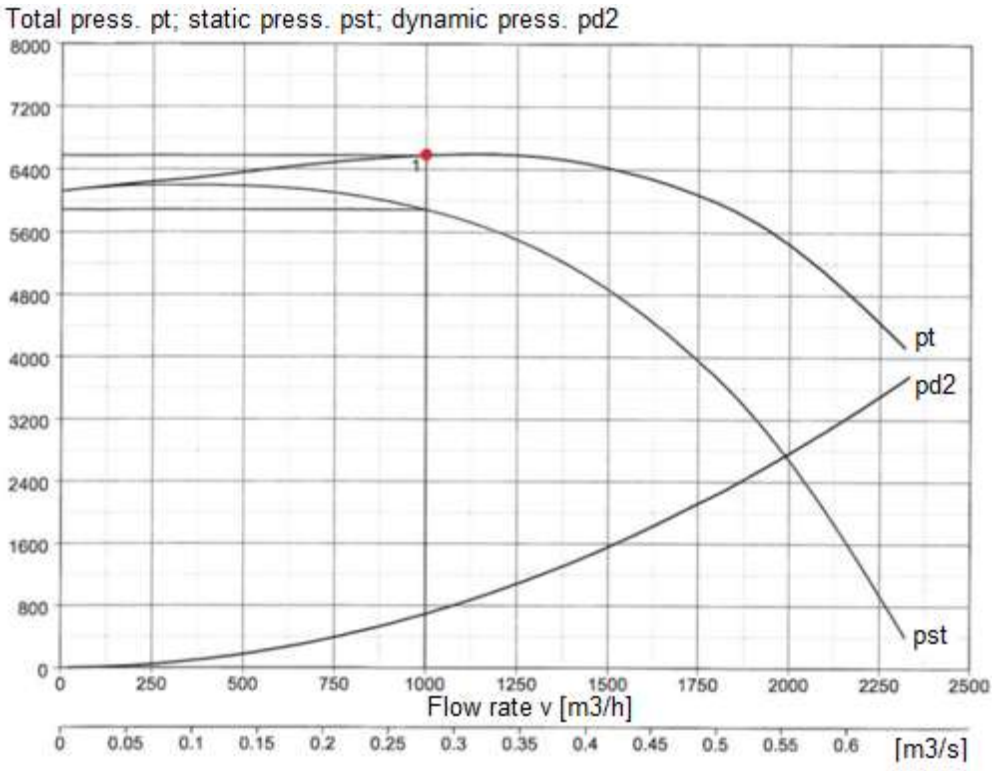

Figure 52 Fan characteristic curves: PT -Total pressure; PS - Static pressure; PD2 -Dynamic pressure

Table 13 Centrifugal fan datasheet

Air density	**ρ**	**kg/m^3**	**1.225**	**Motor frame size**			**132**
Volume flow rate	Q_{BF}	m^3/h	1000	Poles			2
Static pressure	P_{BS}	Pa	5882	Protection class		IP	55
Total pressure	P_T	Pa	6575	Rated voltage	U	V	3x400
Rated speed	N_B	min^{-1}	2811	Rated frequency	f	Hz	50
Operating temperature	t	°C	20	Rated power	P_M	kW	5.5
Shaft power	P_R	kW	2.34				

7.6.2 Fan affinity laws

The fan laws are a particular version of the more general similarity laws that apply to all classes of turbomachinery. They express the relationships among the performance variables and can be used to predict the performance of a fan, provided that performance at corresponding points of rating for a homologous fan are known. The fan laws can be expressed either based on compressible or incompressible flow conditions and for the given parameters the incompressible version is sufficiently accurate.[53]

$$Q_A = Q_B \left(\frac{n_A}{n_B}\right) \tag{7.1}$$

$$P_{AS} = P_{BS} \left(\frac{n_A}{n_B}\right)^2 \tag{7.2}$$

Table 14 shows calculated values of static and total pressure developed by the fan. These values are calculated with respect to varying rotational speed of the fan impeller wheel. Compressibility coefficient for the gas is not included in the calculation due to low operating pressures. Calculated volumetric flow rates are used to establish mass flow rate at discharge from the centrifugal fan and these values are then used to compare mass flow rate through velocity inlet and pressure outlet boundary conditions of the computational fluid flow simulation.

Figure 53 shows relation between different motor supply frequencies, volumetric flow rates and pressure distributions. Linear dependency between flow rate and rotational speed and exponential dependency between pressure and rotational speed can be observed.

Table 14 Flowrates and pressures for different fan speeds

MOT. SUPP. FREQUENCY [Hz]	FAN RPM [min^{-1}]	STATIC PRESSURE [Pa]	TOTAL PRESSURE [Pa]	VOLUMETRIC FLOWRATE [m^3/hr]	VOLUMETRIC FLOWRATE [m^3/s]	MASS FLOWRATE [kg/s]
0	0	0	0	0	0.000	0.000
10	562	235	263	200	0.056	0.067
15	843	529	591	300	0.083	0.100
20	1124	941	1050	400	0.111	0.133
25	1406	1471	1641	500	0.139	0.167
30	1687	2118	2363	600	0.167	0.200
35	1968	2882	3217	700	0.194	0.233
40	2249	3764	4201	800	0.222	0.267
45	2530	4764	5317	900	0.250	0.300
50	2811	5882	6575	1000	0.278	0.333

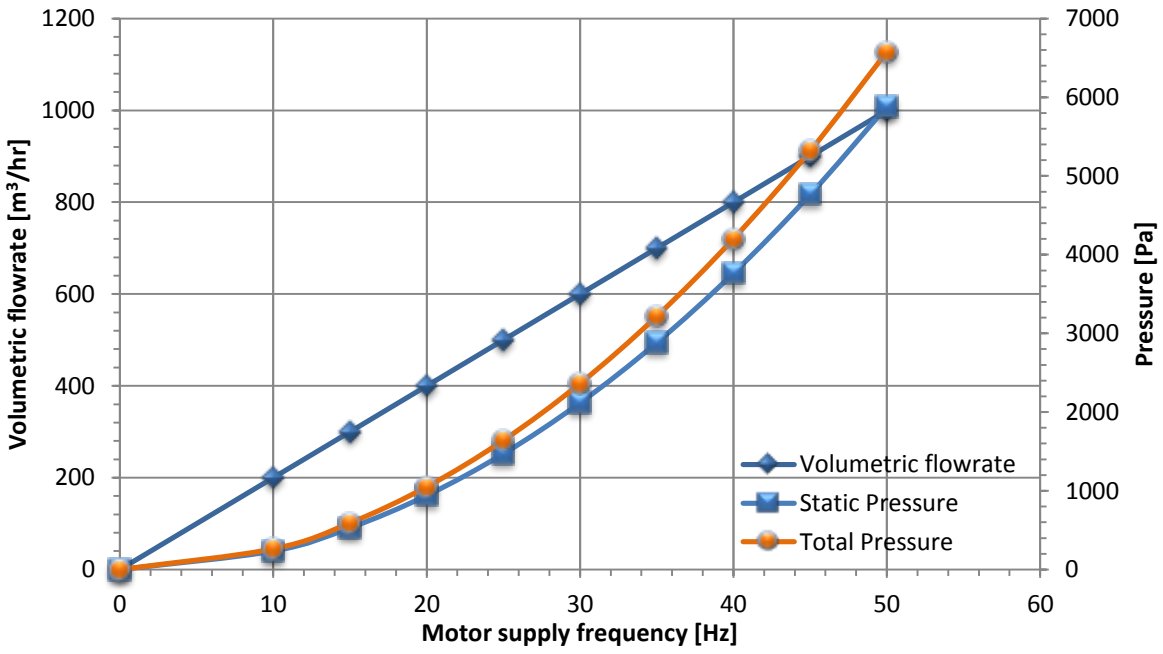

Figure 53 Flow rates, static and total pressure for different fan speeds

7.7 MANOMETER PRESSURE AND VELOCITY READINGS

Digital manometer is used to take static and total pressure readings. Static pressure values are then compared with values calculated by the numerical model.

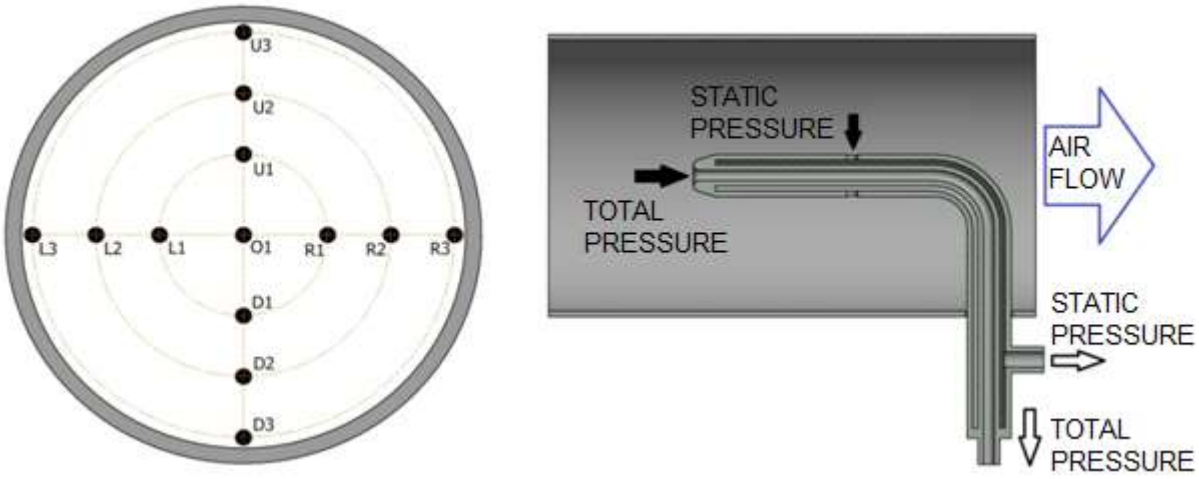

Figure 54 Schematic of pressure measurement with Pitot tube

Resistance curve of the classifier depends on several factors like air velocity magnitude and the resulting higher pressure drop or rotational speed of the classifier rotor. Higher rotational speed translates into greater resistance of the system.

Table 15Measured and averaged inlet velocity

Fan [Hz]	Inlet velocity [m/s] for classifier mot.fr. [Hz]				
	30	**35**	**40**	**45**	**50**
30	18.32	16.84	15.26	13.15	11.6
40	20.1	18.92	17.83	16.48	15.27

Table 15 shows measured values of air velocities for 2 fan speeds and varying classifier rotor speed. With the assumption of incompressible flow, total pressure represents sum of static pressure and dynamic pressure. Velocity of flow for fluid with known density can be calculated with respect to Bernoulli's principle.

$$v_m = \sqrt{\frac{2(P_T - P_S)}{\rho}} \tag{7.3}$$

Where ρ represents density of fluid, P_T represents total pressure, P_S represents static pressure and v_m represents velocity of fluid in the duct. Digital manometer carries out this conversion and velocities are recorded directly. Several readings of velocity are taken for each combination of centrifugal fan and classifier rotor setting. Velocity readings are taken at different positions inside of the duct due to varying velocity distribution in the duct. Velocity in the near wall region is lower than in the core region and therefore resulting measured velocity is calculated as an average of these readings. These values are then cross referenced with velocities calculated with respect to

fan affinity laws. Figure 56 shows measured air velocities in the inlet duct for 30 and 40 Hz fan speed. It can be observed that velocity increases with decreasing classifier rotor speed. It can be observed that air velocities for 50 Hz classifier setting and 30 and 40 Hz fan speed settings calculated with respect to fan affinity laws are lower than measured values. This can be explained by lower system resistance at 50 Hz classifier speed setting than anticipated in fan performance curve. Velocities were measured without any particle loading which would further increase system resistance and therefore decrease measured velocity.

Figure 55 Digital manometer

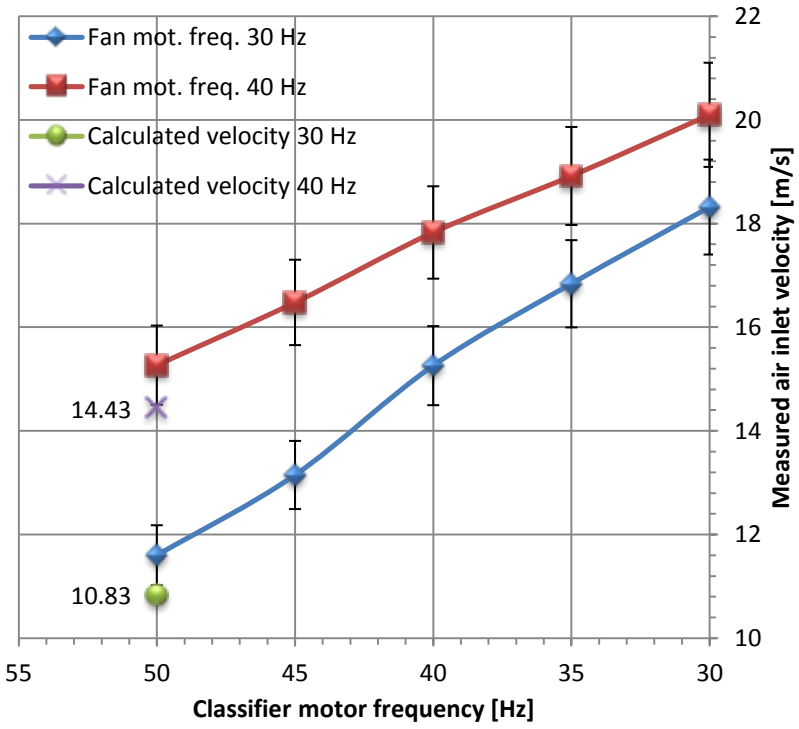

Figure 56 Measured and averaged air velocity in inlet duct

More accurate boundary conditions in numerical model lead to more precise simulation. Velocity values represent an important boundary condition in the numerical simulation and therefore measured values are used. Ten numerical simulations are carried out with 2 fan settings and 5 classifier rotor settings. Figure 55 shows digital manometer used in the measurement.

7.8 FEED MATERIAL

Barite or baryte which is a mineral consisting mainly of barium sulfate $BaSO_4$ is selected for classification trials. Almost 80% of worldwide production of barite is used in petroleum industry as a weighting agent in both aqueous and non-aqueous drilling fluids. It is used in gas and oil exploration and drilling process to suppress high pressure and stop blowouts. Ground barite must be dense with minimum specific gravity 4.1 or larger.

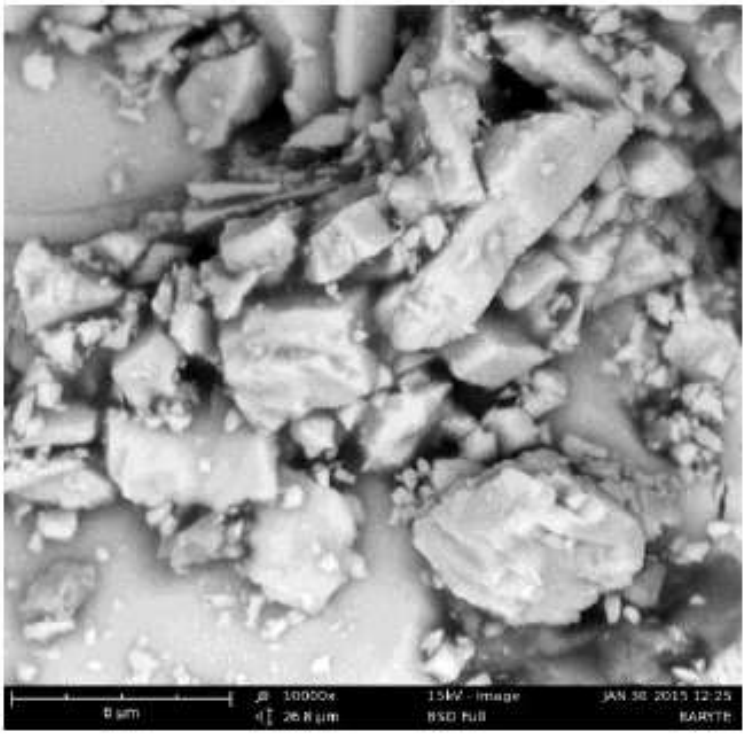

Figure 57 Fine barite under electron photomicrograph [54]

Particle size distribution is especially important due to its influence on drilling process and equipment performance. Too coarse particles cause settling out and on the other hand too fine particles do not provide adequate weighting and could lead to formation damage. American Petroleum Institute therefore specifies that barite used in drilling mud applications should be of certain particle size specification. The percentage of material below 6 microns should not be higher than 30% of weight and the fraction above 75 microns should be minimal. These objectives increase requirements on the comminution and classification process. Throughput of the grinding system and life of wear items could be increased by early removal of particles from the system.

Classification trials with barite feed material are carried out for several combinations of operational parameters of the system. It is a long-established fact that increasing tip velocity decreases cut size. Specific field of interest of this work is attributed to classification of particles in region of ten microns and thus highest available speed of the classifier rotor is required. Other two operating conditions that affect cut size as shown in the theoretical section of this work are air velocity and feed rate. Therefore, influence of these parameters together with classifier speed on cut size is investigated. Table 16 shows trials carried out with barite as a feed material.

Table 16 Trials with barite feed material and operating conditions

TRIAL	CLASSIFIERMOTOR SUPPLY [Hz]	FAN MOTOR SUPPLY [Hz]	FEED RATE [Hz]
TB1	50	50	10
TB2	50	50	20
TB3	50	50	30
TB4	30	50	20
TB5	40	50	20
TB6	30	40	20
TB7	40	40	20
TB8	50	40	20
TB9	30	30	20
TB10	40	30	20
TB11	50	30	20

Particle size distribution curve of feed material is shown in Figure 58.

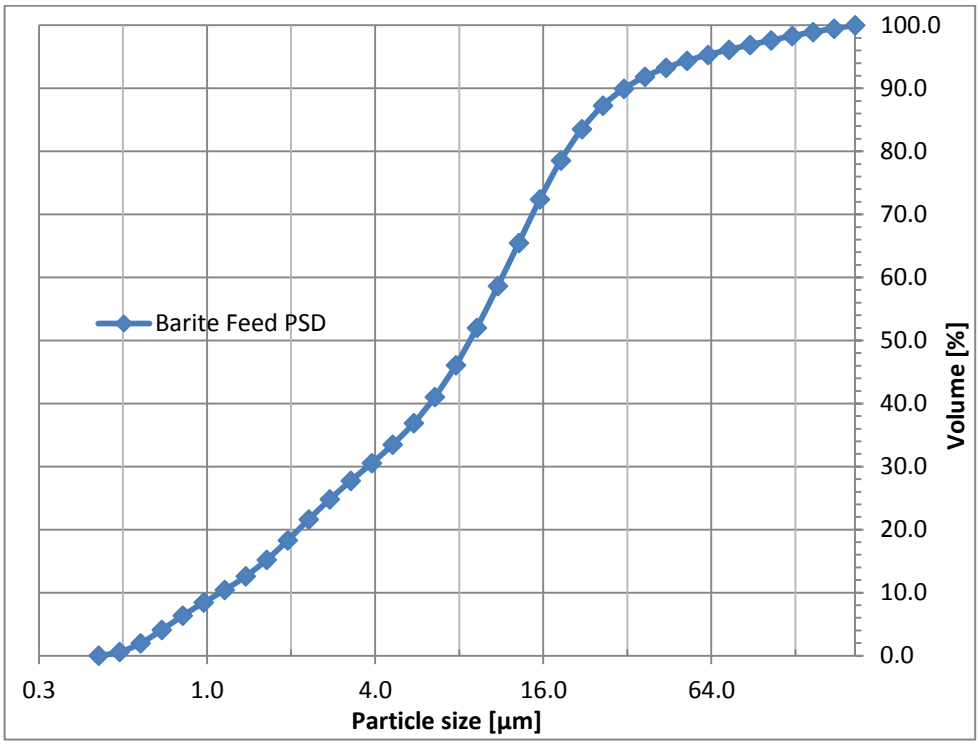

Figure 58 Particle size distribution of barite feed

In order to provide constant setup conditions of the experiment, testing procedure for trials is obeyed. This is to minimize error connected to transitional periods of the classification process, material deposition on the internal walls of cyclone and classifier and representative sampling of fine and coarse powder fraction.

Procedure for one classification trial is as follows:

1. Buckets for fine and coarse material collection are installed and air tight seal is checked
2. Speed of classifier rotor is selected and electric motor is started
3. After the classifier rotor reaches desired speed, the speed of centrifugal fan is selected and electric motor is started
4. Industrial vacuum is started to maintain dust free operation whilst loading feed material into feed hopper
5. 23.5 kilograms of Barite is loaded into the feed hopper vessel
6. Speed of rotary feeder is selected and electric motor is started. Classification process starts and particles are now being fed to classifier
7. Classification process takes place until the content of feed hopper is emptied into classifier
8. Once the feed hopper is empty, further 2 minutes are allowed for remaining particles in the system to be collected.
9. Electric motors are now stopped and further time is allowed for moving parts to stop completely
10. Shock vibrations are applied to cyclone and classifier body in order to agitate particles deposited on the internal walls
11. Buckets containing coarse and fine fraction of particles are removed and weight of each fraction is recorded
12. Fine fraction bucket and coarse fraction bucket are agitated to increase homogeneity of individual fractions
13. Representative samples from fine and coarse fractions are taken and laboratory particle size distribution analysis is carried out by using Microtrac particle analyser system
14. Results are post processed, recorded, discussed and evaluated

7.9 PARTICLE SIZE ANALYSIS – LASER DIFFRACTION

Microtrac S3500 particle size measuring station is used for particle size distribution measurements. It employs laser diffraction method with three red lasers arrangement for improved accuracy. Increased effectiveness of photo detecting devices is achieved by using higher number of light sources. Phenomena of scattered light from these light sources projected through a dry state sample delivered as a stream of particles is used. Light rays which strike particles are scattered into form of angular pattern. Angular variation in intensity of light scattered when laser beam passes through a dispersed particulate stream is measured by photo detector array and evaluated. Figure 59 shows operating principle of S3500 analyser.

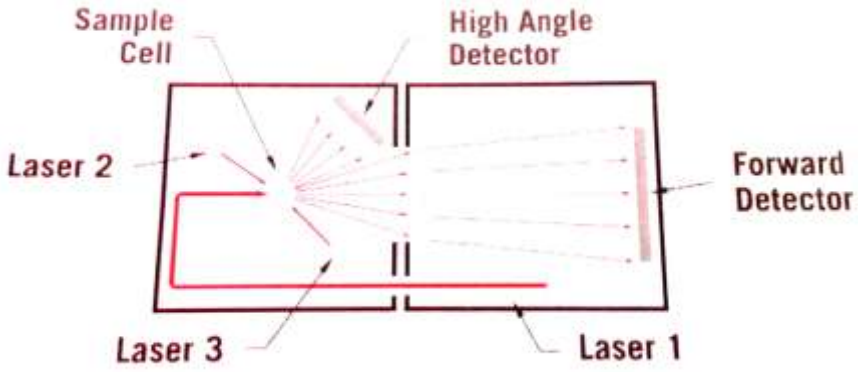

Figure 59 Laser diffraction arrangement schematic[55]

Particulate systems contain agglomerated particles which is an undesirable phenomenon during particle size analysis. Turbotrac dispersion system is employed in order to break apart these particles. It is a linear dry feeder which contains tray holding the sample. Moving aspirator tube draws the sample from the tray and dispersed sample is then delivered to the Microtrac's optical bench. Sample delivery controller acts as a communication interface and controller of sample delivery.

Figure 60 Particle size analysis measuring setup

Industrial vacuum and 6 barg compressor are connected to the system to assist sample dispersion, transport and removal. Air blender is used to control flow ratios between vacuum and compressed air. Dispersion is increased or decreased by adjusting air blender setting and maximum pressure setting.

Figure 61 Compressor used for dispersing particles and Microtrac system

Two approaches to particle morphology are considered. Spherical particles have the largest amplitude of scattered light due to their capability to create optical resonance. Most of the particles coming from crushing process however have irregular shape. Optical resonance is less extreme for irregular shape and therefore irregular approach is selected. Empirically modified Mie theory is applied for non-spherical shape. Refractive index for barium sulphate particles is known and its value is 1,65. It is important to include this parameter as most of the particles are below 25 microns. Measured particle data is evaluated by Microtrac Flex software and particle distribution curves are created.

7.10 PARTICLE IMAGE VELOCIMETRY (PIV)

PIV is an advanced imaging technique used mainly in research for visualization of flow patterns. It allows capturing and visualizing of instantaneous velocity profiles in the flow in form of vectors, contours, etc. Real time velocity maps are especially valuable for verification of numerical model predictions as they can capture flow details like small eddy formations as well large-scale flow patterns. Another considered method for measuring velocities and their patterns in flow is hot wire anemometry. This is however suitable only for simple measurements with good access to investigated volume. Important disadvantage of this measurement are disturbance effects on the flow due to actual presence of the probe in the flow.

Complexity of PIV measurements is determined by the level of spatial detail to be investigated. One camera is used for 2D planar PIV where the investigated area of interest is a plane. Two cameras are used for stereoscopic PIV, where third dimension can be reconstructed by principle of stereoscopic imaging from two different perspectives with use of Scheimpflug lens arrangement. The most complex is tomographic PIV which uses three or four cameras. These are precisely

calibrated and mapped in space in one coordinate system. Tomographic PIV uses principle of tomographic reconstruction of voxel intensities in three-dimensional space. Velocity vectors are reconstructed by iterative three-dimensional cross correlation method using deformed interrogation volumes. Further detail can be added by using time resolved tomographic PIV. Figure 62 shows schematic of working principle of PIV.

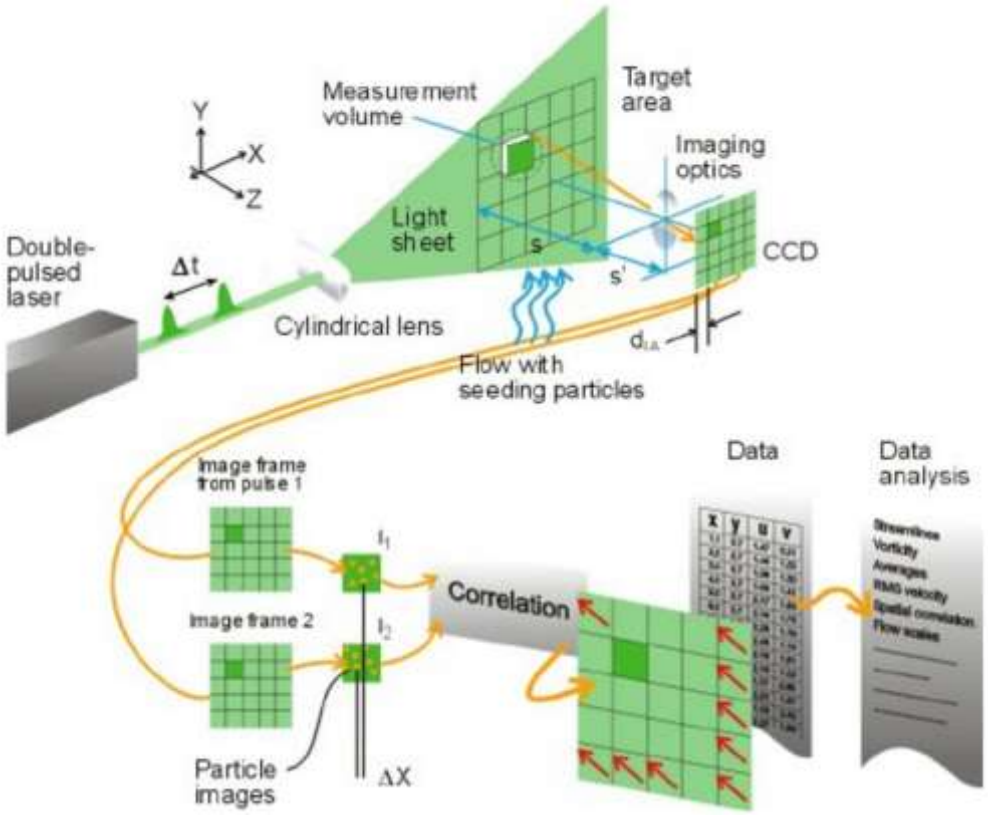

Figure 62 PIV measurement principle [64]

Due to physical construction of the device and spatial limitations in situ, 2D planar PIV is used in the experimental section. Investigated area is a plane aligned with expected flow and intersecting rotor blades of the classifier as per Figure 47.

Experimental setup of 2D PIV consists of several subsystems. Investigated flow must be saturated to specific concentration by seeding particles of certain size. These particles are created by aerosol generator and this subsystem and particle properties are described in following chapters. Particles travelling in the flow are illuminated twice in the plane of laser sheet which determines the investigation plane. Double pulsed laser is used due to its high energy and short pulse capability. Light beam is transformed into a thin sheet by arrangement of spherical and cylindrical lenses. Heat generated in the laser is removed by cooling liquid circulating in the system by two umbilical cables. Time interval between the two pulses can be adjusted and it depends on the velocity of the particles.

Double shutter camera is used to record light shattered by particles on two frames. Shutter speed is selected in such a way that the second frame captures displacement of original particles from the first frame. It is linked to laser via synchronizer whose main function is to synchronize and trigger both camera shutter and laser pulses. Timing of each frame in sequence together firing

of lasers can be controlled with 1 ns accuracy. After successfully exposing camera sensor in two successive frames, the digitized output recordings are transferred into computer memory.

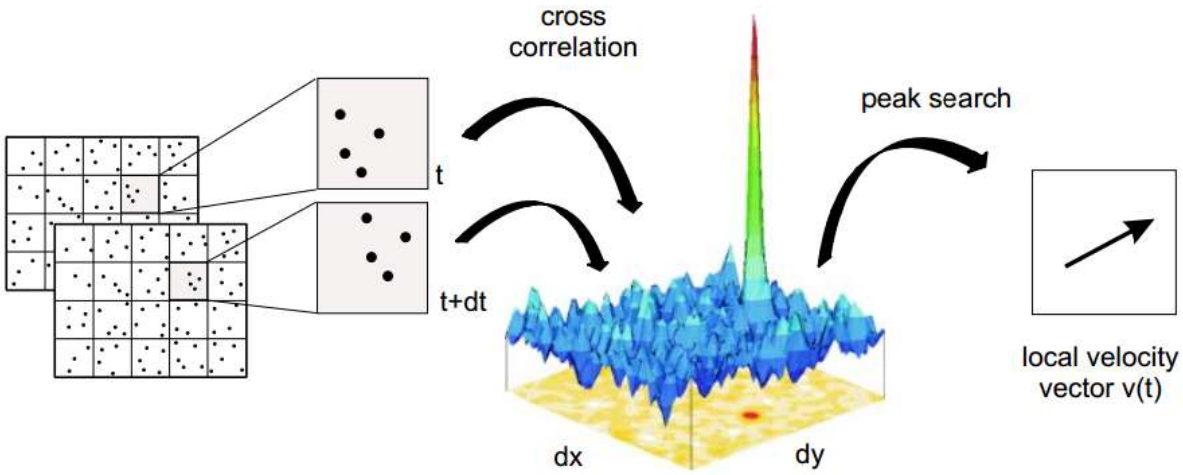

Figure 63 Evaluation of PIV recordings using cross-correlation [65]

Software evaluation of collected data can be essentially described as mapping of average displacements of group of particles. Both frames are divided into a number of small sub areas called interrogation areas. Each interrogation area on the first frame is then compared with interrogation area at the same location on the second frame. Cross correlation technique is then used, resulting into the most probable displacement vector for particular group of particles. This process is repeated for each interrogation area until the complete vector diagram is achieved. Displacement vectors are then converted into velocity vectors based on known time between the laser shots and known physical size of each pixel on the camera.

7.10.1 Aerosol generator

Aerosol generator is used to generate polydisperse aerosol by atomizing liquids, in this case oil, into particles in the submicron range. Investigated fluid system is then seeded with these particles. Generator in experiment can sustain constant counter pressure of 10 bars and thus by far exceeding maximum pressure value in the system. Several atomizer nozzles are incorporated into the liquid vessel. Particle concentration can be adjusted by modifying pressure or by closing or opening nozzles. High velocity jet is created by gas passing through the atomizer nozzle producing droplets suspended in the flow. Droplets with greater size are eliminated by design of the liquid vessel resulting into particle sizes in submicron range. Figure 64 shows operating principle of the generator. Di-Ethyl-Hexyl-Sebacate (DEHS) is fluid used by aerosol generator to seed investigated flow domain. It is a colourless and soluble liquid and in combination with given aerosol generator, the most particle penetration size is below 1 µm. Approximate lifetime of particle with size 0.5 µm is in region of 4 hours. Density of DEHS is 0.91 g/cm^3 and its dynamic viscosity is 22-25 mPa. Table 17 shows typical particle distribution in produced aerosol. Seeding or tracer particles are crucial component of every PIV measurement. Careful consideration of investigated fluid and of expected flow properties is carried out. Choice of particle material is usually dependent on properties of fluid and for gaseous problems, oil droplets are used.

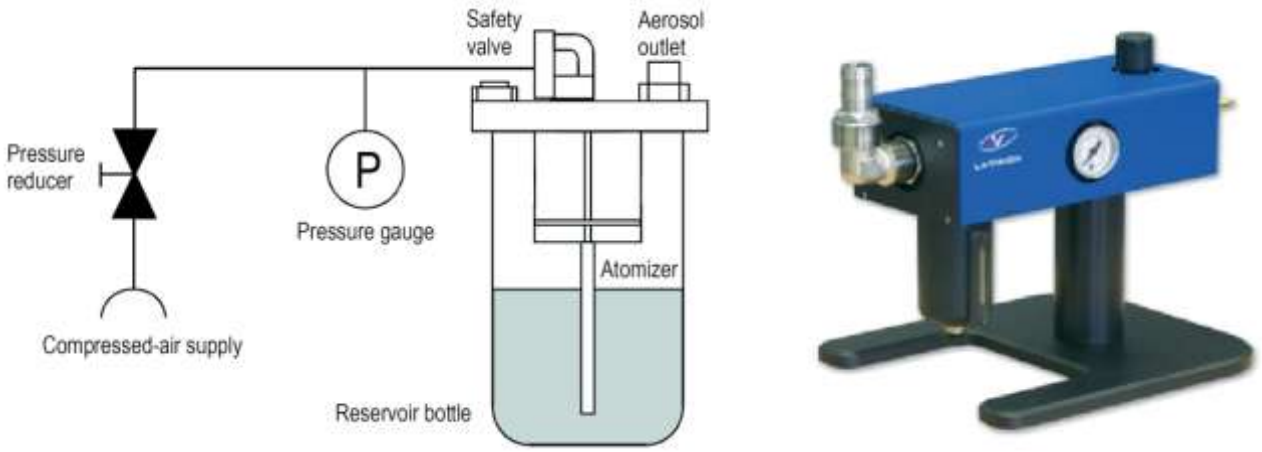

Figure 64 Aerosol generator operating schematic

Refractive index of particles must be different to the one of the fluid so that once the plane is illuminated by laser sheet, only light scattered off the particles is reflected and captured by the camera. Ideal particles should be spherical and should have density similar to the one of the fluid. Size of the particles must be small enough to accurately follow motion of the fluid with relatively short reaction time to changes in the flow. Due to particle size, their motion is dominated by Stokes drag law. Particles must be however large enough to scatter enough laser light for the CMOS sensor to record usable frame. Concentration of particles in fluid domain must be reasonably high so that once the image taken by camera is divided into interrogation areas, there are several particles in each area. This may pose a significant problem for some single pass systems with high volumetric flow. In the case of classifier, air is re-circulating in the system. Particles generated by aerosol generator are being added into the system at constant rate until achieved particle concentration is sufficient for the measurement. If the concentration decreases due to deposition on walls, generator is started again and the flow is saturated with particles again.

Table 17Aerosol specification for DEHS

DROPLET SIZE	CONCENTRATION
0.2 µm	$2x10^7$ #/cm^3
0.5 µm	$5x10^7$ #/cm^3
1 µm	$1x10^3$ #/cm^3
0.3-0.5 µm	$1.5x10^7$ #/cm^3
0.5-1.0 µm	$8x10^6$ #/cm^3
TOTAL	$>10^8$ #/cm^3

7.10.2 Imager cCMOS camera

This particular camera is specially designed for demanding laser imaging applications. Low light imaging capability combined with significant signal variations makes it suitable for particle image velocimetry. It provides high temporal and spatial resolution for large regions of interest illuminated by laser sheet. Figure 65 shows camera used for image capturing.

Figure 65sCMOS camera used for image capturing

Double exposure camera is primarily designed to capture two frames with a very short time period in between them. This inter-framing time essentially represents shutter speed in between two successive frames and it is an important parameter to consider when selecting camera for particle image velocimetry. In order to be able to capture particles moving with high velocity, its value must be small enough to capture particles travelling through the interrogated window in both taken images. Due to very short shutter speeds required for high velocity flows, these cameras are mainly used in combination with double laser head light sources.

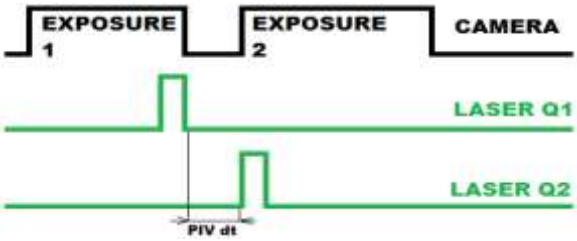

Figure 66 Schematic of shutter and laser timing

After recording process, both the images are transferred into connected computer and camera is the prepared for the next pair of images. Table 18 shows specification of camera used in the experimental part.

Table 18 General specification of the camera

DOUBLE SHUTTER	**120 ns inter-framing time**	**NO. OF PIXELS**	**2560x2160**
EXPOSURE TIME	15 µs-100 ms	PIXEL SIZE	6.5µm x 6.5µm
DIGITAL OUTPUT	16 bit	ACTIVE AREA	16.6mm x 14mm
INTERFACE	PCI-Express Card	SPECTRAL RANGE	370-1100 nm

Endoscope with 8 mm diameter and a set of lenses inside has been considered for the measurement. It connects to camera lenses and allows closer observation of flow patterns without noise created by particles present in between the plane illuminated by laser and camera optics. It would however decrease size of the region of interest. It also would have disturbed the flow in the

area of interest. After careful consideration of advantages and disadvantages it has been decided to use camera with suitable configuration of lenses instead. Camera is located on the outside of the classifier behind a glass window thus allowing observing larger sections of flow. Advantage of this arrangement is that the method becomes non-invasive and measuring devices do not create any undesired disturbances in the flow. Support frame for the camera is designed in such a way that distance from investigated plane and camera lenses is optimal for dept of field of the camera lenses. This parameter has a direct influence over sharpness of the image and its correct value increases quality of captured frames for further digital post processing.

7.10.3 Nd:YAG PIV Laser

Two pulsed neodymium-doped yttrium aluminium garnet laser is used as a light source for PIV measurement. It consists of dual cavity to provide stable green light pulsed light source. The 1064 nm laser beams are polarization combined and are then entering second harmonic generator producing visible 532 nm light sheet. Dichroic mirrors are then used to separate the residual infrared light from the visible part and the light beam is then directed to the experiment. Figure 67 shows laser setup with double laser head, power source and programmable timing unit used in the experiment.

Figure 67Double laser head with umbilical cables and power supply unit

Programmable timing unit PTU is used to vary time delay between the two pulses. This allows adjusting parameters of the measuring station with respect to studied physics. Table 19 shows characteristics of the double laser used in experimental part.

Table 19 Laser characteristics

BEAM DIAMETER	PULSE WIDTH	ENERGY STABILITY	ENERGY @ 532 nm	REPETITION RATE	DIVERGENCE	POINTIN. STABILITY	POWER SUPP.
6.5 mm	6-9 ns	± 2% RMS	200 mJ	0-15 Hz	~ 3 mrad	< 100 µrad	650 W

8 EXPERIMENTAL RESULTS AT LIMITING OPERATING PARAMETERS OF CLASSIFIER

Experimental part can be divided into two main sections where the first section focuses on data collected by particle image velocimetry (PIV). It includes velocity vector maps of flow patterns for different operating parameters. These measurements were carried out with oil droplets to provide trustworthy visualization of flow structures, of velocity magnitudes and of eddy formations. Second chapter includes particle size distributions for fine and coarse fraction obtained in classification trials. Effects of changing operating parameters are presented graphically.

8.1 EXPERIMENTAL PIV FLOW FIELD MEASUREMENTS

Ten data collection campaigns were performed to measure flow field in the rotor cage region and in the blade passageway. Actual position of the rotor cage is not synchronized with the camera sampling frequency due to extended complexity of the measurement and due to limited resources. Therefore, each measuring campaign involves capturing of one thousand pairs of images. Total number of images taken for the spectrum of operating parameters is 20 000. Table 20 designates measurement campaigns and assigns operating parameters for these trials.

Table 20 Parameters for measurements carried out with DEHS

TRIAL	FAN MOT. SUPPLY [Hz]	MEA. AVE. INLET VELOCITY [m/s]	CLASSIFIER MOT. SUPPLY [Hz]	TIP VELOCITY [m/s]	VELOCITY AT R114 MM [m/s]
TO1	30	18.32	30	25.23	21.49
TO2	30	16.84	35	29.42	25.07
TO3	30	15.26	40	33.65	28.65
TO4	30	13.15	45	37.96	32.23
TO5	30	11.6	50	42.06	35.81
TO6	40	20.1	30	25.23	21.49
TO7	40	18.92	35	29.42	25.07
TO8	40	17.83	40	33.65	28.65
TO9	40	16.48	45	37.96	32.23
TO10	40	15.27	50	42.06	35.81

Before the start of measuring campaign, flow domain is seeded by DEHS particles to sufficient level. Operating parameters for fan motor and classifier motor are selected and both are started. Each dataset includes comprehensive post processing. Results for every trial are presented below where the first trial also shows steps involved in data post processing.

8.1.1 Trial TO1 - Fan motor 30Hz & Classifier motor 30Hz

Initial post processing of raw images is carried out by Davis software.

1. PIV setup with camera allows online real-time transfer of situation in the region of interest during initiation phase. This is not however possible during data collection. Therefore, particle seeding is checked before the measuring campaign is initiated.

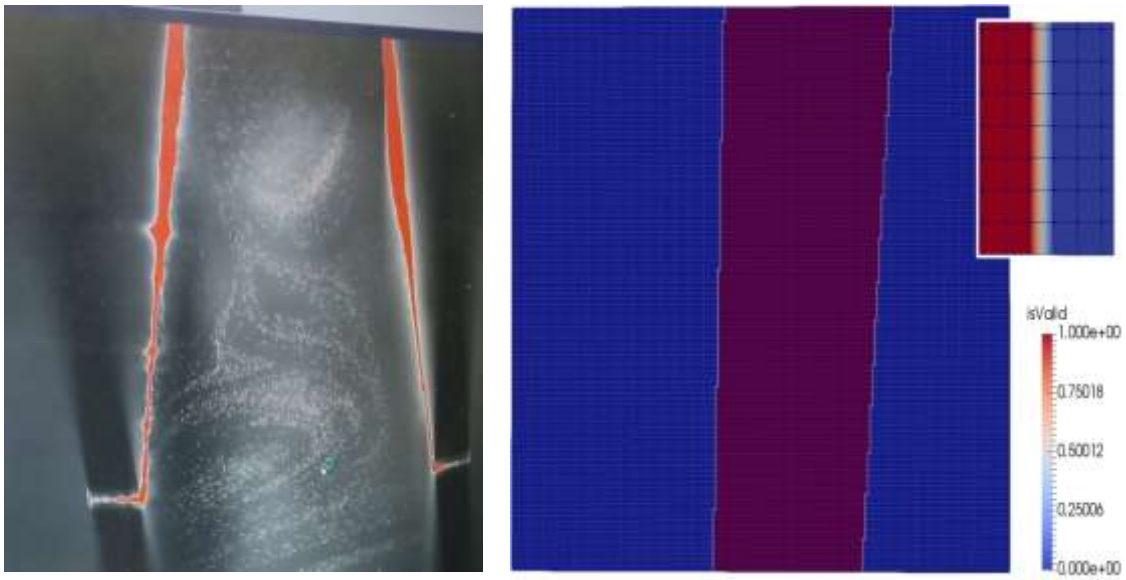

Figure 68 Particle seeding with stationary blades and laser reflections& interrogation windows

2. Classifier and the fan are started and sample image pair is taken with estimated time in between them. Particle displacement vector is then manually evaluated based on the two images. Desired particle shift for further processing should be in region of 4-8 pixels. Time step is adjusted so that particles fulfil the above-mentioned criteria. Measuring campaign is started and one thousand image pairs is collected for the given operating parameters.

3. Sliding background subtraction filter with filter length 8 pixels is used during image pre-processing. It is used because of intensity fluctuations in the background due to reflections. Laser light reflections could not have been prevented due to metal nature of the machine. These can be observed in Figure 68. As a high pass filter, large intensity fluctuations are filtered out while the small intensity fluctuations of the particle signal pass through.

4. Polygonal geometric mask is created at the fixed location of the laser light sheet during PIV processing. Multi-grid interrogation with final window size of 48x48 pixels is defined with 75% overlap and final vector grid spacing of 12 pixels. Each cross-correlation of single pair of interrogation windows results into single displacement vector. All vectors are then combined to form a final 2D vector field of the image.

5. Median filter with interpolation and smoothing for filling up empty spaces after outlier removal are used during PIV post processing.

6. Velocity vectors are recorded in an inertial reference frame. Constant value of velocity is subtracted in order to transfer vectors from inertial to non-inertial reference frame of the rotor. In reality, the velocity changes with radius. Blades are however narrow and therefore approximation of the velocity value is acceptable. It is calculated based on blade radius centre value 114 mm and angular velocity for each set of operating parameters.

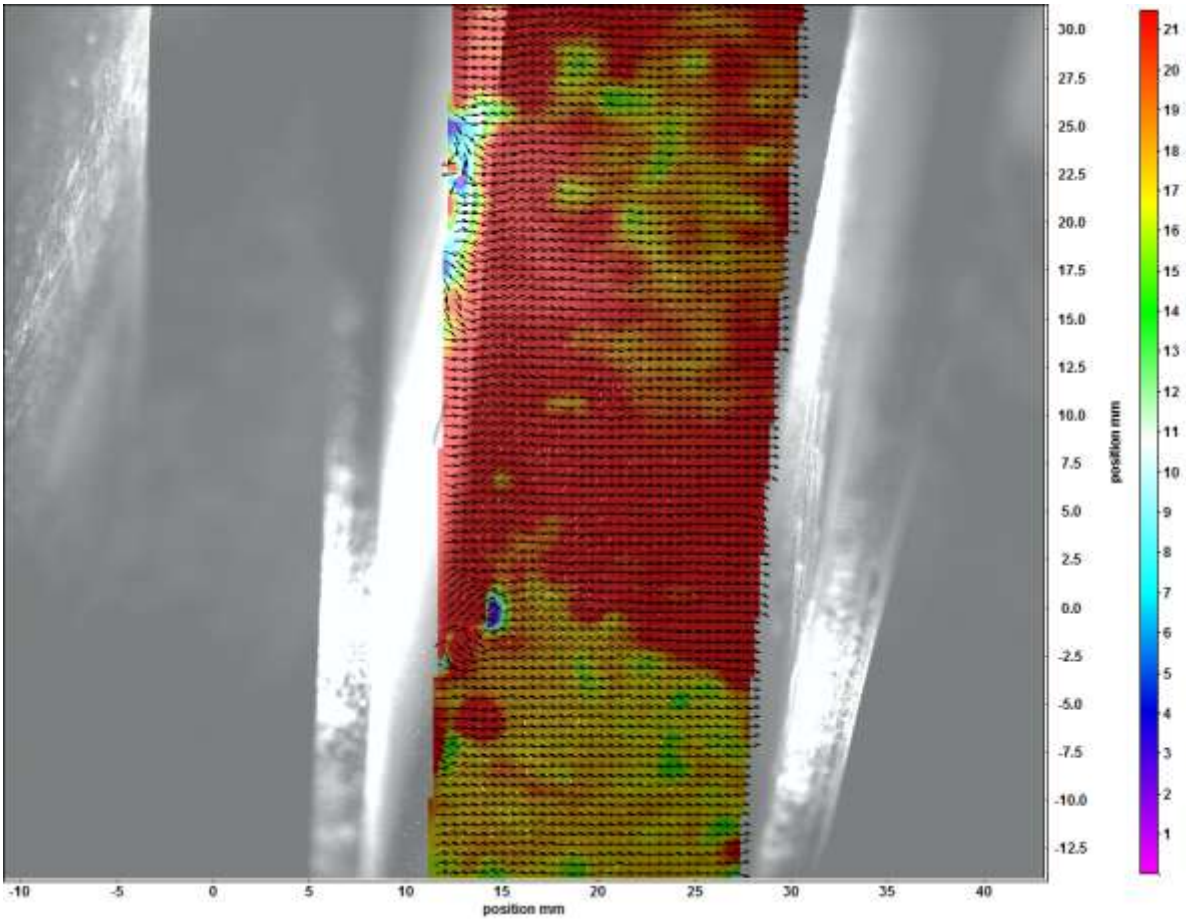

Figure 69 Velocity vectors displayed in inertial reference frame

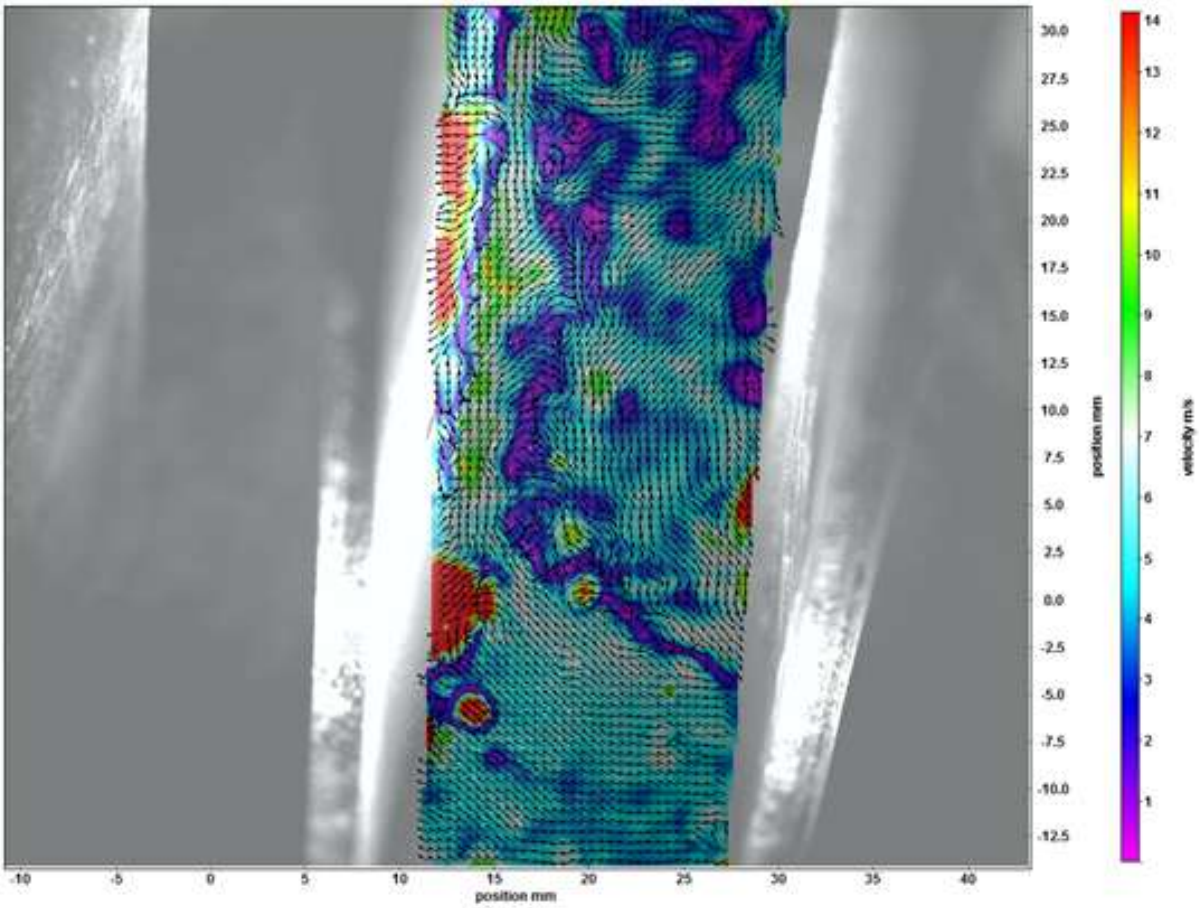

Figure 70 Velocity vectors displayed in non- inertial reference frame

7. The full set of one thousand image pairs is processed in the above-mentioned fashion. Some of the images are however distorted due to reflections and background noise, some images then display blades interfering with geometric mask. Therefore, images are manually evaluated and inappropriate ones are deleted.

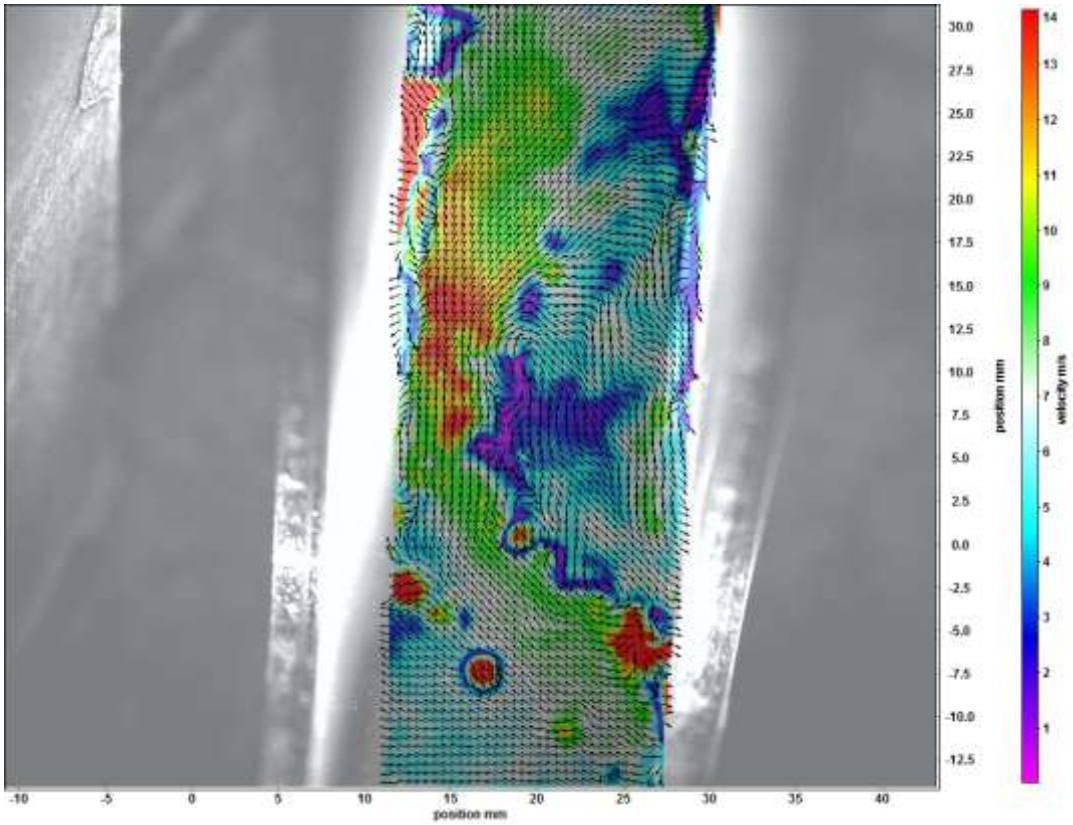

Figure 71 Image selected for averaging

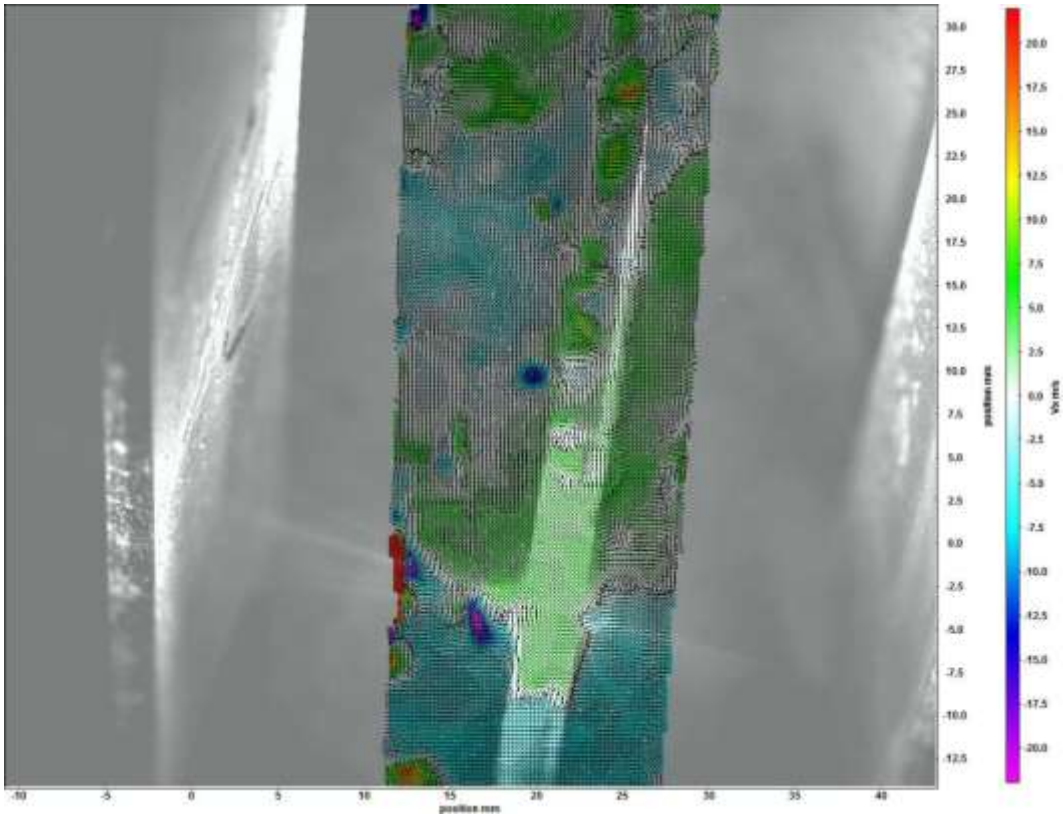

Figure 72 Image deleted due to incorrect position of blades

8. Remaining images are then averaged and exported from Davis software as .jpeg and .dat file. Vector field as exported in .jpeg and .dat format from Davis software is shown on Figure 73. It can be observed that the vector field is distorted by laser light reflections along the top left edge of the geometric mask. This is caused by imperfect camera alignment with laser light sheet and by metal nature of the rotor blades.

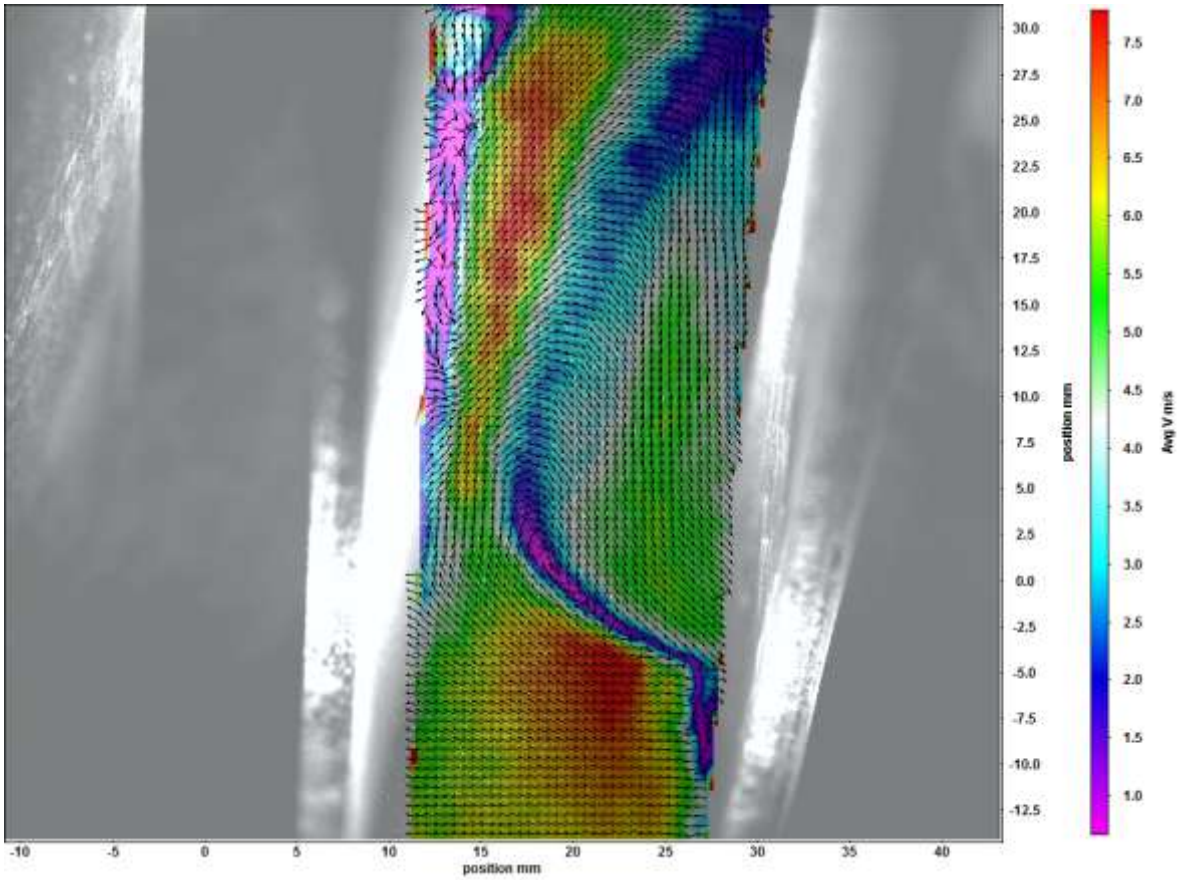

Figure 73 Averaged velocity vector field and .dat output from Davis software

9. In the next step, the .dat file is imported into Paraview software for further post processing. In order to visualize vector field and magnitude values, several layers of filters are applied to the imported TECPLOT files. This file represents point values of velocity in X and Y direction.

```
TITLE = "B00001"
VARIABLES = "x", "y", "Vx", "Vy", "isValid"
ZONE T="Frame 0", I=214, J=180, F=POINT
12.5493475944 31.2042385787 -2.6663190045 -1.3865281105 1
12.8028691858 31.2042385787 -1.5755362348 -1.6779621267 1
13.0563907772 31.2042385787 -0.752407151 -0.9573825664 1
13.3099123687 31.2042385787 -0.8913982155 -1.4544110561 1
13.5634339601 31.2042385787 -0.5370741945 -0.8813004405 1
13.8169555515 31.2042385787 -0.7865210066 -0.6561200756 1
14.0704771429 31.2042385787 -0.6711990083 -0.61898608 1
14.3239987344 31.2042385787 -0.6341988984 -0.3061060975 1
14.5775203258 31.2042385787 -0.6448559169 -0.1946688292 1
14.8310419172 31.2042385787 -0.5613946097 0.0465496852 1
15.0845635086 31.2042385787 -0.4475919009 -0.0796292916 1
15.3380851001 31.2042385787 -0.5118415399 -0.1208425662 1
```

Figure 74 Dat file example

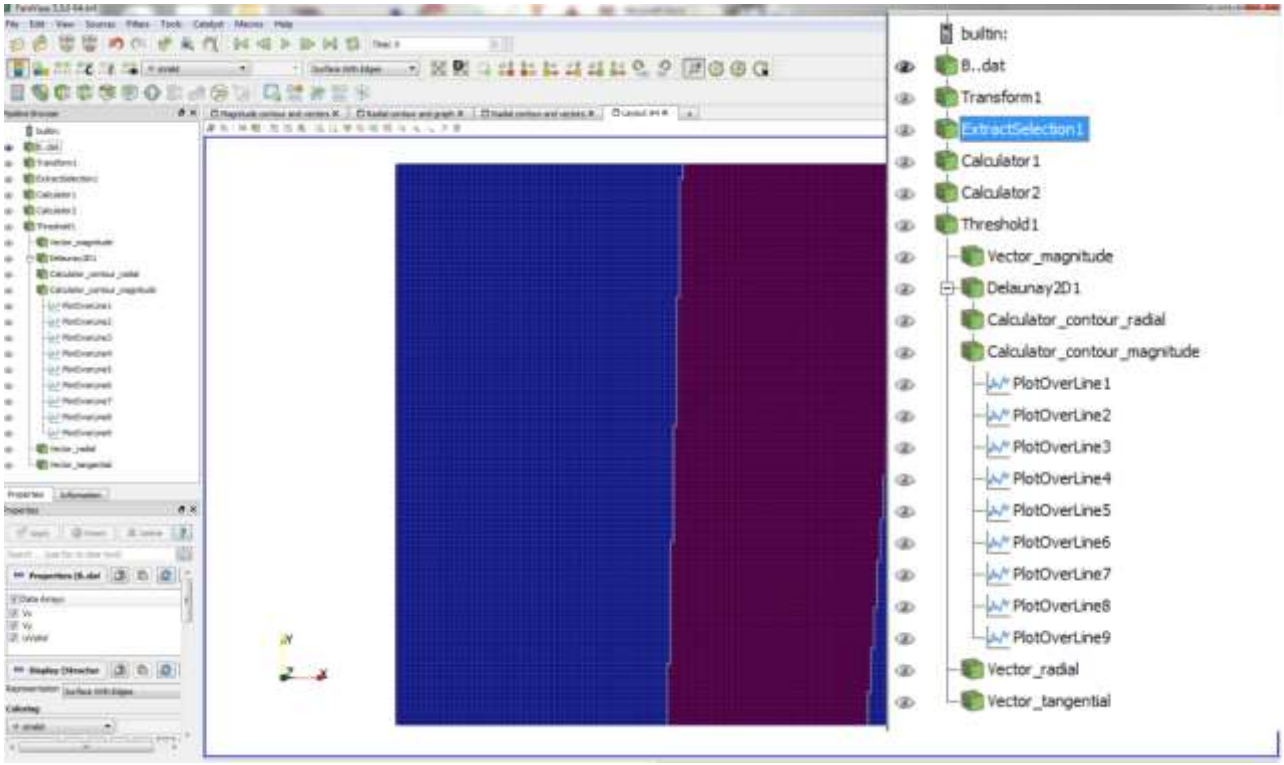

Figure 75Paraview interface and list of filters applied to visualize vector field

- Reference frame is transformed in such a way that its origin is located in the bottom left corner of the geometric mask.
- The selection where the geometric mask is valid is extracted by extract selection conditional filter.
- Two calculator filters are used to convert point data to vectors and their magnitudes.
- Threshold filter is applied and tuned to filter out peak values caused by reflections alongside the left and right edge.
- Glyph filter is used to display vector field with velocity magnitude scale colour map.
- Delaunay 2D filter is used to map the geometric mask with mesh in order to display velocity contours in X & Y direction (assumed tangential and radial direction)
- Another two calculator filters are used to display contours of velocity magnitude in Y direction (radial) and general velocity magnitude.
- Plot over the line filter is used multiple times to display velocity profiles in Y direction (radial) at programmed locations
- And lastly, glyph filter is used to display vector field with Y component scale colour map.

Maximum velocity and 2D vector field

Classifier rotor cage rotates anti-clockwise and therefore the right edge of the images represents leading blade while the left edge represents trailing blade. Blades and their position with respect to coordinate system and eddy formation are indicated in Figure 76. There is 30 blades equi spaced along the circumference of the rotor and are approximately 30 mm deep with 20 mm gap in between them.

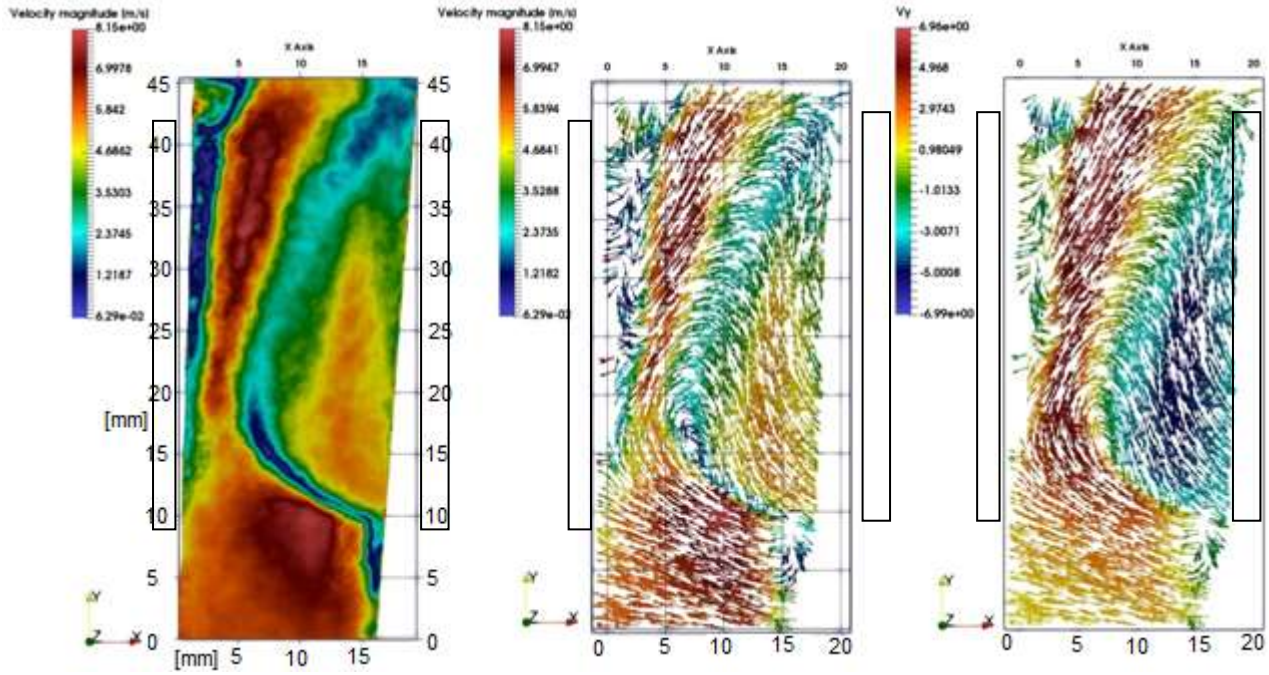

Figure 76 Maximum velocity contour; vector field by max velocity; vector field by radial velocity for 30-30 setting

The air enters blade passageway from the area outside the blades Figure 76 (Y=0-10mm). Here the flow direction is almost tangential with a very weak radial component of the velocity. This is beneficial for particle classification and it has been proven by various researches and experiments. Maximum velocity can be observed in this region and its value is 8.15 m/s.

Radial velocity profiles and 2D vector field

It can be observed that there is a recirculation eddy formed in the area behind the leading blade. It is an area where the airflow has opposite, outward direction. This phenomenon result into restricted passageway in between the blades. As a result, the airflow accelerates in the unrestricted region passing alongside this flow structure. As the air enters blade passageway the tangential component of the velocity becomes weaker and the radial becomes dominant component. Figure 77 shows contours of radial velocity where the location with maximum positive and negative radial velocity can be observed. Radial velocity is positive in the unrestricted region of the passageway whilst maximum negative radial velocity can be observed in the recirculation area. Values of radial velocity are plotted over lines which intersect the passageway by 5 mm increments. The location where radial velocity changes from positive to negative can be established by intersecting profiles with zero value. For the given fan and classifier settings, both positive and negative values reach to +7 and -7 m/s. Velocity profiles are slightly distorted in the

proximity of the blades due to laser light reflections and due to imperfect geometric constraints between classifier rotor, laser and the camera. This results into geometric mask which is not completely rectangular.

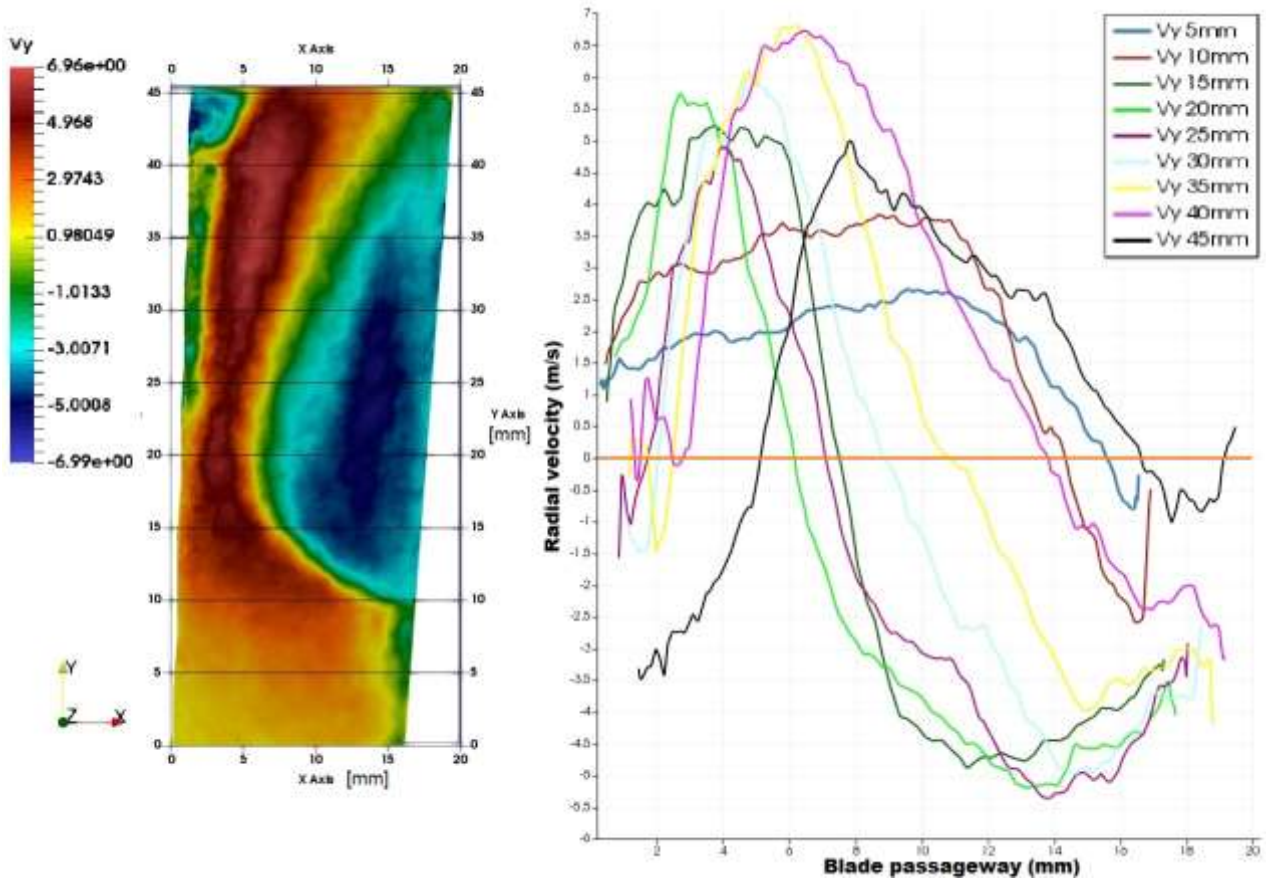

Figure 77 Radial velocity profiles with relation to position in the passageway for 30-30 setting

Vector field with glyphs colour map representing value of radial velocity is shown in Figure 76 It corresponds with radial velocity contour shown in Figure 77.

8.1.2 Trial TO2 - Fan motor 30Hz & Classifier motor 35Hz

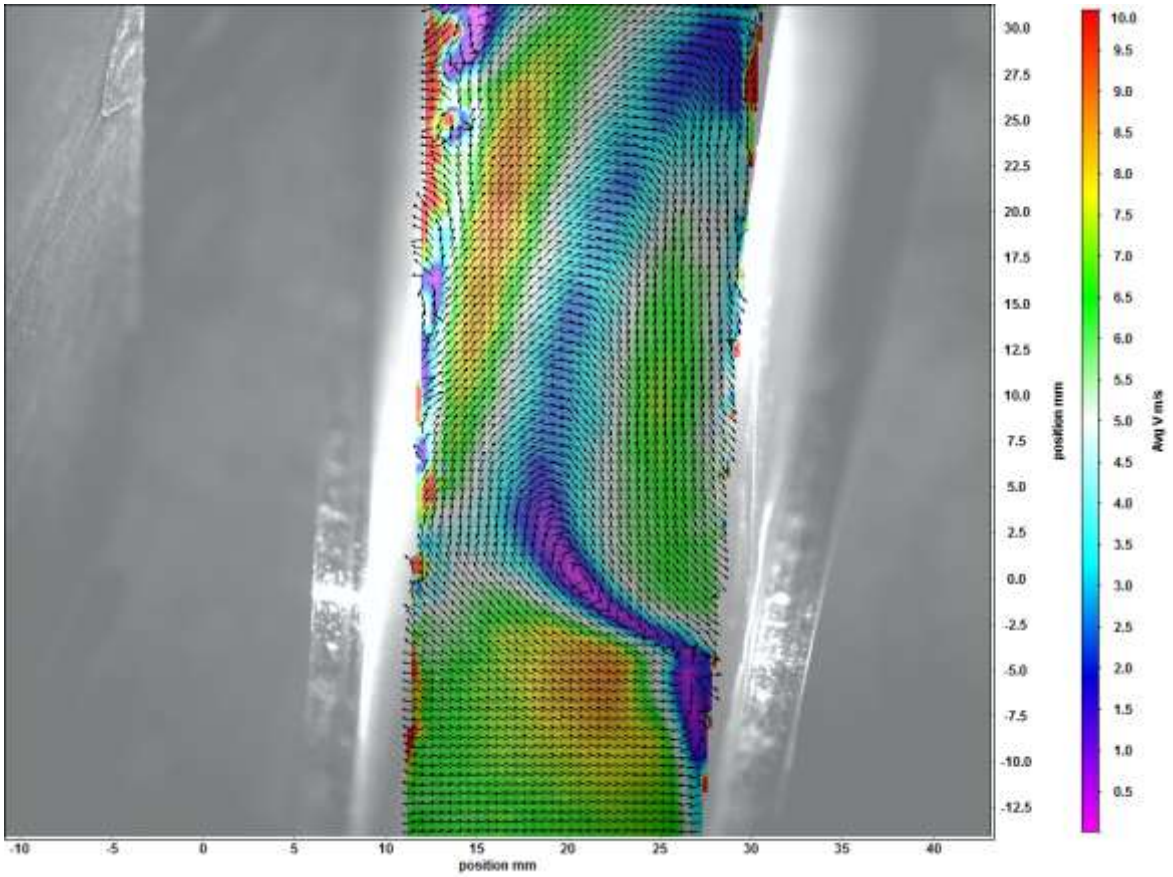

Figure 78 Vector field for 30-35 setting as computed by Davis software, overlaid over blades

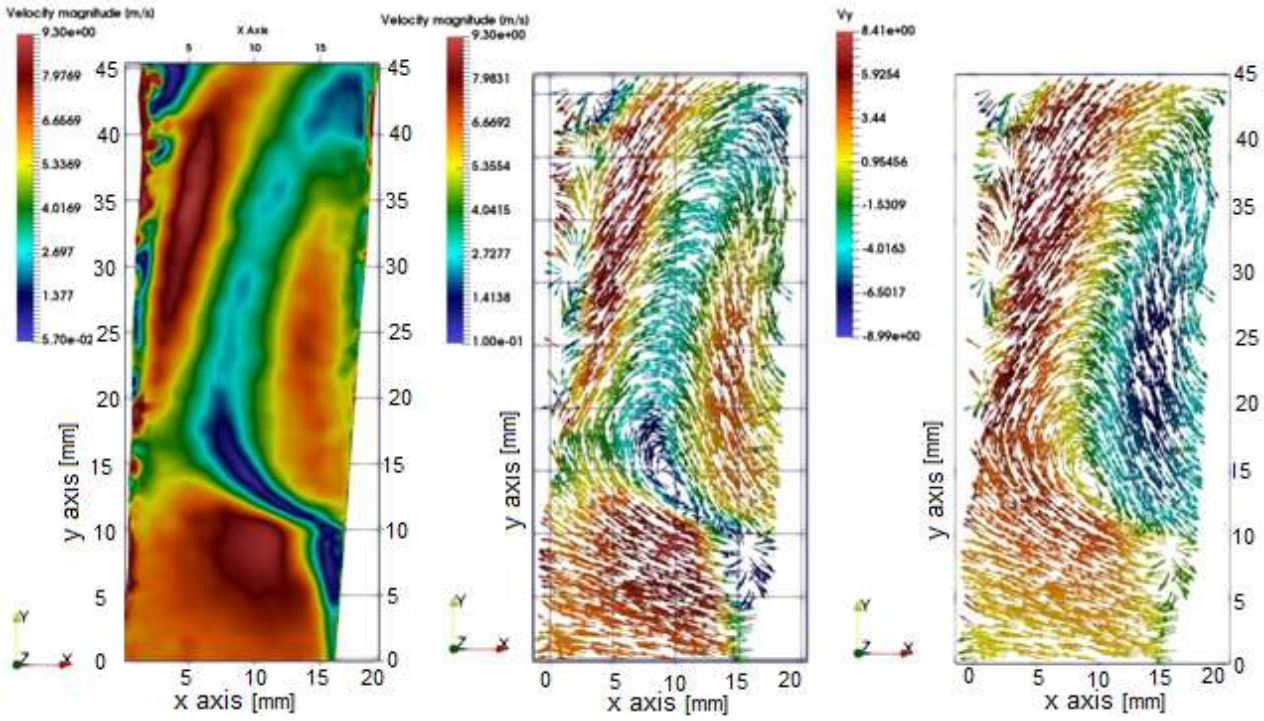

Figure 79 Maximum velocity contour; vector field by max velocity; vector field by radial velocity for 30-35 setting

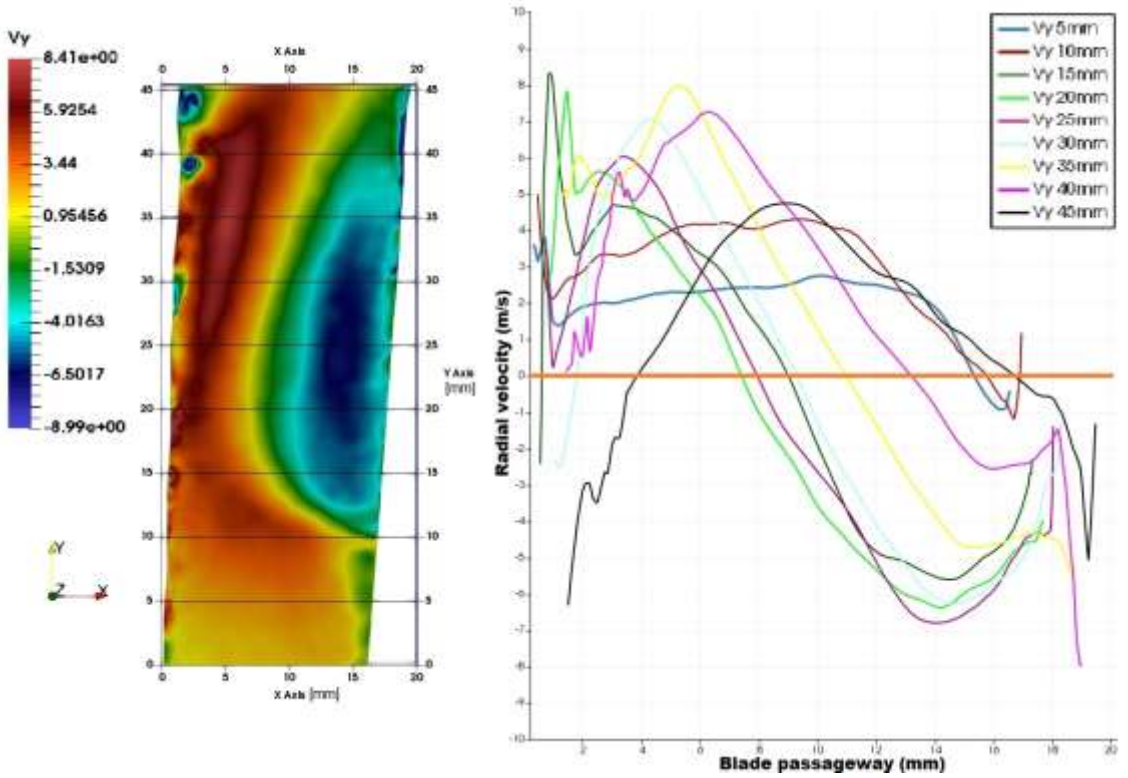

Figure 80 Radial velocity profiles with relation to position in the passageway for 30-35 setting

8.1.3 Trial TO3 - Fan motor 30Hz & Classifier motor 40Hz

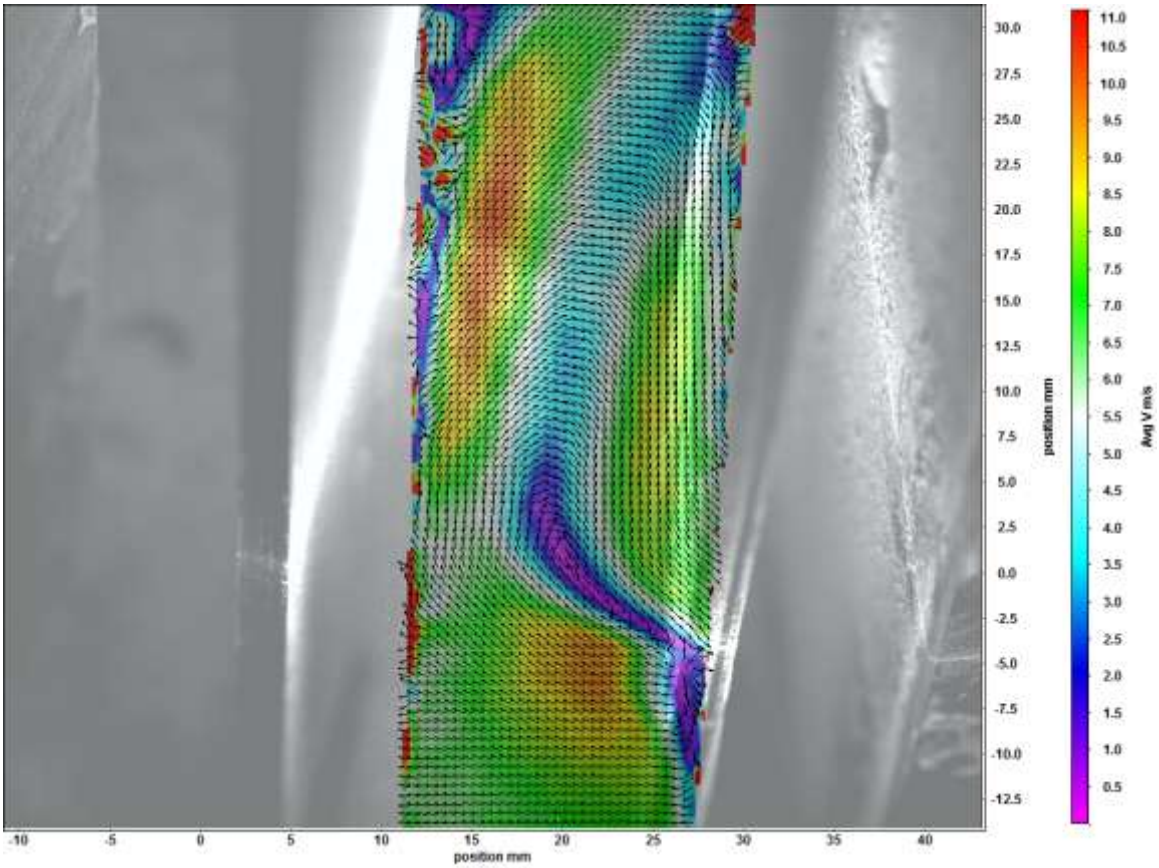

Figure 81 Vector field for 30-40 setting as computed by Davis software, overlaid over blades

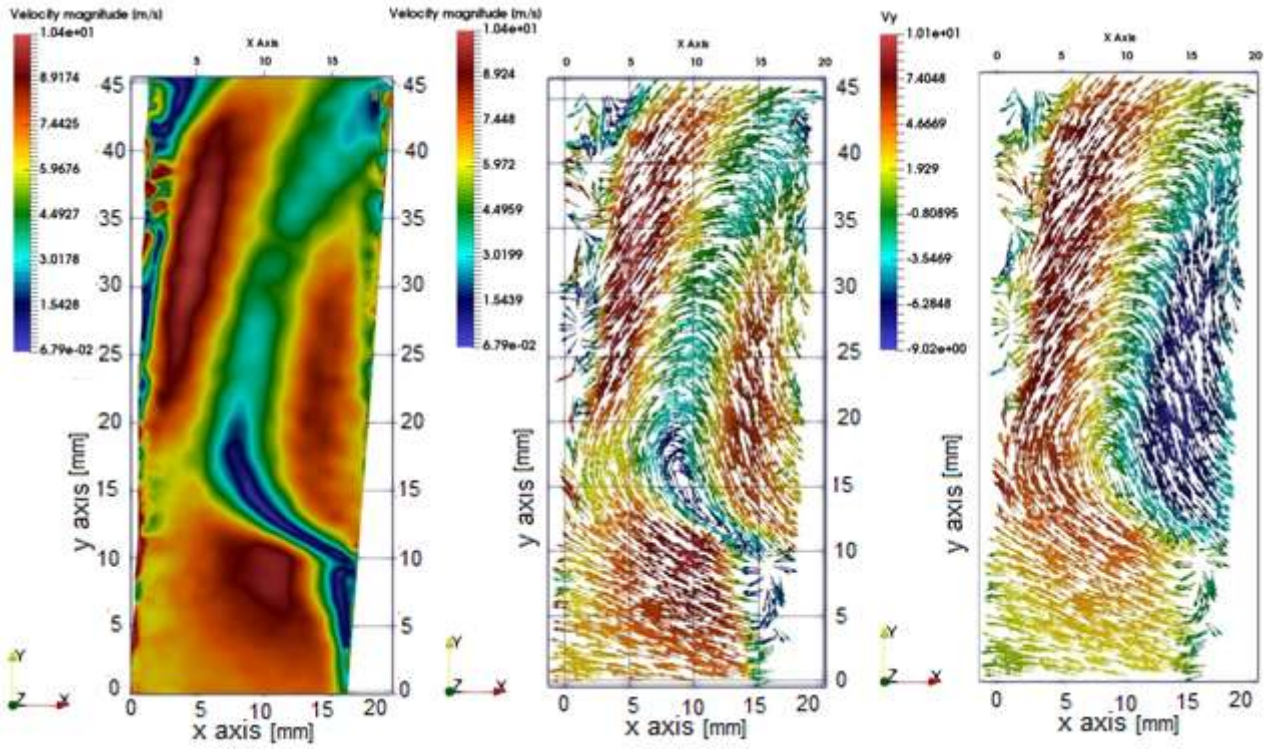

Figure 82 Maximum velocity contour; vector field by max velocity; vector field by radial velocity for 30-40 setting

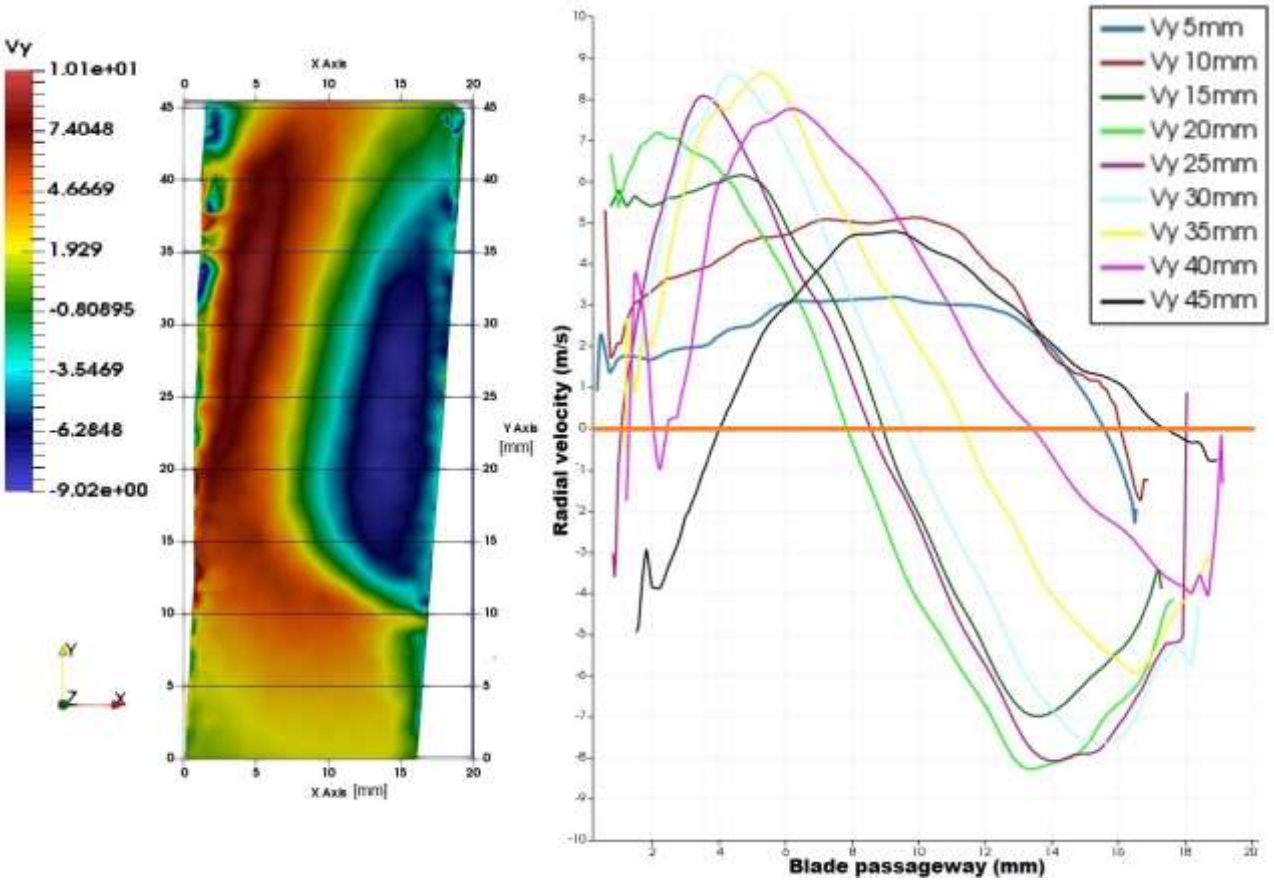

Figure 83 Radial velocity profiles with relation to position in the passageway for 30-40 setting

8.1.4 Trial TO4 - Fan motor 30Hz & Classifier motor 45Hz

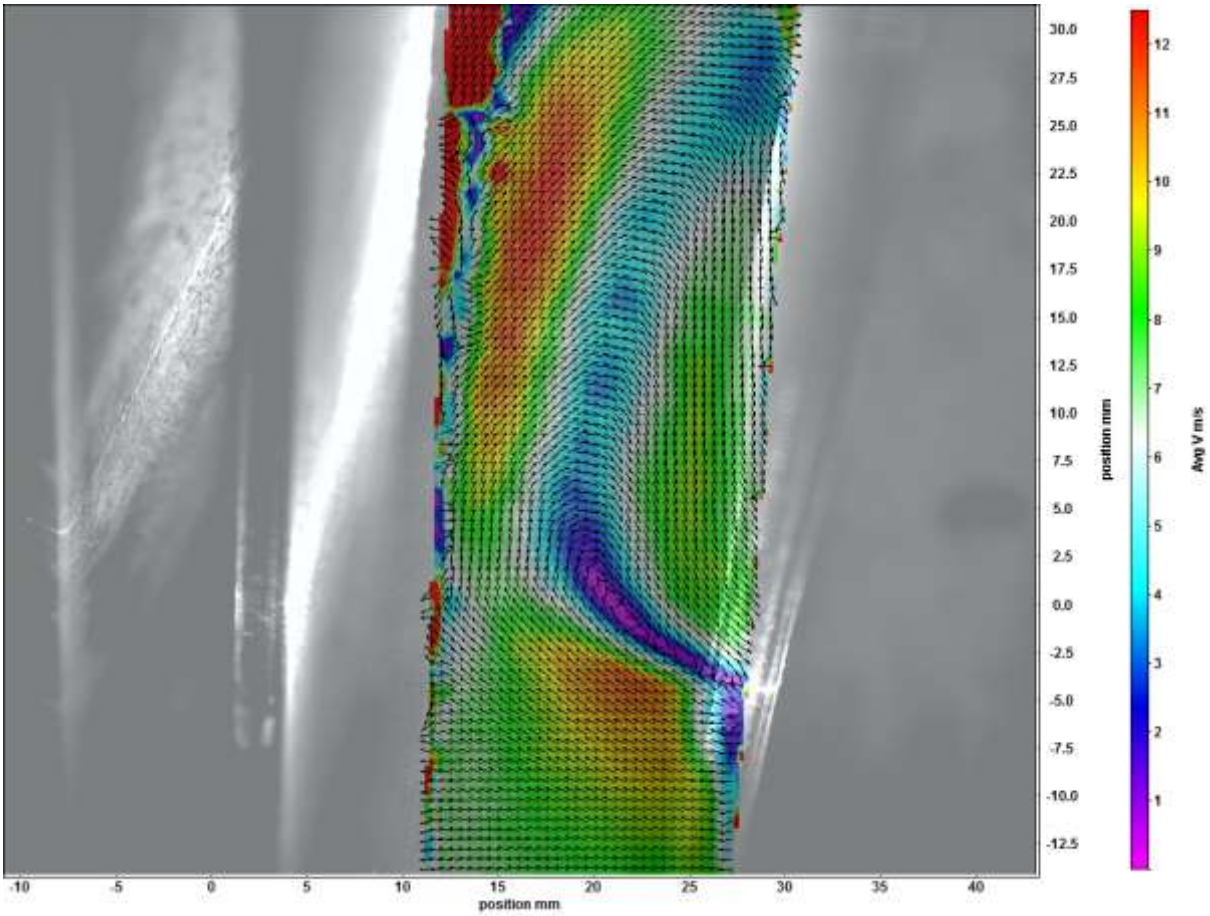

Figure 84 Vector field for 30-45 setting as computed by Davis software, overlaid over blades

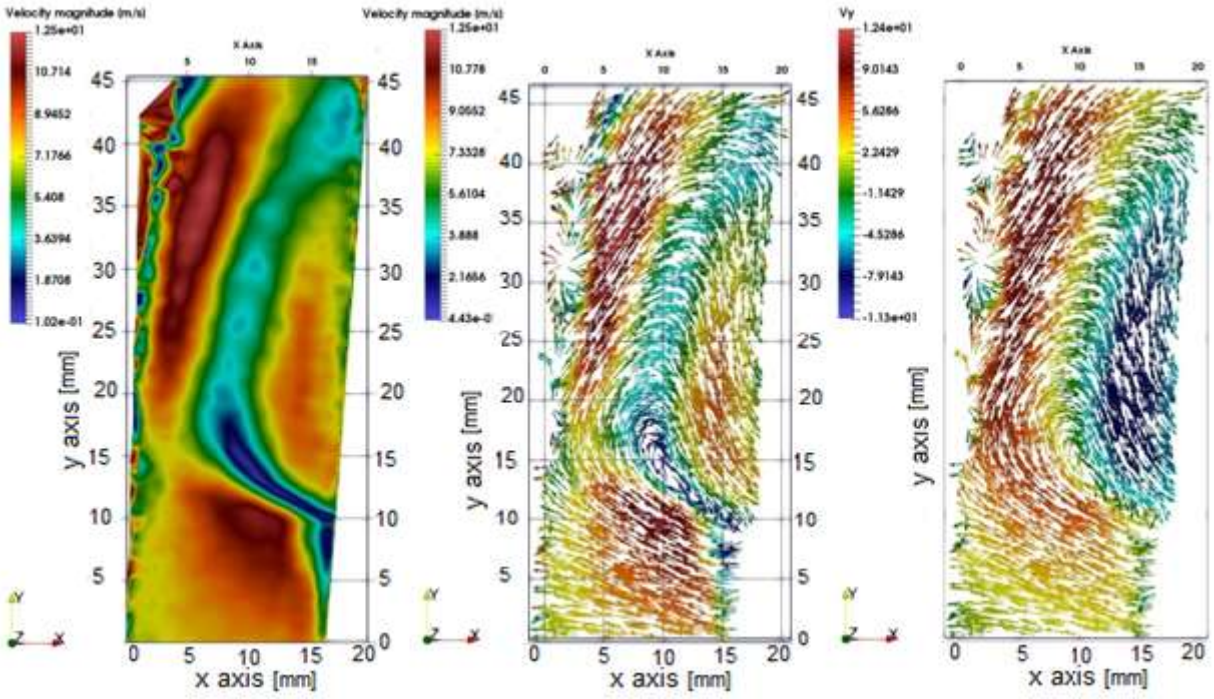

Figure 85Maximum velocity contour; vector field by max velocity; vector field by radial velocity for 30-45 setting

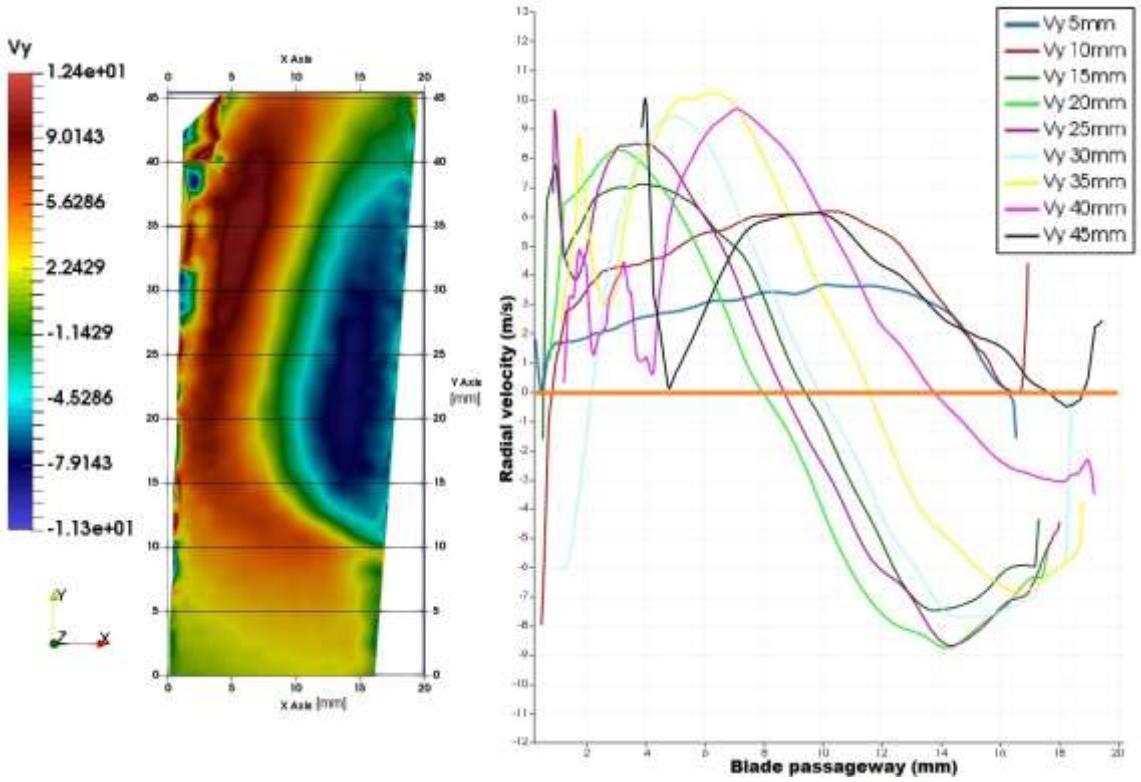

Figure 86 Radial velocity profiles with relation to position in the passageway for 30-45 setting

8.1.5 Trial TO5 - Fan motor 30Hz & Classifier motor 50Hz

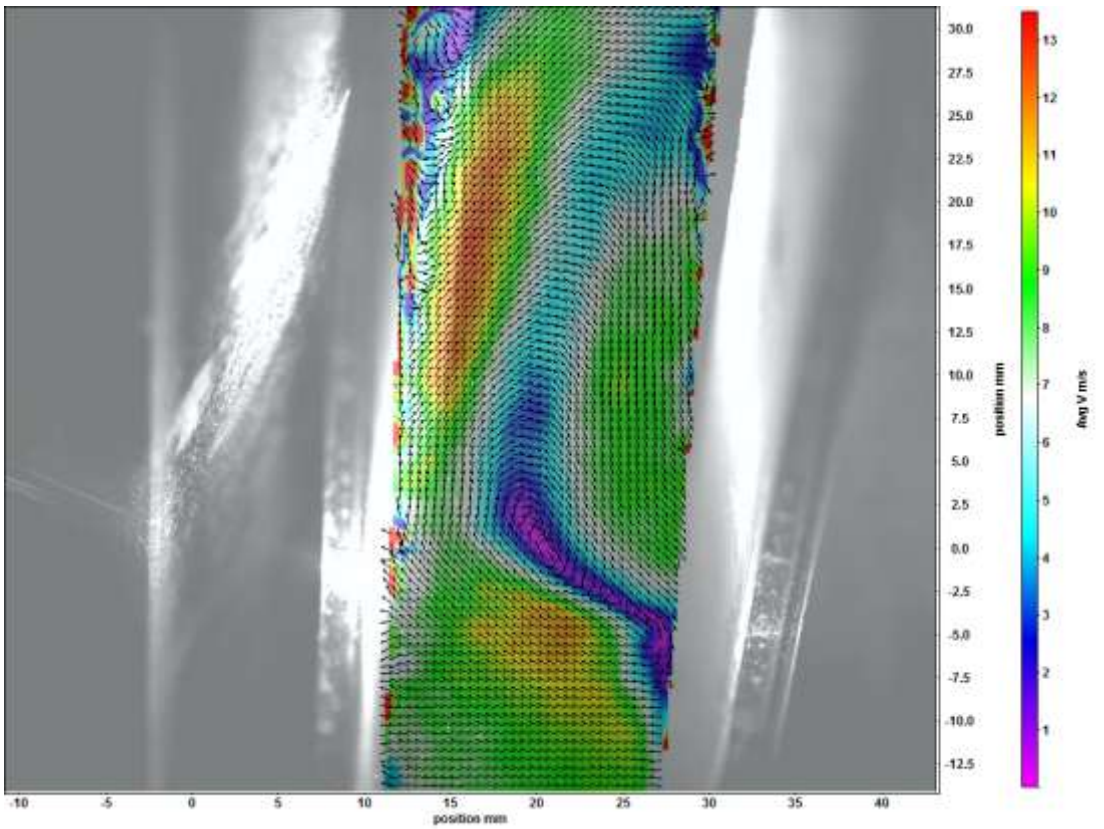

Figure 87Vector field for 30-50 setting as computed by Davis software, overlaid over blades

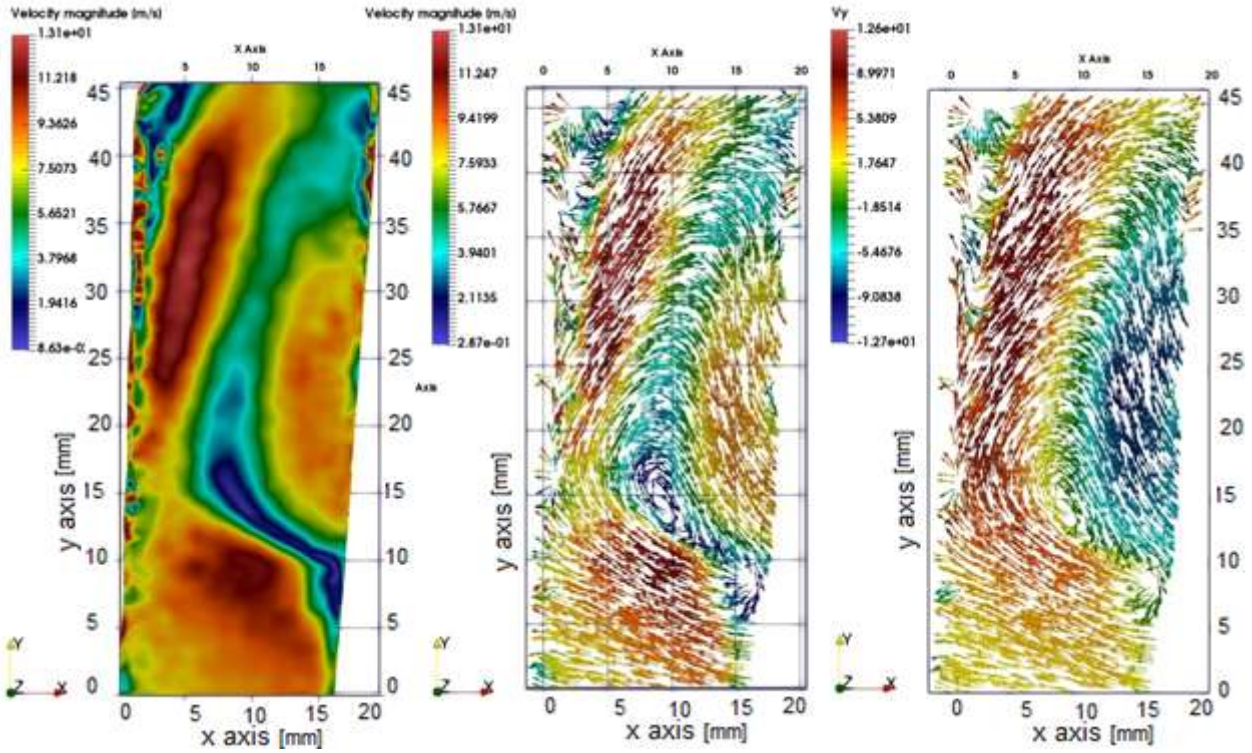

Figure 88 Maximum velocity contour; vector field by max velocity; vector field by radial velocity for 30-50 setting

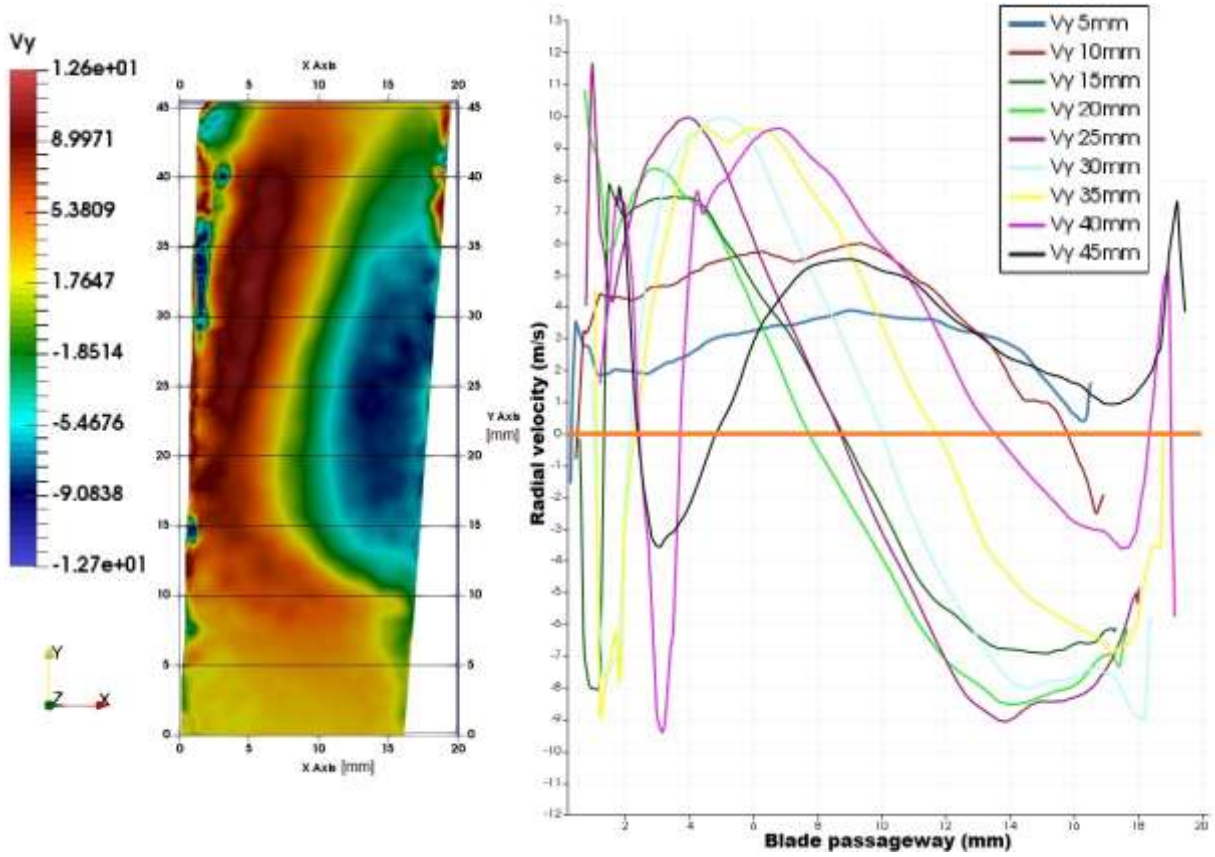

Figure 89 Radial velocity profiles with relation to position in the passageway for 30-50 setting

8.1.6 Trial TO6 - Fan motor 40Hz & Classifier motor 30Hz

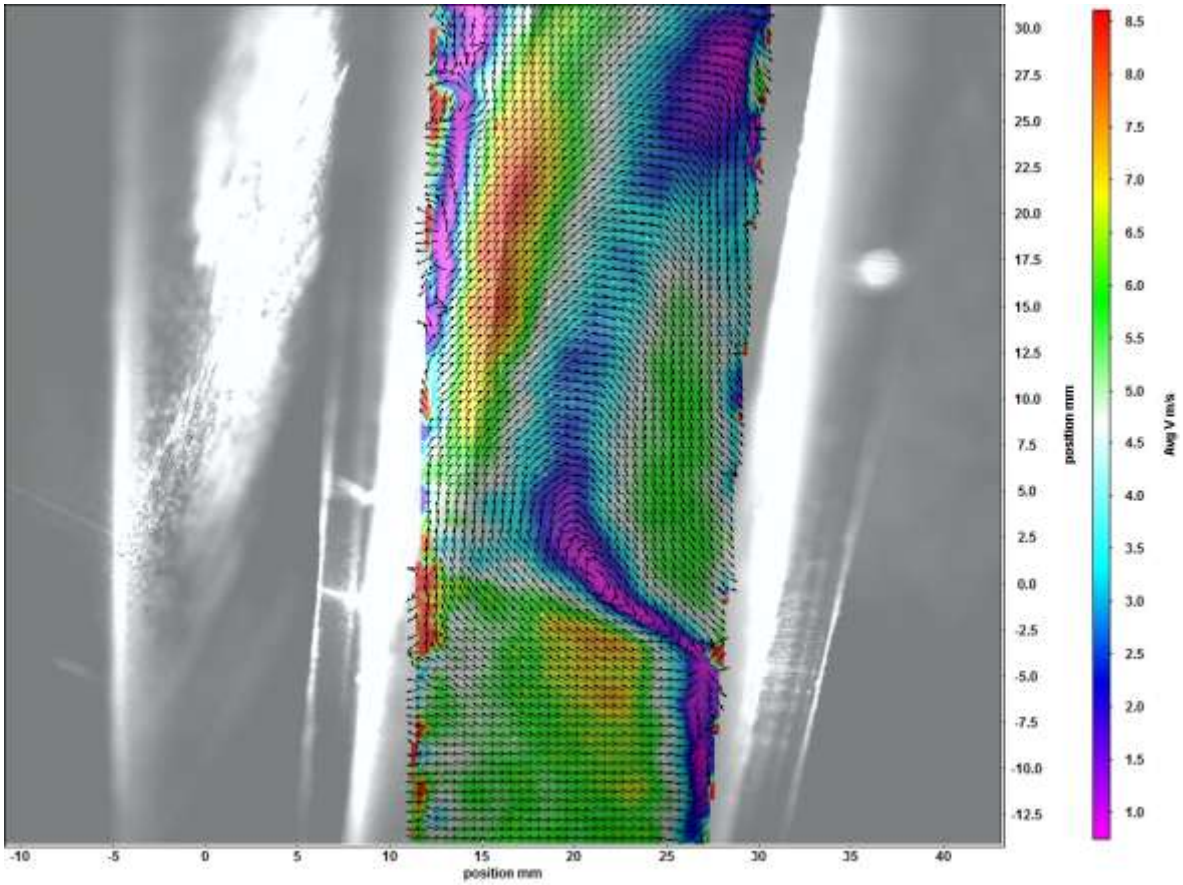

Figure 90 Vector field for 40-30 setting as computed by Davis software, overlaid over blades

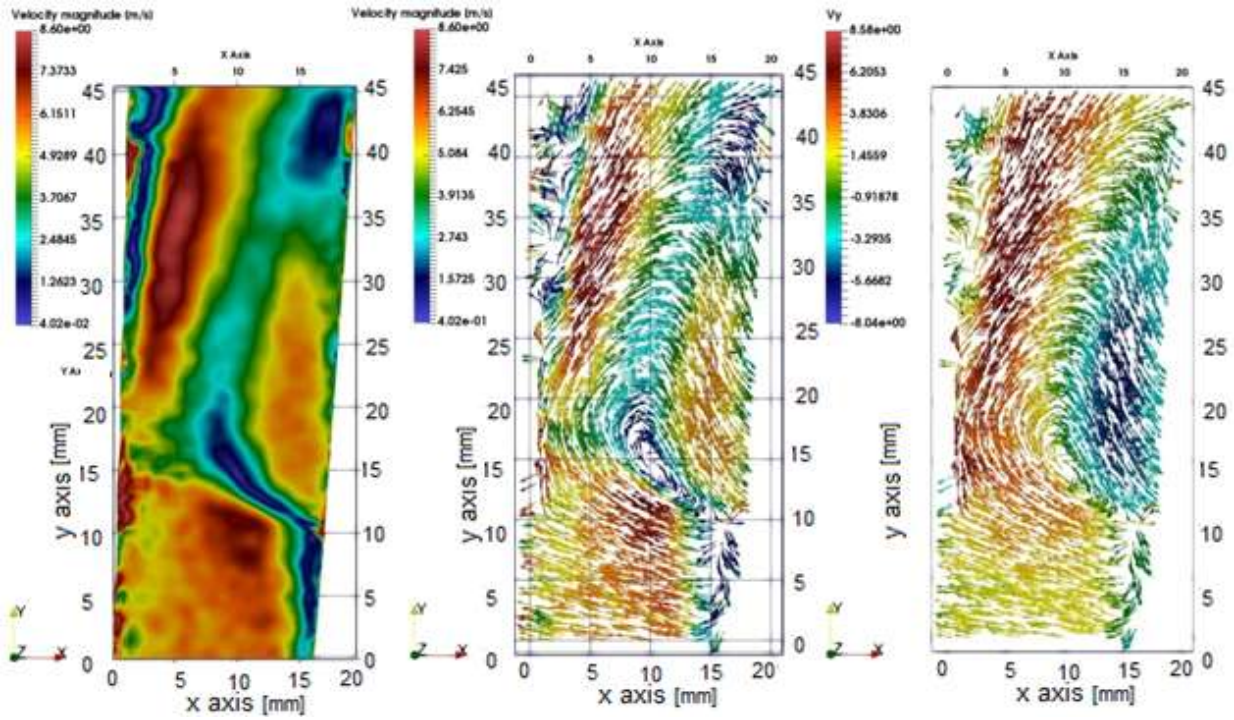

Figure 91Maximum velocity contour; vector field by max velocity; vector field by radial velocity for 40-30 setting

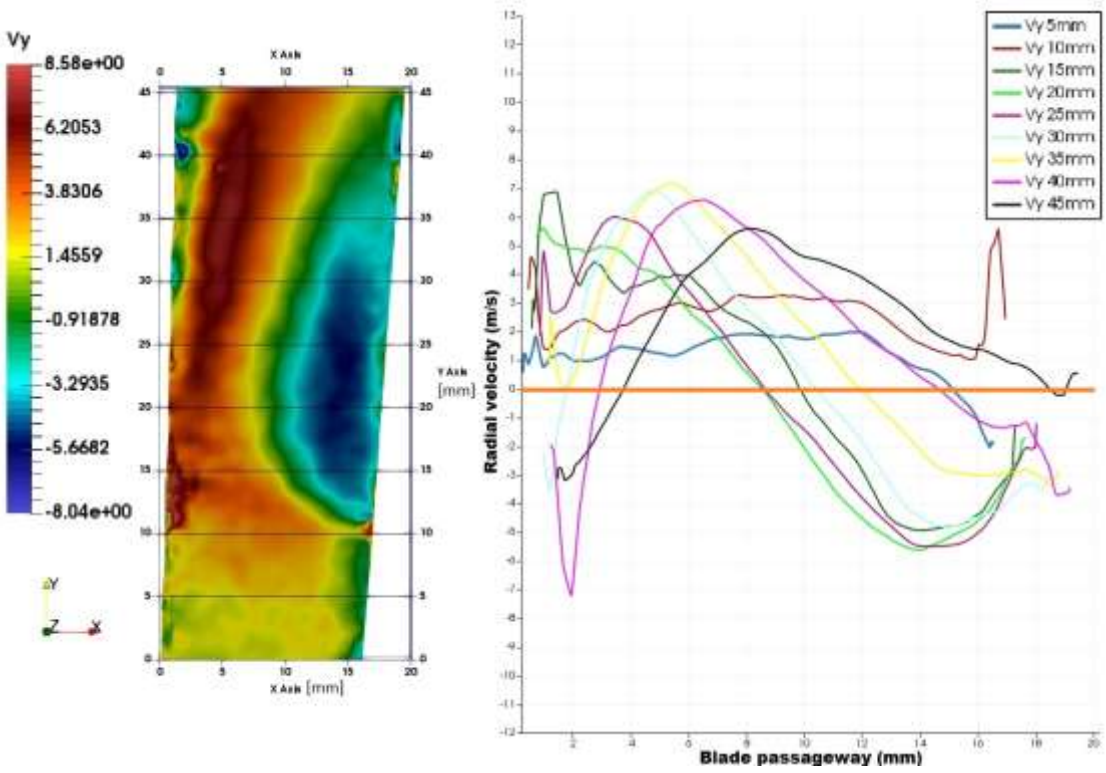

Figure 92 Radial velocity profiles with relation to position in the passageway for 40-30 setting

8.1.7 Trial TO7 - Fan motor 40Hz & Classifier motor 35Hz

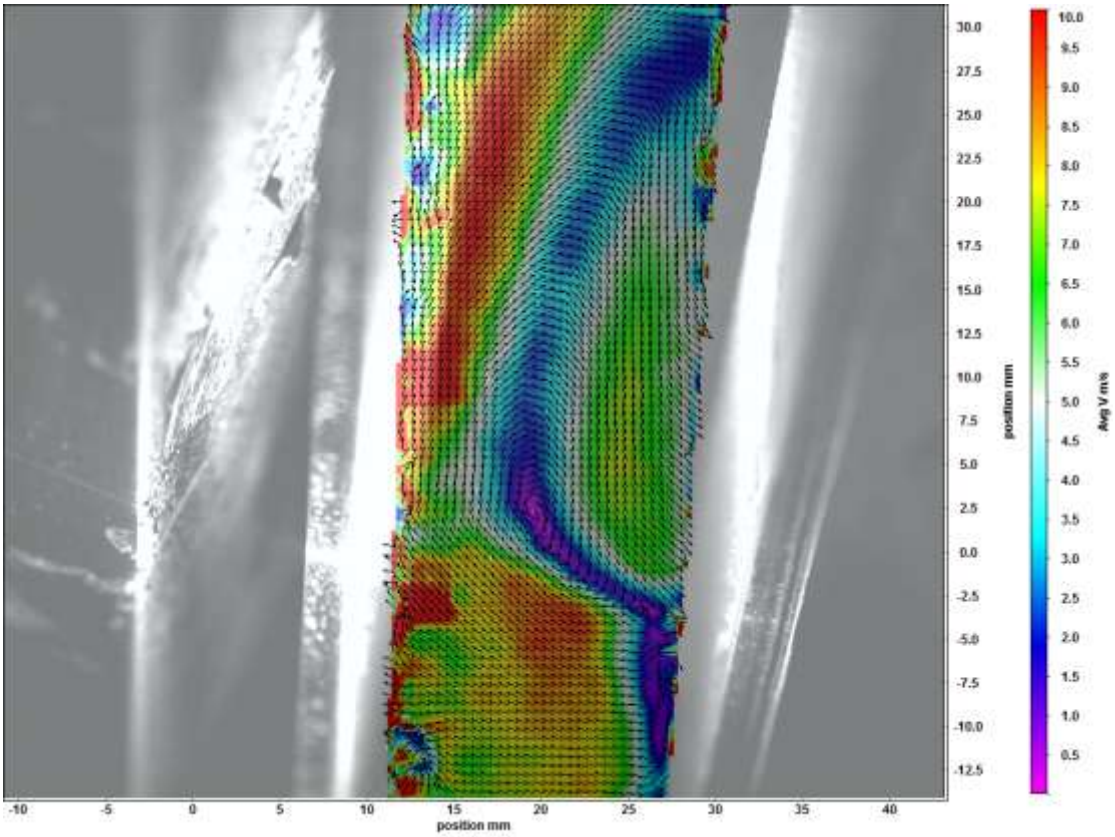

Figure 93 Vector field for 40-35 setting as computed by Davis software, overlaid over blades

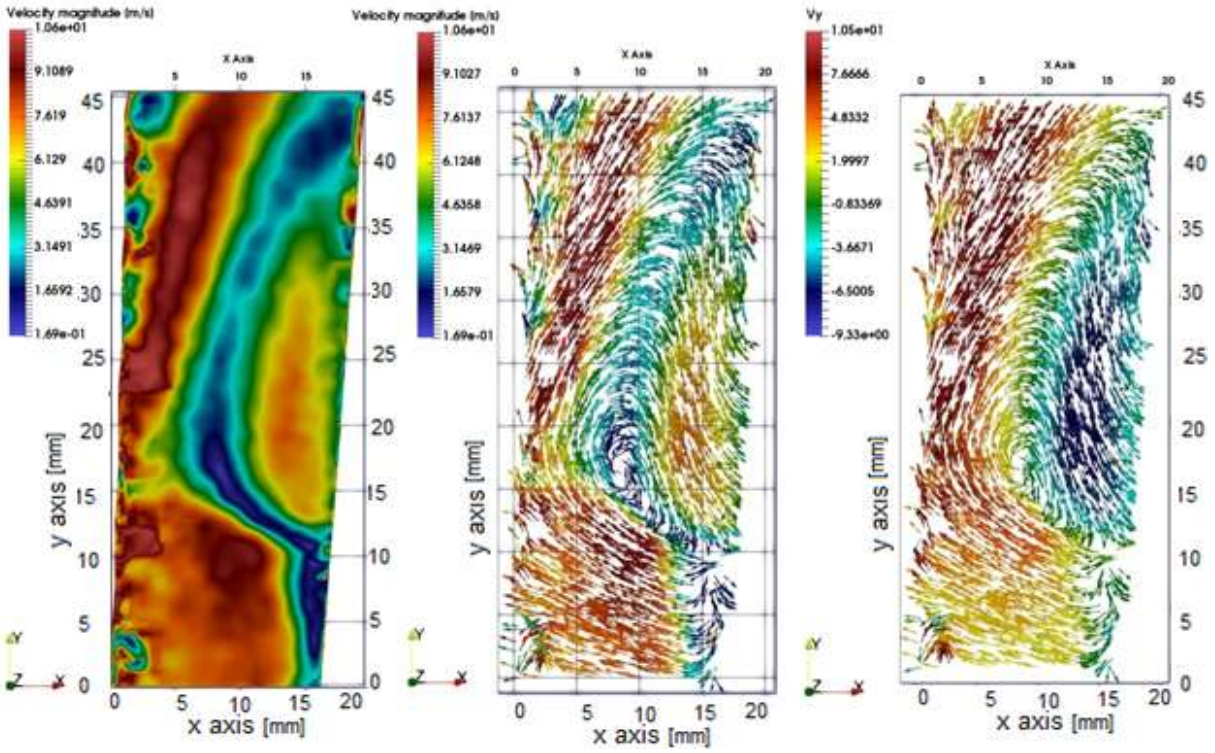

Figure 94 Maximum velocity contour; vector field by max velocity; vector field by radial velocity for 40-35 setting

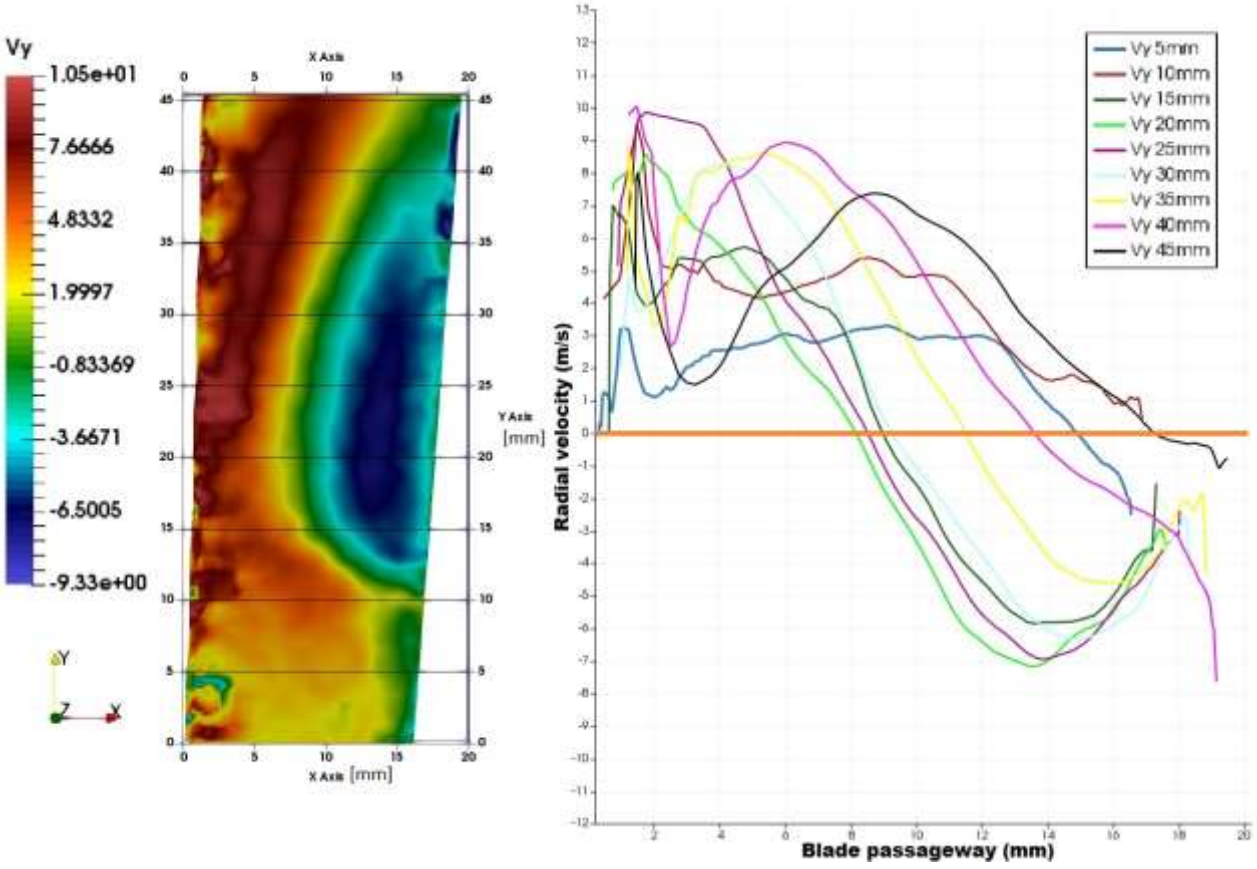

Figure 95 Radial velocity profiles with relation to position in the passageway for 40-35 setting

8.1.8 Trial TO8 - Fan motor 40Hz & Classifier motor 40Hz

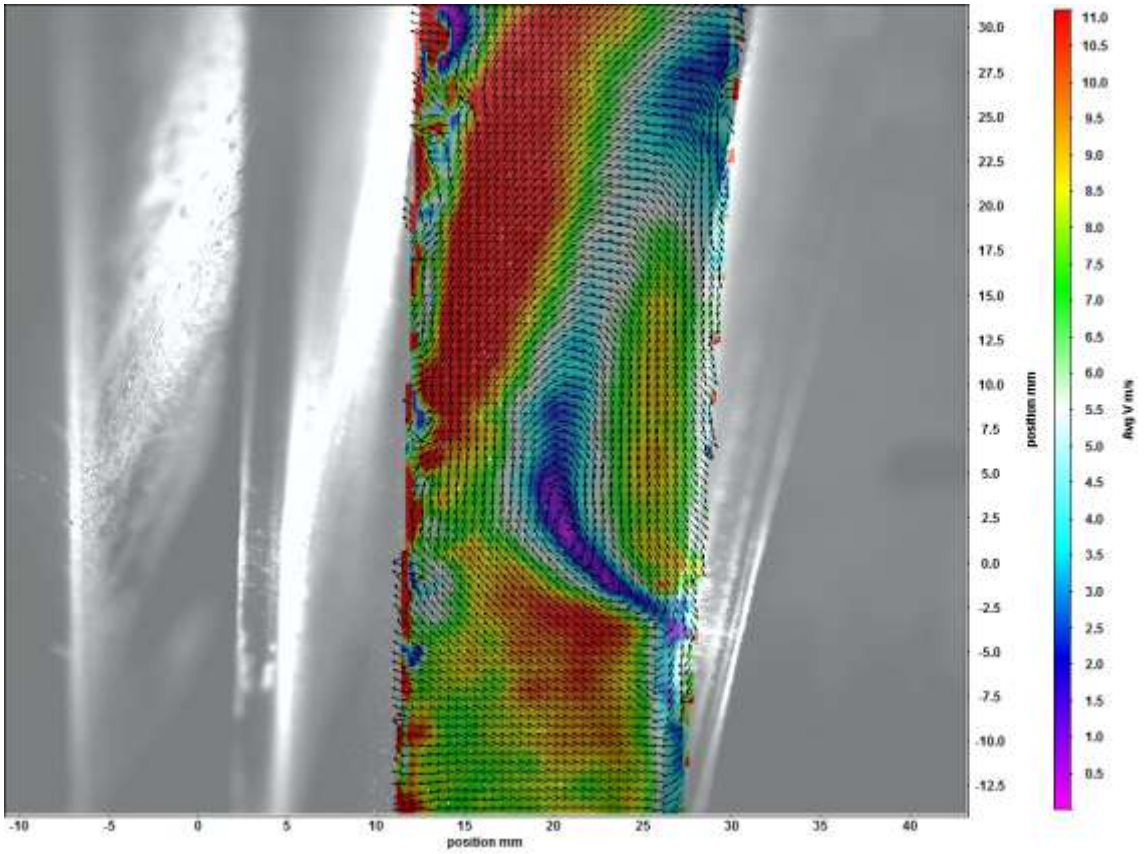

Figure 96 Vector field for 40-40 setting as computed by Davis software, overlaid over blades

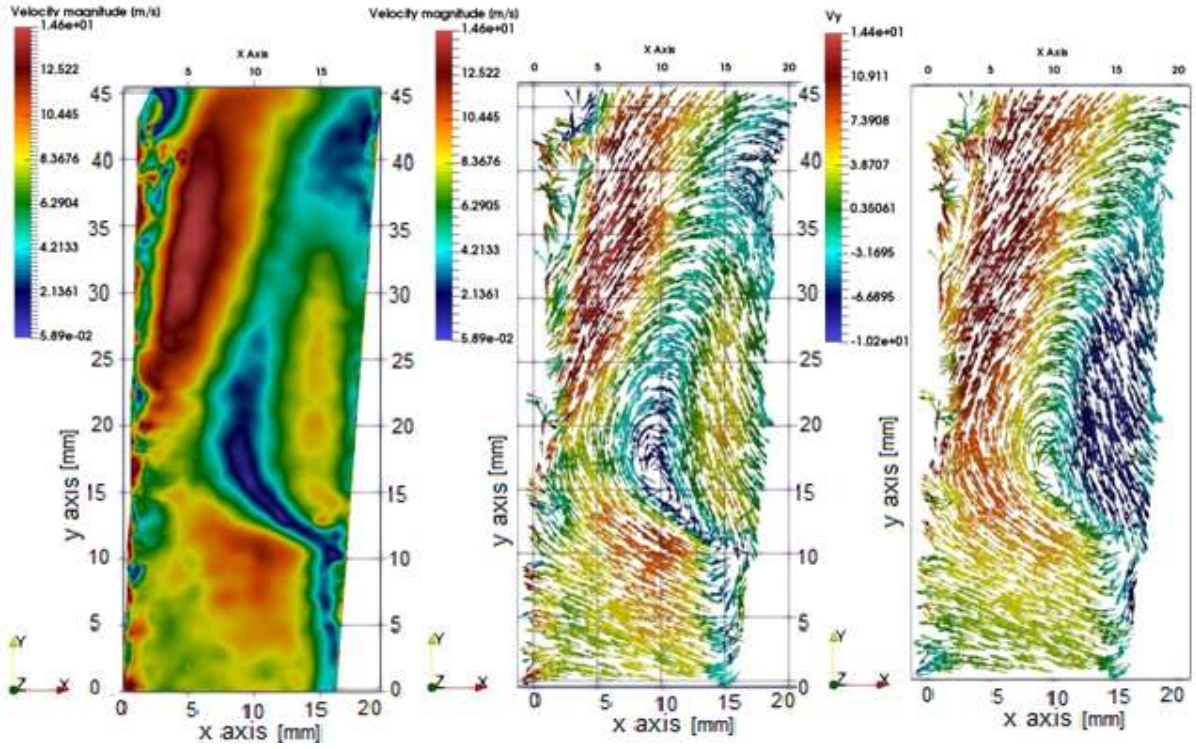

Figure 97Maximum velocity contour; vector field by max velocity; vector field by radial velocity for 40-40 setting

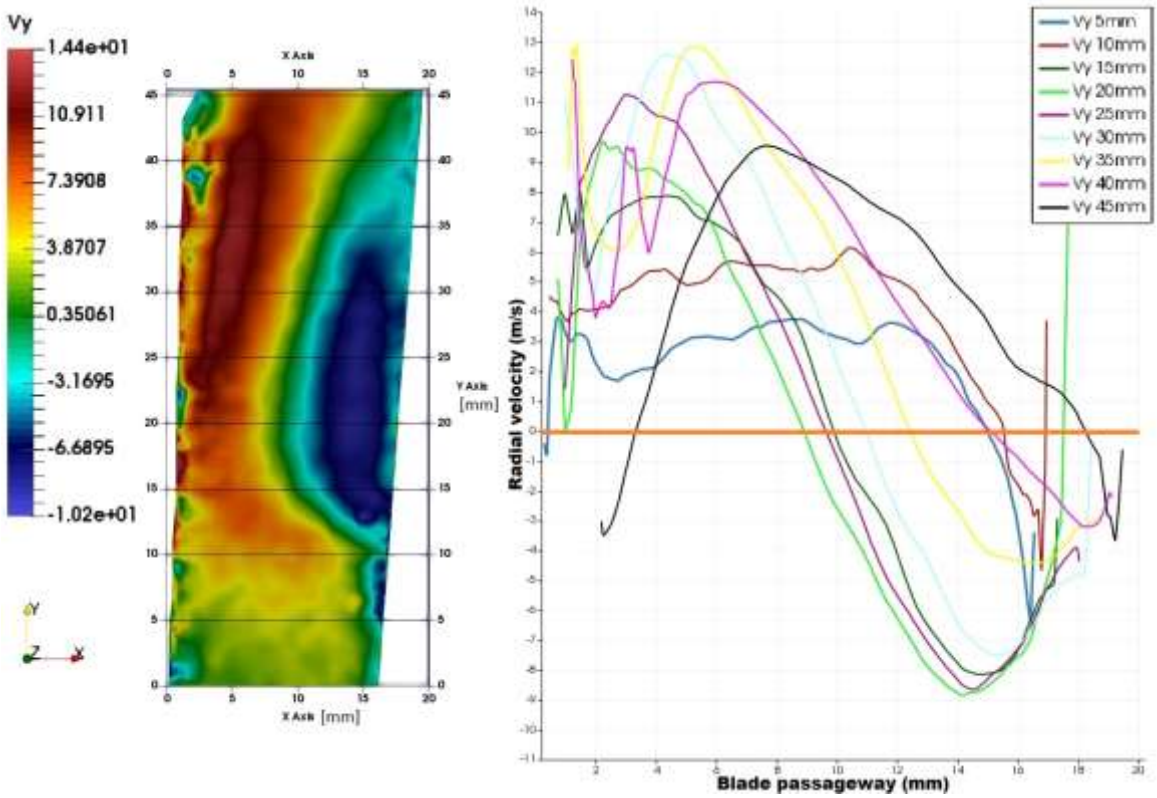

Figure 98 Radial velocity profiles with relation to position in the passageway for 40-40 setting

8.1.9 Trial TO9 - Fan motor 40Hz & Classifier motor 45Hz

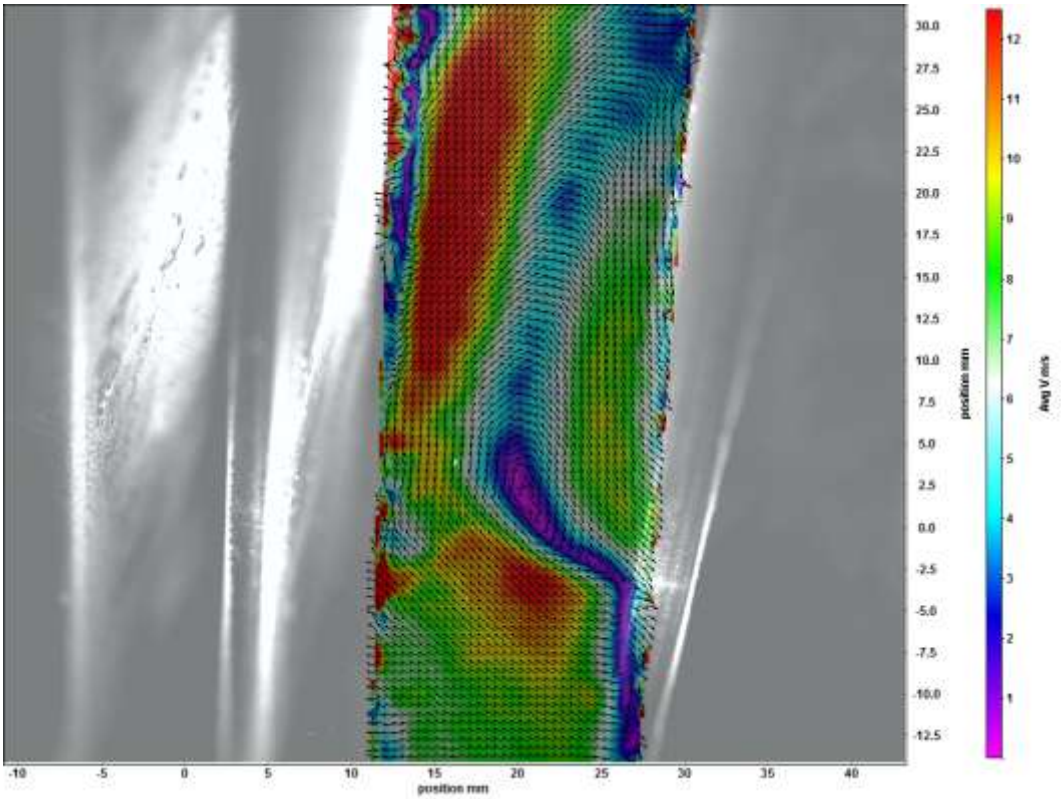

Figure 99 Vector field for 40-45 setting as computed by Davis software, overlaid over blades

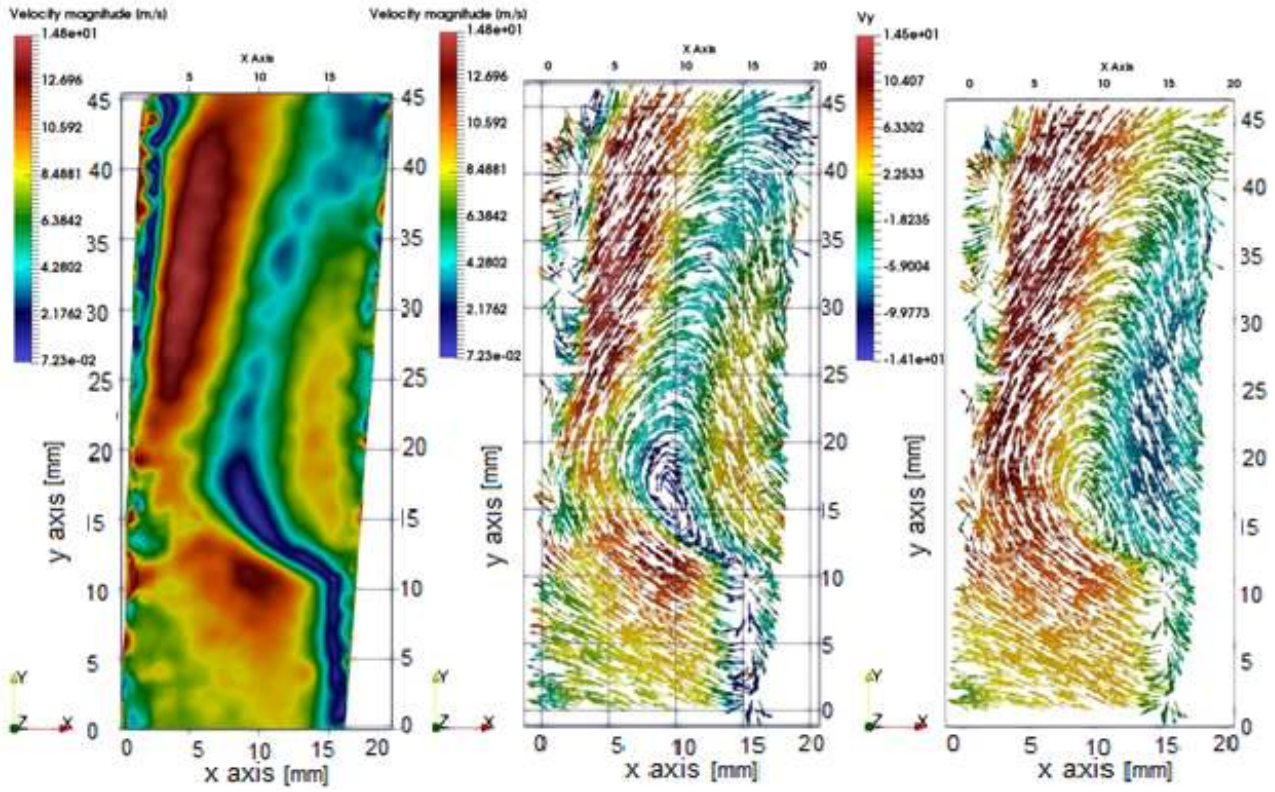

Figure 100Maximum velocity contour; vector field by max velocity; vector field by radial velocity for 40-45 setting

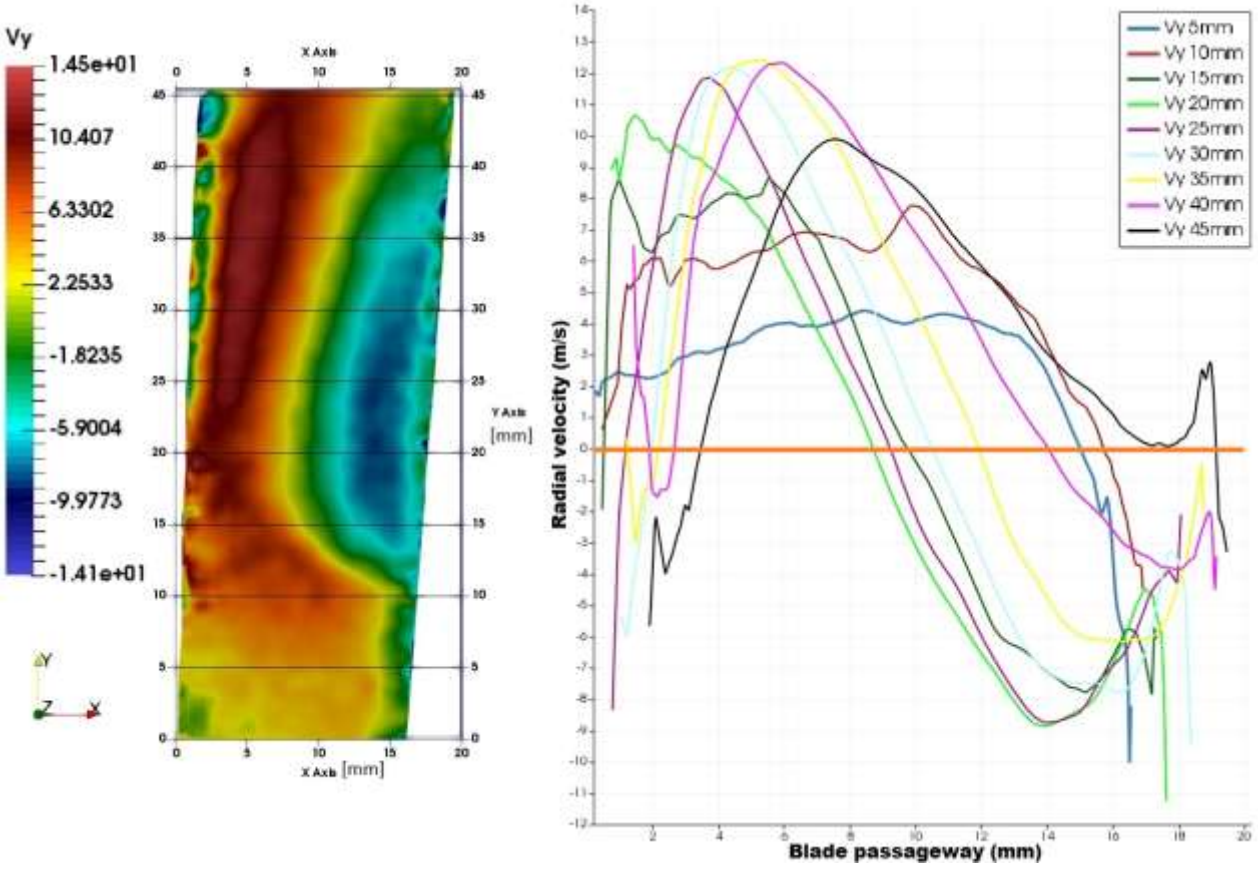

Figure 101Radial velocity profiles with relation to position in the passageway for 40-45 setting

8.1.10 Trial TO10 - Fan motor 40Hz & Classifier motor 50Hz

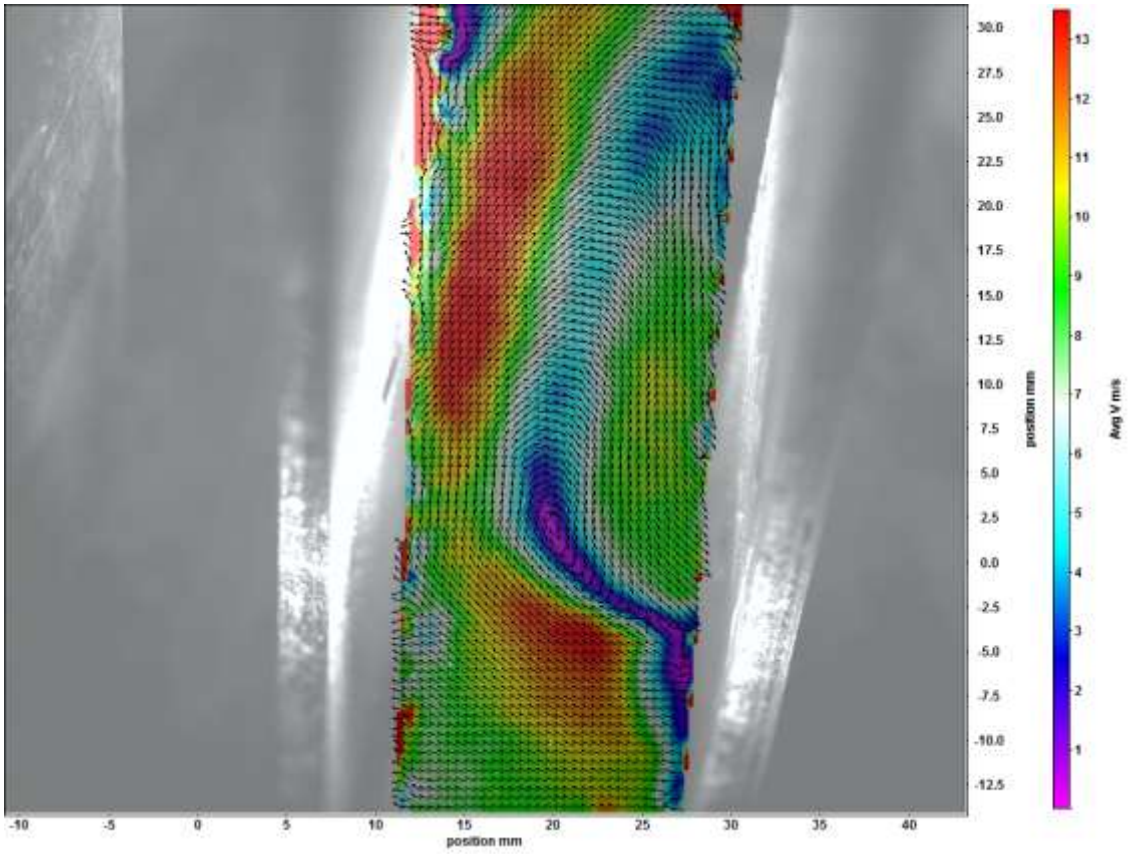

Figure 102 Vector field for 40-50 setting as computed by Davis software, overlaid over blades

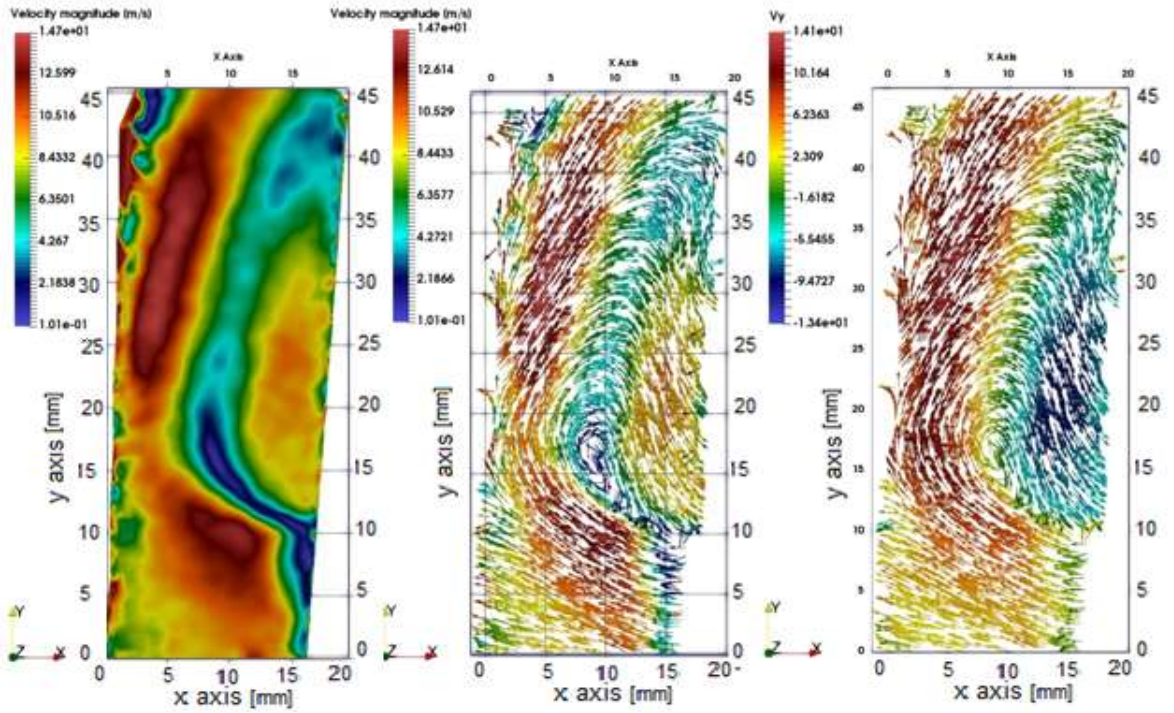

Figure 103Maximum velocity contour; vector field by max velocity; vector field by radial velocity for 40-50 setting

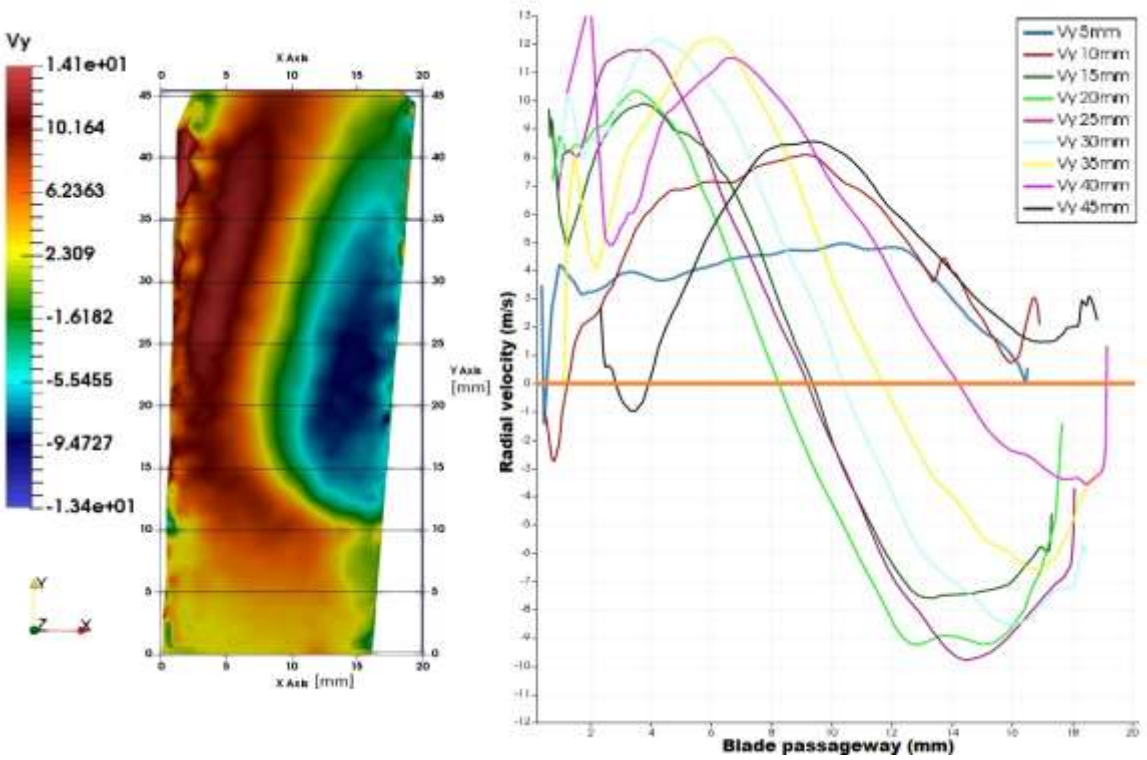

Figure 104 Radial velocity profiles with relation to position in the passageway for 40-50 setting

8.2 PIV RESULTS SUMMARY AT LIMITING OPERATING PARAMETERS OF CLASSIFIER

All ten measuring campaigns manifest similar flow behaviour with forced vortex forming in the area behind leading rotor blade. This phenomenon results into restricted blade passageway which consequently results into the increased radial velocity in the region before tailing rotor blade. The vortex occupies approximately one half of the passageway and becomes less significant as the air flow enters further in and it diminishes as it approaches exit from the passageway.

Table 21 Maximum observed radial velocities and maximum radial velocities on sampled lines

TRIAL	SETTINGS	MAGNITUDE		RADIAL VELOCITY CONTOUR		RADIAL VELOCITY LINE SOURCE	
		MIN	MAX	MIN	MAX	MIN	MAX
TO1	30F30R	0	8.15	-6.99	6.96	-5.3	6.8
TO2	30F35R	0	9.3	-8.99	8.41	-6.8	8
TO3	30F40R	0	10.4	-9.2	10.1	-8.2	8.6
TO4	30F45R	0	12.5	-11.3	12.4	-8.8	10.2
TO5	30F50R	0	13.1	-12.7	12.6	-9	10
TO6	40F30R	0	8.6	-8.4	8.58	-5.7	7.2
TO7	40F35R	0	10.6	-9.33	10.5	-7.1	9
TO8	40F40R	0	14.6	-10.2	14.4	-8.8	12.9
TO9	40F45R	0	14.8	-14.1	14.5	-8.9	12.5
TO10	40F50R	0	14.7	-13.4	14.1	-9.8	12.2

The maximum velocity is observed for all cases at the inlet to the passageway in the region after leading blade. Tangential component is dominant in this area and as the air proceeds, it becomes less significant and the radial component becomes major component. It has been observed that intensity of this vortex depends on both classifier and fan speed. Higher rotational speed of classifier cage translates into more air being accelerated radially out due to centrifugal force. For constant fan setting, maximum positive and negative radial velocity magnitude increases with increasing classifier speed as shown in Figure 105. Intensity of the vortex and maximum radial velocities also increase with increasing fan speed.

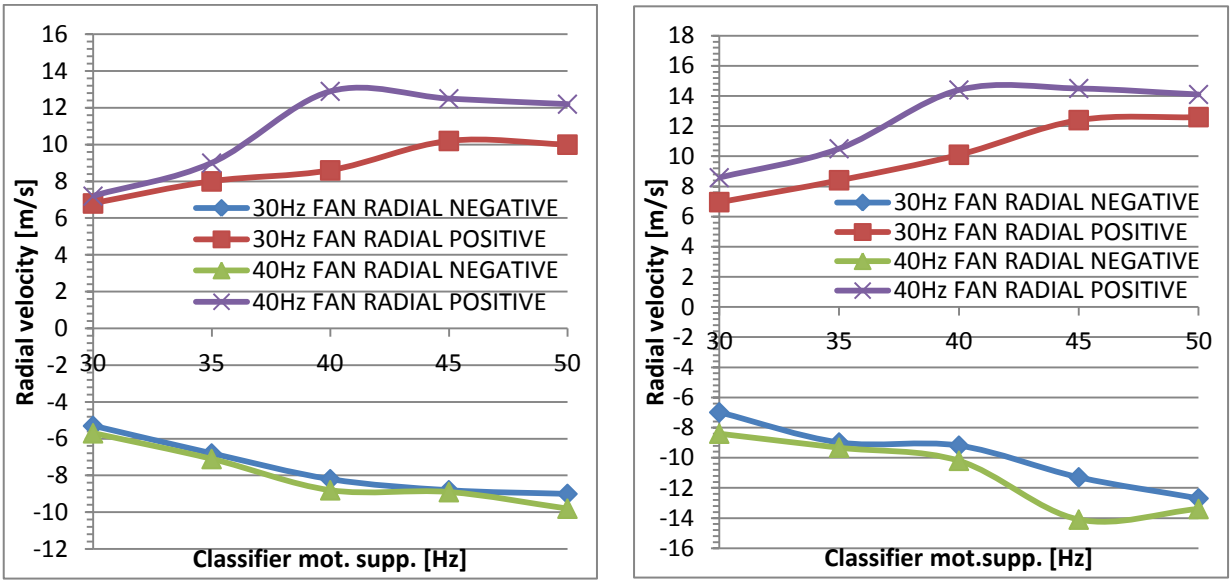

Figure 105Positive and negative radial velocities on sampled lines and pos. and neg. radial velocities observed

Table 22 Position of radial velocity inverse points

Y dist.[mm]	Min radial velocity at X distance [mm]				
	30F30R	**30F35R**	**30F40R**	**30F45R**	**30F50R**
10	14.32	14.6	14.85	15.41	15.45
15	7.48	8.96	9.05	9.36	8.76
20	6.12	7.36	7.84	7.92	7.72
25	7.08	7.92	8.52	8.64	8.68
30	8.8	9.28	9.6	9.84	10.04
35	10.84	10.96	11.32	11.56	11.72
40	13.8	13.16	13.4	13.72	13.76
	40F30R	**40F35R**	**40F40R**	**40F45R**	**40F50R**
10	16.1	16.28	16.42	16.37	16.26
15	9.84	8.96	9.88	9.72	9.36
20	8.52	8.12	8.88	8.68	8.24
25	8.6	8.48	9.6	9.2	9.16
30	10.4	9.24	10.92	10.48	10.36
35	11.92	11.48	12.4	11.88	11.68
40	14.6	13.56	15.08	14	14.2

Area of the negative radial velocity in the blade passageway is bordered by locations where it changes from positive to negative. These are identified by analysis and filtering of the system and their positions for various operating parameters are plotted with respect to passageway dimensions as shown in Figure 106. For the fan setting at 30 Hz it can be observed that the area of negative radial velocity (eddy recirculation area) decreases in size with increasing classifier rotor cage speed. The most significant size change occurs from 30 Hz to 35 Hz. This trend is less profound for fan setting at 40 Hz. This can be explained by the fact that the PIV camera was not synchronized with classifier rotor position and therefore the recorded data may not completely overlay. Position of the grid has been however adjusted for every investigated case to minimize overlay errors. It is assumed that the presence of this recirculation vortex has a negative impact on particle classification, energy consumption and wear rate. It is assumed that portion of the particles entering the blade passageway are drawn into the vortex instead of continuing on the trajectory into the internal area of rotor and out to fines outlet. This increases chances of particles within the cut size specification to be classified as coarse and therefore decreasing classification efficiency. Also, some of the oversize particles are classified as fine due to the vortex and therefore decreasing grade efficiency curve. Classifiers are very often installed on top of the mills to control particle size distribution. Wear rates of the grinding elements in the mill are increased by over grinding particles that are rejected by classifier that already meet size distribution criteria. This fact also decreases capacity of the grinding system and consequently increases energy consumption. Presence of the vortex in the blade passageway increases resistance of the system to air flow and therefore increasing pressure drop across the classifier. This directly translates into increased energy consumption of the main system fan.

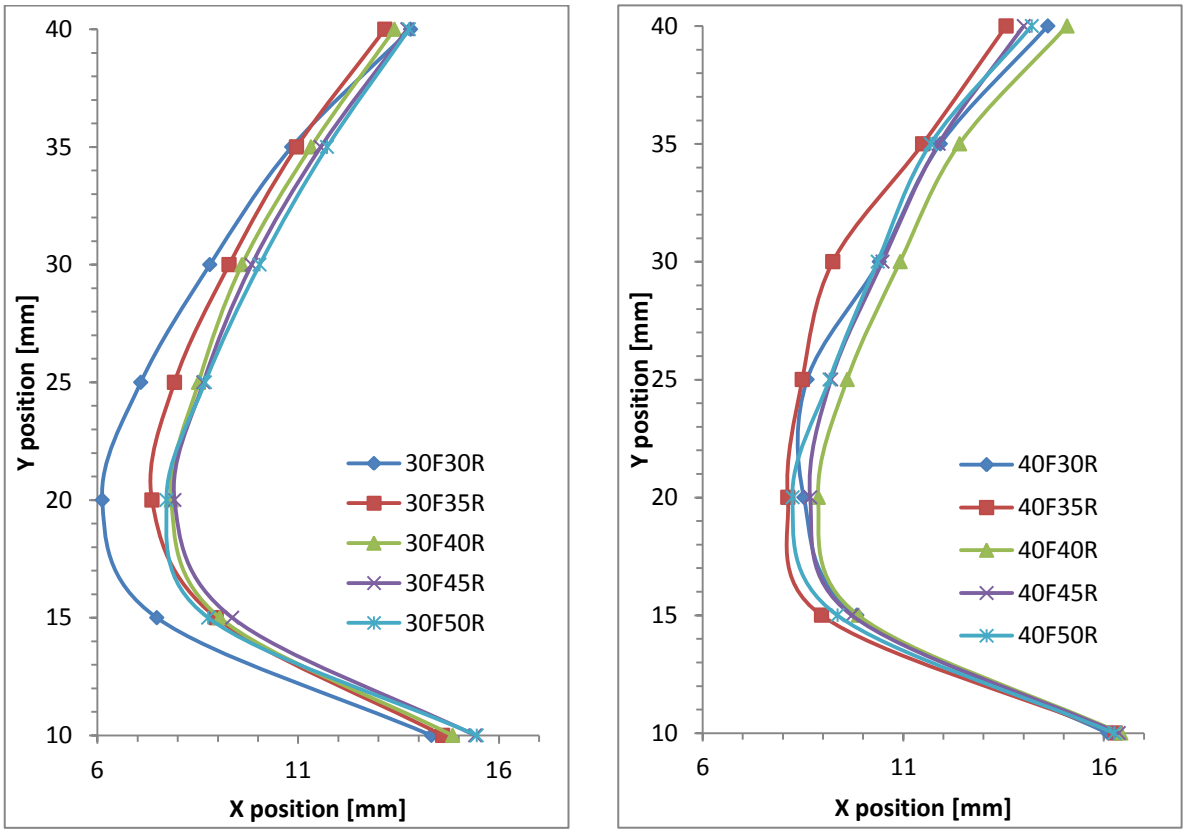

Figure 106 Position of inversion points for different operating parameters

8.3 CLASSIFICATION TRIALS WITH BARITE FEED MATERIAL

Eleven classification trials have been realized with barite feed material. For each group of three trials, two operating parameters are selected to be constant and third parameter is varying. Effects of the varying parameters on classification in sub 10-micron range are established. Results are presented in chapter 8.4

8.3.1 Trial TB1 & TB2 & TB3

In order to establish effect of feed rate on the amount of fines recovered and particle size distribution of fine particles a group of 3 trials (TB1, TB2, TB3) is carried out for varying feed rate and constant fan 50 Hz and classifier 50 Hz setting.

Table 23 Tabular particle size distribution for fine fractions

Size [µm]	TB1		TB2		TB3	
	% Chan	% Pass	% Chan	% Pass	% Chan	% Pass
37	0.38	100.00	0.45	100.00	0.00	100.00
31.11	0.61	99.62	0.82	99.55	0.17	100.00
26.16	0.93	99.01	1.29	98.73	0.27	99.83
22	1.22	98.08	1.63	97.44	0.31	99.56
18.5	1.45	96.86	1.74	95.81	0.41	99.25
15.56	1.83	95.41	1.88	94.07	0.38	98.84
13.08	2.65	93.58	2.31	92.19	0.39	98.46
11	4.17	90.93	3.21	89.88	0.66	98.07
9.25	6.14	86.76	4.52	86.67	1.18	97.41
7.78	7.33	80.62	5.66	82.15	2.05	96.23
6.54	7.36	73.29	5.91	76.49	2.96	94.18
5.5	6.27	65.93	5.25	70.58	3.57	91.22
4.62	5.18	59.66	4.41	65.33	3.92	87.65
3.89	4.62	54.48	4.05	60.92	4.43	83.73
3.27	4.72	49.86	4.43	56.87	5.46	79.30
2.75	5.39	45.14	5.55	52.44	7.08	73.84
2.312	6.28	39.75	6.93	46.89	8.69	66.76
1.945	6.73	33.47	7.50	39.96	9.29	58.07
1.635	6.31	26.74	7.10	32.46	8.75	48.78
1.375	5.35	20.43	6.04	25.36	7.90	40.03
1.156	4.54	15.08	5.34	19.32	7.67	32.13
0.972	4.10	10.54	5.20	13.98	8.46	24.46
0.818	3.57	6.44	4.87	8.78	8.82	16.00
0.688	2.20	2.87	3.05	3.91	5.71	7.18
0.578	0.67	0.67	0.86	0.86	1.47	1.47
0.486	0.00	0.00	0.00	0.00	0.00	0.00

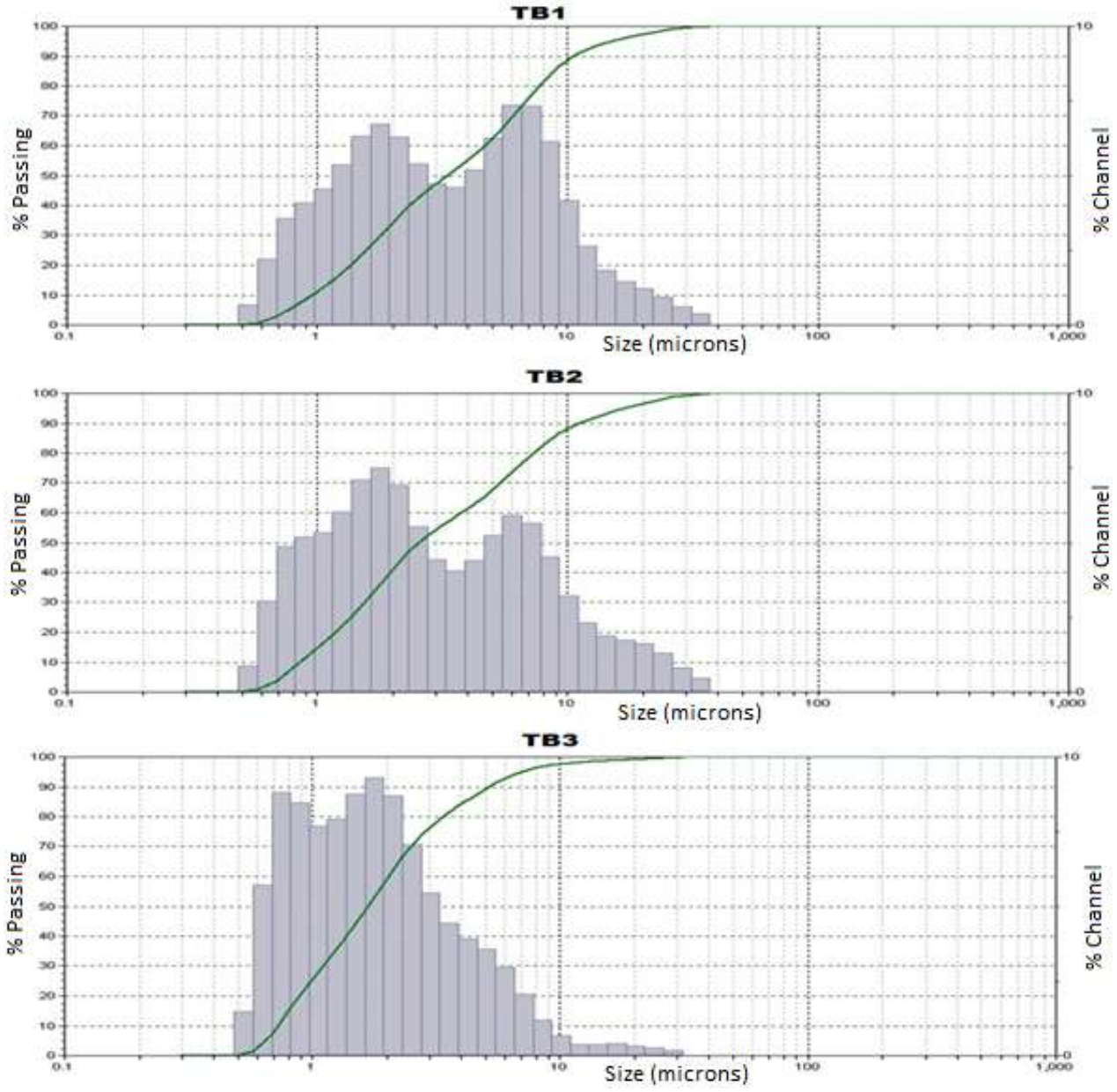

Figure 107 Graphical representation of distribution curves for TB1, TB2 and TB3

In order to create Tromp curves, particle size analysis of coarse fractions are carried out and can be found in the attachments. Tromp curves or grade efficiency curves as described in theoretical part are plotted for all three trials. In order to establish sharpness of classification the 25% and 75% passing values are required. The cut size is represented by 50% passing value and in order to establish these, Tromp curves are reduced. Results are discussed at the end of the chapter.

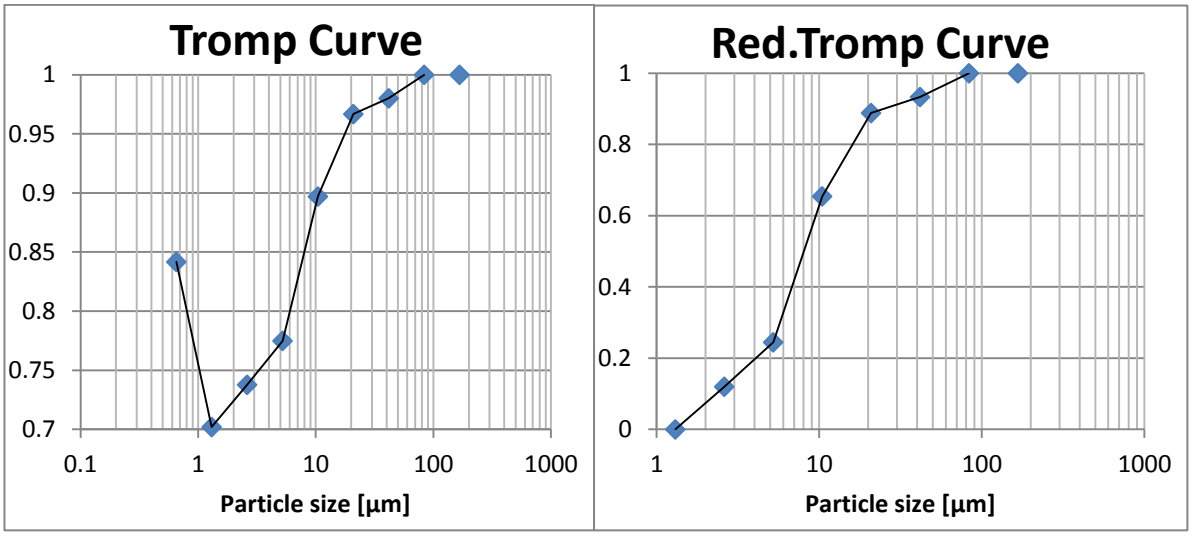

Figure 108 Tromp curve and reduced Tromp curve for TB1

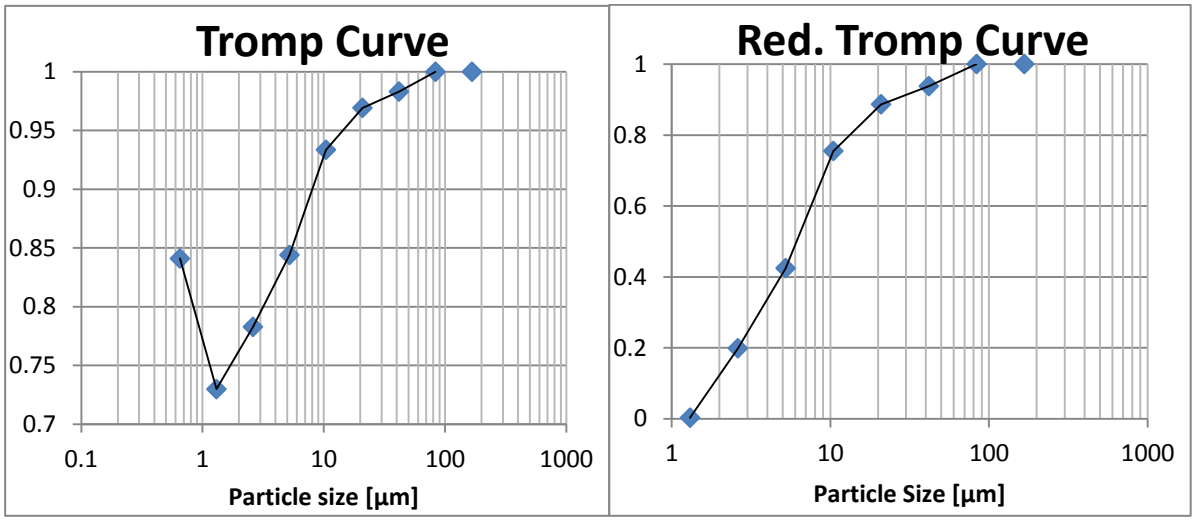

Figure 109Tromp curve and reduced Tromp curve for TB2

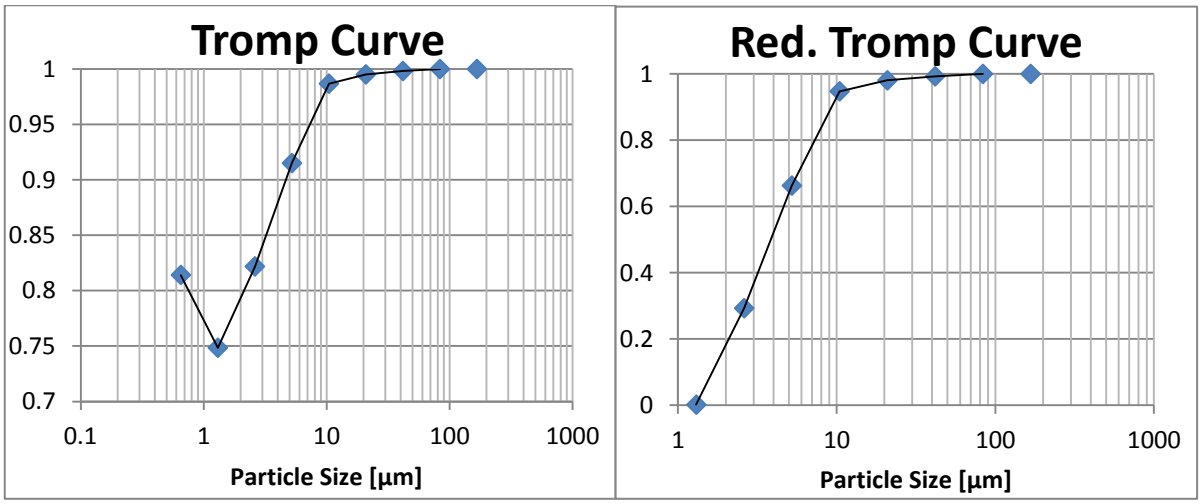

Figure 110Tromp curve and reduced Tromp curve for TB3

8.3.2 Trial TB4 & TB5 & TB2

For the following classification trials, feed rate is set to a constant value of 20 Hz. Fan setting for the presented trials TB4, TB5 and TB2 is also set to a constant value of 50 Hz. Effects of varying classifier rotor cage speed on fine and coarse fraction size characterization are measured and presented.

Table 24Tabular particle size distribution for fine fractions

Size [µm]	TB4		TB5		TB2	
	% Chan	% Pass	% Chan	% Pass	% Chan	% Pass
37	0.00	100.00	0.00	100.00	0.45	100.00
31.11	0.00	100.00	0.33	100.00	0.82	99.55
26.16	0.00	100.00	0.47	99.67	1.29	98.73
22	0.42	100.00	0.64	99.20	1.63	97.44
18.5	0.83	99.58	0.88	98.56	1.74	95.81
15.56	1.54	98.75	1.28	97.68	1.88	94.07
13.08	2.79	97.21	2.01	96.40	2.31	92.19
11	4.83	94.42	3.27	94.39	3.21	89.88
9.25	7.42	89.59	5.01	91.12	4.52	86.67
7.78	9.18	82.17	6.67	86.11	5.66	82.15
6.54	9.04	72.99	7.32	79.44	5.91	76.49
5.5	7.39	63.95	7.20	72.12	5.25	70.58
4.62	5.70	56.56	6.52	64.92	4.41	65.33
3.89	4.80	50.86	6.08	58.40	4.05	60.92
3.27	4.74	46.06	6.16	52.32	4.43	56.87
2.75	5.30	41.32	6.63	46.16	5.55	52.44
2.312	6.07	36.02	7.01	39.53	6.93	46.89
1.945	6.42	29.95	6.82	32.52	7.50	39.96
1.635	5.97	23.53	6.01	25.70	7.10	32.46
1.375	4.99	17.56	5.01	19.69	6.04	25.36
1.156	4.06	12.57	4.29	14.68	5.34	19.32
0.972	3.46	8.51	3.95	10.39	5.20	13.98
0.818	2.85	5.05	3.52	6.44	4.87	8.78
0.688	1.69	2.20	2.22	2.92	3.05	3.91
0.578	0.51	0.51	0.70	0.70	0.86	0.86
0.486	0.00	0.00	0.00	0.00	0.00	0.00

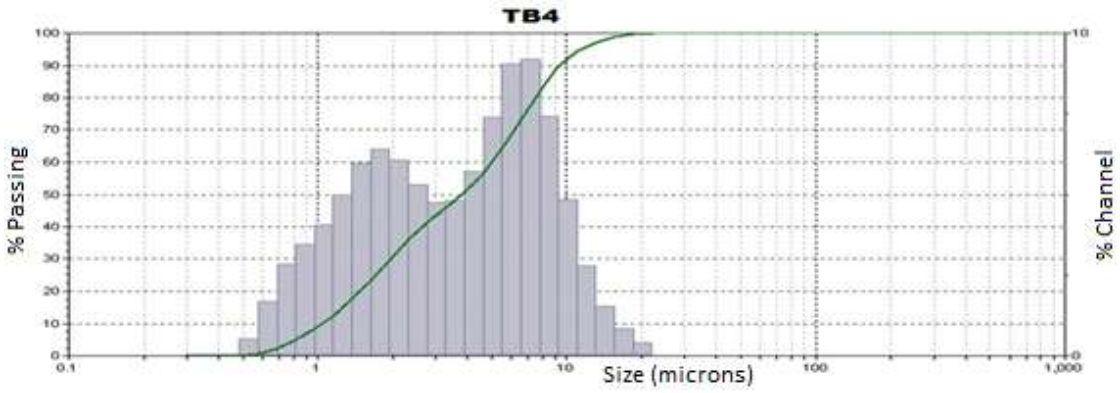

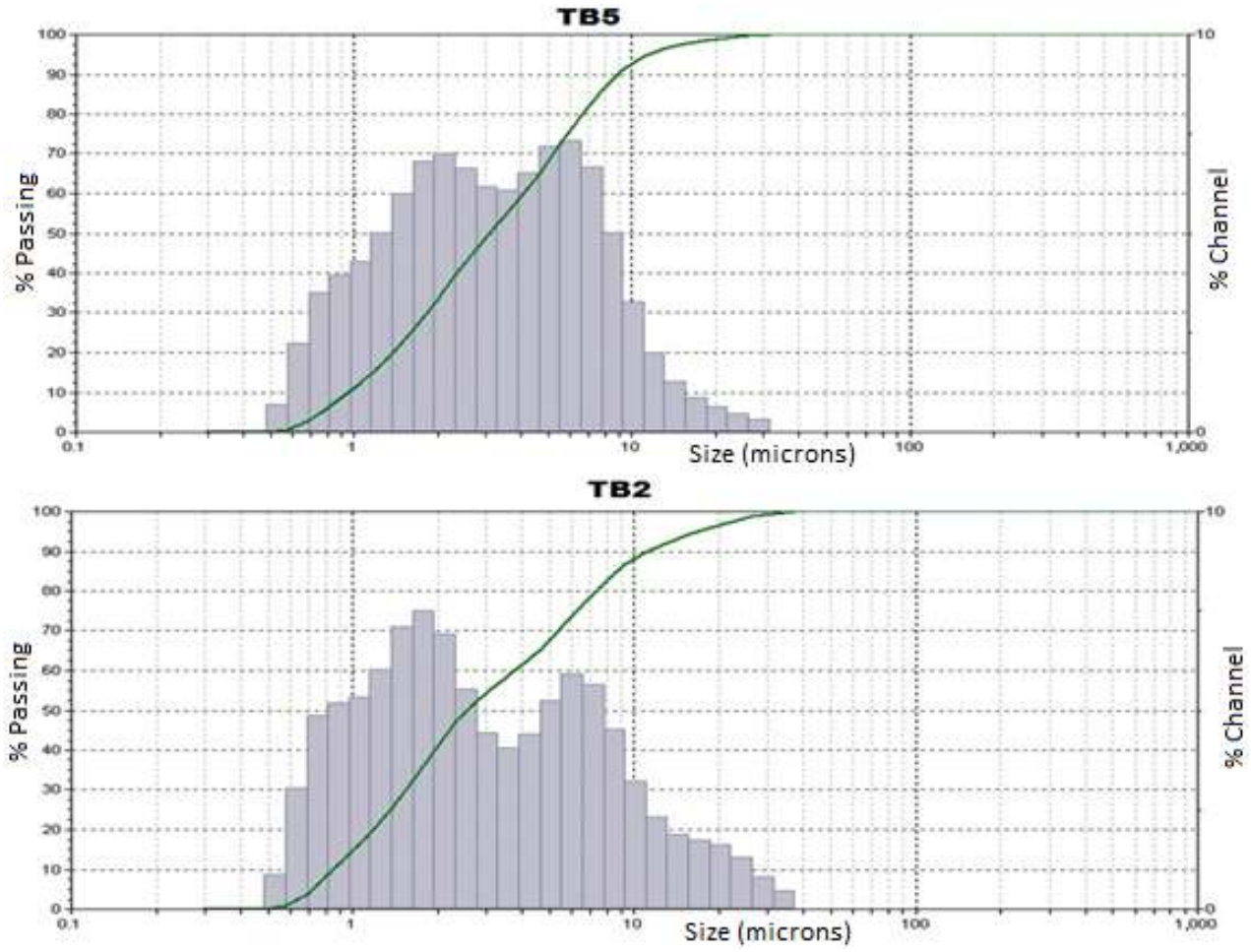

Figure 111Graphical representation of distribution curves for TB4, TB5 and TB2

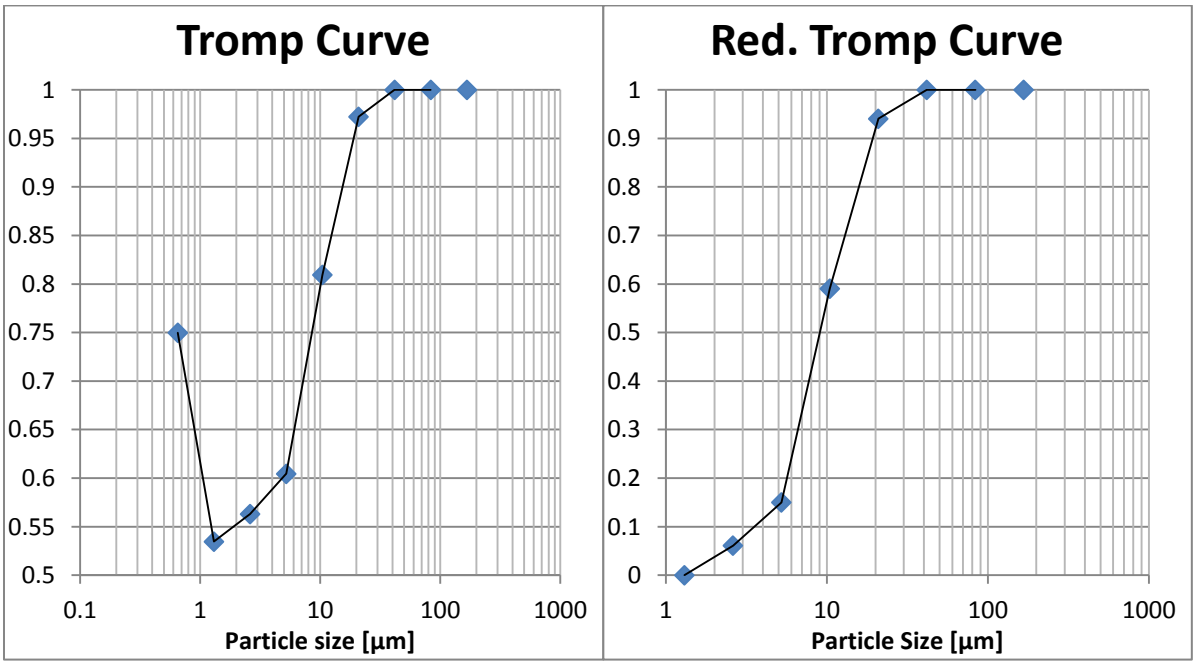

Figure 112Tromp curve and reduced Tromp curve for TB4

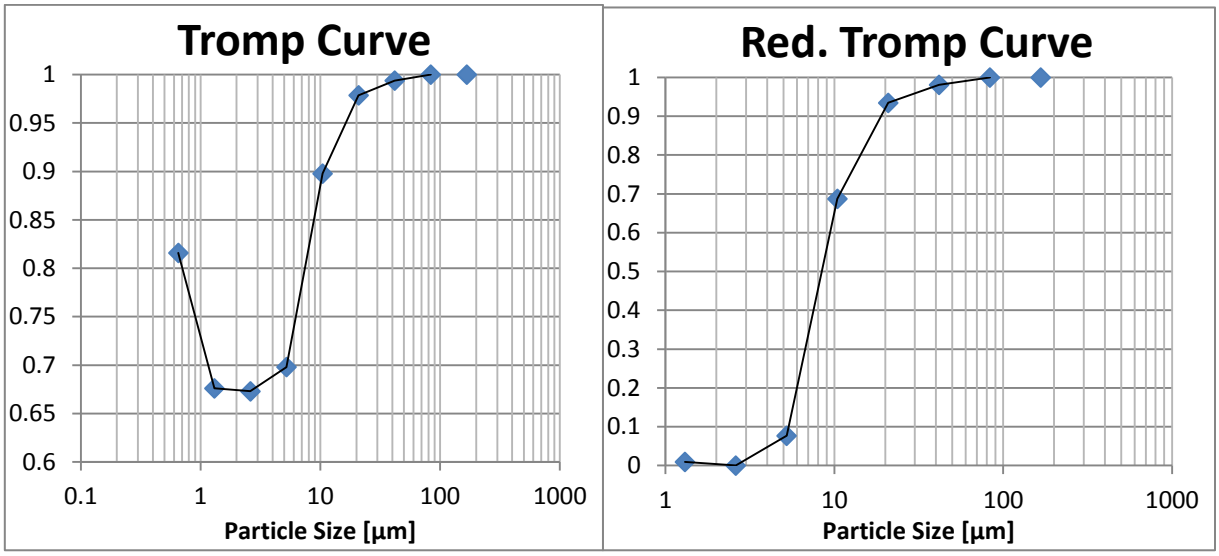

Figure 113 Tromp curve and reduced Tromp curve for TB5

Tromp curves for trial TB2 can be found in the first group of trials with constant classifier and fan settings. Particle size analysis of coarse fractions and tabular data for Tromp curve calculations are presented in the attachments. Results are compared and discussed at the end of the chapter.

8.3.3 Trial TB6 & TB7 & TB8

For the following classification trials, feed rate is again set to a constant value of 20 Hz. Fan setting for the presented trials TB6, TB7 and TB8 is set to a constant value of 40 Hz. Effects of varying classifier rotor cage speed on fine and coarse fraction size characterization are measured and presented.

Table 25 Tabular particle size distribution for fine fractions

Size [µm]	TB6		TB7		TB8	
	% Chan	% Pass	% Chan	% Pass	% Chan	% Pass
37	0.00	100.00	0.00	100.00	0.00	100.00
31.11	0.00	100.00	0.00	100.00	0.00	100.00
26.16	0.00	100.00	0.00	100.00	0.16	100.00
22	0.40	100.00	0.39	100.00	0.24	99.84
18.5	0.68	99.60	0.58	99.61	0.32	99.60
15.56	1.20	98.92	0.88	99.03	0.42	99.28
13.08	2.19	97.72	1.53	98.15	0.68	98.86
11	3.90	95.53	2.90	96.62	1.49	98.18
9.25	6.22	91.63	5.22	93.72	3.12	96.69
7.78	8.16	85.41	7.60	88.50	5.49	93.57
6.54	8.43	77.25	8.40	80.90	7.24	88.08
5.5	7.47	68.82	7.69	72.50	7.39	80.84
4.62	6.07	61.35	6.26	64.81	6.60	73.45
3.89	5.25	55.28	5.27	58.55	5.98	66.85
3.27	5.18	50.03	5.10	53.28	6.07	60.87
2.75	5.71	44.85	5.72	48.18	6.84	54.80

2.312	6.37	39.14	6.69	42.46	7.79	47.96
1.945	6.56	32.77	7.19	35.77	8.05	40.17
1.635	6.01	26.21	6.68	28.58	7.49	32.12
1.375	5.11	20.20	5.59	21.90	6.30	24.63
1.156	4.39	15.09	4.73	16.31	5.38	18.33
0.972	4.06	10.70	4.39	11.58	5.00	12.95
0.818	3.65	6.64	3.97	7.19	4.49	7.95
0.688	2.30	2.99	2.49	3.22	2.73	3.46
0.578	0.69	0.69	0.73	0.73	0.73	0.73
0.486	0.00	0.00	0.00	0.00	0.00	0.00

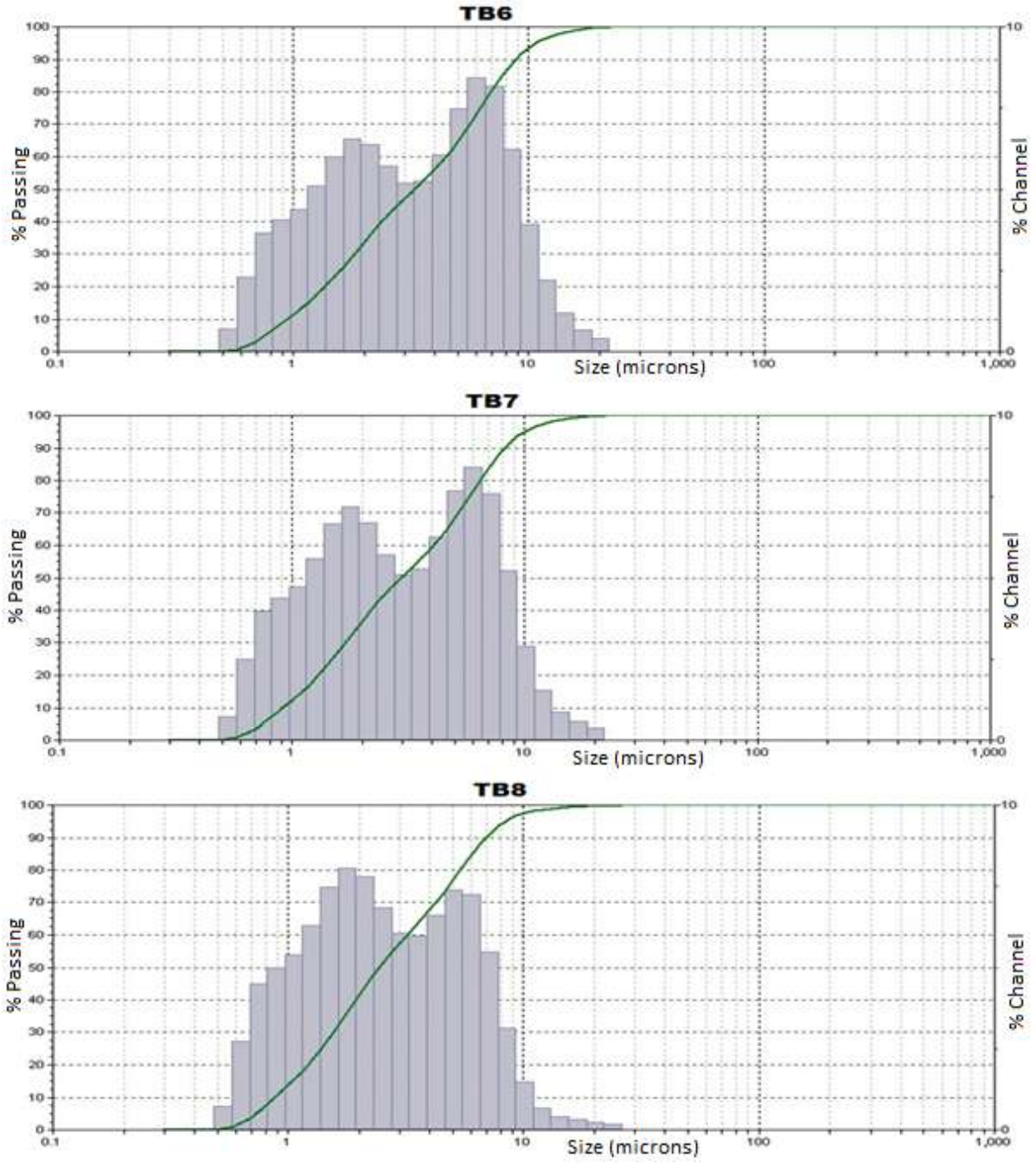

Figure 114 Graphical representation of distribution curves for TB6, TB7 and TB8

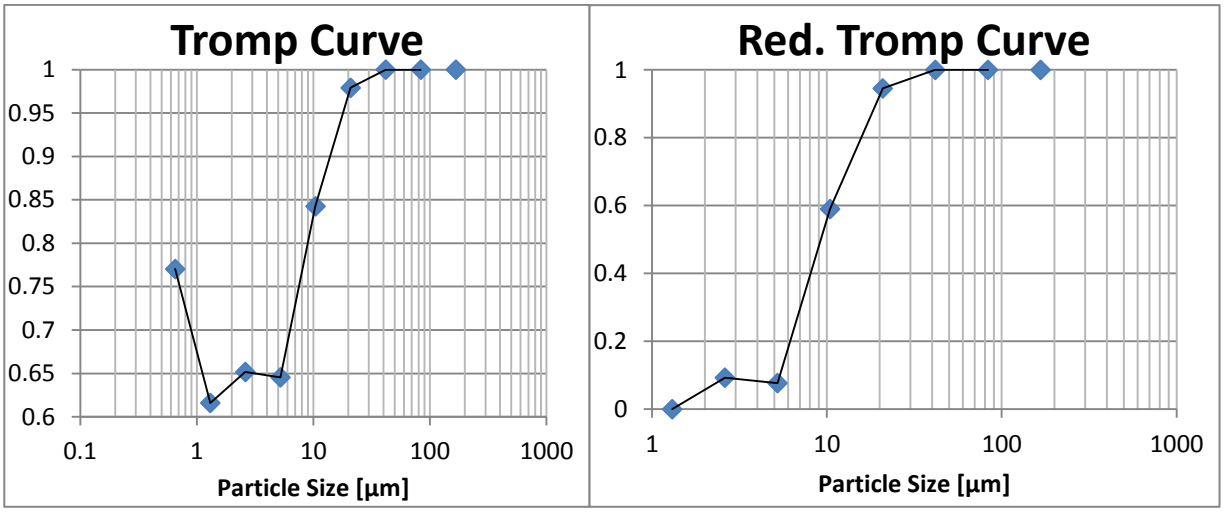

Figure 115 Tromp curve and reduced Tromp curve for TB6

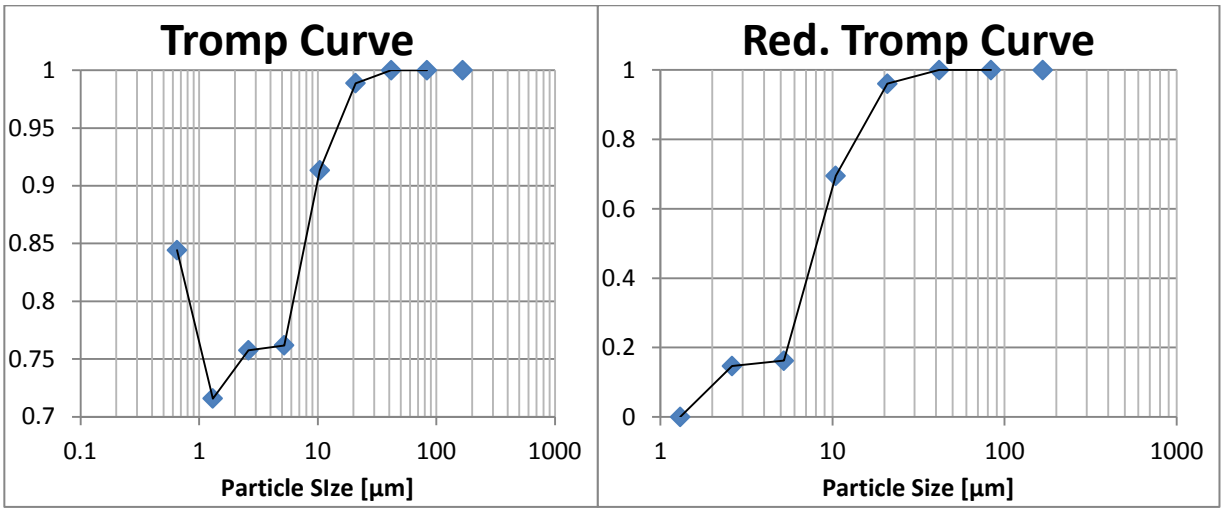

Figure 116 Tromp curve and reduced Tromp curve for TB7

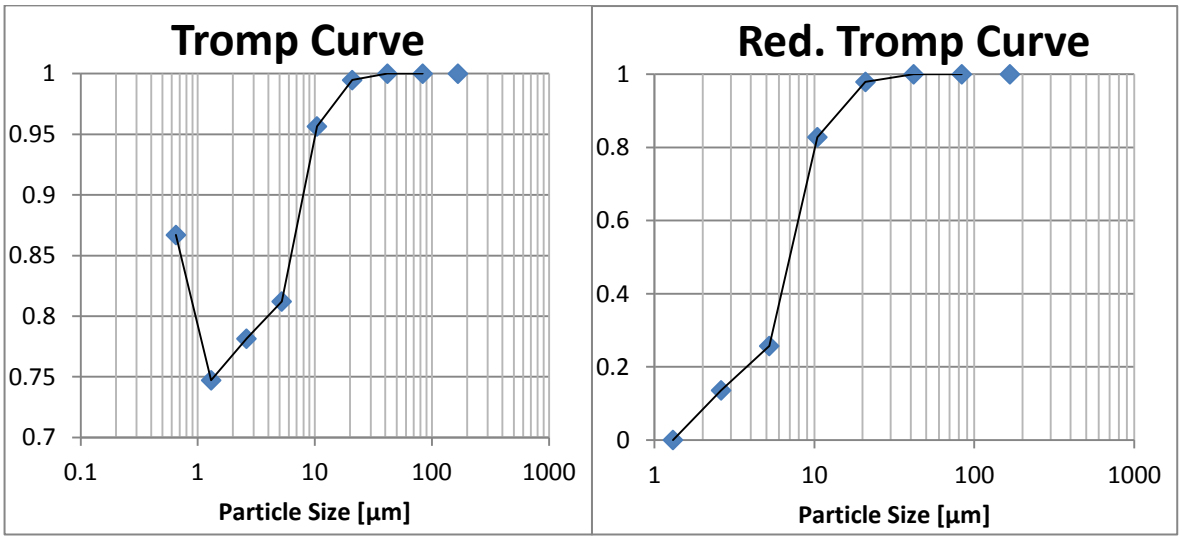

Figure 117 Tromp curve and reduced Tromp curve for TB8

8.3.4 Trial TB9 & TB10 & TB11

For the following classification trials, feed rate is again set to a constant value of 20 Hz. Fan setting for the presented trials TB6, TB7 and TB8 is set to a constant value of 30 Hz. Effects of varying classifier rotor cage speed on fine and coarse fraction size characterization are measured and presented.

Table 26 Tabular particle size distribution for fine fractions

Size [µm]	TB9		TB10		TB11	
	% Chan	% Pass	% Chan	% Pass	% Chan	% Pass
37	0.11	100.00	0.12	100.00	0.00	100.00
31.11	0.19	99.89	0.20	99.88	0.10	100.00
26.16	0.29	99.70	0.30	99.68	0.14	99.90
22	0.52	99.41	0.57	99.38	0.32	99.76
18.5	0.77	98.89	0.85	98.81	0.46	99.44
15.56	1.03	98.12	1.08	97.96	0.80	98.98
13.08	1.56	97.09	1.55	96.88	1.33	98.18
11	2.58	95.53	2.47	95.33	2.27	96.85
9.25	4.09	92.95	3.94	92.86	3.67	94.58
7.78	5.62	88.86	5.48	88.92	5.11	90.91
6.54	6.41	83.24	6.23	83.44	5.87	85.80
5.5	6.19	76.83	5.93	77.21	5.70	79.93
4.62	5.49	70.64	5.24	71.28	5.15	74.23
3.89	5.04	65.15	4.90	66.04	4.91	69.08
3.27	5.25	60.11	5.24	61.14	5.37	64.17
2.75	6.18	54.86	6.21	55.90	6.52	58.80
2.312	7.39	48.68	7.31	49.69	7.85	52.28
1.945	7.84	41.29	7.70	42.38	8.26	44.43
1.635	7.31	33.45	7.24	34.68	7.69	36.17
1.375	6.13	26.14	6.31	27.44	6.50	28.48
1.156	5.35	20.01	5.63	21.13	5.77	21.98
0.972	5.26	14.66	5.57	15.50	5.80	16.21
0.818	5.11	9.40	5.39	9.93	5.71	10.41
0.688	3.33	4.29	3.53	4.54	3.69	4.70
0.578	0.96	0.96	1.01	1.01	1.01	1.01
0.486	0.00	0.00	0.00	0.00	0.00	0.00

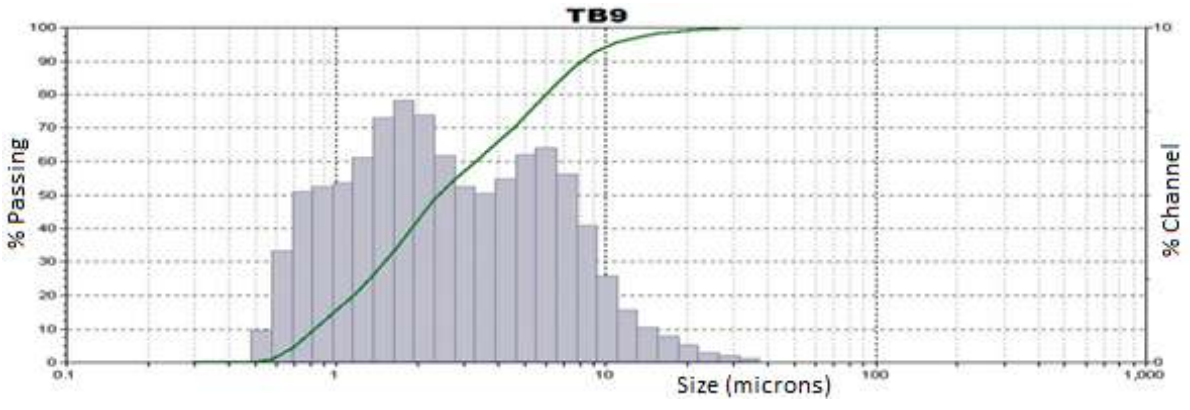

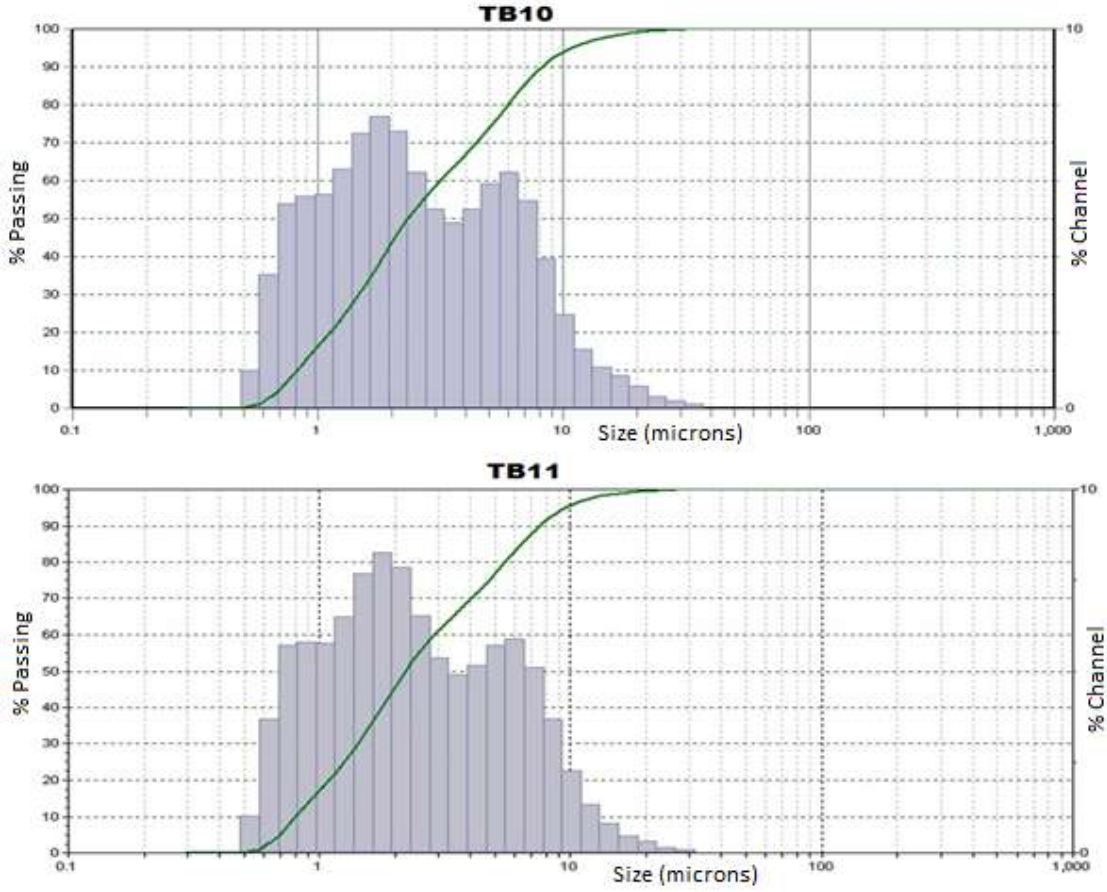

Figure 118 Graphical representation of distribution curves for TB9, TB10 and TB11

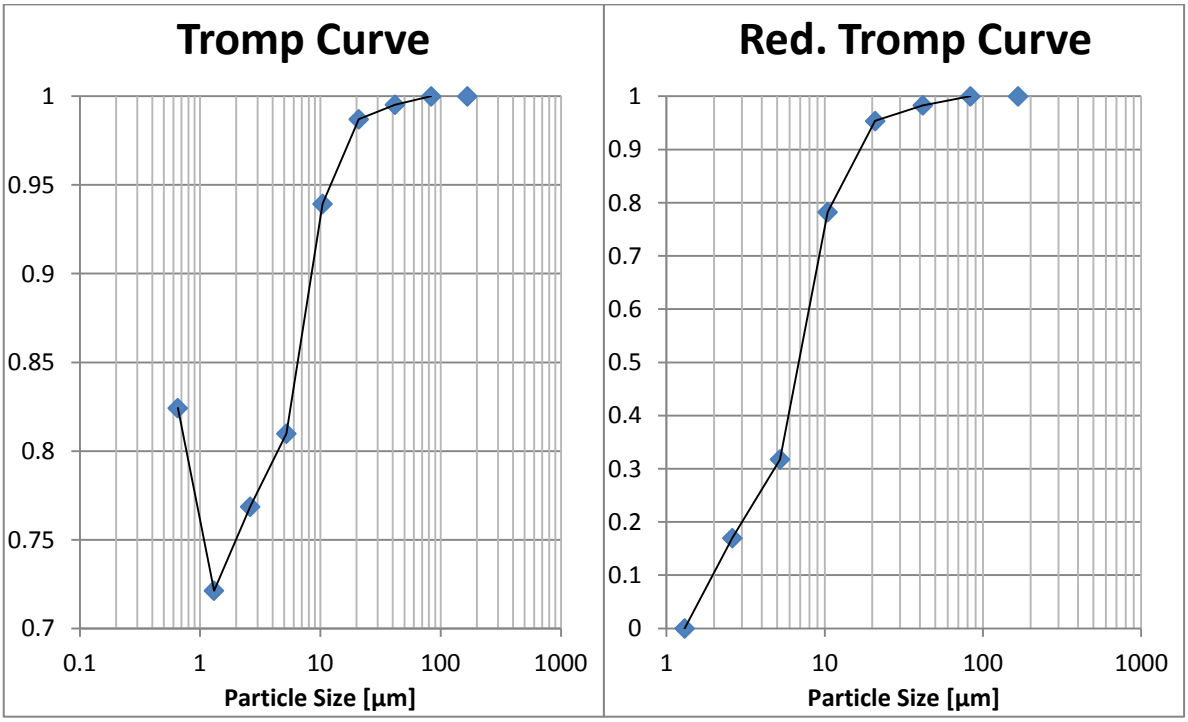

Figure 119 Tromp curve and reduced Tromp curve for TB9

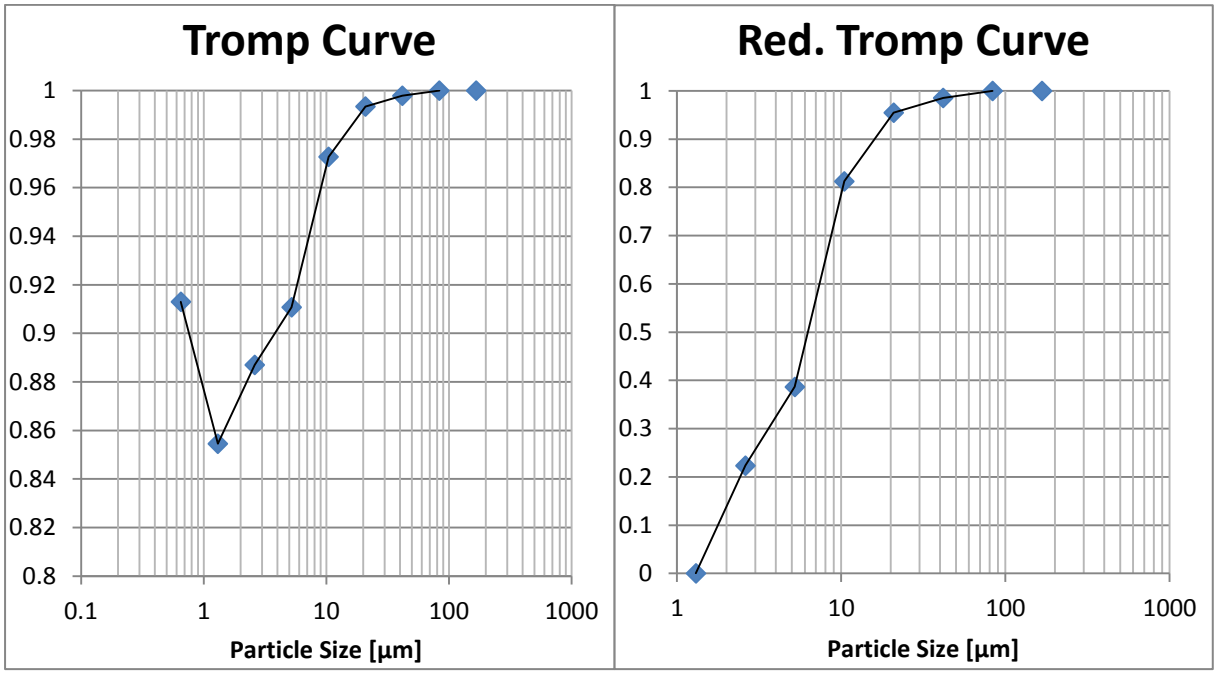

Figure 120 Tromp curve and reduced Tromp curve for TB10

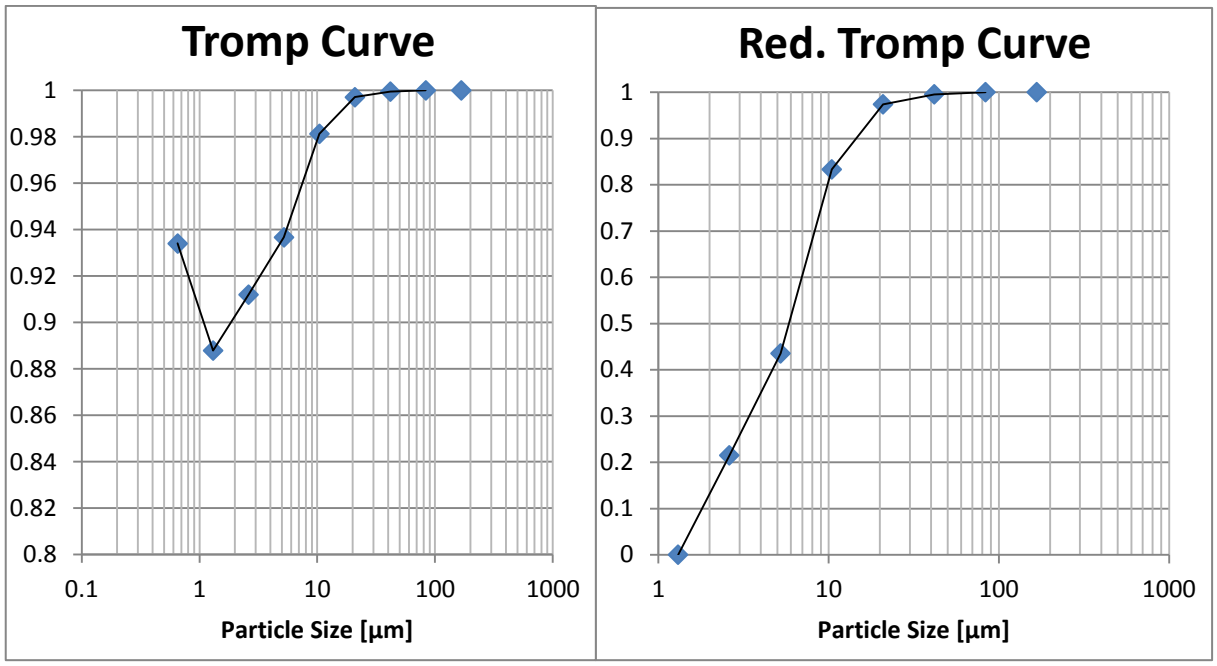

Figure 121 Tromp curve and reduced Tromp curve for TB11

8.4 SUMMARY - CLASSIFICATION RESULTS AND LIMIT MODES OF CLASSIFIER

Four groups with three classification trials in each group were carried out in order to establish effects of varying operating parameters on particle classification in the sub 10-micron range. Main operating parameters affecting classification process and particle size distribution of fine and coarse fraction are identified as classifier rotor cage speed, fan speed and feed rate. Procedures followed during classification trials and particle size distribution analysis have been described in chapters 7.8 and 7.9 Particle size distribution curves for fine and coarse fraction are established by taking 3 measurements for each set of operating parameters and by averaging them. Pre-averaging tests are carried out to select correct air blending and pressure settings on Microtrac and only after good repeatability rates are achieved, the measurements for averaging were taken. Table 27 identifies trials and corresponding operating parameters together with main points of particle distribution curves for fine fraction.

Table 27 List of classification trials with barite feed and corresponding D values for fine fraction

Trial	Fan [Hz]	Classifier [Hz]	Feed [Hz]	Feed [kg]	Fines [kg]	Coarse [kg]	Recov. [%]	25% AVE. [µm]	50% AVE. [µm]	75% AVE. [µm]	95% AVE. [µm]
TB1	50	50	10	24.4	3.31	21.1	13.56	1.562	3.29	6.8	14.9
TB2	50	50	20	24.6	2.6	22	10.57	1.362	2.536	6.26	11.09
TB3	50	50	30	25.3	1.9	23.4	7.51	0.984	1.674	2.844	6.95
TB4	50	30	20	25	5.4	19.6	21.60	1.702	3.77	6.79	11.33
TB5	50	40	20	23.6	3.5	20.1	14.83	1.605	3.06	5.89	11.5
TB2	50	50	20	24.6	2.6	22	10.57	1.362	2.536	6.26	11.09
TB6	40	30	20	25	4.8	20.2	19.20	1.582	3.27	6.25	10.68
TB7	40	40	20	25.3	3.2	22.1	12.65	1.494	2.923	5.79	9.87
TB8	40	50	20	26.3	2.5	23.8	9.51	1.388	2.43	4.8	8.31
TB9	30	30	20	24.7	2.7	22	10.93	1.335	2.394	5.24	10.53
TB10	30	40	20	23.9	1.3	22.6	5.44	1.29	2.331	5.17	10.7
TB11	30	50	20	25.1	1	24.1	3.98	1.258	2.194	4.74	9.5

With respect to results of trial TB1, TB2 and TB3 it can be observed that both the amount of fines recovered from cyclone and major D values of fine fraction are decreasing with increasing feed rate as shown in Figure 122. This can be attributed to increased particle loading in the air stream and resulting increased particle-particle interactions. As a result, particles start to agglomerate and form groups of particles. This effectively reduces dispersion and increases weight of the particle group and therefore reduces chances of particles being classified as fines. Increased particle loading also affects momentum exchange between flowing air and the particles. For a constant fan setting this effectively means that the amount of air supplied to classifier has to accelerate greater number of particles. Increased particle loading increases system resistance and therefore reduces amount of air supplied to the system (with respect to fan performance curve) which again consequently reduces amount of fine particles recovered from cyclone and also reduces size of major particle distribution points (25%, 50%, 75%, 95%) of the fine fraction.

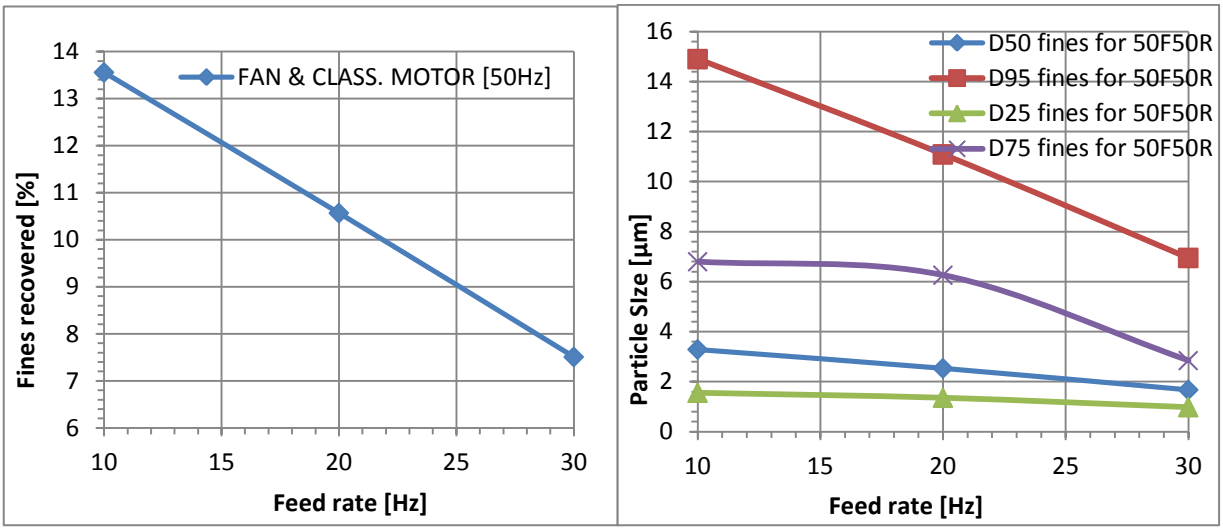

Figure 122 Amount of fines recovered and fines 50% passing value for varying feed rates (TB1, TB2, TB3)

Figure 123 shows influence of different operating parameters of fan and classifier on the amount of fines recovered from cyclone and their corresponding 50% passing values. For matching classifier motor settings, influence of increasing fan speed on amount of fines can be observed. For all tested classifier speeds the amount of recovered fines increased with increasing fan speed. Greater drag force acting on a particle as a result of higher fan speed translates into increased cut size of the classifier. The theoretical particle size (cut size) for which two major forces are in balance is now greater in size. Therefore, more particles are able to pass through rotating rotor cage, resulting into greater amount of fine particles recovered from the cyclone. It can be observed at the same time that for a constant fan setting and increasing classifier speed, the amount of fines is decreasing. Higher tip speed of the rotor cage translates into greater centrifugal force and the resulting theoretical particle size (cut size) for which two major forces are in balance is now smaller in size. Therefore, fewer particles are able to pass through rotating rotor cage.

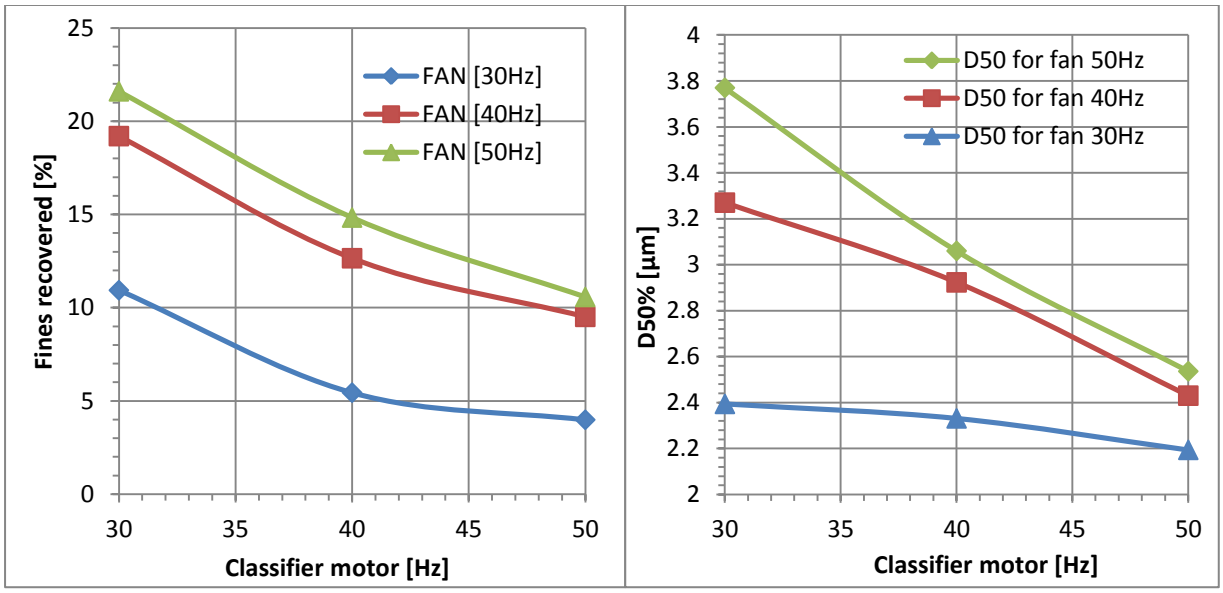

Figure 123 Amount of fines recovered and50% passing particle sizes for varying fan and classifier setting

Achieved 50% passing values for fine fraction are shown in Figure 123. For a constant feed rate of 20 Hz, the finest cut is achieved for operating parameters classifier 50 Hz and fan 30 Hz. The finest cut in all the trials is observed for feed rate setting at 30 Hz and both classifier and fan at 50 Hz. The fines recovery at these settings is however only 9.84%.

Major % passing values of particle size distribution curves for coarse fraction recovered from bottom section of the air classifier are presented in Table 28.

Table 28 List of classification trials with barite feed and corresponding D values for coarse fraction

Trial	Fan [Hz]	Classifier [Hz]	Feed [Hz]	Feed [kg]	Fines [kg]	Coarse [kg]	Recov. [%]	25% AVE. [µm]	50% AVE. [µm]	75% AVE. [µm]	95% AVE. [µm]
TB1	50	50	10	24.41	3.31	21.1	86.44	3.73	9.83	16.8	46.4
TB2	50	50	20	24.6	2.6	22	89.43	3.65	9.86	17.9	50.6
TB3	50	50	30	25.3	1.9	23.4	92.49	3.26	9.4	17.1	57.6
TB4	50	30	20	25	5.4	19.6	78.40	5.38	11.17	19.2	60.2
TB5	50	40	20	23.6	3.5	20.1	85.17	4.29	10.9	19.2	63.9
TB2	50	50	20	24.6	2.6	22	89.43	3.65	9.86	17.9	50.6
TB6	40	30	20	25	4.8	20.2	80.80	3.68	10.18	18	51.9
TB7	40	40	20	25.3	3.2	22.1	87.35	3.36	9.49	17.2	51
TB8	40	50	20	26.3	2.5	23.8	90.49	3.17	9.28	16.5	49.5
TB9	30	30	20	24.7	2.7	22	89.07	3.53	9.9	17.5	56.1
TB10	30	40	20	23.9	1.3	22.6	94.56	3.3	9.59	17.4	55
TB11	30	50	20	25.1	1	24.1	96.02	3.15	9.36	17	51.5

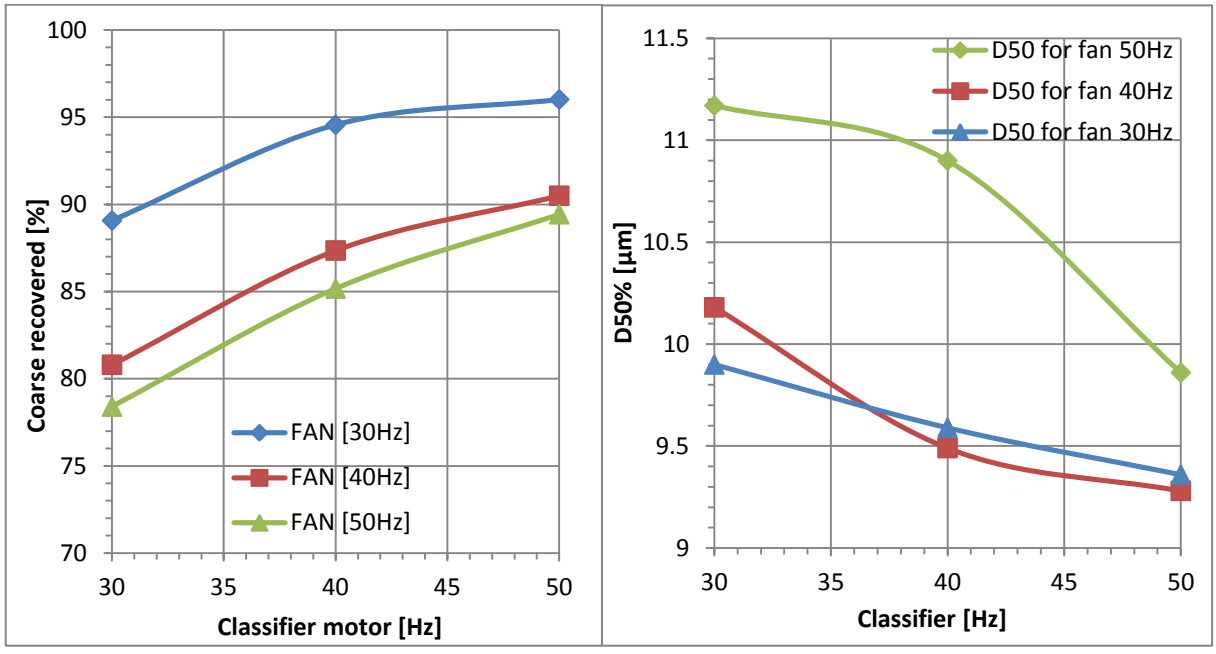

Figure 124 Amount of coarse recovered and50% passing particle sizes for varying fan and classifier setting

The amount of coarse particles recovered in each trial corresponds to conservation of mass and to expected trends. For identical classifier motor setting, increasing fan speed amounts to a greater drag force acting on a particle and resulting increased cut size of the classifier. Therefore, greater number of particles is able to pass through rotating rotor cage, resulting into fewer particles classified into coarse fraction. At the same time, for a constant fan setting and increasing classifier speed, the amount of recovered coarse particles increase. Comparison plot of coarse fraction particle size distribution curves is shown in Figure 125. It can be noticed that these curves do not manifest significant difference. This can be explained by the mass split ratio between coarse and fine fraction and also by the by-pass value of the classification process.

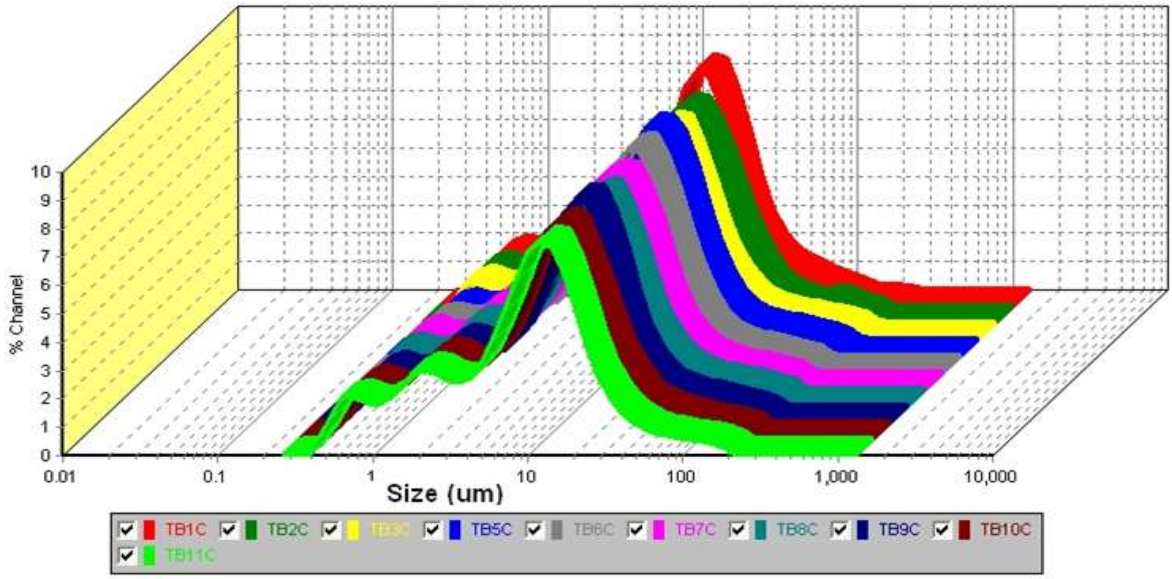

Figure 125 Coarse fractions comparison plot

Tromp curves or grade efficiency curves are used as one of the tools to evaluate performance of the air classifier. They are plotted for each classification trial and can be found in the previous chapter.

Table 29 Major % passing values obtained from Tromp curves together with sharpness of separation and by-pass

	75%	50%	25%	β	BY-PASS
TB1	14.70	8.46	5.28	0.36	0.702
TB2	10.36	6.41	3.20	0.31	0.730
TB3	6.80	4.06	2.42	0.36	0.748
TB4	15.20	9.36	6.40	0.42	0.534
TB5	13.07	8.80	6.69	0.51	0.673
TB6	15.10	9.50	6.97	0.46	0.616
TB7	14.70	8.46	5.28	0.36	0.715
TB8	9.71	7.43	5.06	0.52	0.747
TB9	10.06	7.26	4.02	0.40	0.721
TB10	9.65	6.59	3.03	0.31	0.856
TB11	9.34	6.06	3.02	0.32	0.888

It can be observed on the Tromp curves for different operating parameters that the classification process is not 100% efficient. Tromp values on the y-axis never reach down to 0% and this portion below the curve is called bypass of the classifier. Tromp values can be defined as the ratio of the quantity of particles of size *d* in the coarse fraction to that in the feed. Bypass of the classifier can be defined as a portion of fine material not undergoing classification process and ending in coarse fraction. The bypass fraction is influenced mainly by operating parameters and by classifier design. Increased particle concentration of the air stream increases particle agglomeration and bypass of the classifier. Relation between classifier bypass and feed rate is shown in Figure 126. Here it can be seen that bypass increases with increasing feed rate. Structural parameters of the classifier affect dispersion of the feed material and poor dispersion results into higher bypass. For a constant classifier speed setting, greater airflow through the classifier leads into better dispersion of particles, more efficient classification and thus lower bypass. Cut size of the classifier is however increasing. For a constant fan setting and increasing classifier speed, cut size of the classifier is decreasing at a cost of greater bypass as it can be seen in Figure 126.With respect to bypass values under different operating parameters it can be concluded that in order to achieve fine fraction with particle size distributions in region of 90% passing 10 microns a specific set of operating parameters needs to be selected. This set of parameters negatively affects efficiency of classification process. For comparison, typical values of bypass for classification of fines in region of 90% passing 75 microns are typically 10%. Bypass values for trials carried out with varying feed rate were in region of 73%. Bypass values for varying fan and classifier setting varied from 53% to 88%. In order to establish 25%, 50% and 75% passing values the Tromp curve is reduced.

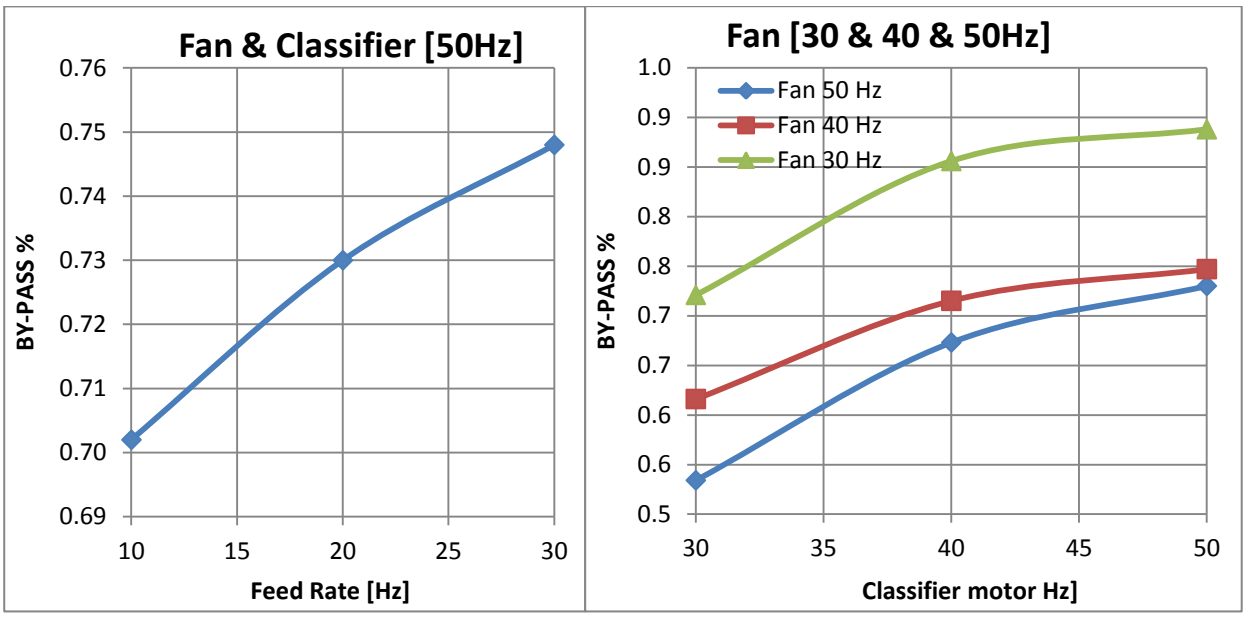

Figure 126 By-pass of the classifier for various operating parameters settings

Sharpness of the classification process is represented by β values which are ratio of 25% and 75% passing values with respect to Tromp curves. For an ideal theoretical classification, it has value of unity as shown in Figure 9. The calculated values fluctuate between 0.31 and 0.52 and no particular trends have been observed.

The 50% passing value based on Tromp curve represent particle with specific size for which the forces acting on the particle are in equilibrium and thus the particle has 50% probability of being classified either into fine or coarse fraction. This value represents cut size of the classifier.

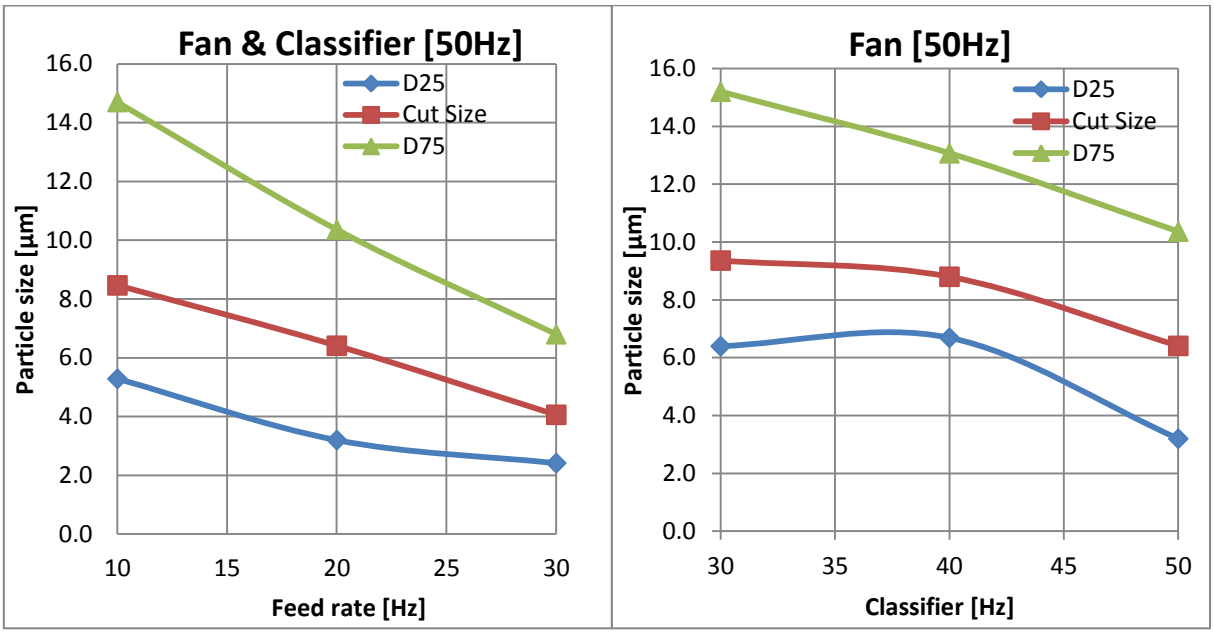

Figure 127 Major % passing values based on Tromp curve for increasing feed rate at constant fan and classifier setting and increasing classifier speed at constant fan and feed rate setting

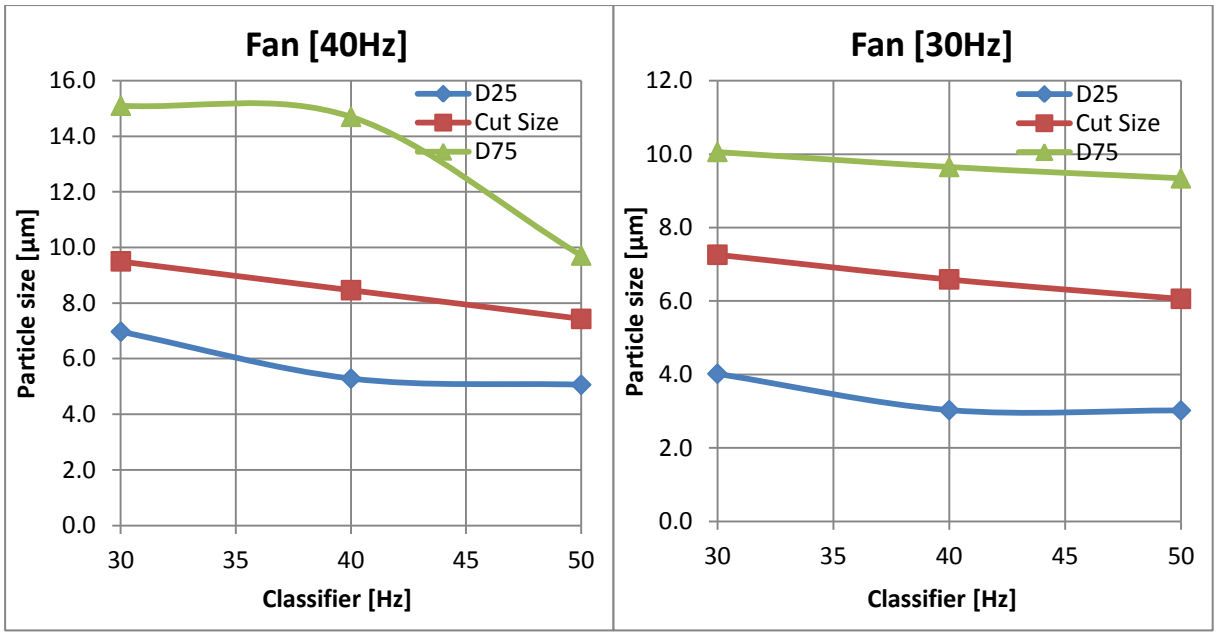

Figure 128 Major % passing values from Tromp curve for increasing classifier speed at constant fan and feed rate

It can be concluded that increasing feed rate decreases cut size of the classifier while the difference in sharpness of separation remains insignificant. It can be observed that a rather large increase in classifier speed (from 30 Hz to 50 Hz) corresponds to only a small decrease in cut size, in region of 2 microns.

9 COMPUTATIONAL FLUID DYNAMICS SIMULATION

Computational fluid dynamics is a field of fluid mechanics which uses numerical analysis to solve systems involving fluid flow, heat transfer and associated phenomena by means of computer simulation. Technological advancement in computer science enables CFD to obtain precise solutions to still more and more complex turbulent flows. The results of CFD analysis are relevant for product development, conceptual studies of new designs etc. CFD analysis should be however always complemented by experimental data collection and verification. Following chapters describe workflow and individual steps involved in obtaining numerical results.

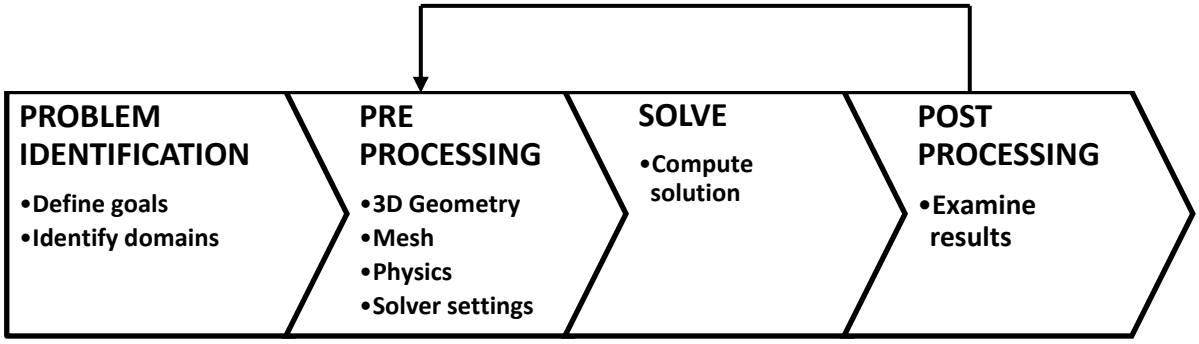

Figure 129 CFD simulation working process

9.1 PRE-PROCESSING AND 3 DIMENSIONAL MODEL

In order to carry out a CFD analysis of the investigated system a thorough decomposition of the problem is required. All the aspects of different simplification approaches are considered and region of interest is selected. Cyclone efficiency depends on several factors where one of them is size of the particles to be separated from the flow. As a general rule, cyclones are more efficient with increasing particle size. Therefore, a fraction of the fine particles is carried over back to classifier where they re-enter classification process. Particle-particle interaction is not included in the simulation and therefore additional particle loading can be neglected.

Classifier system used in the experimental part is realized as a closed loop circuit. Aim of this work is to investigate flow patterns inside of the classifier and therefore the loop is broken and classifier itself is selected as the region of interest. Cyclone is not part of the simulation.

Simplified three-dimensional geometry is created in Autodesk Inventor professional. Simplification is carried out with attention to functional design of the device and to be selected modelling approach in CFD software. Important step is to constrain the assembly to coordinate system within the CAD environment. Figure 130 shows geometry divided into 4 closed solid bodies representing rotor blades and fluid zones of the classifier.

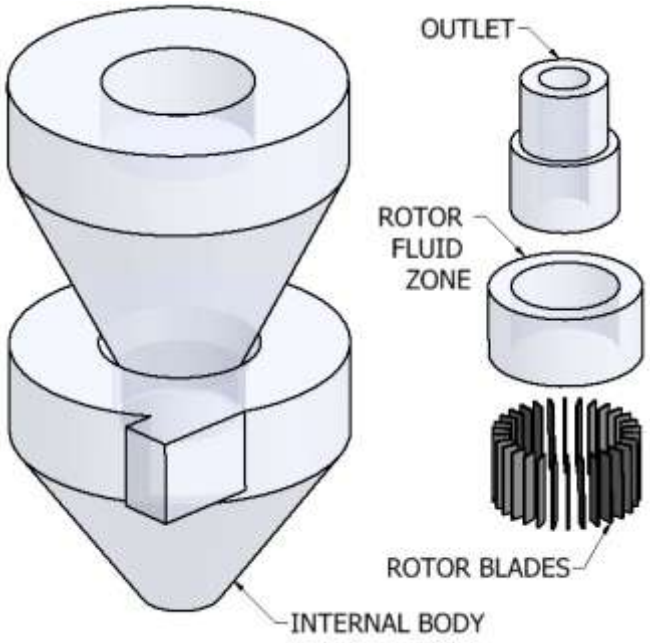

Figure 130 3D models of fluid zones and rotor blades

9.2 FINITE VOLUME METHOD AND DISCRETIZATION

The Finite Volume Method is a numerical technique that transforms the partial differential equations representing conservation laws over differential volumes into discrete algebraic equations over finite volumes. [56]

Fluid domain is subdivided into number of non-overlapping control volumes. Partial differential equations are discretized into a system of algebraic equations and it is then solved to compute values of the dependent variable for each of the elements. This results into a discrete distribution of mass, momentum and energy. These variables are stored at centroid of control volume and interpolation profiles are then used to determine variation of variables between centroids. Conservation of these quantities is satisfied for any control volume and therefore also for the whole computational domain with any number of elements. Thus, finite volume method is a conservative method. Based on the aforementioned it is obvious that quality of the grid is a crucial factor to be considered in the discretization process. Main parameters used to evaluate quality of the mesh are:

- Number of elements in the grid
- Size of the elements and y+ value
- Orthogonal quality
- Skewness
- Aspect ratio

Number of elements in the grid is proportional to storage and computational time requirements. Therefore, compromise between desired accuracy of the numerical results and number of control volumes needs to be made. Control volumes in 3 fluid zones are distributed in a manner which

minimizes discretization error. Particular detail is required in the proximity of rotor blades and therefore rotor fluid zone grid is finely refined.

Walls are the main sources of mean vorticity and turbulence. Turbulence models are significantly affected by the no slip condition valid for wall boundary conditions. Large gradients in mean velocity cause production of turbulent kinetic energy. Modelling of the flow in the near wall region significantly affects numerical robustness of the solution and an accurate representation of the flow in this region determines successful prediction of wall bounded turbulent flow. Non- dimensional distance from wall Y+ is introduced to describe how fine or coarse is the mesh in wall bounded flows. Cell centroids for a standard wall function and k-epsilon realizable turbulence model should be located within Y+ =30÷60.

$$Y^+ = \frac{yU_\tau}{\nu} \tag{9.1}$$

$$U_\tau = \sqrt{\frac{\tau_w}{\rho}} = U_e \cdot \sqrt{\frac{C_f}{2}} = U_e \cdot \sqrt{\frac{0.039}{Re^{\frac{1}{4}}}} \tag{9.2}$$

Where y is the distance between wall and first centroid, U_τ is friction velocity, ν is kinematic viscosity, U_e is parallel velocity, C_f is skin friction coefficient and Re is Reynolds number.

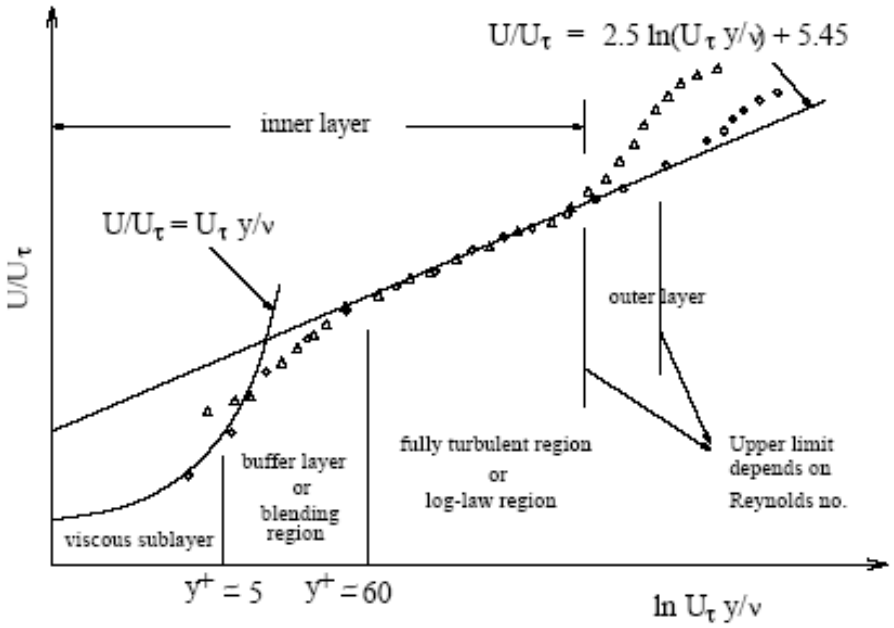

Figure 131 Subdivisions of the near wall region [57]

Experiments have shown that the near wall region can be subdivided into three layers as shown in Figure 131. The layer closest to the wall is the viscous sublayer and the flow in this layer is almost laminar. Velocity parallel to the wall varies linearly with distance from wall and viscosity plays dominant role in momentum exchange in this region. Outer layer is a turbulent layer and turbulence plays the major role in this region. Effects of molecular viscosity and turbulence are equally important the buffer layer which is the region in-between those two layers.

Wall function approach and near wall model are the two approaches available to model effects of turbulence in the near wall region. Choice in between them directly influences design of the mesh in the near wall region. Viscous sublayer and buffer layer are not resolved in wall function approach and instead a semi empirical formula (wall function) is used to resolve these layers. This approach reduces requirements on Y+ values in the near wall region and therefore significantly reduces computational cost. First cell height from wall is calculated and mesh is generated with respect to wall function. Y+ values on the walls are displayed and checked in the post processing and adjustments to the mesh are carried out in the regions of non-compliant Y+ values. Meshed domains are shown in Figure 132

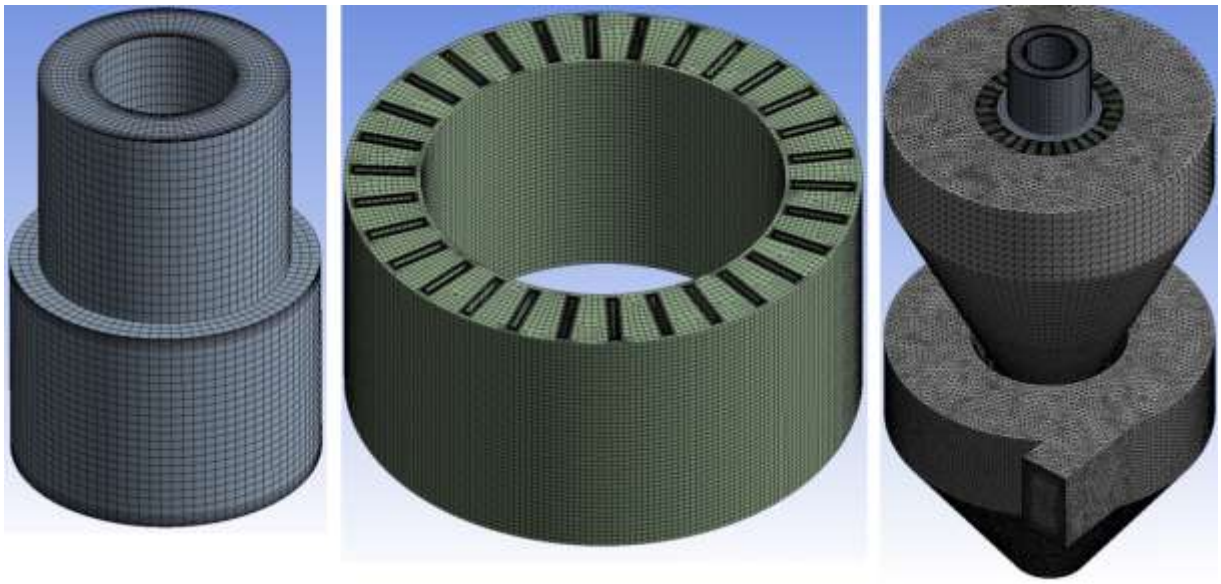

Figure 132 Mesh representation for outlet, rotor domain and internal body

Structured mesh is created for outlet and rotor domain using hexa elements. This mesh type is space efficient and provides the highest accuracy of solution.

Outlet domain mesh is created using multizone meshing method. Mapped mesh type is built out of hexa elements while free mesh type used is tetra. Local body sizing with hard behaviour is applied and element size is selected to be 6,79 mm. Inflation layer is created with respect to observed Y+ values.

Rotor domain mesh is also created by multizone meshing method. Mapped mesh type is built out of hexa elements while free mesh type used is hexa dominant. Local body sizing with soft behaviour is applied and element size is selected to be 3,2 mm. Inflation layer is created around rotor blades with respect to observed Y+ values. Internal body is meshed with tetra and prism elements. Cylindrical and conical surfaces are map face meshed and inflation layer is created to allow turbulence model to resolve boundary layers. Main indicators considered whilst evaluating quality of the mesh were skewness, orthogonal quality and aspect ratio. The solution would benefit from finer mesh but this would significantly influence computational cost. Therefore, a reasonable compromise between cost and accuracy is selected. Several meshes were tested in early stage of the simulations to guarantee mesh independent solution. Table 30 shows number of elements in individual domains and associated mesh quality indicators.

Table 30 Overview of quality indicators and elements in domain

	NODES	ELEMENTS	SKEWNESS		ORTHOGONAL QUALITY		ASPECT RATIO	
	NO.	NO.	MIN	MAX	MIN	MAX	MIN	MAX
INTERNAL BODY	352 174	1 069 541	0.00018	0.84	0.21	0.99	1.16	14.01
OUTLET	68 185	158 516	0.0062	0.7	0.34	0.99	1.19	15.27
ROTOR DOMAIN	389 180	353 503	0.00045	0.72	0.47	0.99	1.01	16.54

Figure 133 shows distribution of different element types in the whole domain for three main quality indicators. The average value of aspect ratio is 4.12, average value of skweness is 0.25 and the average orthogonal quality is 0.87.

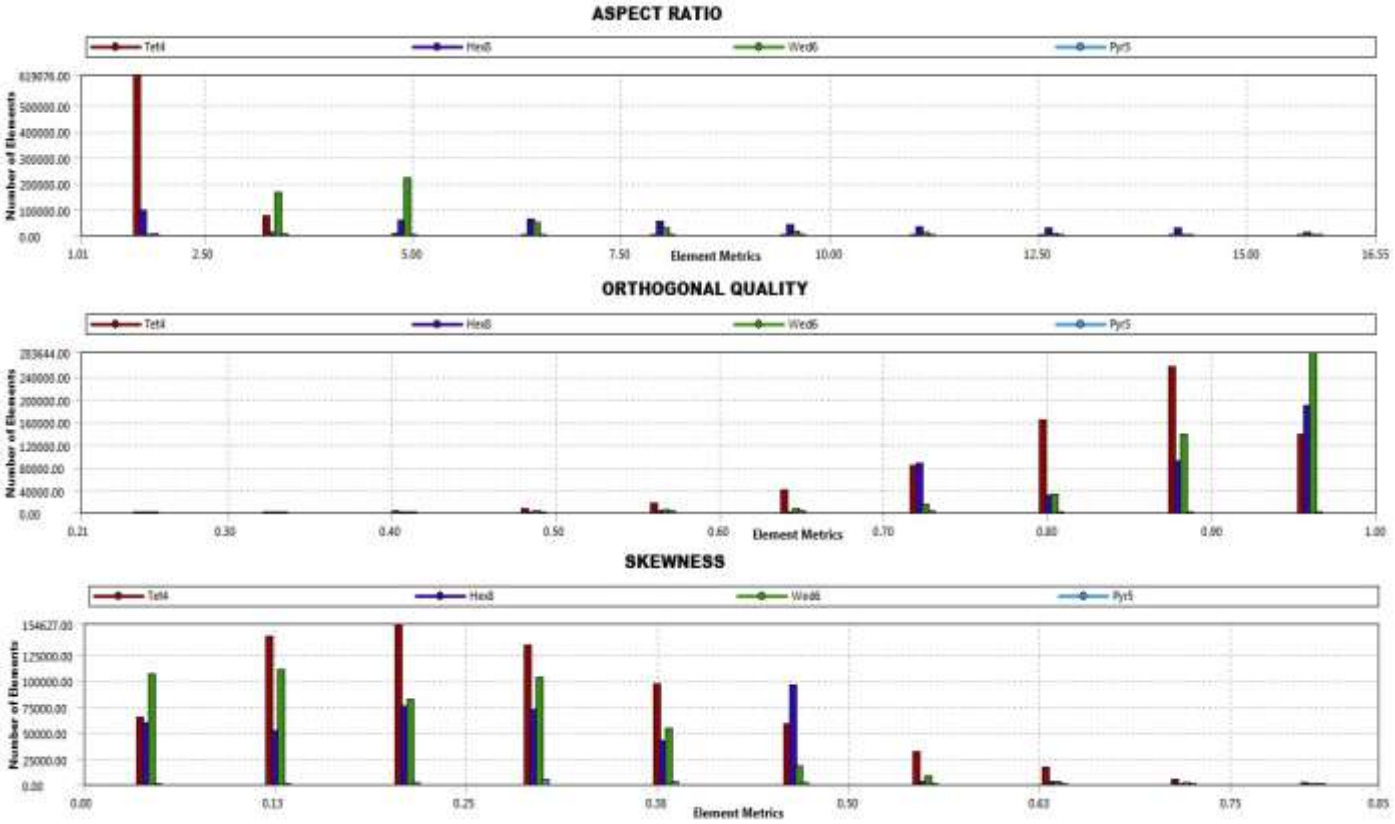

Figure 133Aspect ratio, orthogonal quality and skewness distribution

9.3 SPATIAL DISCRETIZATION

Discrete values of the scalar ϕ are stored in centres of the cells. Face values are required to calculate convection terms and therefore they are interpolated from the centre values. Several interpolation schemes are available in Ansys Fluent. Due to complex nature of the flow in the domain and structure of the grid, second order upwind is used to obtain face values for momentum, turbulent kinetic energy and turbulent dissipation rate. This is a second order accuracy scheme and provides better results for complex flows involving swirl and high streamline curvature. Quantities at cell faces are determined based on two neighbouring cell centre‘s values in

the upwind direction by using multidimensional linear reconstruction. Figure 134 shows second order upwind interpolation schematic.

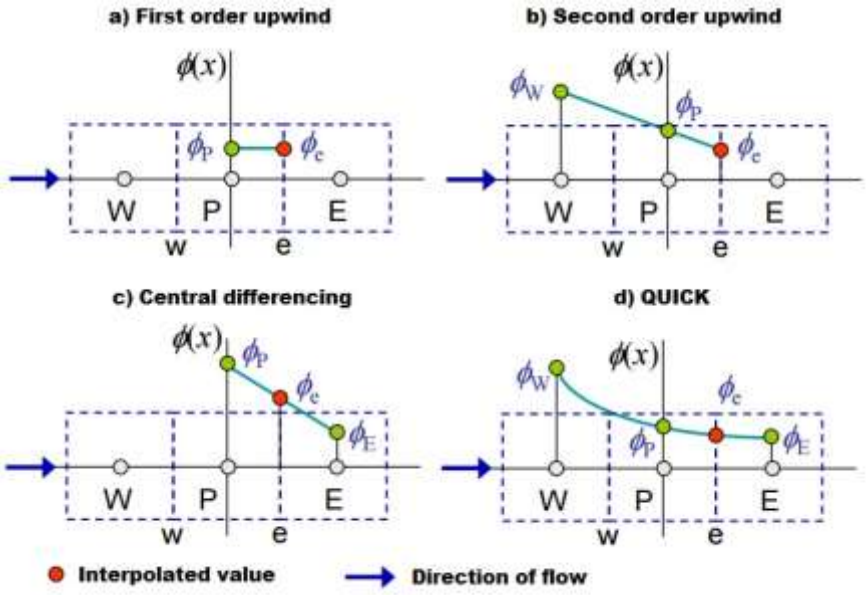

Figure 134Interpolation methods available in Ansys Fluent

There is a number of pressure interpolation schemes available for pressure based solver. Presto! and second order scheme are used for pressure interpolation due to its suitability for problems with large body forces, flows with high swirl number and rotating flows in strongly curved domains.

9.4 FLOW CHARACTERIZATION

Flow of fluid can be divided into a laminar and turbulent regime. In fluid mechanics, Reynolds number which is a dimensionless number is often used to help predict flow patterns and transitions from laminar to turbulent flow regime. It represents a ratio of inertial to viscous forces in the fluid that is subjected to internal movement due to different fluid velocities. Fluid friction generated by relative velocities propagates developing turbulent flow. Increasing viscosity of the fluid has just the opposite effect as more kinetic energy is absorbed and thus inhibiting turbulence. In this particular case it is used to confirm assumption that the flow inside of the air classifier is of turbulent nature and therefore turbulence modelling needs to be included in the simulation. Reynolds number can be calculated for number of regions of the classifier but turbulence modelling is implemented for the whole domain. General term for calculation of Reynolds number takes form designated for cylindrical vessel, agitated by central rotating rotor.

$$Re = \frac{\rho N D^2}{\mu} \tag{9.3}$$

Where ρstands for air density, N stands for rotational speed, D stands for diameter of the rotor and μ stands for dynamic viscosity of air. Computed Reynolds number is higher than the limit for

laminar flow by several orders of magnitude and therefore the flow in air classifier is fully turbulent.

Turbulent flows are time and coordinate dependent flows which are diffusive and chaotic, causing rapid mixing. They involve three-dimensional vorticity fluctuations with a wide range of time and length scales. The most accepted theory of turbulence is based on energy cascade according to which the turbulence is composed of eddies with different sizes. Those eddies contain different amounts of energy depending on their sizes. The larger eddies break up into smaller eddies and those undergo the very same energy cascade process. This process continues until the smallest possible eddy size is achieved and turbulent kinetic energy is dissipated into heat. Some of the factors that can be used to describe properties of turbulence are below:

- **Randomness**– Turbulent flow is defined by its random character where values of velocity, pressure, temperature etc. are dependent on time and three-dimensional coordinate. Fluctuations of these values are usually smaller than their average value by an order of magnitude and statistical methods are employed to describe these values.
- **Dissipation**– Turbulence is a dissipative process and it is responsible for an increased transfer of kinetic energy into heat. It is an irreversible process which is part of work of viscous stresses. Energy of the fluid is being increased at the expense of kinetic energy and therefore the turbulence ceases to exist without a constant inflow of energy.
- **Vorticity**– Turbulence involves eddies which has rotational component of velocity. Turbulent flows therefore contain randomly rotating eddies of different sizes where the maximum size is limited by characteristic dimension and smallest by viscosity of fluid. Field of vorticity is essentially three dimensional and it has significant dynamical effect on the flow. Vorticity of dissipative areas is usually higher by an order of magnitude than average value of vorticity in the whole domain.
- **Non-linearity** – Turbulence is nonlinear and it is represented by a non-linear acceleration term in Navier-Stokes equations.
- **Diffusion**– Turbulence is significantly increasing flux of mass and energy in the flow field due to diffusion effect. It transports physical quantities from given fluid volume to adjacent volume.

9.5 NAVIER-STOKES GOVERNING EQUATIONS

Three-dimensional flow of viscous fluid and relation between velocity, pressure, temperature and density is described by Navier-Stokes equations. They are nonlinear partial differential equations and they represent mathematical statements of the conservation laws for mass, momentum in three directions and energy. Heat transfer is not part of the air classifier simulation and therefore it is not described in the chapter.

Conservation of mass is represented by continuity equation. It can be defined for compressible or incompressible flow. Effects of compressibility are mainly encountered in flows with high velocities and pressure variations. Fluid density is a function of pressure, temperature etc in these flows. Compressibility effects are negligible for fluid flows with low Mach number and therefore

density of fluid is pronounced to be constant. Mach number is a dimensionless number representing ratio of flow velocity around an object to speed of sound. It is used to determine whether the effects of compressibility can be neglected for the particular flow and whether it can be deemed as incompressible.

$$M = \frac{U_{MAX}}{c} \tag{9.4}$$

Where U_{MAX} is the maximum velocity observed in fluid flow and c is the speed of sound in the medium. Maximum velocity in the system is in the region of throat and its value is 55 m/s. Speed of sound in the medium is 343 m/s and for the given conditions the value of Mach number is 0,16. This value is significantly lower than value of unity and therefore the continuity equation takes form for incompressible flow.

$$\frac{\partial u}{\partial x} + \frac{\partial v}{\partial y} + \frac{\partial w}{\partial z} = 0 \tag{9.5}$$

Where u, v, w represent velocity components of the fluid. The equation is called a convective term and it represents net flow of mass out of the element across its boundaries.

Conservation of momentum equations are obtained by applying Newton's law of motion to an element of fluid. It states that the rate of change of momentum of a fluid parcel equals to the sum of forces acting on the parcel.

We distinguish two types of forces acting on the particle [58]:

a. Surface forces
   - Pressure forces
   - Viscous forces

b. Body forces
   - Gravity force
   - Centrifugal force
   - Coriolis force

Navier-Stokes equations representing conservation of momentum for a 3-dimensional flow are displayed below.

$$\frac{\partial u}{\partial t} + \frac{\partial (uu)}{\partial x} + \frac{\partial (uv)}{\partial y} + \frac{\partial (uw)}{\partial z} = -\frac{1}{\rho}\frac{\partial P}{\partial x} + \nu\left(\frac{\partial^2 u}{\partial x^2} + \frac{\partial^2 u}{\partial y^2} + \frac{\partial^2 u}{\partial z^2}\right) + f_x \tag{9.6}$$

$$\frac{\partial v}{\partial t} + \frac{\partial (vu)}{\partial x} + \frac{\partial (vv)}{\partial y} + \frac{\partial (vw)}{\partial z} = -\frac{1}{\rho}\frac{\partial P}{\partial y} + \nu\left(\frac{\partial^2 v}{\partial x^2} + \frac{\partial^2 v}{\partial y^2} + \frac{\partial^2 v}{\partial z^2}\right) + f_y \tag{9.7}$$

$$\frac{\partial w}{\partial t} + \frac{\partial (wu)}{\partial x} + \frac{\partial (wv)}{\partial y} + \frac{\partial (ww)}{\partial z} = -\frac{1}{\rho}\frac{\partial P}{\partial z} + \nu\left(\frac{\partial^2 w}{\partial x^2} + \frac{\partial^2 w}{\partial y^2} + \frac{\partial^2 w}{\partial z^2}\right) + f_z \tag{9.8}$$

Where u, v, w are components of velocity, t is time, P is pressure, ρ is density, ν is kinemaitc viscosity and $f_{x,y,z}$ represent outside body forces. First term on the left-hand side represent rate of change in the fluid. Other three terms represent convective terms. Convection is a physical process that occurs in fluid flow in which some property is transported by the ordered motion of the fluid. First term on the right-hand side represent pressure gradient. The following three terms represent diffusion terms. Diffusion is a process where some property is transported by the random motion of the molecules of the fluid and it is related to stress tensor and viscosity of the fluid. Last term represents additional body forces present in the system like gravity, centrifugal and Coriolis force.

In the air classifier, rotor-stator interaction is relatively weak and therefore multiple reference frame approach can be employed to simulate rotating blades. This approach does not account for the relative motion of rotating and inertial cell zone. Advantage of this model however is that a problem which is unsteady in an inertial frame can be rendered as a steady problem with respect to steadily rotating reference frame. It allows to model problems involving rotating parts by allowing moving reference frames in selected cell zones. Flow domain is divided into several cell zones with interfaces defined in between them. Absolute velocity formulation is selected and governing equations for the fluid are written with respect to particular subdomain's reference frame. No special transformation is required on the interface between fluid domains because velocities are stored in the absolute frame. Scalar variables like pressure are computed locally from adjacent cells.

In the absolute velocity formulation used by Ansys Fluent, centripetal and Coriolis acceleration can be simplified into a single term and a generalized equation representing conservation of momentum in a steadily rotating fluid domain can be written as:

$$\frac{\partial}{\partial t}\rho\vec{v} + \nabla(\rho\,\overrightarrow{v_R}\overrightarrow{v}) + (\vec{\omega} \times \vec{v}) = -\nabla P + \nabla\boldsymbol{\tau} + \vec{F} \qquad (9.9)$$

Where $\overrightarrow{v_R}$ is vector of relative velocity (viewed in the moving reference frame), $\overrightarrow{v}$is vector of absolute velocity (as viewed from the inertial frame), $\vec{\omega}$ is vector of angular velocity,$\boldsymbol{\tau}$represents shear tensor from viscous stresses.

Navier-Stokes equations describing fluid flow can be solved using three different methods. First approach is to use direct numerical simulation (DNS) with a very small time step. This method is however limited only to simple studies due to its prohibitive computational cost. Second approach is to use large eddy simulation (LES) which is a direct simulation of large eddies. Small scale eddies are filtered by a spatial statistical filter and then are discarded. This method is still however very costly. To reduce high computational cost, statistical analysis is used to simplify resolution of turbulent flows. This method is called Reynolds time averaging (RANS).

9.6 REYNOLDS AVERAGED NAVIER-STOKES EQUATIONS

It is the most commonly used approach for simulating industrial turbulent flow problems. Reynolds time averaging is a statistical analysis based on time dependent nature of turbulence. The main principle is to decompose the variables into a time mean value component and fluctuating value component.

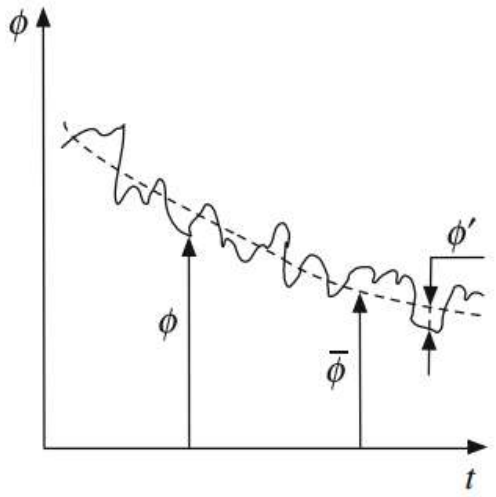

Figure 135 Fluctuating and mean variable component [5]

Where ϕ represents any flow variable at position **x** and in time t, $\bar{\phi}$ stands for mean value and ϕ' stands for fluctuating value.

$$\phi(\boldsymbol{x}, t) = \bar{\phi}(\boldsymbol{x}, t) + \phi'(\boldsymbol{x}, t) \tag{9.10}$$

Averaging rules needed to derive RANS equations are introduced, time averaging applied and terms are then substituted into Navier-Stokes equations (9.5) (9.6) (9.7) (9.8).Resulting RANS continuity and momentum equations are then rearranged and take following form.

$$\frac{\partial \overline{u_J}}{\partial x_j} = 0 \tag{9.11}$$

$$\frac{\partial(\overline{u_i})}{\partial t} + \frac{\partial(\overline{u_i u_j})}{\partial x_j} + \frac{\partial(\overline{u_i' u_j'})}{\partial x_j} = -\frac{1}{\rho}\frac{\partial(\bar{P})}{\partial x_i} + \nu\left(\frac{\partial^2(\overline{u_i})}{\partial x_j^2}\right) + \overline{f_i} \tag{9.12}$$

These RANS equations then solve averaged turbulent flow which is not a random function of time. Momentum equations now contain additional averaged products of the fluctuating components caused by a non-linear convection term. This term $(\overline{u_i' \cdot u_j'})$ is after multiplying by density called a Reynolds stress tensor and it contains nine new components from for a three-dimensional problem. Tensor is symmetric with respect to the main diagonal and therefore only

six components are independent. This tensor causes additional deformations of the fluid present in turbulent flows.

$$\boldsymbol{\tau} = \rho \begin{bmatrix} (\overline{u'u'}) & (\overline{u'v'}) & (\overline{u'w'}) \\ (\overline{v'u'}) & (\overline{v'v'}) & (\overline{v'u'}) \\ (\overline{w'u'}) & (\overline{w'v'}) & (\overline{w'w'}) \end{bmatrix} \tag{9.13}$$

Equations for individual components of the tensor again take the form of convective-diffusive equation. As a result, RANS equations are not a closed system and Reynolds stresses are required. The actual process of establishing Reynolds stresses is called turbulence modelling. Purpose of turbulence modelling is to close the system of equations. At this stage, two approaches are available. First of them is Reynolds stress model of turbulence (RSM) which again has several different models. Fundamentally, this approach solves six independent Reynolds stresses directly by solving the corresponding differential equations. Equation for dissipation is added to keep the system stable. If the energy was considered too, this model would have to solve 12 differential equations. It can be seen that computational cost if this model is high. The second approach is based on Boussinesq hypothesis.

9.7 BOUSSINESQ HYPOTHESIS

The hypothesis is basis for a whole group of turbulence models. It represents analogy with Newton relation for shear stresses in a simple two-dimensional laminar flow which is represented by:

$$\tau_L = \mu \frac{du}{dy} \tag{9.14}$$

Where τ_L represents shear stresses, μ represents dynamic viscosity, durepresents velocity and dy represents coordinate in direction perpendicular to flow direction. The hypothesis assumes that tensor of Reynolds stresses can be replaced with Newton relation and thus reducing 9 variables (6 independent) to just one. This variable is called turbulent eddy viscosity and it has same unit as dynamic viscosity.

$$\tau_{ij} = -\rho\left(\overline{u_i'u_j'}\right) = \tau_t = \mu_t \frac{d\bar{u}}{dy} \tag{9.15}$$

Where τ_{ij} represents Reynold stress tensor and μ_t repsesents turbulent eddy viscosity which is not property of the fluid but a property of flow regime. This assumption is generally expressed as:

$$-\rho\left(\overline{u_i'u_j'}\right) = \mu_t \left(\frac{\partial(\overline{u_i})}{\partial x_j} + \frac{\partial(\overline{u_j})}{\partial x_i}\right) - \frac{2}{3}\rho k \delta_{ij} \tag{9.16}$$

$$k = \frac{1}{2}\left(\overline{u_j'u_j'}\right) \tag{9.17}$$

Where k represents turbulent kinetic energy and δ_{ij} represents Kronecker delta. This approximation transforms calculation of Reynold stresses into calculation of turbulent kinetic energy and turbulent eddy viscosity.

9.8 K-E TURBULENCE MODELS

K-Epsilon realizable and RNG turbulence models belongs to a family of K-Epsilon semi-empirical models. These models then belong to a family of two equation turbulence models which are the most commonly used models in industrial applications due to their reasonable accuracy, robustness and economy. The model solves differential equation for turbulent kinetic energy and dissipation rate and it is valid for fully turbulent core flows where effects of molecular viscosity are negligible.

K-E realizable turbulence model

The model is the latest addition to this group of models and it differs from standard K-E model in two aspects. It adopts a new formula for turbulent viscosity calculation and a modified transport equation for dissipation rate. It is the only model from group of K-E models that satisfies mathematical constraints for Reynolds stresses valid with the physics of turbulent flow. The realizability of the model which essentially means positivity of normal stresses and Schwarz inequality for shear stresses is achieved by sensitizing turbulent viscosity to the mean flow and turbulence. This model shows significant improvements over standard K-E model for flows that involve rotation, vortices and a strong streamline curvature. Transport equations for turbulent kinetic energy and dissipation rate are as follows.

$$\frac{\partial}{\partial t}(\rho k) + \frac{\partial}{\partial x_j}(\rho k u_j) = \frac{\partial}{\partial x_j}\left[\left(\mu + \frac{\mu_t}{\sigma_k}\right)\frac{\partial k}{\partial x_j}\right] + G_k + G_b - \rho\varepsilon - Y_M + S_k \qquad (9.18)$$

$$\frac{\partial}{\partial t}(\rho \varepsilon) + \frac{\partial}{\partial x_j}(\rho \varepsilon u_j) = \frac{\partial}{\partial x_j}\left[\left(\mu + \frac{\mu_t}{\sigma_\varepsilon}\right)\frac{\partial \varepsilon}{\partial x_j}\right] + \rho C_1 S\varepsilon - \rho C_2 \frac{\varepsilon^2}{k+\sqrt{\nu\varepsilon}} + C_{1\varepsilon}\frac{\varepsilon}{k}C_{3\varepsilon}G_b + S_\varepsilon \qquad (9.19)$$

Where G_k represents generation of turbulent kinetic energy due to mean velocity gradients, G_b represents generation of turbulent kinetic energy due to buoyancy, Y_M represents contribution of the fluctuating dilatation in compressible turbulence to the overall dissipation rate, C_1 and C_2 are constants, σ_k and σ_ε are turbulent Prandtl numbers and S_k and S_ε are source terms. Turbulent viscosity is then calculated as.

$$\mu_t = \rho C_\mu \frac{k^2}{\varepsilon} \qquad (9.21)$$

Where C_μ is no longer a constant like in standard and RNG model, but is calculated as follows.

$$C_\mu = \frac{1}{A_0 + A_S \frac{kU^*}{\epsilon}} \quad (9.22)$$

Where

$$U^* \equiv \sqrt{S_{ij}S_{ij} + \tilde{\Omega}_{ij}\tilde{\Omega}_{ij}} \quad (9.23)$$

And

$$\tilde{\Omega}_{ij} = \Omega_{ij} - 2\varepsilon_{ijk}\omega_k \quad (9.24)$$

$$\Omega_{ij} = \overline{\Omega_{ij}} - 2\varepsilon_{ijk}\omega_k \quad (9.25)$$

Where $\overline{\Omega_{ij}}$ is the mean rate of rotation tensor with respect to moving reference frame and ω_k is the angular velocity. A_0 and A_S are model where $A_0 = 4{,}04$; $A_S = \sqrt{6}cos\phi$; $C_{1\varepsilon} = 1{,}44$; $C_2 = 1{,}2$; $\sigma_k = 1$; $\sigma_\varepsilon = 1{,}2$

K-E rng turbulence model

The model is based on renormalization group statistical method. With comparison to standard K-E model it improves accuracy for rapidly strained flows and includes effect of swirl on turbulence. Whilst standard K-E model is valid for high Reynolds numbers, K-E rng provides differential formula for effective viscosity which accounts for low Reynolds numbers. This extends model's accuracy for the flows in the near wall region. Swirl modification can be included in the model for flows involving high streamline curvature. Rng model accounts for effects of swirl or rotation by modifying turbulent viscosity calculation by adding swirl number, which represents intensity of swirling patterns in the flow. Default value in Ansys Fluent is 0,07. Both above mentioned models are used as part of convergence strategy in numerical simulation.

9.9 DISCRETE PHASE MODEL (DPM)

Equations describing physics of fluid phase which is treated as continuum were described in previous chapter. Two approaches are incorporated in Ansys Fluent for numerical simulation of multiphase flows. Euler-Euler approach which treats different phases as interpenetrating continuums and conservation equations are derived for each phase. Euler-Lagrange approach is selected for simulating discrete phase. Dispersed phase is solved by tracking number of parcels moving through fluid phase. Trajectories of particles are computed individually. For cases where discrete phase occupies low volume fraction and even though high mass loading, particle-particle interactions can be neglected. For this assumption in Fluent to remain valid, particle volume loading should be under 10-12%. This simplifies the calculation of trajectories and saves computational time.

Fluid and discrete phase can be treated in coupled or uncoupled fashion. In coupled simulation, particles are progressed through the fluid phase after selected number of time steps. Fluid phase affects particles due to drag force, but particles affect fluid phase by exchange of momentum too.

This results into particles influencing fluid phase. In uncoupled simulation, particle loading effects on fluid phase are neglected. Particle tracking is then requested in post-processing and its main purpose is to display particle tracks. This approach is selected due to its lower computational cost.

Steady particle tracking is selected. In this scheme, particles are released from defined boundary condition surface. Particles are then tracked until they reach their final destination specified by additional boundary conditions or until maximum number of steps allowed for tracking is reached. When this happens, Fluent stops calculating particular trajectory and the fate of the particle is flagged as incomplete. Limit on maximum number of steps is used to treat particles that are captured in recirculation zones, otherwise their trajectories would be calculated indefinitely.

9.9.1 Equations of motion for particles

Trajectories of particles in Lagrangian reference frame are calculated by integrating force balance on particle. This formula equates forces acting on particle with the particle inertia.

$$\frac{d\overrightarrow{u_P}}{dt} = F_D(\vec{u} - \overrightarrow{u_P}) + \frac{\vec{g}(\rho_P - \rho)}{\rho_P} + \vec{F} \tag{9.26}$$

Where $\vec{u}$ is fluid phase velocity, $\overrightarrow{u_P}$ is particle velocity,$\vec{g}$ is gravitational acceleration,$F_D(\vec{u} - \overrightarrow{u_P})$ represent drag force per unit particle mass (function of the relative velocity) and $\vec{F}$ represents additional acceleration (force/unit particle mass).This term can include for example pressure gradient, thermophoretic force, Brownian motion, Saffman lift, rotating reference frame, etc. Moving reference frame model is employed for a steady state approximation of rotation of rotor and therefore $\vec{F}$ term on the right-hand side of force balance equation includes forces arising due to rotation of this reference frame. Drag force is calculated as.

$$F_D = \frac{18\mu C_D R_e}{24\rho_P d_P^2} \tag{9.27}$$

Where μ is molecular viscosity, ρ_P is density of particle, d_P is diameter of particle, C_D is drag coefficient and R_e is relative Reynolds number.

$$Re = \frac{\rho d_P |\vec{u}_P - \vec{u}|}{\mu} \tag{9.28}$$

9.9.2 Spherical drag law

Spherical and non-spherical approach to drag law is considered. Difference in between them is the way the drag coefficient is calculated. Drag coefficient is a dimensionless number and spherical drag law coefficient is calculated as:

$$C_D = a_1 + \frac{a_2}{Re} + \frac{a_3}{Re^2} \tag{9.29}$$

Where $a_1,\ a_2,\ a_3$ are constants that apply for smooth spherical particles over several ranges of Re given by Morsi and Alexander [59].

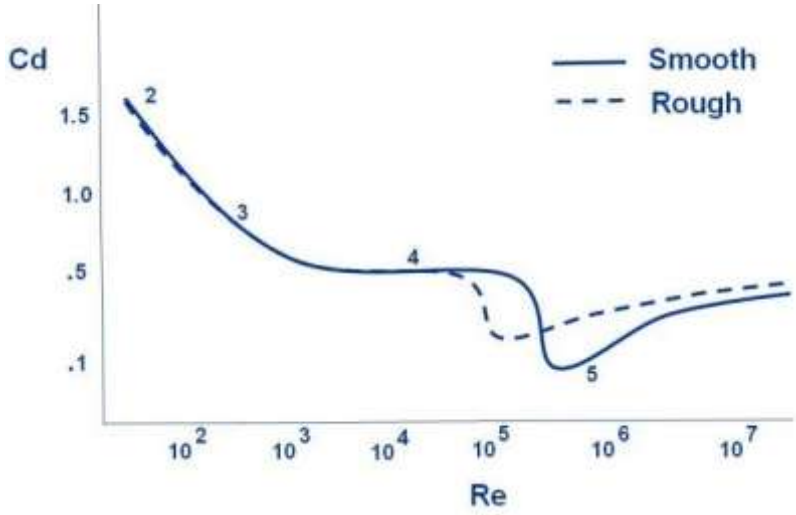

Figure 136Drag of a sphere [60]

It can be observed in Figure 136 that for a smooth spherical particle, drag coefficient varies significantly with Reynolds number. It can be seen that the drag coefficient achieves highest values for small Reynolds number. Drag force for sub-micron particles is then formulated as Stokes drag law.[61]

$$F_D = \frac{18\mu}{C_c \rho_P d_P^2} \tag{9.30}$$

Where C_c represents Cunningham correction factor to Stokes drag law and it is calculated as:

$$C_c = 1 + \frac{2\lambda}{d_P}\left(1.257 + 0{,}4e^{-\left(\frac{1.1 d_P}{2\lambda}\right)}\right) \tag{9.31}$$

Where λ represents molecular mean free path.

9.9.3 Non-spherical drag law

Haider and Levenspiel developed correlation for non-spherical particles. [62]

$$C_D = \frac{24}{Re_{SPH}}\left(1 + b_1 Re_{SPH}^{b_2}\right) + \frac{b_3 Re_{SPH}}{b_4 Re_{SPH}} \tag{9.32}$$

Where Re_{SPH} is the Reynolds number calculated with diameter of sphere having the same volume and the $b_1,\ b_{2,}\ b_3,\ b_4$ coefficients are calculated as follows:

$$b_1 = exp\ (2{,}3288 - 6{,}4581\phi + 2{,}4486\phi^2) \tag{9.33}$$

$$b_2 = 0{,}0964 + 0{,}5565\phi \tag{9.34}$$

$$b_3 = exp\,(4{,}905 - 13{,}8944\phi + 18{,}4222\phi^2 - 10{,}2599\phi^3) \tag{9.35}$$

$$b_3 = exp\,(1{,}4681 + 12{,}2584\phi - 20{,}7322\phi^2 + 15{,}8855\phi^3) \tag{9.36}$$

Where ϕ is the shape factor which is described as ratio between surface area „s“ of sphere which has the same volume as the particle and actual surface area of the particle „S“. For a theoretical sphere it reaches its maximum value of unity.

$$\phi = \frac{s}{S} \tag{9.37}$$

Shape factor for material used in experimental part is estimated to be 0,72 with respect to [63]

9.9.4 Turbulent dispersion of particles

Stochastic tracking model is included to predict dispersion of particles due to turbulence in the fluid flow. If the flow is turbulent, Ansys Fluent by default predicts trajectories of particles based on mean velocities of fluid phase. Discrete random walk model includes effects of turbulent velocity fluctuations on individual particle trajectories. These effects are accounted for along the particle trajectory during the integration. Eddies are characterized by Gaussian distributed random velocity fluctuations and a time scale. Number of tries is selected as ten which means that trajectory is computed ten times. Each trajectory now contains new stochastic representation of fluctuating velocity contribution to the trajectory.

9.9.5 Rosin Rammler distribution

In order to introduce particle size distribution data from experimental part into Ansys Fluent, this data needs to be formulated as Rosin Rammler distribution equation. This distribution assumes that there is an exponential relation between particle diameter and mass fraction of particles with diameter greater than d,Yd.

$$Y_d = e^{-(\frac{d}{\bar{d}})^n} \tag{9.38}$$

Where $\bar{d}$ represents mean diameter, d is particle diameter, n is spread diameter and Y_d represents mass fraction. Mean diameter is obtained from particle size distribution analysis and its value is 17,323 μm. Spread diameter is then calculated as:

$$n = \frac{ln\,(-lnY_d)}{ln\,(\frac{d}{\bar{d}})} \tag{9.39}$$

Numerical value of spread diameter is then obtained as average value of calculated spread diameters. Its value is calculated as 1,07. In the discrete phase model, input parameters required are first and last diameter of the distribution, mean diameter, spread diameter, mass flow rate and injection velocity. Particle distribution fitted to Rosin Rammler equation and measured data are shown in Figure 137

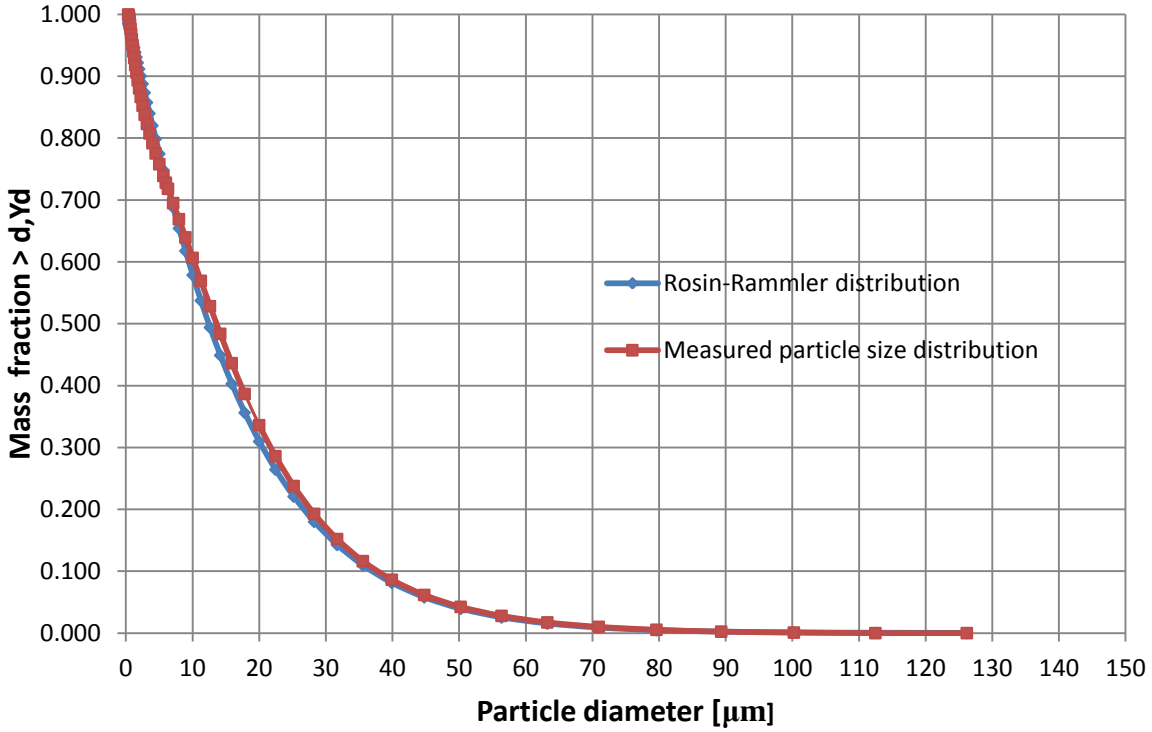

Figure 137 Measured particle size distribution and Rosin Rammler distribution

Table 31Particle size distribution and Rosin Rammler distribution

DIA	Yd	PSD	SD	DIA	Yd	PSD	SD	DIA	Yd	PSD	SD	DIA	Yd	PSD	SD
[µm]	%>d	%>d	n	[µm]	%>d	%>d	n	[µm]	%>d	%>d	n	[µm]	%>d	%>d	n
0.36	0.986	1.000	2.371	1.59	0.931	0.906	0.970	6.33	0.720	0.718	1.097	28.25	0.180	0.193	1.019
0.40	0.985	0.999	1.926	1.78	0.922	0.894	0.961	7.10	0.688	0.695	1.133	31.70	0.143	0.152	1.048
0.45	0.982	0.998	1.662	2.00	0.912	0.880	0.954	7.96	0.654	0.669	1.173	35.57	0.110	0.116	1.065
0.50	0.980	0.994	1.449	2.24	0.900	0.867	0.951	8.93	0.618	0.640	1.217	39.91	0.081	0.086	1.074
0.56	0.977	0.989	1.326	2.52	0.888	0.853	0.952	10.02	0.579	0.607	1.267	44.77	0.058	0.062	1.078
0.63	0.974	0.983	1.235	2.83	0.874	0.838	0.955	11.25	0.537	0.569	1.329	50.24	0.039	0.043	1.080
0.71	0.971	0.976	1.169	3.17	0.858	0.823	0.963	12.62	0.494	0.528	1.419	56.37	0.025	0.028	1.080
0.80	0.967	0.969	1.117	3.56	0.840	0.808	0.975	14.16	0.449	0.484	1.587	63.25	0.015	0.017	1.080
0.89	0.963	0.960	1.077	3.99	0.820	0.792	0.991	15.89	0.403	0.436	2.161	70.96	0.009	0.010	1.080
1.00	0.958	0.950	1.044	4.48	0.799	0.775	1.012	17.83	0.356	0.387	1.782	79.62	0.005	0.005	1.081
1.13	0.952	0.940	1.020	5.02	0.775	0.758	1.037	20.00	0.310	0.336	0.602	89.34	0.002	0.003	1.091
1.26	0.946	0.930	0.999	5.64	0.748	0.739	1.065	22.44	0.264	0.286	0.868	100.24	0.001	0.001	1.101
1.42	0.939	0.918	0.983	6.00	0.733	0.728	1.082	25.18	0.221	0.238	0.968	112.47	0.000	0.000	1.187
												126.19	0.000	0.000	1.118

9.10 BOUNDARY CONDITIONS

In order to compute a unique solution to a problem a set of physical boundary conditions is defined. These include information about known or approximated flow variables at the boundaries of fluid domain. Inlet and outlet locations for fluid phase are identified and corresponding boundary conditions are assigned. Boundary conditions for discrete phase are defined at dedicated locations.

9.10.1 Velocity inlet

Rectangular inlet surface of the swept duct joining bottom section of the classifier tangentially is identified as a velocity inlet and it is the entry of fluid phase into the domain. Turbulence at this boundary is considered insignificant when compared to domain and therefore the calculation is relatively insensitive to inflow values. Dimensions of the inlet are 154x100mm and hydraulic diameter is calculated in order to specify uniform turbulence intensity at this boundary. Direction of the velocity is specified as normal to boundary. Numerical simulation is carried out with three different inlet velocities to simulate different fan speeds. Effects of these changes on flow field and particle trajectories are then evaluated. Discrete phase model boundary for this surface is set to reflect, even though in real scenario particles will never terminate trajectory on this surface.

Table 32Velocities defined at velocity inlet boundary conditions

Fan [Hz]	Inlet velocity [m/s] for classifier mot.fr. [Hz]				
	30	35	40	45	50
30	18.32	16.84	15.26	13.15	11.6
40	20.1	18.92	17.83	16.48	15.27

9.10.2 Pressure outlet and Outflow

Outlet boundary of fluid phase and fine particles of discrete phase is identified as annulus surface at the top of the classifier. Both pressure outlet and outflow boundary condition were used in early stages of the simulation. Outflow boundary condition is used when values of pressure and velocity are not known prior to calculation. It applies a zero-diffusion flux condition for flow variables at the boundary and therefore assumes no impact on upstream flow. Extrapolated outflow velocity and pressure take form of a fully developed flow. This is a type of flow where velocity profile does not change in the direction of flow. Pressure outlet requires value of static pressure at the boundary. Backflow conditions were prescribed due occurrence of reverse flow at this boundary. The reversed flow is caused by rotation of rotor and centrifugal force acting on an element of fluid. This is essentially a principle of a fan, in this case inefficient fan acting against the main fan which develops velocity and pressure in the system and determines flow direction. In order to minimize reversed flow at the pressure outlet boundary, outlet domain fluid zone would have to be extended to guarantee a fully developed from at the outlet boundary. This would however increase number of elements and consequently increase computational cost. Boundary condition for discrete phase at this surface is specified as escaped. Trajectory calculation of all the particles that come to contact with this surface is terminated and their fate is reported as escaped.

9.10.3 Internal body and outlet domain

Stationary wall boundary condition is defined for internal body and outlet domain. Boundary condition for discrete phase is set to reflect. Particles that come to contact with these surfaces are reflected back into the domain. Specification method for tangential coefficient of restitution is set to be constant value of 0,8. Normal coefficient of restitution is selected to be constant and its value is set to 0,2. Coefficients of restitution represent change in particle momentum after rebounding off the boundary.

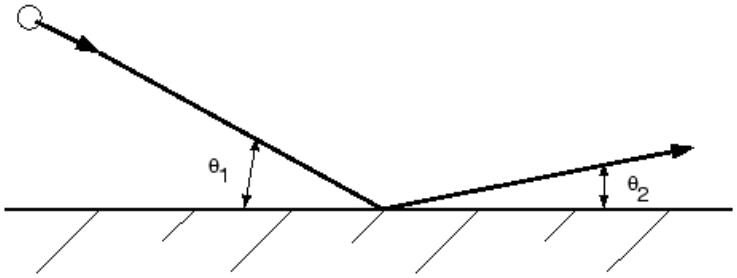

Figure 138 Reflect boundary condition for discrete particles

$$e_n = \frac{v_{2n}}{v_{1n}} \tag{9.40}$$

Where e_n represent normal coefficient or restitution and it defines the amount momentum preserved after collision, v_{2n}represents normal component of particle velocity after collision and v_{1n}represents normal component of particle velocity before collision. Tangential coefficient of restitution is defined similarly.

9.10.4 Feed inlet

Circular surface at the top face of the classifier body is identified as feed inlet and is prescribed a stationary wall boundary condition. Contact between fluid phase and this boundary is treated in fluid phase-wall manner. Injection of powder material is specified at this surface with respect to Rosin Rammler distribution which was introduced in previous chapter. Particles are injected into domain from surface centroids at prescribed injection velocity of 5 meters per second. Due to turbulent nature of the flow and its diffusive effects, discrete phase boundary condition is specified as reflect. Particles that come to contact with this surface after being injected into the domain are reflected back into the domain. Specification method for tangential and normal coefficients of restitution is selected to be constant and their value is set to 0,9.

9.10.5 Coarse outlet

Circular surface at the bottom of the classifier body is identified as coarse outlet and is prescribed a stationary wall boundary condition. Contact between fluid phase and this boundary is treated in fluid phase-wall manner. Boundary condition for discrete phase at this surface is specified as trapped. Trajectory calculations of all the particles that come into contact with this surface are terminated and their fate is reported as trapped.

9.10.6 Rotor blades zone

Cell zone located between internal body and the outlet zone is a rotor blade zone. Two interface surfaces are defined at this cylindrical zone where the first one is couples with internal body and the second one couples with outlet cell zone. In order to compute fluxes between different cell zones, interface definition is required by. Rotor cell zone is defined with rotating reference frame and this allows simulating rotation of the rotor. Three different rotor speeds are simulated in combination with different inlet velocities as shown in Table 33

Table 33Simulated rotor speeds

MOT. SUPP. FREQUENCY [Hz]	CLASSIFIER RPM [min^{-1}]	ANGULAR VELOCITY [rad/s]	TIP VELOCITY [m/s]
30	1785	186.92	25.23
35	2081	217.92	29.42
40	2380	249.23	33.65
45	2685	281.17	37.96
50	2975	311.54	42.06

Discrete phase boundary condition for the walls representing rotor blades is specified as reflect. Walls are defined by moving wall condition and a relative rotational speed between cell zone and walls is defined to be zero. Particles that come to contact with surface representing blade are reflected back into the domain. Specification method for tangential coefficient of restitution is set to be constant value of 0,8. Normal coefficient of restitution is constant and its value is set to 0,5.

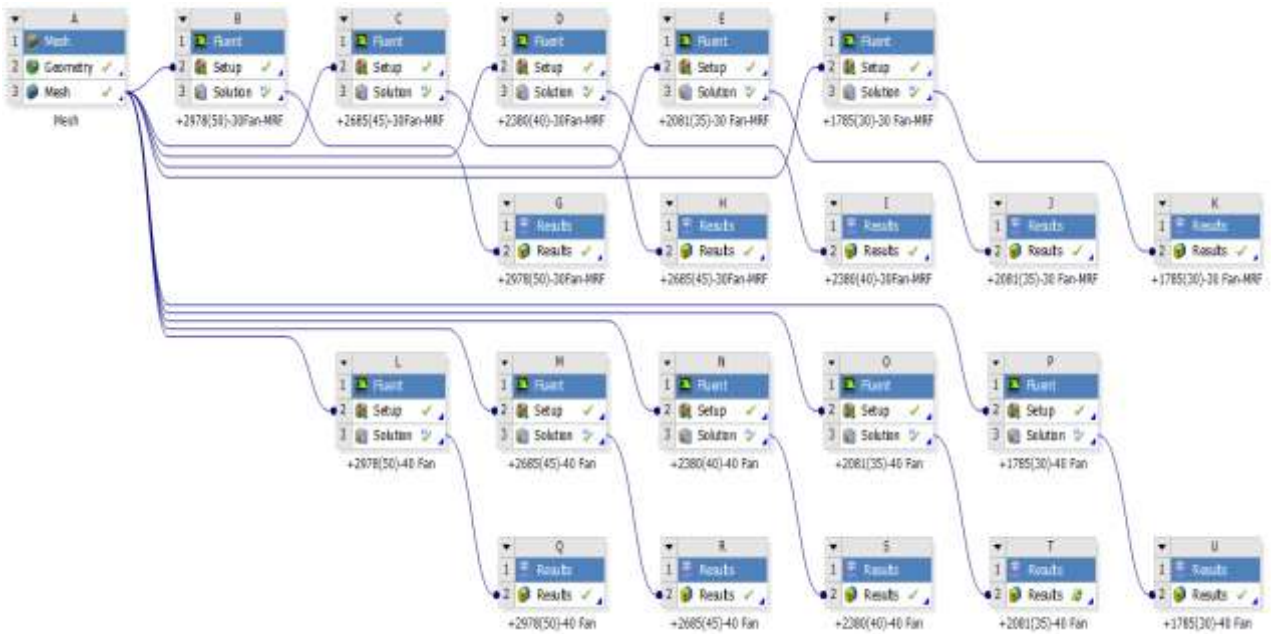

Figure 139 Project schematic

10 NUMERICAL SIMULATION RESULTS

Individual numerical simulations are carried out for total number of ten cases with varying operating parameters, namely fan and classifier rotor setting. Converged solutions of fluid phase are exported and further post-processed in CFD-POST where the main areas of interest are identified as rotor blades passageway, upper classifying chamber, lower classifying chamber and the inner cone throat. Flow structure is visualized by use of vector maps, positive and negative radial and axial velocity contours. Locations containing flow recirculation zones are illustrated together with velocity magnitudes.

10.1 RADIAL VELOCITY IN BLADE PASSAGEWAY

Grid of nine sampling lines is created over the blade passageway area in order to take readings of desired variables. Passageway selected for sampling is located at 45-degree inclination angle with air inlet duct centreline as this was the exact field of view of the camera in the experimental section. These lines are spaced at every 5 millimetres of passageway depth in the radial direction. Values of positive and negative radial velocity are then plotted across the grid of these lines where for displayed charts, positive component has inward direction. Contours of radial velocities and 3D streamlines for every set of parameters are presented below together with vector map overlay. 3D streamlines are released from internal body - rotor interface surface and are displayed only for the rotating domain and in a non-inertial frame of reference.

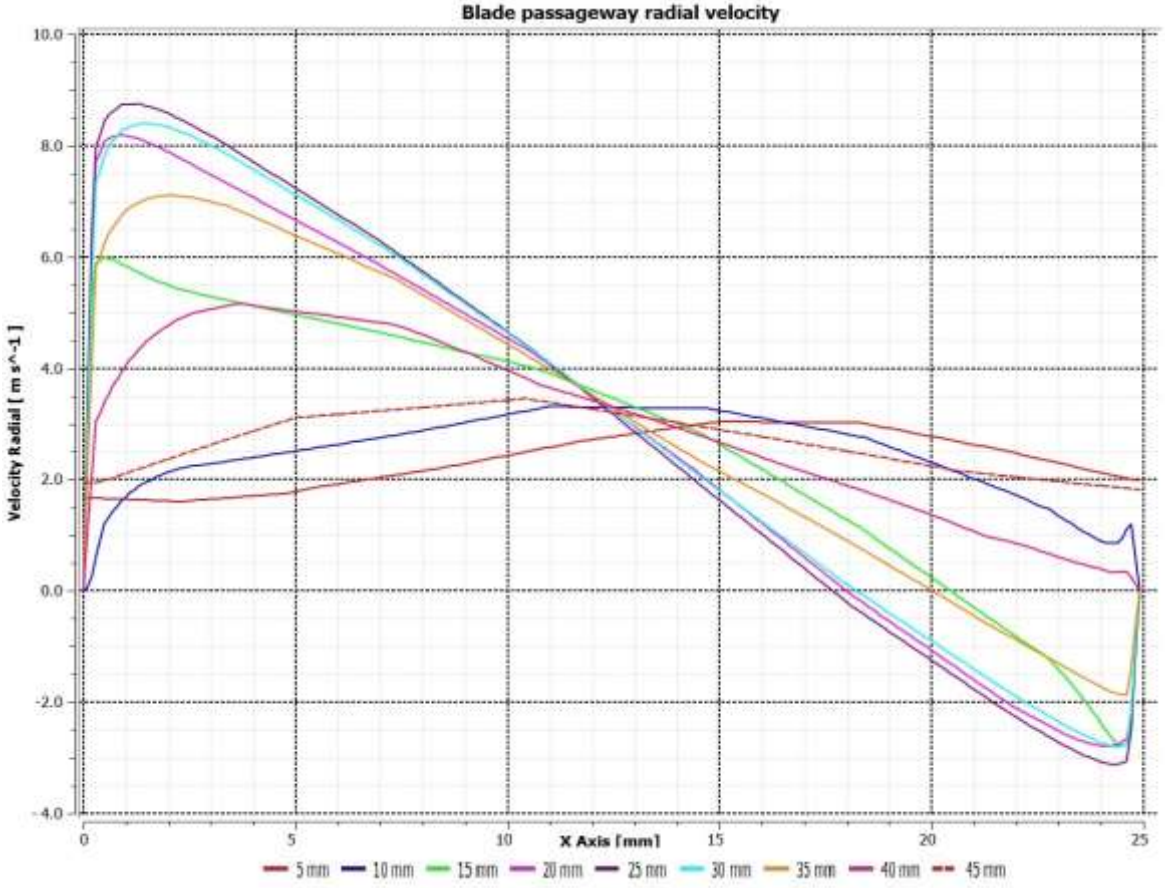

Figure 140 Radial velocity profiles for changing position in the blade passageway for 30f-30r setting

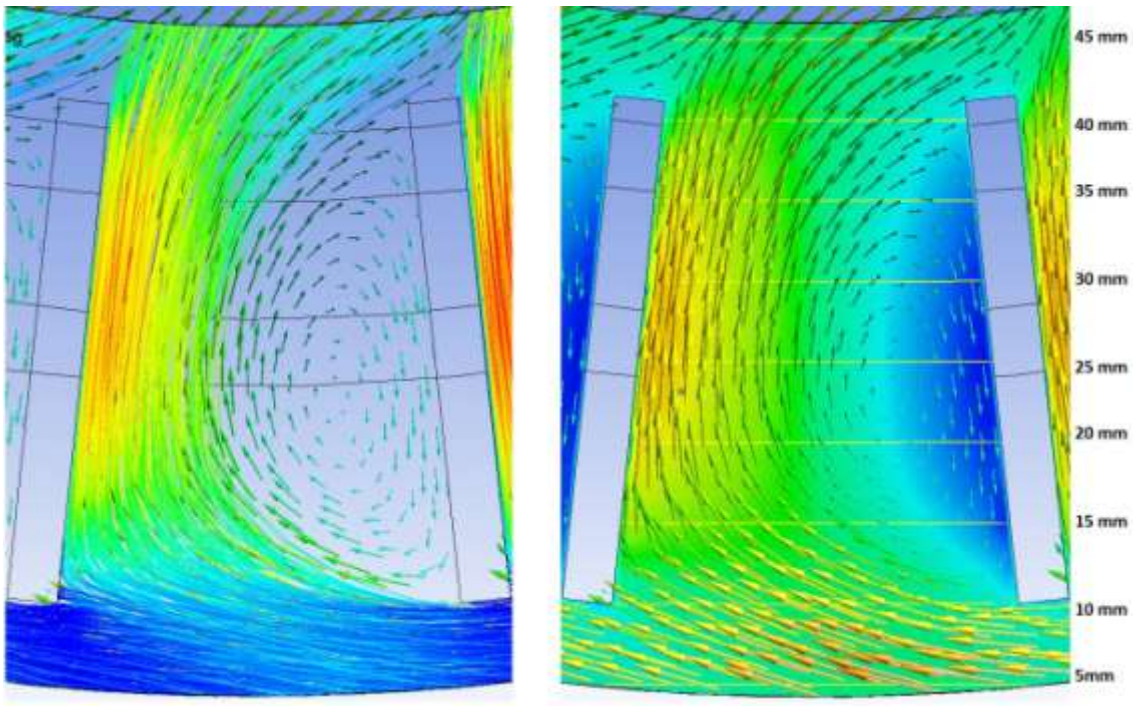

Figure 141 Vector map in examined plane overlaid by streamlines and radial velocity contour for 30f-30r setting

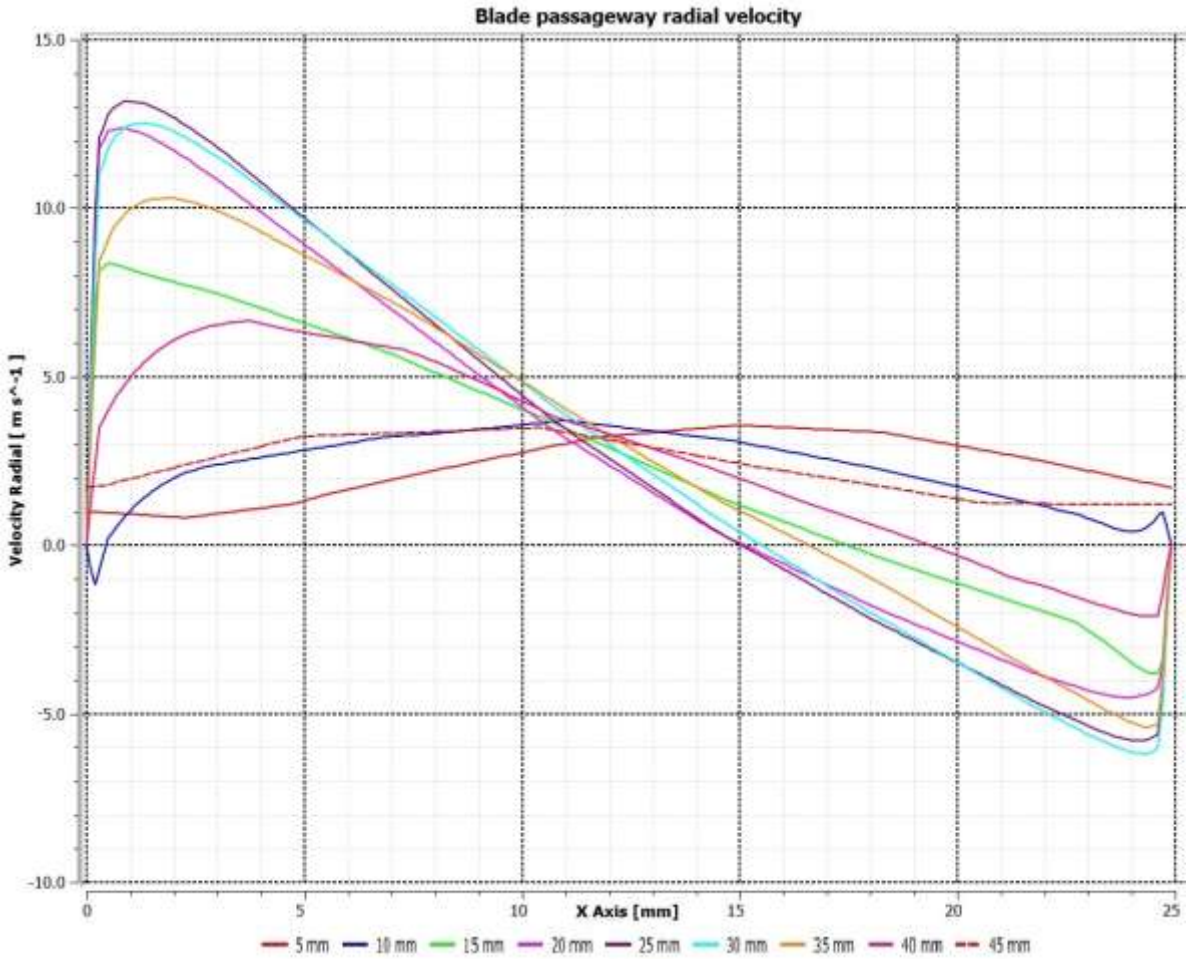

Figure 142 Radial velocity profiles for changing position in the blade passageway for 30f-35r setting

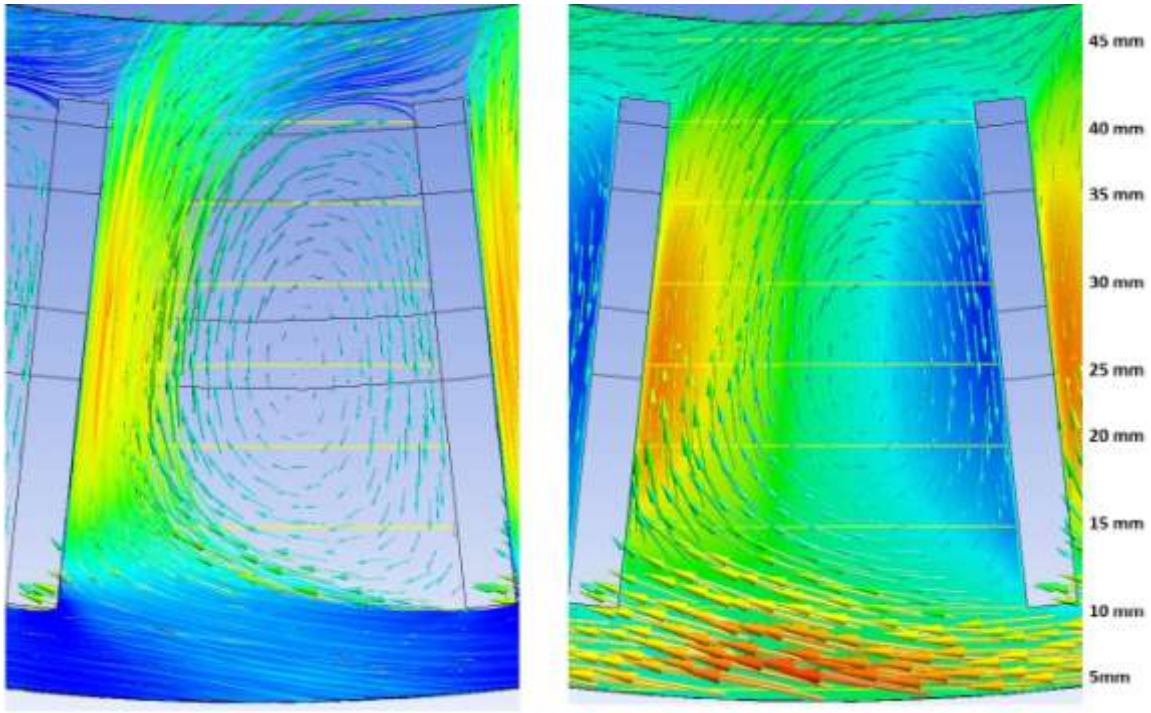

Figure 143 Vector map in examined plane overlaid by streamlines and radial velocity contour for 30f-35r setting

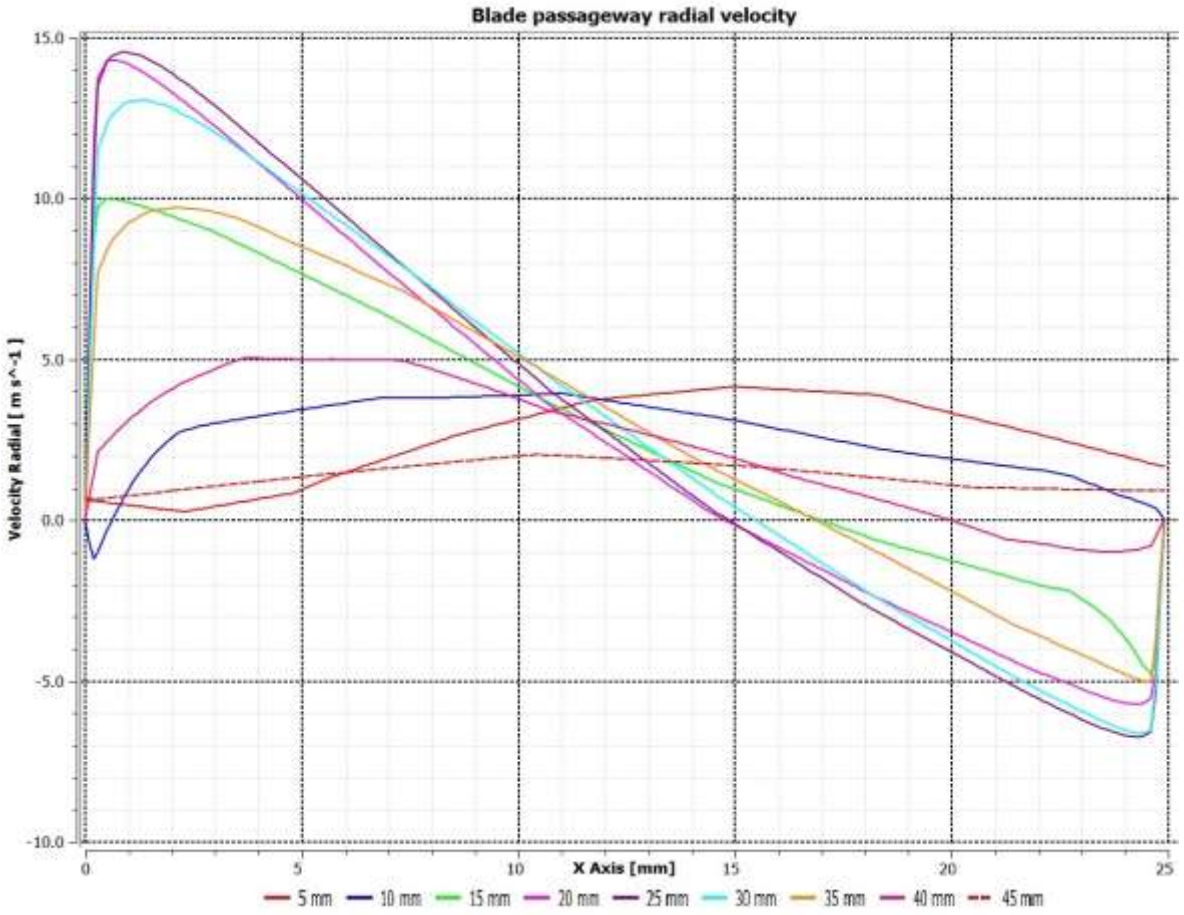

Figure 144 Radial velocity profiles for changing position in the blade passageway for 30f-40r setting

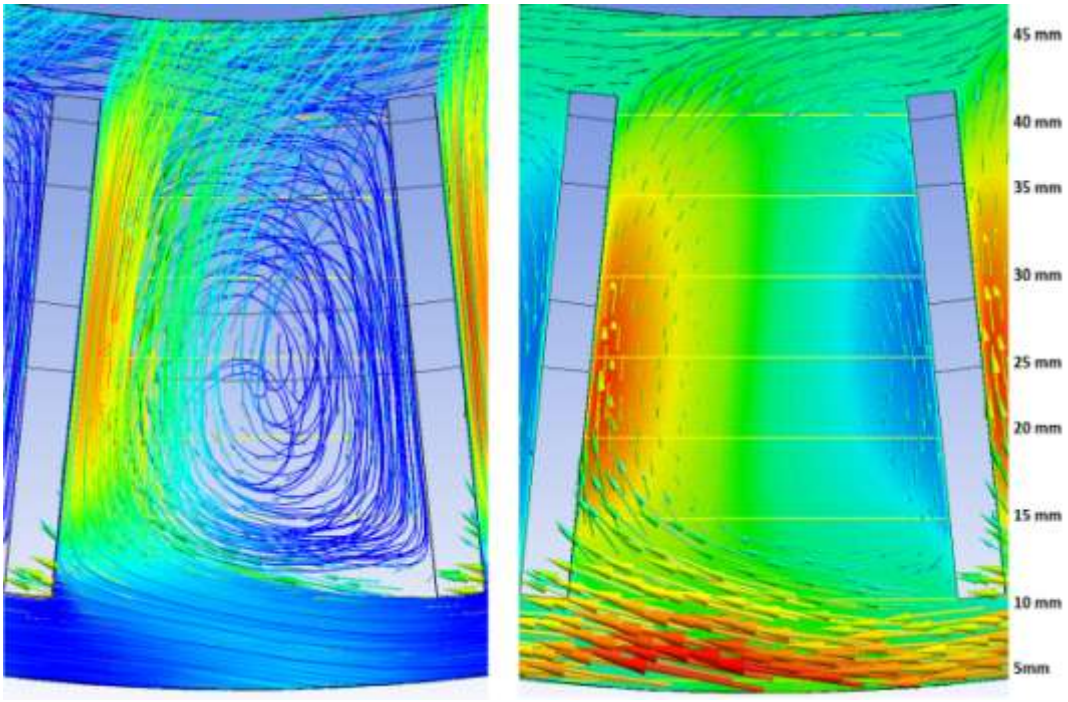

Figure 145 Vector map in examined plane overlaid by streamlines and radial velocity contour for 30f-40r setting

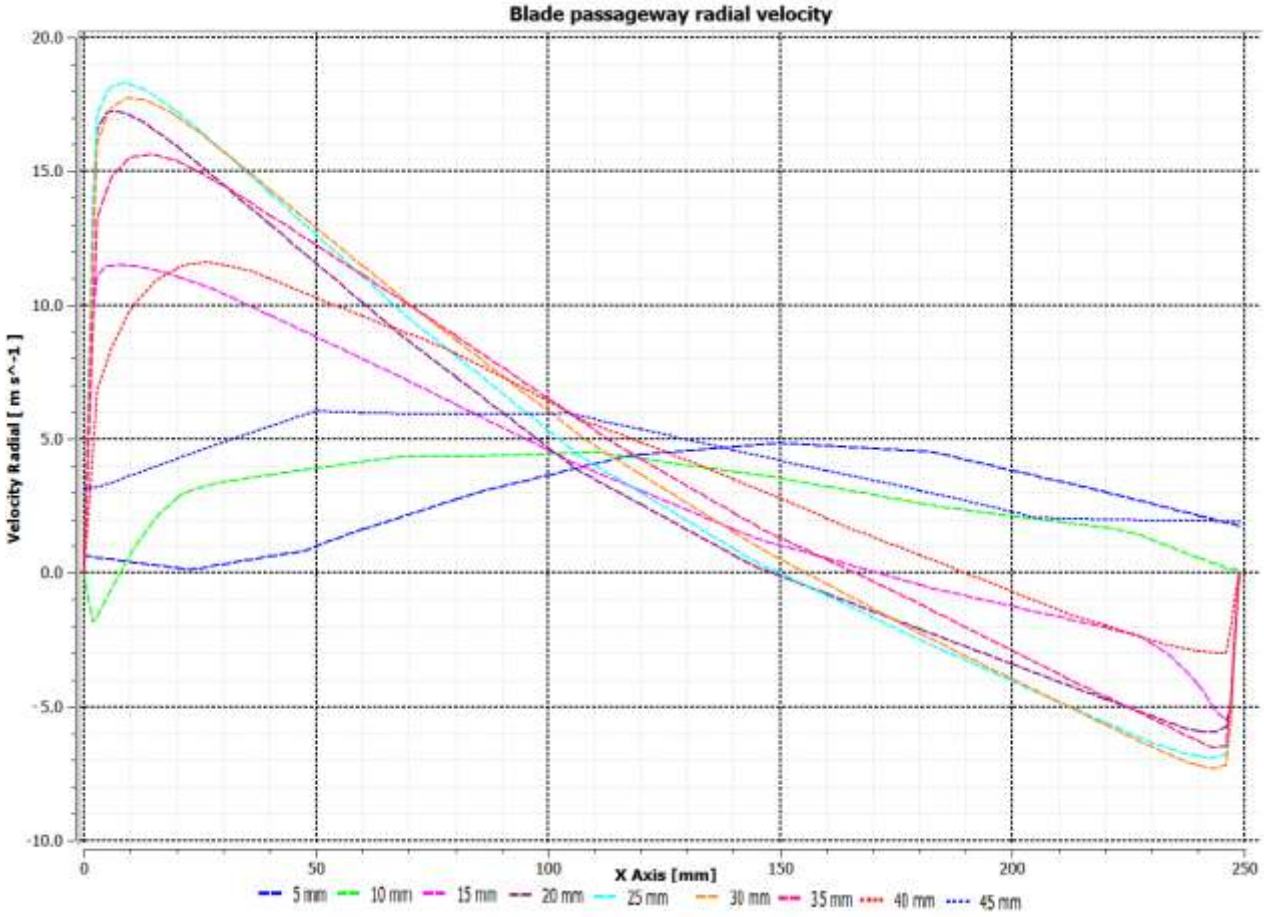

Figure 146 Radial velocity profiles for changing position in the blade passageway for 30f-45r setting

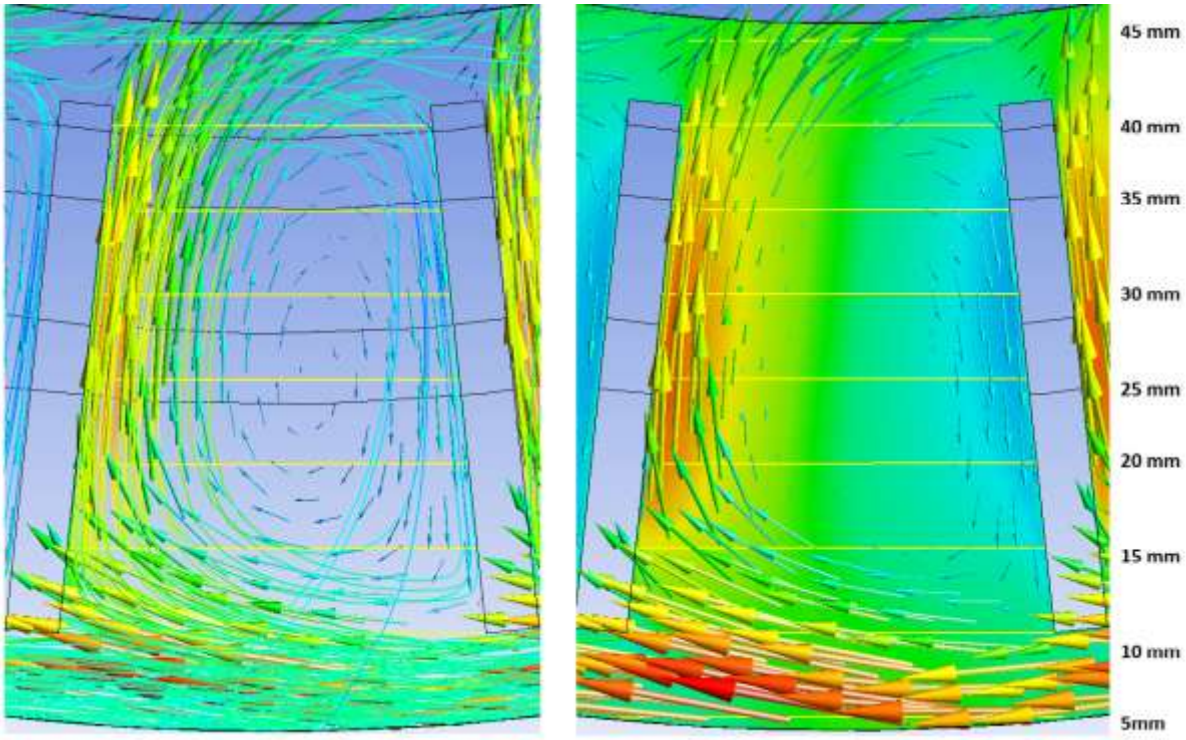

Figure 147 Vector map in examined plane overlaid by streamlines and radial velocity contour for 30f-45r setting

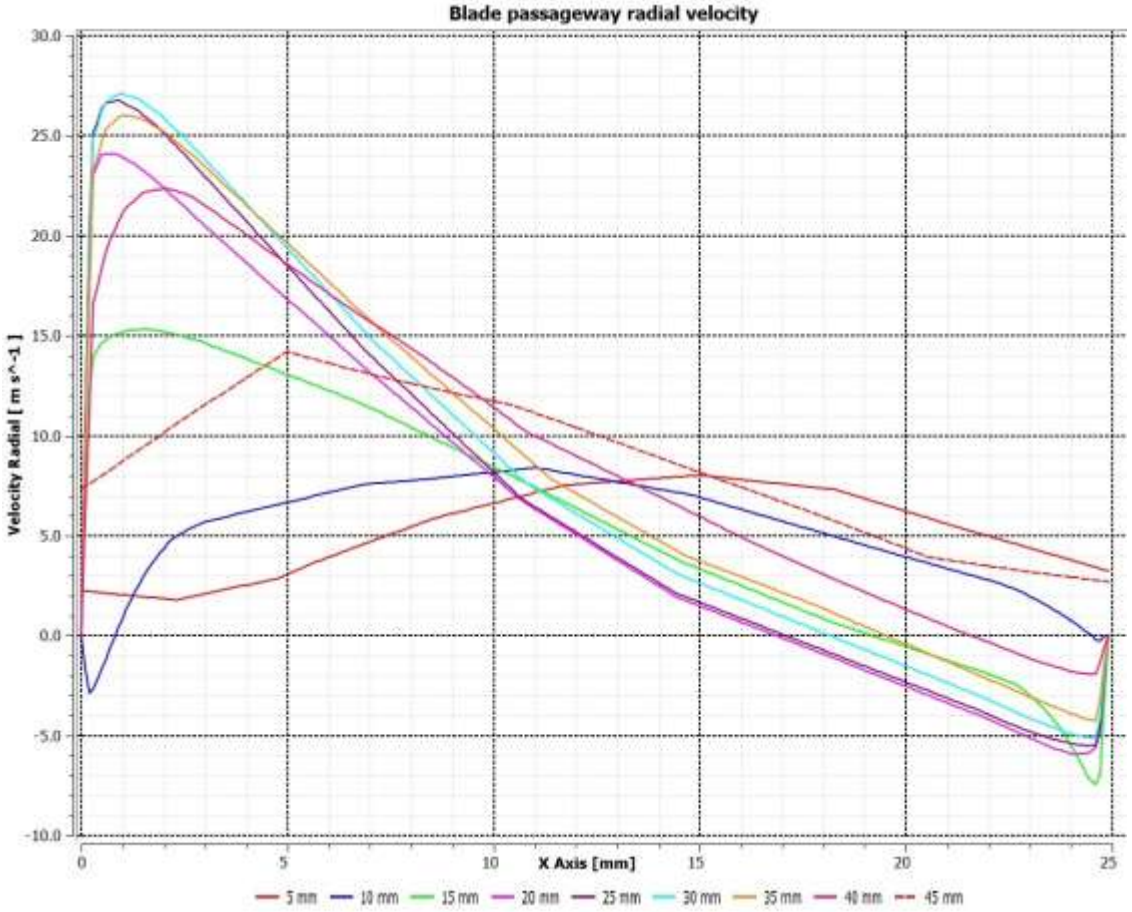

Figure 148 Radial velocity profiles for changing position in the blade passageway for 30f-50r setting

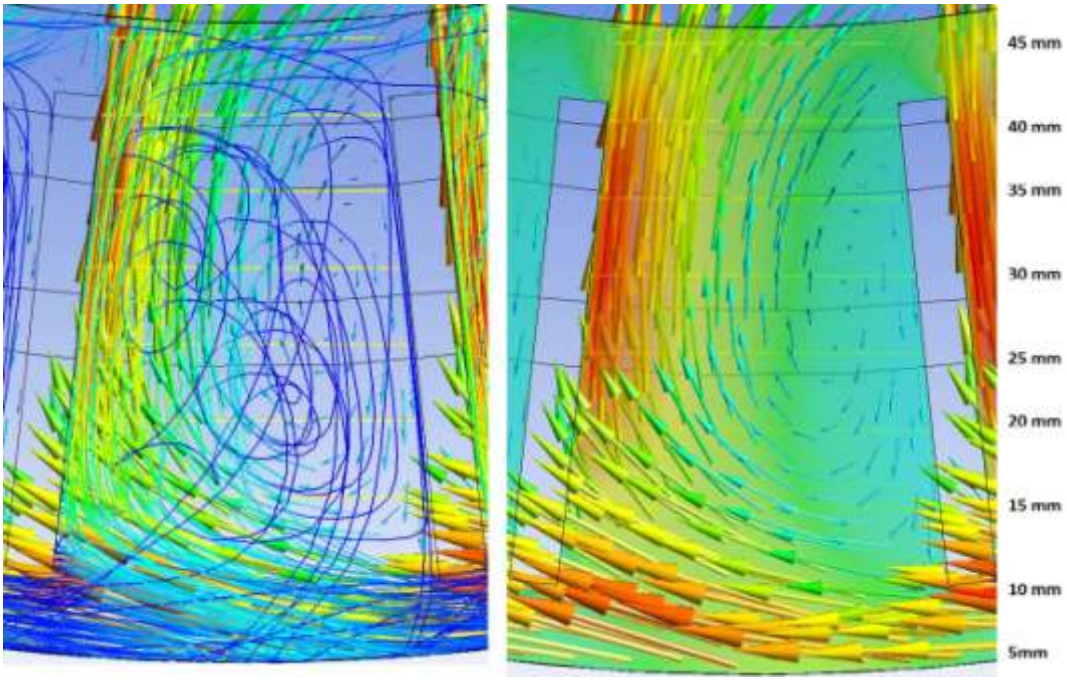

Figure 149 Vector map in examined plane overlaid by streamlines and radial velocity contour for 30f-50r setting

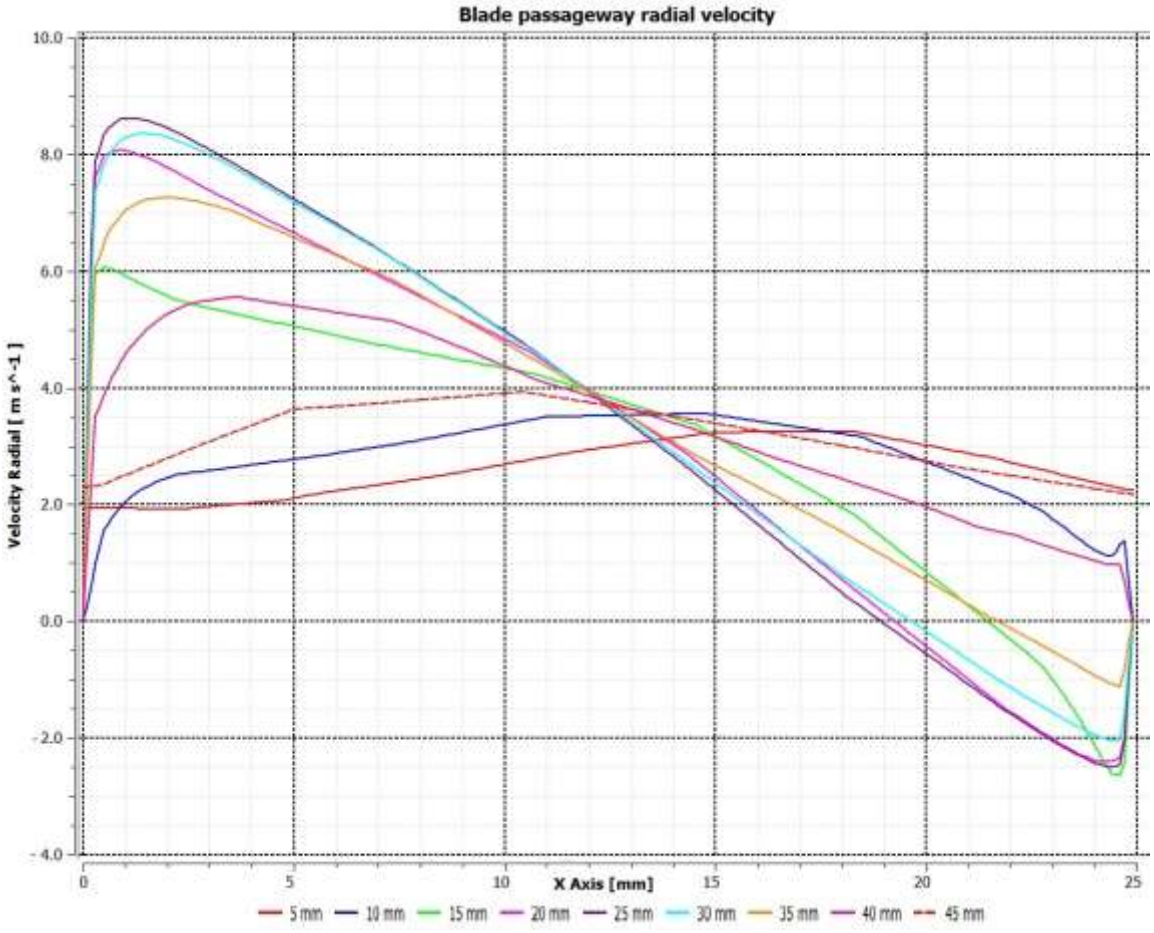

Figure 150 Radial velocity profiles for changing position in the blade passageway for 40f-30r setting

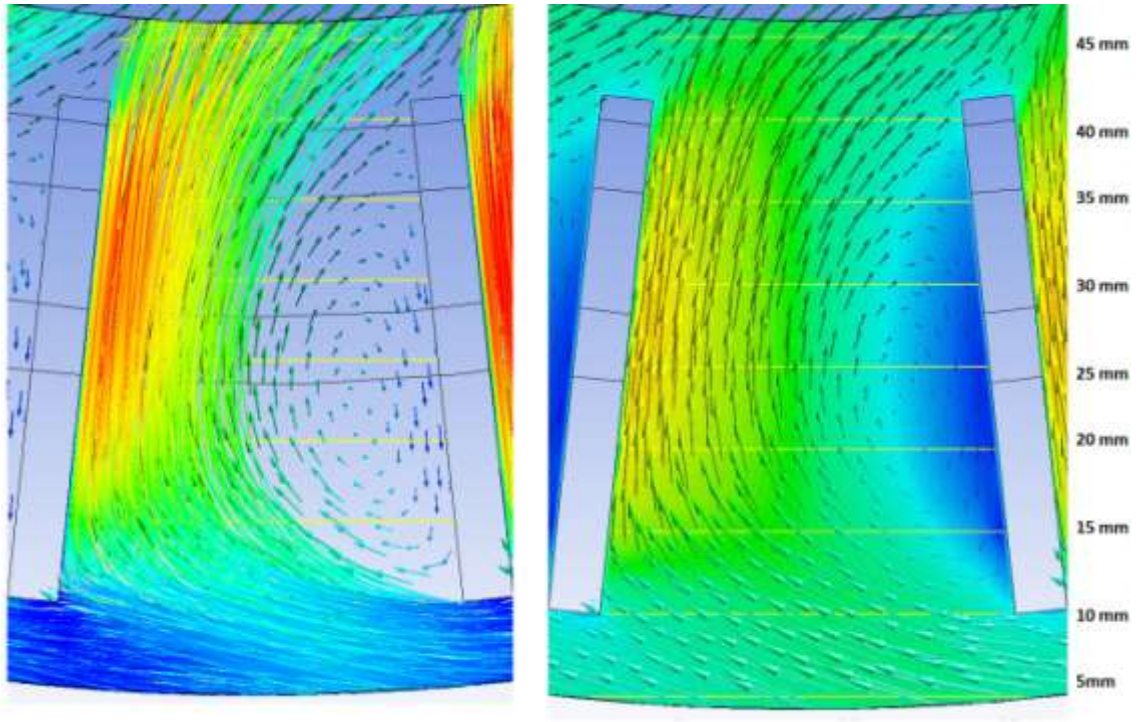

Figure 151 Vector map in examined plane overlaid by streamlines and radial velocity contour for 40f-30r setting

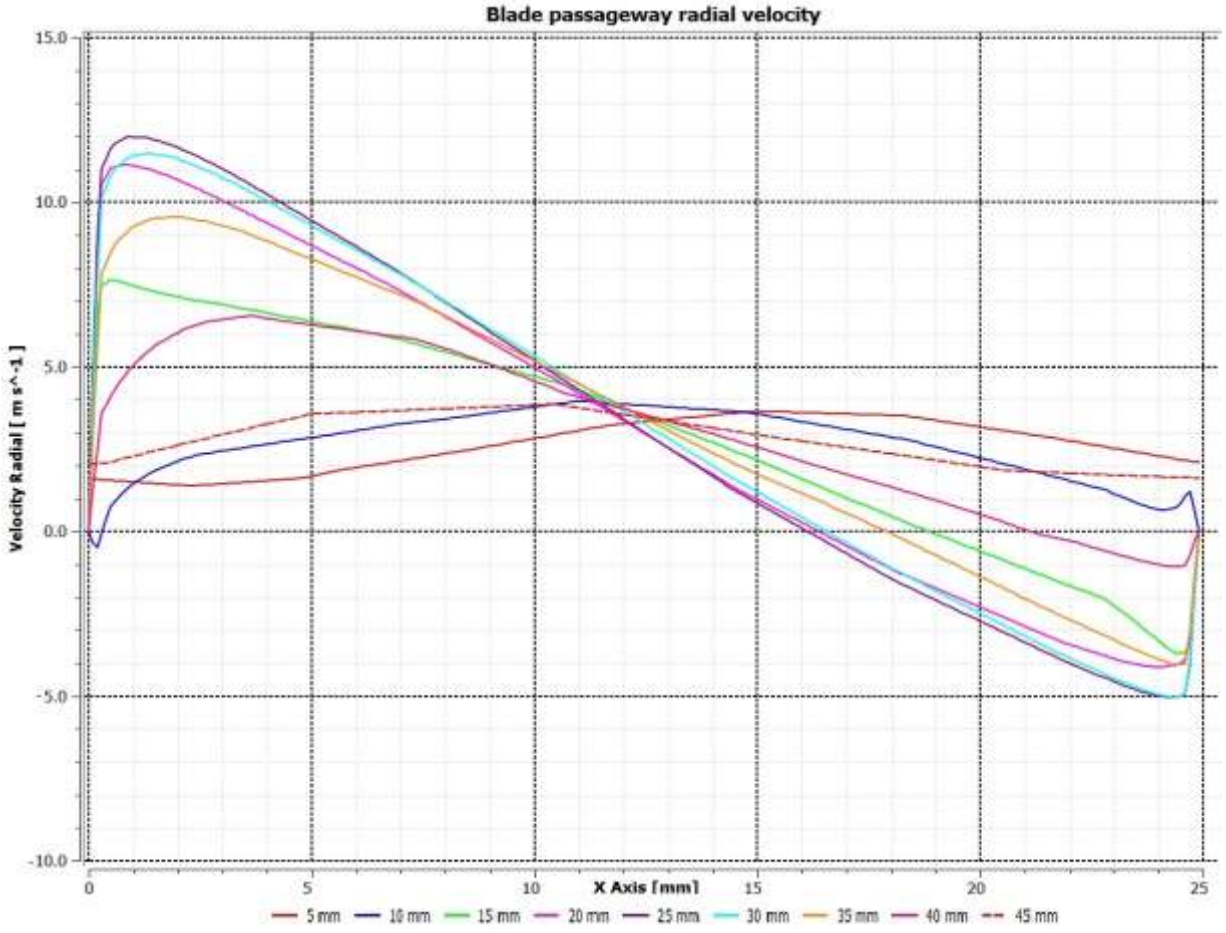

Figure 152 Radial velocity profiles for changing position in the blade passageway for 40f-35r setting

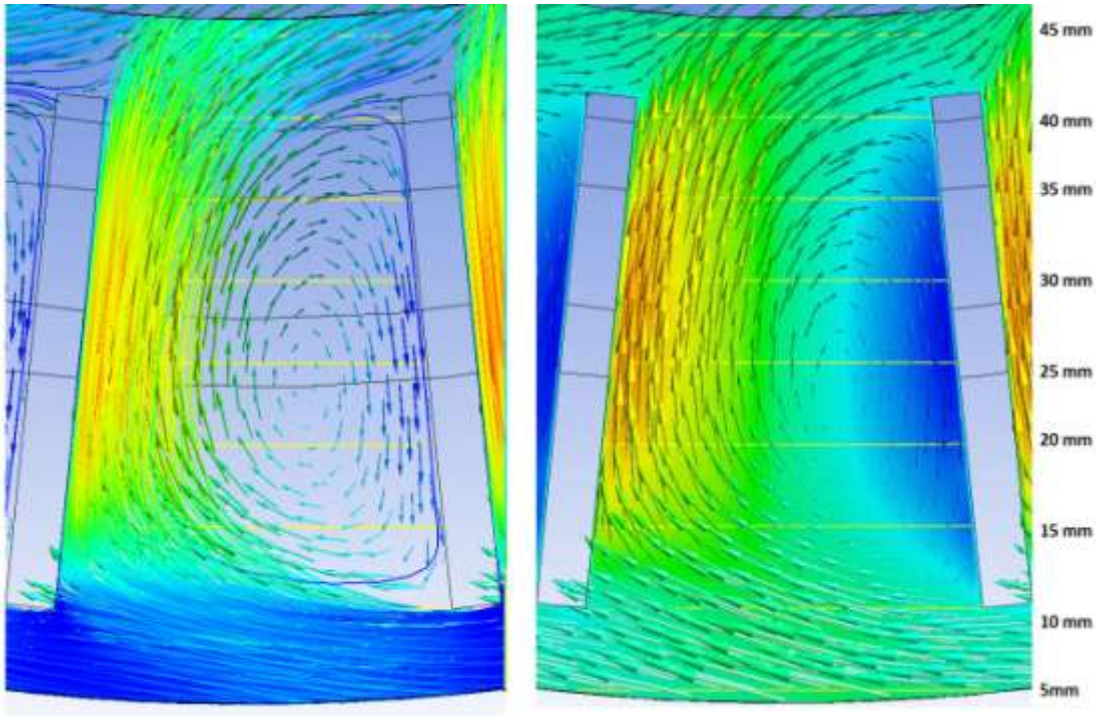

Figure 153 Vector map in examined plane overlaid by streamlines and radial velocity contour for 40f-35r setting

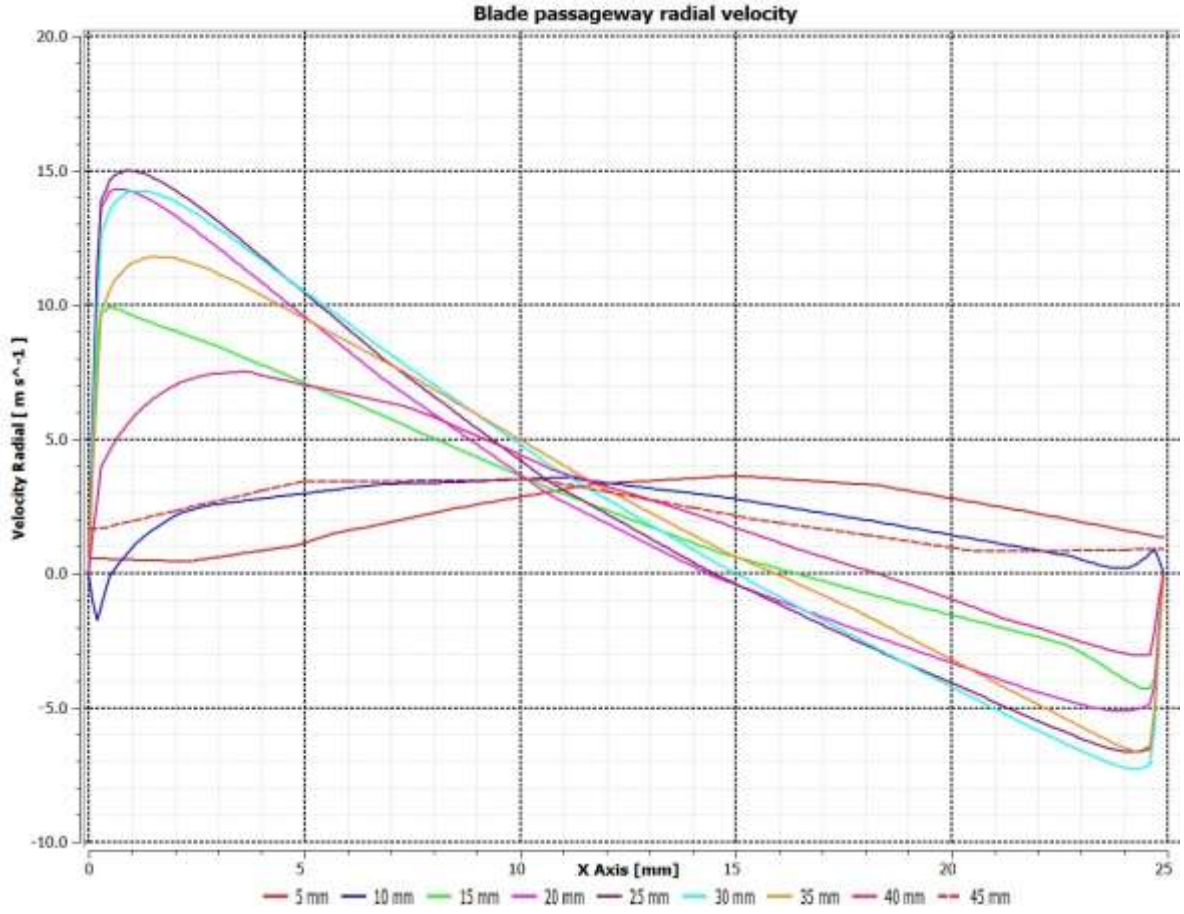

Figure 154 Radial velocity profiles for changing position in the blade passageway for 40f-40r setting

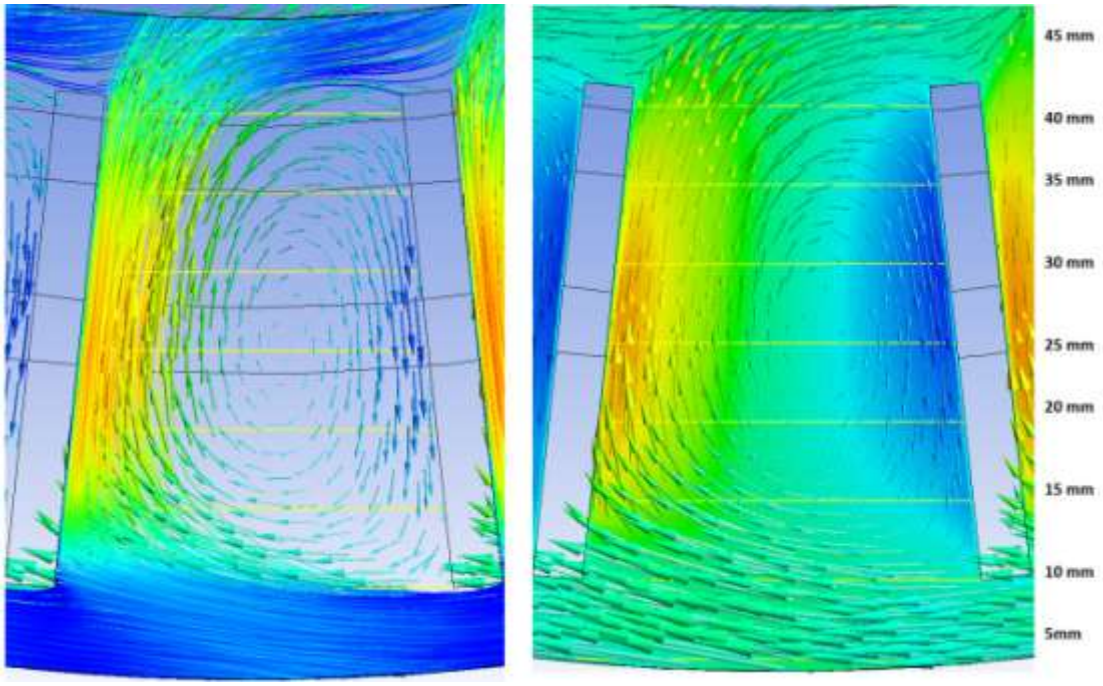

Figure 155 Vector map in examined plane overlaid by streamlines and radial velocity contour for 40f-40r setting

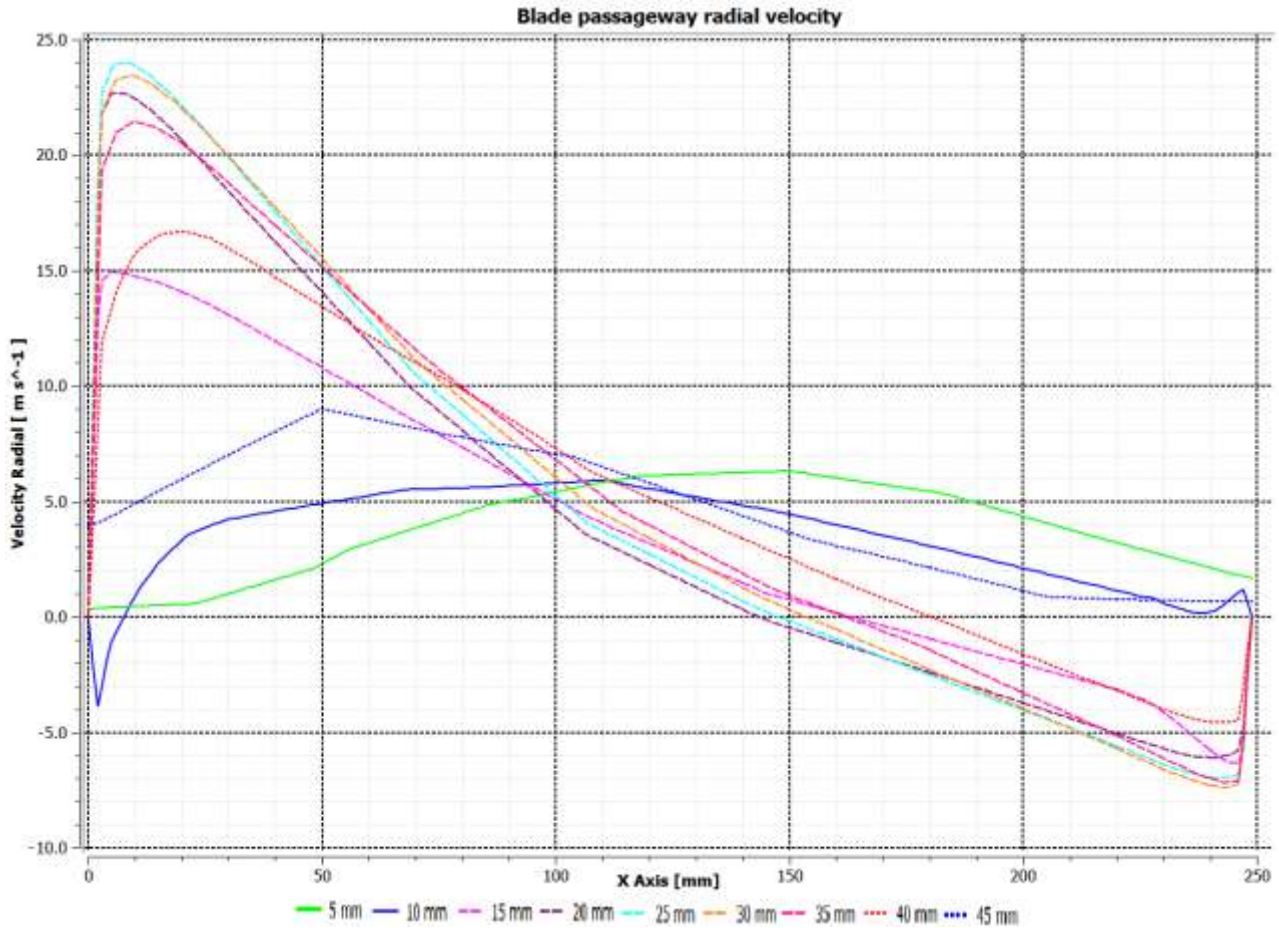

Figure 156 Radial velocity profiles for changing position in the blade passageway for 40f-45r setting

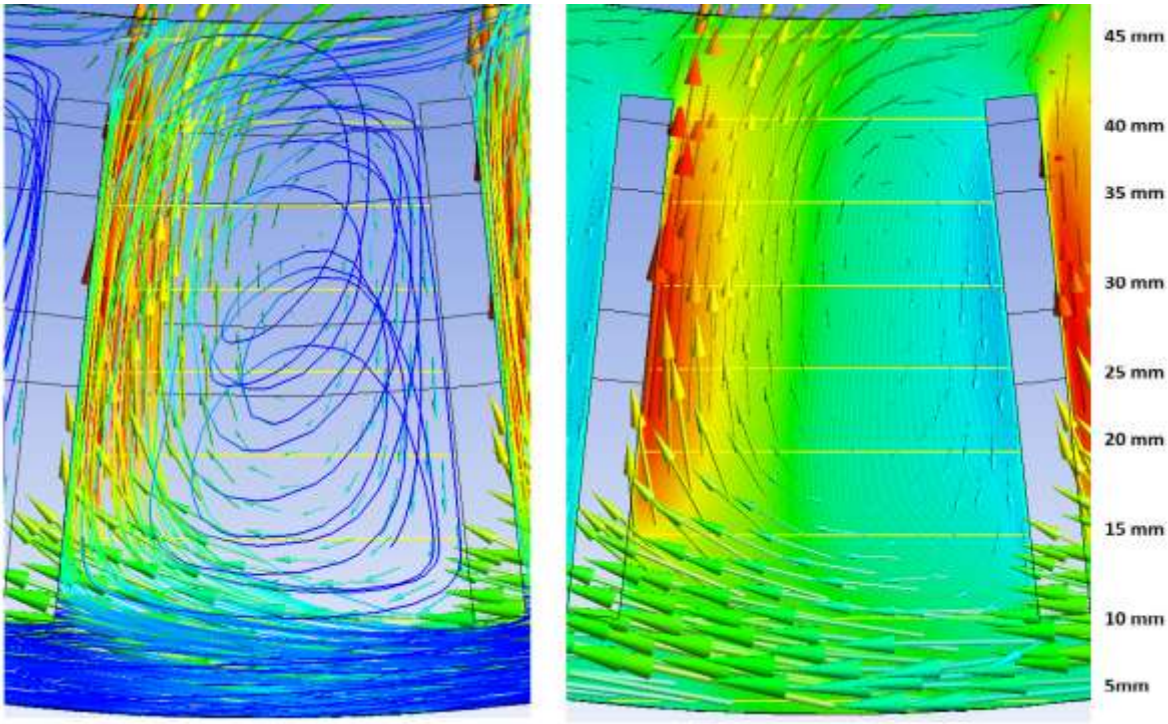

Figure 157 Vector map in examined plane overlaid by streamlines and radial velocity contour for 40f-45r setting

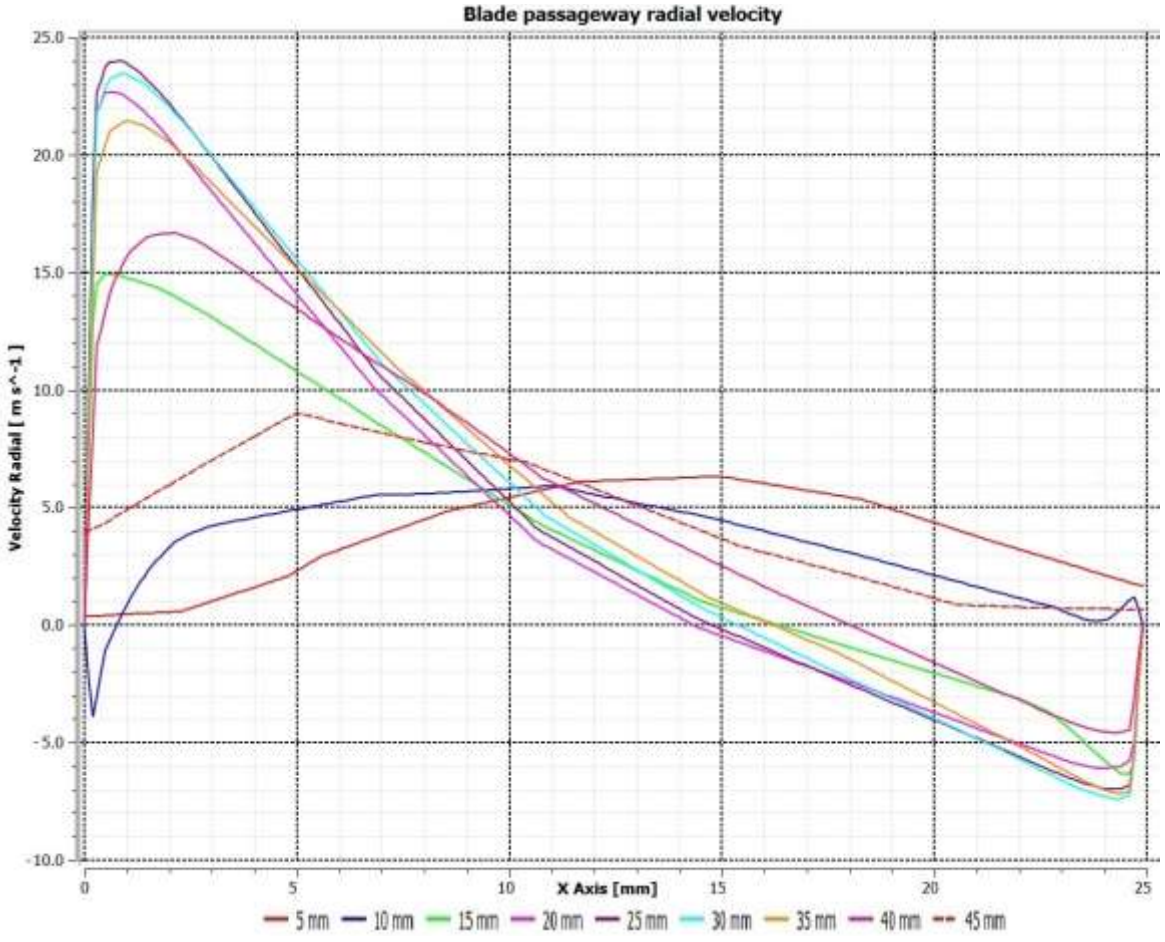

Figure 158 Radial velocity profiles for changing position in the blade passageway for 40f-50r setting

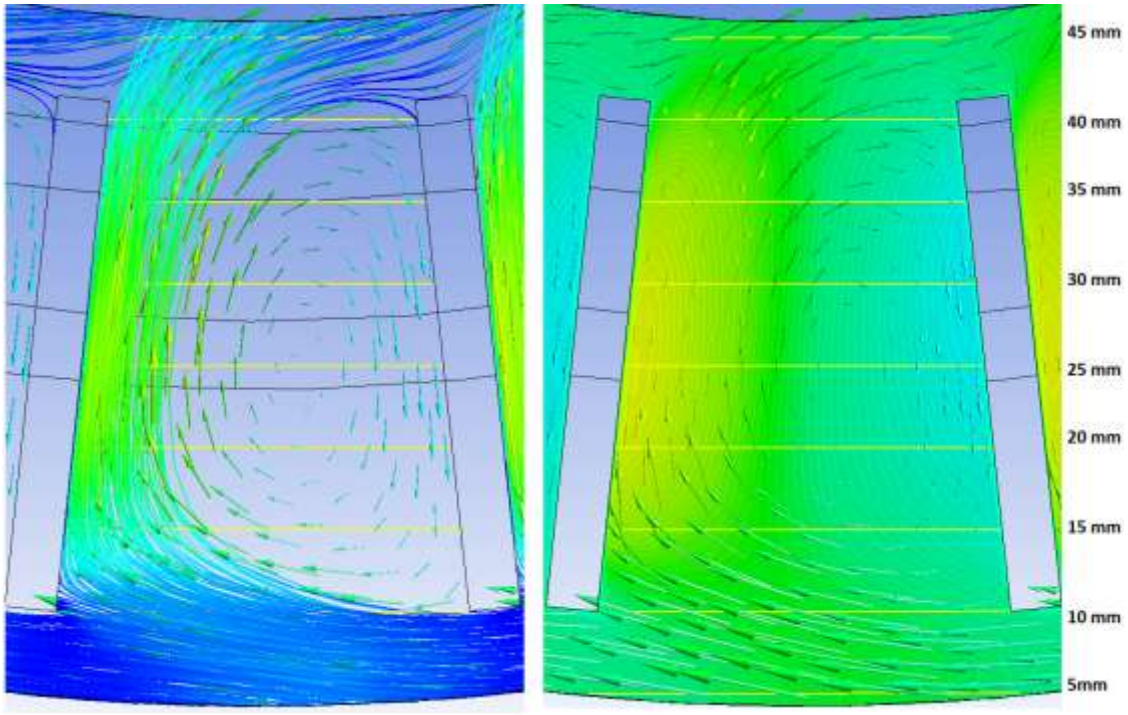

Figure 159 Vector map in examined plane overlaid by streamlines and radial velocity contour for 40f-50r setting

10.2 COMPARISON &SUMMARY OFNUMERCIAL RESULTS

Two sets with 30 Hz and 40 Hz fan setting with five simulations in each set for varying rotor speed were carried out. It can be observed that for all the ten cases with anti-clockwise rotor rotation (Figure 140-Figure 159), the numerical simulation predicts formation of vortex in the area behind the leading blade. Positive radial velocity is relatively low at the inlet to blade passageway and this can be attributed to swirling nature of the flow in the cylindrical body of the classifier. This flow regime is defined by high tangential velocities and low radial velocities. It can be seen that as the airflow enters the geometrically radial blade passageway, the tangential velocity component diminishes and the radial component becomes major. All the contours below (in individual planes) are displayed in their local ranges instead of global in order to allow more visual distinction of local flow patterns.

Table 34 Positive and negative radial velocities on sampling lines obtained in numerical simulation

ROTOR SPEED [Hz]	30 Hz FAN		40 Hz FAN	
	POSITIVE	NEGATIVE	POSITIVE	NEGATIVE
30	8.75	-3.12	8.61	-2.65
35	13.18	-6.19	11.7	-4.97
40	14.57	-6.73	15.01	-7.31
45	18.3	-7.37	23.87	-7.4
50	27.08	-8.36	24.06	-7.62

Maximum and minimum radial velocities observed on sampling lines are displayed in Table 34. The radial velocity component of the airflow is further increased due to presence of the recirculation vortex behind the leading blade which restricts flow area in the blade passageway. As the airflow exits the passageway, its radial component becomes minor whilst the tangential component increases. In several cases it was observed that streamlines which exited blade passageway then repeatedly re-entered the following passageway. This is a negative factor as the streamlines represent lines with tangents always parallel to local velocity and therefore mean that some of the air is re-circulating in an undesired pattern.

In all the cases the radial velocity in the area right behind the leading blade is negative with outwards direction. This is a negative factor as the airflow magnitude and direction is one of the two major variables determining fates of the particles. It can be observed that the eye of the vortex is approximately in the centre of the blade passageway.

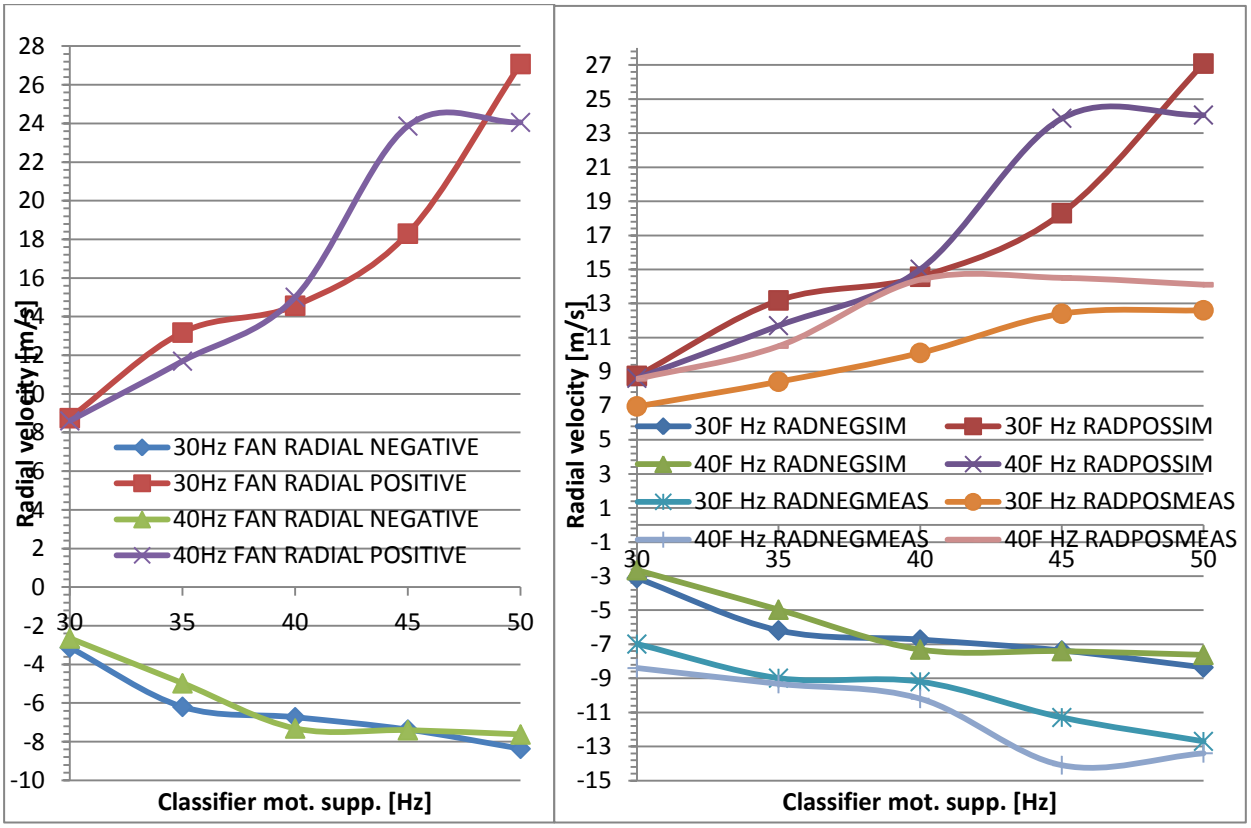

Figure 160 Simulated positive and negative radial velocity and comparison with measured data

Figure 160 shows values of radial velocities obtained from the numerical simulation and their comparison to values obtained by PIV measurement. Numerical simulation correctly predicts increasing magnitude of both positive and negative radial velocity with increasing rotor speed. The actual magnitudes do vary considerably due to several reasons. It has been found out that radial velocity profiles in different blade passageways vary with geometrical position of the passageway with relation to other geometrical realities and design of the classifier. It has been observed that from total number of 30 passageways, 15 of them were described by more profound vector field with higher velocities whilst the other half of the rotor had radial velocities significantly lower.

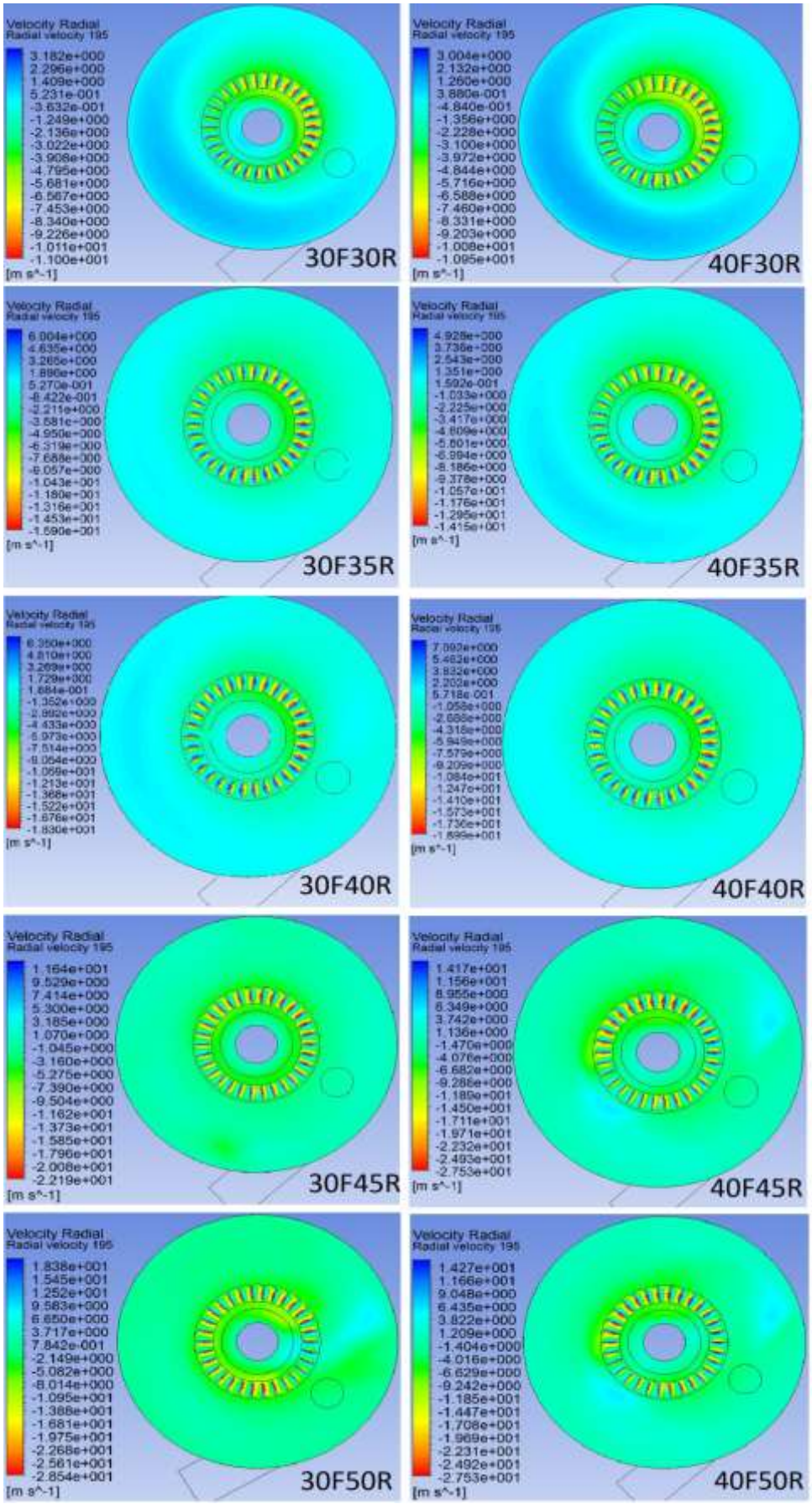

Figure 161 Contours of radial velocity at horizontal plane through rotor

Figure 161 shows contours of radial velocity of all the ten simulated cases. It can be seen that intensity of radial velocity changes with relation to angular position. This can be noticed not only in the rotor domain but also in the internal body flow domain.

This phenomenon has been discovered at all the ten simulations and the author sees several possible explanations for this:

a) Due to high computational cost, the meshing method and size of the control volumes of the mesh for the numerical simulation were optimized in such a way, that the elements are as large as possible whilst maintaining reasonable mesh quality criteria. The elements are not small enough for complex geometrical design of the classifier to form a completely structured mesh. Therefore, some numerical dispersion errors may be introduced into the results, where the numerical solution oscillates around the true solution.

b) Due to high computational cost, all the calculations were carried out as steady simulations and the action of rotor was modelled as a steady state approximation by use of multiple reference frame model. It is possible that the problem is due to turbulence by nature transient and that transient simulation is required to describe changing flow field in the classifier.

c) It was originally assumed that the three-dimensional flow field between classifier inner cone and rotor is pre-dominantly symmetric axially where the considered axis of symmetry was axis of rotation. The three-dimensional model in this section of the classifier is axially symmetric with exception of the discrete phase injection surface. This is however only a surface and not a 3D feature. Also, the coupling between particles and fluid phase was switched off and therefore particles are not responsible for this behaviour.

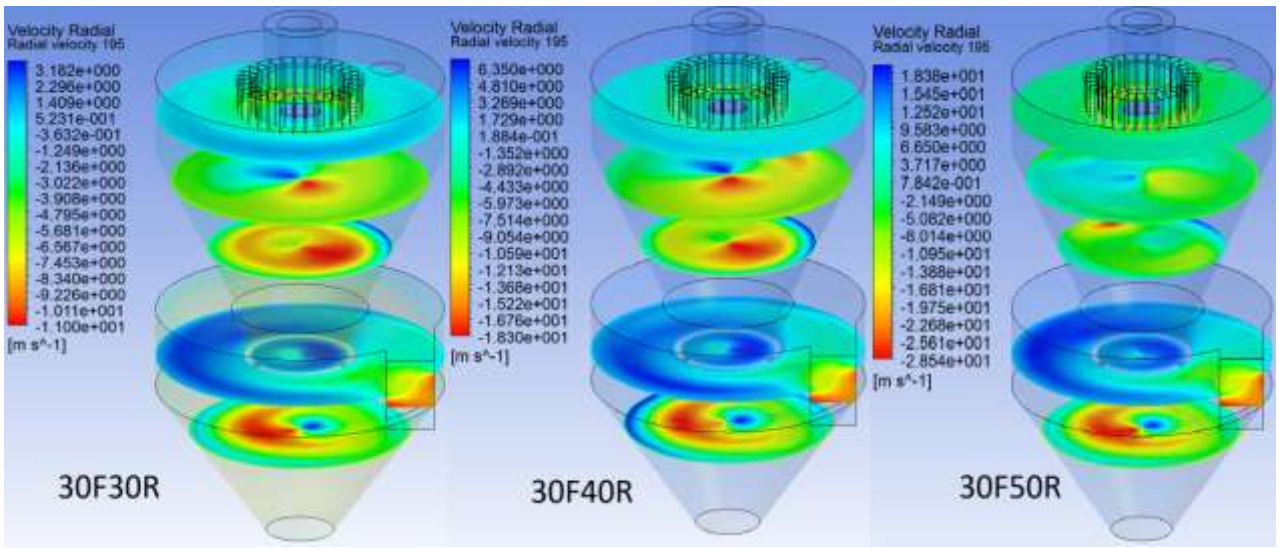

Figure 162 Radial velocity contours for selected settings on horizontal planes at different levels

Contours of radial velocity for selected settings can be seen in Figure 162 and Figure 163. For all the below presented figures, positive radial velocity has outward direction. It has been established that the axis of rotation of the swirling flow, even though in cylindrical body, is not concentric with axis of the cylindrical body. Position of the axis of rotation is affected by two factors. First and dominant factor is identified as lip leakage. Bottom section of the classifier has tangential air inlet connected to outlet of the centrifugal fan. The tangential inlet creates swirling

flow pattern in the bottom section of the classifier which is separated from the top section by the inner cone. It was observed that the throat of the inner cone leaks the air into the top section in a specific location. This location further determines position of the axis of the rotation of the swirling flow and consequently determines which half of the classifier top body contains mainly positive and which mainly negative components of radial velocity. These patterns are distinctive mainly in the area under the rotor.

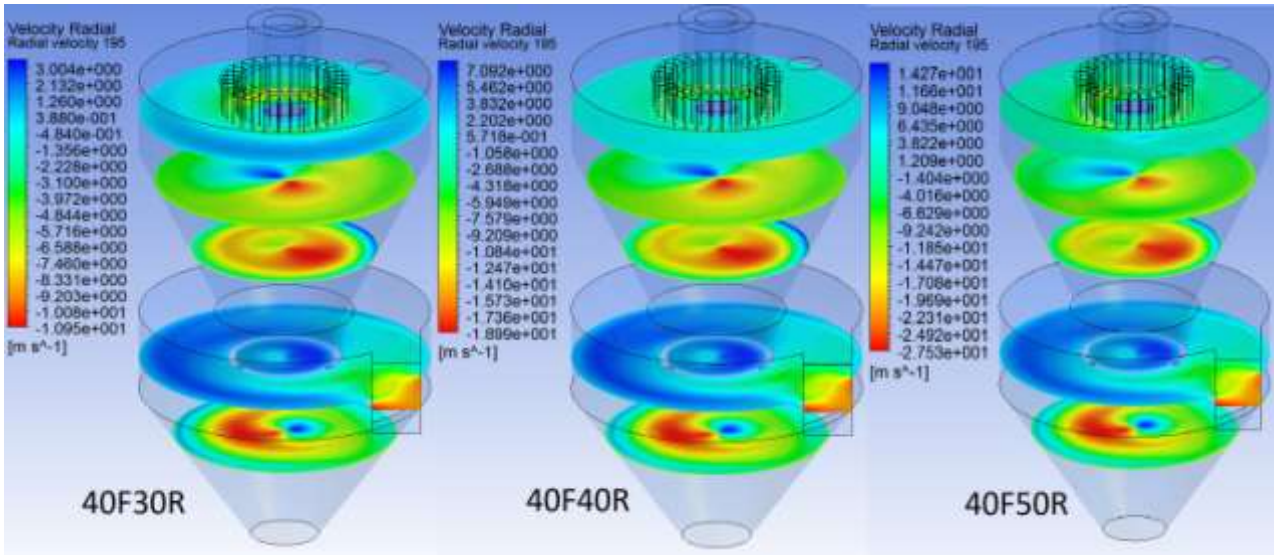

Figure 163 Radial velocity contours for selected settings on horizontal planes at different levels

Second factor affecting spatial position of the axis of rotation is angular velocity of the rotor. Action of the rotor breaks this pattern apart. This can be noticed mainly in the vertical section of the classifier where the rotor is present. It was observed that increasing rotor speed decreases intensity and the difference between positive and negative component. Furthermore, it centralizes axis of the rotation of the swirling flow.

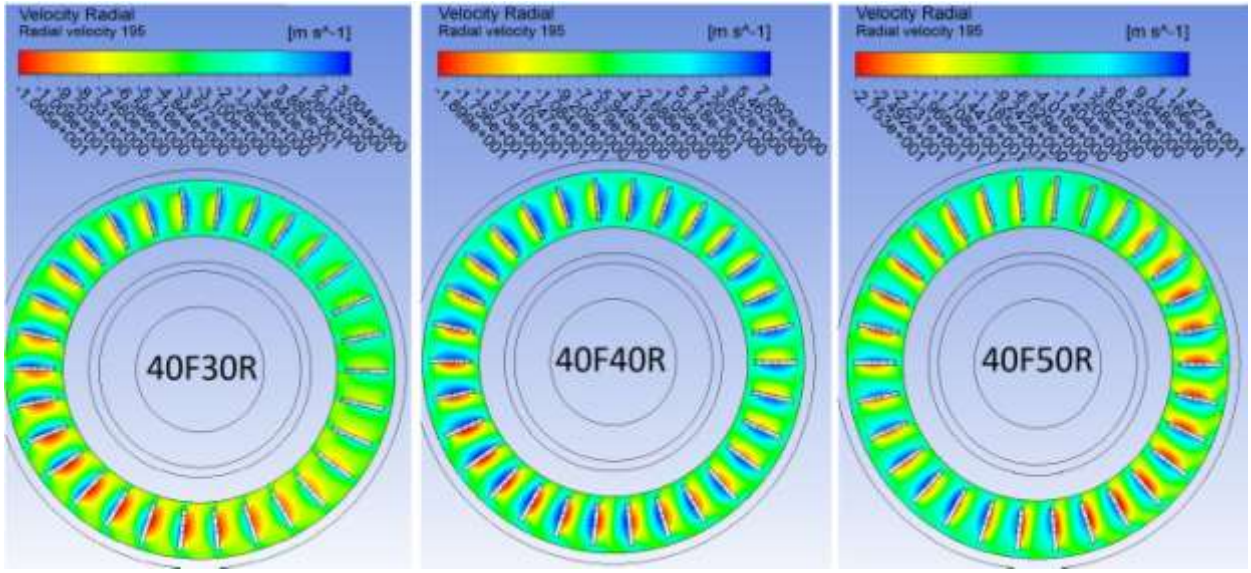

Figure 164 Section through rotor on radial velocity for varying operating parameters

Effects of this pattern are however still present in the rotor domain and are manifesting themselves by uneven distribution of radial velocity in all the blade passageways as shown in Figure 161 and Figure 164. Also, it can be observed, that at some locations on the horizontal level of the rotor, the radial velocity is negative and therefore pointed towards walls of the classifier body. This is an undesired flow pattern due to negative effects on the classification efficiency.

Similar flow pattern logic is discovered to be present for both fan speeds and therefore for better overview, one fan speed and three rotor speeds are discussed. Figure 165 shows position of lip leakage in the area 1 mm under the lip of the inner cone throat. It is noticed that in the lower section of the classifier, leakage position is determined by position of the tangential air inlet. Radial velocity has decreasing tendency for increasing rotor speed which confirms rotor's effects on axis of the swirling flow described previously.

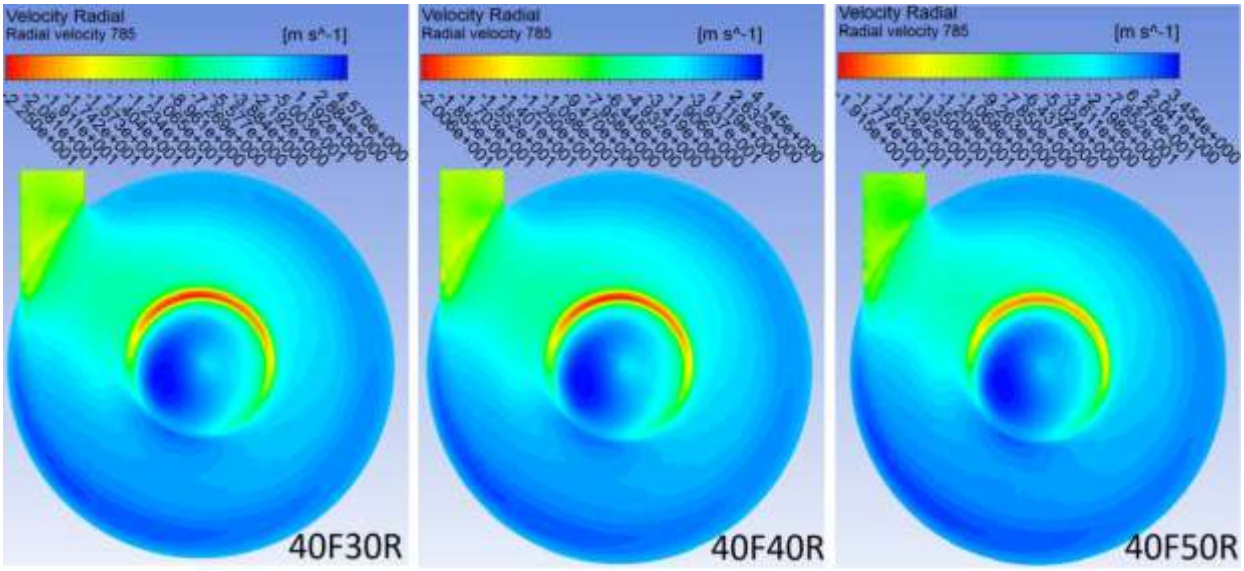

Figure 165 Lip leakage for 40Hz fan speed and 30, 40, 50 Hz rotor speed

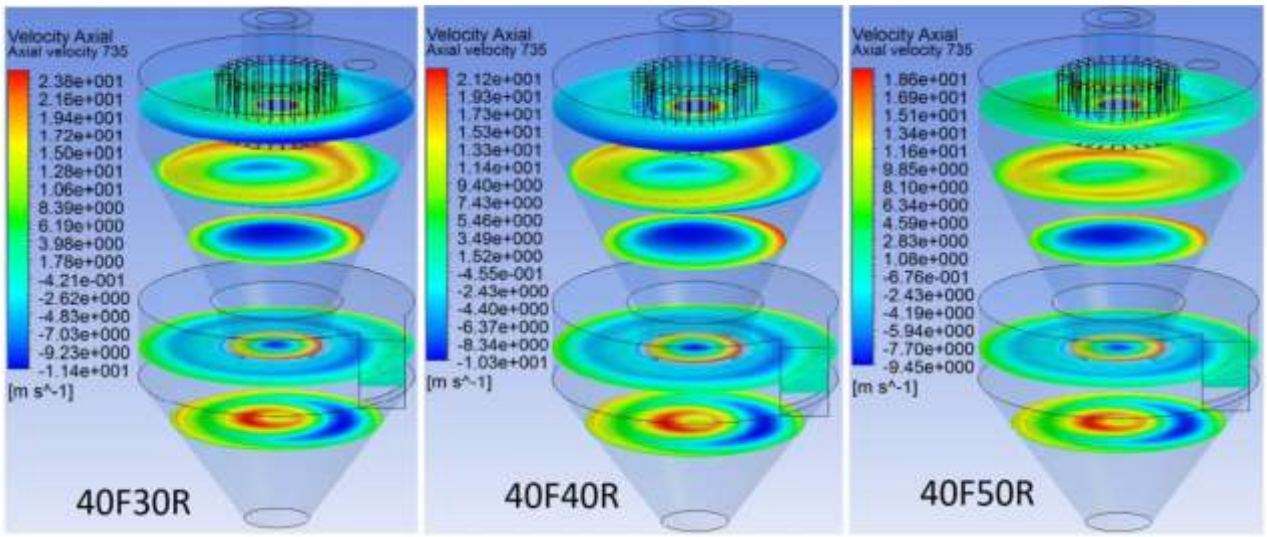

Figure 166 Axial velocity profiles for 40Hz fan and 30, 40, 50Hz rotor

Surface of revolution with 240 mm diameter is created in such a way that it cuts vertically down through rotor blades. Contours of radial velocity are then plotted on this surface for three cases. It can be seen in isometric view of Figure 167 that maximums and minimums of radial velocity vary also depending on vertical position of rotor. The maximum positive values with direction inwards are present in the lower half of the rotor just before trailing blades.

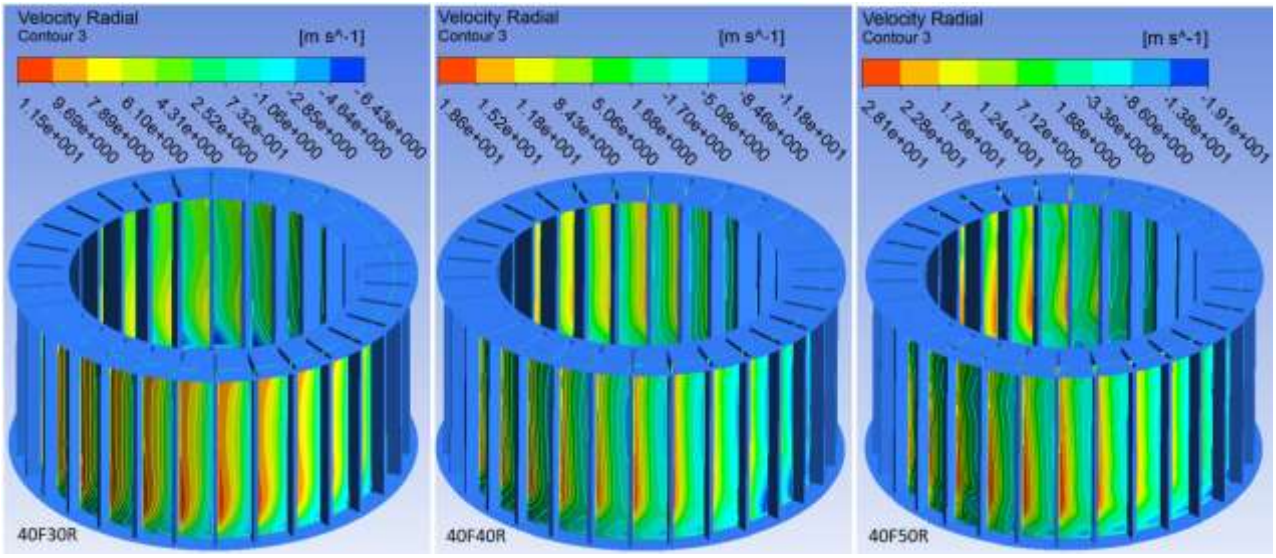

Figure 167 Radial velocity plotted on surface of revolution through rotor blades

Increasing rotational speed of classifier rotor affects radial and tangential velocity components of the air flow in the region around the rotor. Higher rotational speed translates into increased tangential velocity of the swirling field and lower radial velocity. It can be observed in Figure 168 that maximum tangential velocity occurred for all the three cases inside of the rotor cage where maximum velocity is present at greatest rotational speed. XY plane used for tangential velocity plots displayed below cuts through classifier rotor.

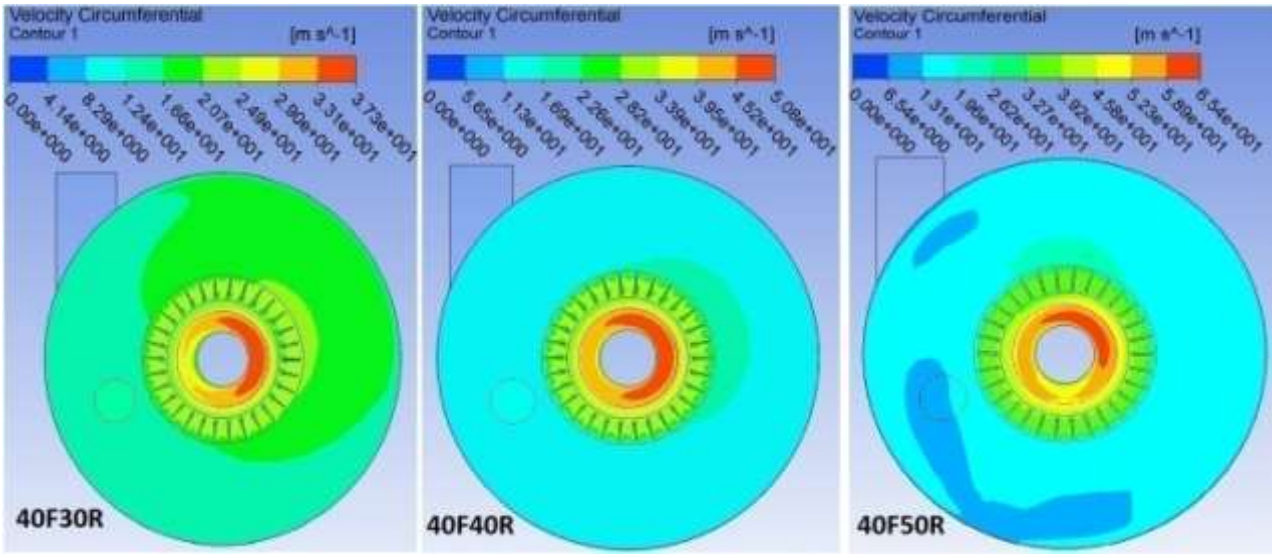

Figure 168 Circumferential velocities for 30, 40 and 50 Hz classifier motor settings

Radial velocity profiles and flow patterns in the air classifier were discussed above. Effects of radial and tangential velocity flow patterns on particle trajectories are discussed later in the work. Another component of the flow which has crucial impact on particle trajectories is axial velocity. Figure 166 shows profiles of axial velocity for different operating parameters. It can be observed that the flow rises axially up in the swirling pattern from the location of the lip leakage and only in the outer layer of the throat in the near wall region. The flow further propagates into conical section of the upper body of the classifier in the swirling pattern in outer layer in the near wall region. There is a point on the outer wall of the classifier where this V-shaped swirling vortex propagating in the upwards direction, separates from the wall and starts heading towards the rotor. Inner surfaces of this vortex do border an area of the classifier where the axial velocity propagates upwards as it can be seen in Figure 169 (green colour for upward axial flow). The axial velocity in the core of this vortex is negative and thus flow occurs downwards, creating a large recirculation zone in the area under the rotor down to lower body of the classifier. Figure 170 shows decreasing vortex intensity strength for increasing angular velocity of the rotor. Ideal fluid flow pattern in the air classifier is a swirling flow with high tangential velocity, low inward directing and axially symmetric radial velocity and with upward directing axial velocity.

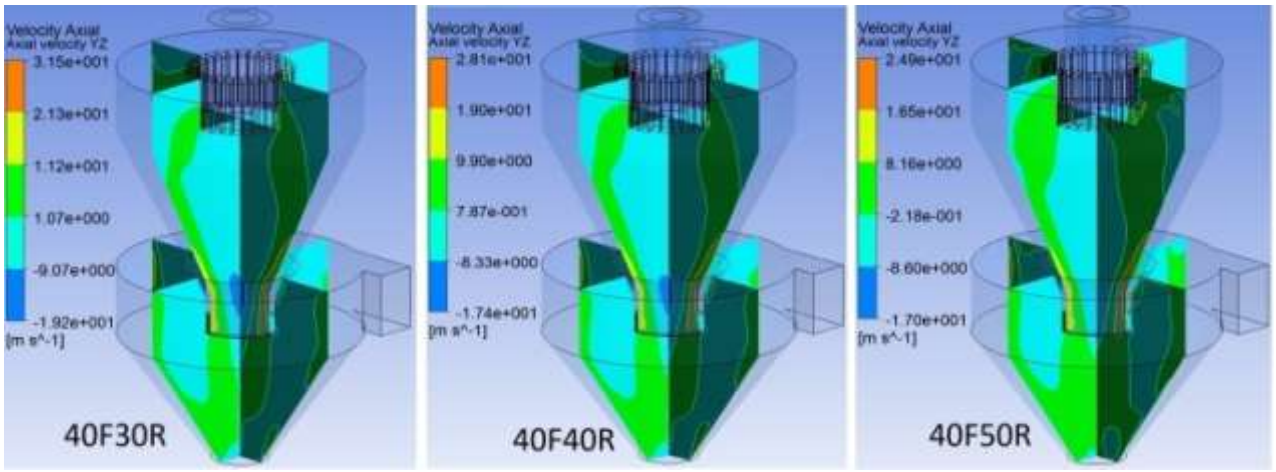

Figure 169 Axial velocities in YZ & XZ plane

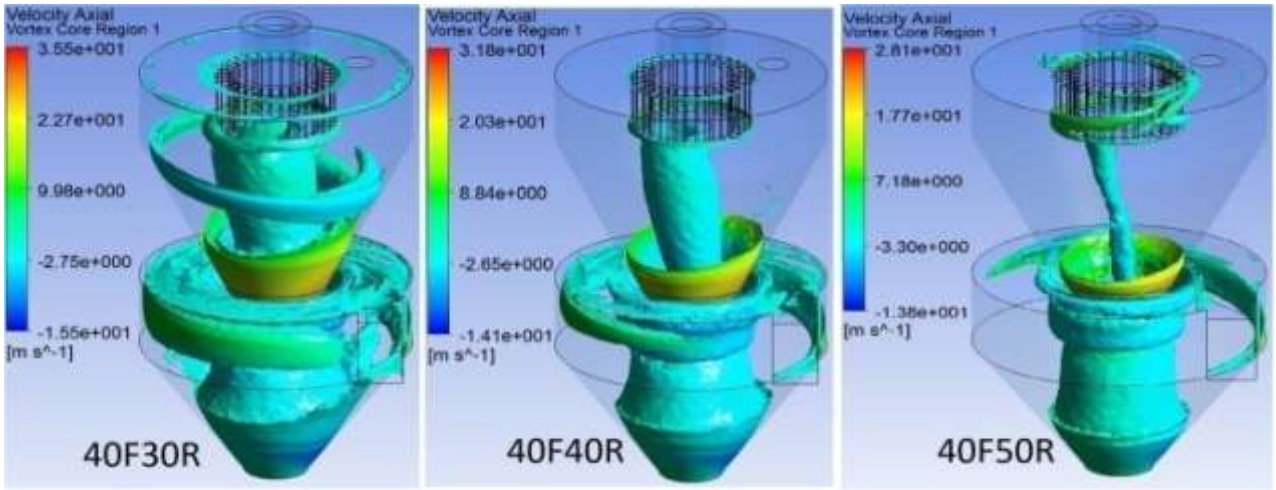

Figure 170 Vortex core for three settings with swirling strength filtration set at 0.015 and axial velocity colouring

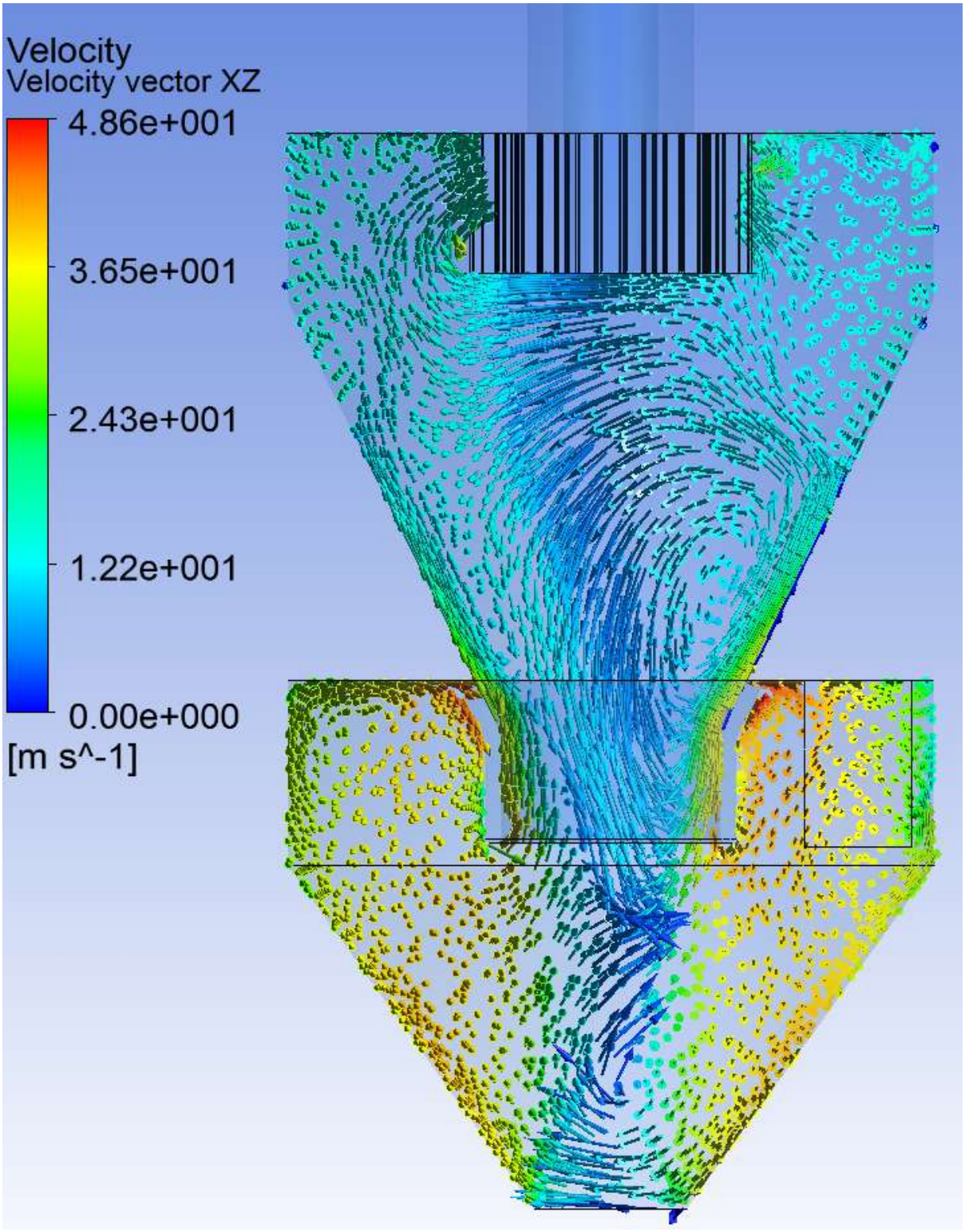

Figure 171 Section view on XZ plane through centre of the classifier

Figure 171 shows section through the classifier. Vectors are coloured by velocity magnitude. Separation of the axially positive swirling flow from the conical wall can be observed in the upper right half. Vortex core with the negative axial velocity and formed recirculation area can be observed in the centre of the classifier. Maximum velocity is observed where the tangential air inlet discharges towards throat of the inner cone.

10.3 SUMMARY - PARTICLE TRAJECTORIES

Barite particles are tracked and trajectories are visualized in order to better understand particle behaviour and effects of local flow structures on fate of the particles. Trajectory history is calculated by Ansys Fluent and is then exported into CFD-Post for further post processing. Particles with both spherical and irregular shape were simulated with relation to drag coefficient. No significant difference in particle trajectories was observed and therefore particle trajectories for spherical drag law are presented. Due to high computational cost, particles were tracked in post processing and momentum coupling with continuum phase was not considered. Particles were tracked with limited number of steps to limit computation time due to particles trapped in recirculation zones. Discrete random walk model was used for stochastic tracking to simulate effects of turbulent dispersion. Time constant is selected to be 0,05 and total number of tries for each particle is five. Particles are injected into the classifier through circular surface in the top face of the classifier. Trajectories are presented and discussed in depth for three simulations with constant fan setting at 40Hz and three rotor angular velocity settings, 30, 40, 50Hz.

Table 35 Major D values as measured in the experimental section

Trial	Fan [Hz]	Classifier [Hz]	25% AVERAGED [µm]	50% AVERAGED [µm]	75%AVERAGED [µm]	95% AVERAGED [µm]
TB6	40	30	1.58	3.27	6.25	10.68
TB7	40	40	1.49	2.923	5.79	9.87
TB8	40	50	1.39	2.43	4.8	8.31

10.3.1 Particle Trajectories for 40F30R Simulation

For the reason of clarity and more distinctive trajectory visualization, particles are divided into two groups by size where the first group only contains particles with sizes below 98% passing diameter. This group represents very fine particles which are able to pass through the rotating rotor of the classifier. Figure 172 shows particle trajectories for five different particle diameters. It can be seen that particles are injected from surface in the top face. Largest particle in the group, 13 microns, is represented by red colour. After entering air flow in the classifier, the particles of this size are dragged by swirling flow and follow spiralling trajectory as they are accelerated towards the outer wall. Some of these particles are repeatedly hit by rotor blades as they try to get inside. It can be observed that a limited number of these particles are able to enter internal area of the rotor. This can be explained by uneven distribution of radial velocity in the area around the rotor, caused by eccentric position of axis of rotation of the swirling flow. It can be also observed that in the other half of the classifier, where radial velocity has negative direction and therefore air does not enter internal area of the rotor, no particles enter this area. On the opposite spectrum of particle sizes, the smallest particle in the group, 0.35 microns, is represented by blue colour. These particles readily follow flow patterns and they quickly enter blade passageway area. Here, they progress on a curved trajectory due to curvature of the flow as correctly predicted by simulation and confirmed experimentally by PIV vector map visualizations. No particles below 98% passing size report to coarse fraction due to particle-particle interaction not included in the model.

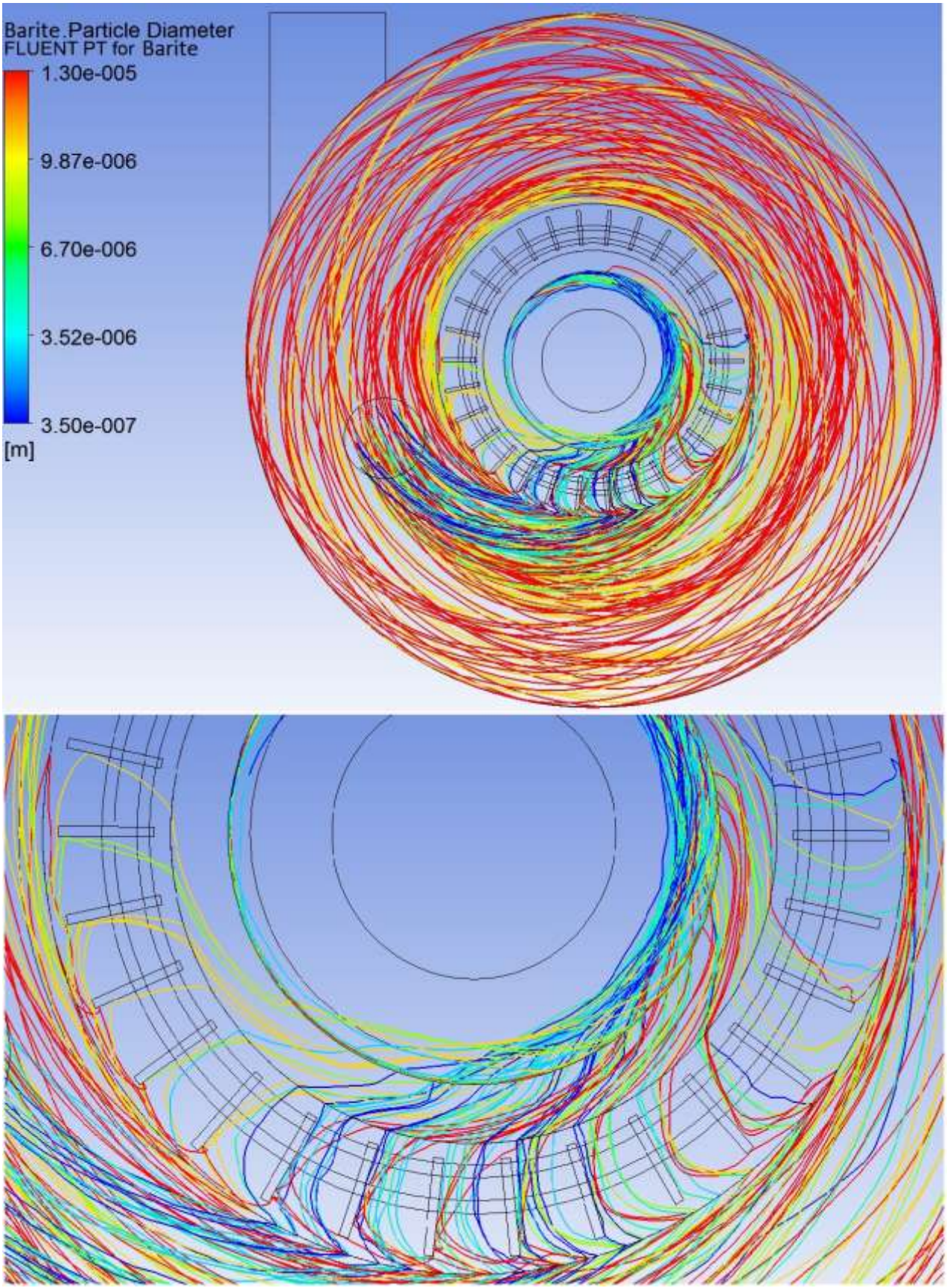

Figure 172Trajectories of barite particles with 98% passing 13.8 micron for 40F30R

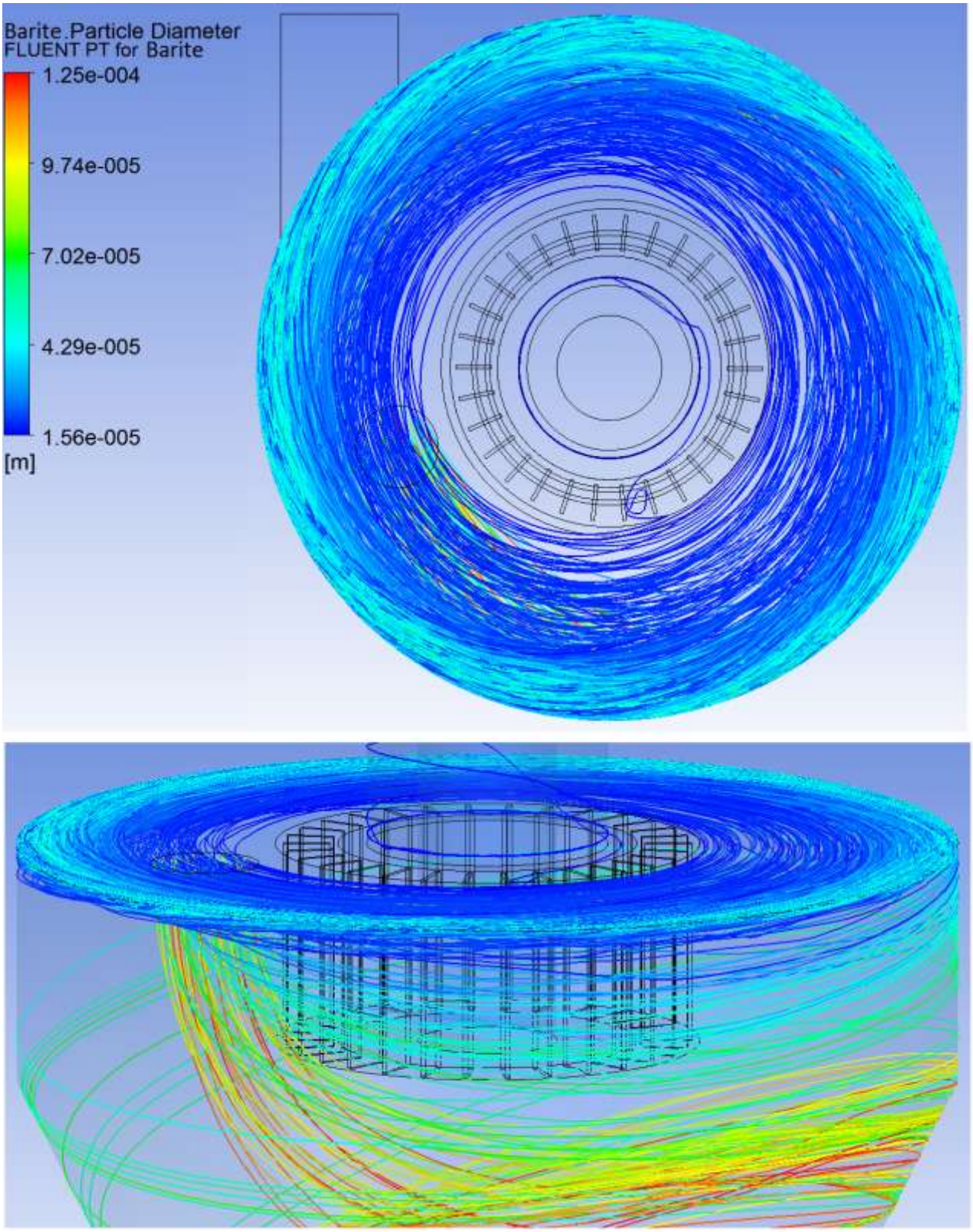

Figure 173 Trajectories of barite particles with size above 13.8 micron for 40F30R

It can be seen in the Figure 173 that almost none of the particles with diameter above 13 microns manage to enter internal area of the rotor. Most of these particles is separated by centrifugal action of the swirling flow and do not even enter proximity of the rotor. It can be seen

that there is a significant amount of the particles with sizes up to 42.9 microns re-circulating in the top section of the classifier. These particles would normally follow descending swirling trajectory towards coarse discharge. The largest particles with sizes above 42.9 up to 125 microns start their descending swirling trajectory right after they are injected into the classifier. These particles do not approach proximity of the rotor nor the blade passageway. This is a positive fact as these particles are the most responsible for wear of the blades. Total number of 2195 particles was tracked whilst 166 particles were terminated as escaped and thus classified into fine fraction.

10.3.2 Particle Trajectories for 40F40R Simulation

Based on equations for cut size predictions presented in theoretical part, increasing tip velocity of the rotor translates into finer cut sizes. Simulation correctly predicts this behaviour. Particles are again divided into two groups, where the first group is represented by five particle diameters below 12.7 microns which represents 98% passing value at this particular rotor setting. It can be observed in Figure 174 that particles exhibit similar trajectories. Most of the particles enter area of the rotor in approximately the same location when compared to previous case. The main entry area is however slightly rotated anticlockwise, agreeing with rotor rotation direction. This is caused by slightly different position of area with increased positive radial velocity. Smallest particles manage to escape through the rotor relatively easily and have the shortest residence time. The largest particle in this group, having diameter 10.5 microns follows the longest trajectory in the classifier. These particles carry out several circuits around the rotor before they even enter proximity of rotor blades. Most of these particles are able to pass through the rotor which indicates that the 98% passing value lies between size 10.5 and 12.7 microns. It can however be seen that these particles take several attempts to pass through the rotor as they are repeatedly rejected by rotor blades. Also, these particles which due to their size are travelling at lower speed are at several occasions trapped in the recirculation area in the blade passageway, which is observed by both experimental and numerical methods. They carry out several circuits in the blade passageway which means they remain in this area for an increased period of time. Both these facts are negative for classification as increased frequency of particle contact with blades leads into increased wear rates. Chances of particle collisions and re-agglomeration are increased as these particles remain in the passageway for longer periods of time when compared to smaller particles. The other group represents particles with sizes above 12.7 microns are is represented by five different particle diameters as shown in Figure 175. The smallest particle in this group is represented by 13-micron diameter and it can be seen that at one occasion was this particle able to pass through blade passageway into fine fraction. At several occasions, particles of this size came into contact with blades and were rejected into coarse fraction. Also, some of these particles got into blade passageway and circulated one time around recirculation pattern and then re-entered classifier body into coarse fraction. It can be again observed that there is a considerable amount of particles with sizes up to 41 microns re-circulating in top section of the classifier. These particles do in reality follow descending swirling trajectory towards coarse discharge. Particle interactions are neglected and only a limited number of steps is allowed in the simulation for particle tracking and therefore these particles are reported as incomplete. Largest particles with sizes above 41 up to 125 microns start their descending swirling trajectory right after they are injected into the classifier as observed also in the previous case. Total number of 2195 particles was tracked whilst 148 particles were terminated as escaped and thus classified into fine fraction.

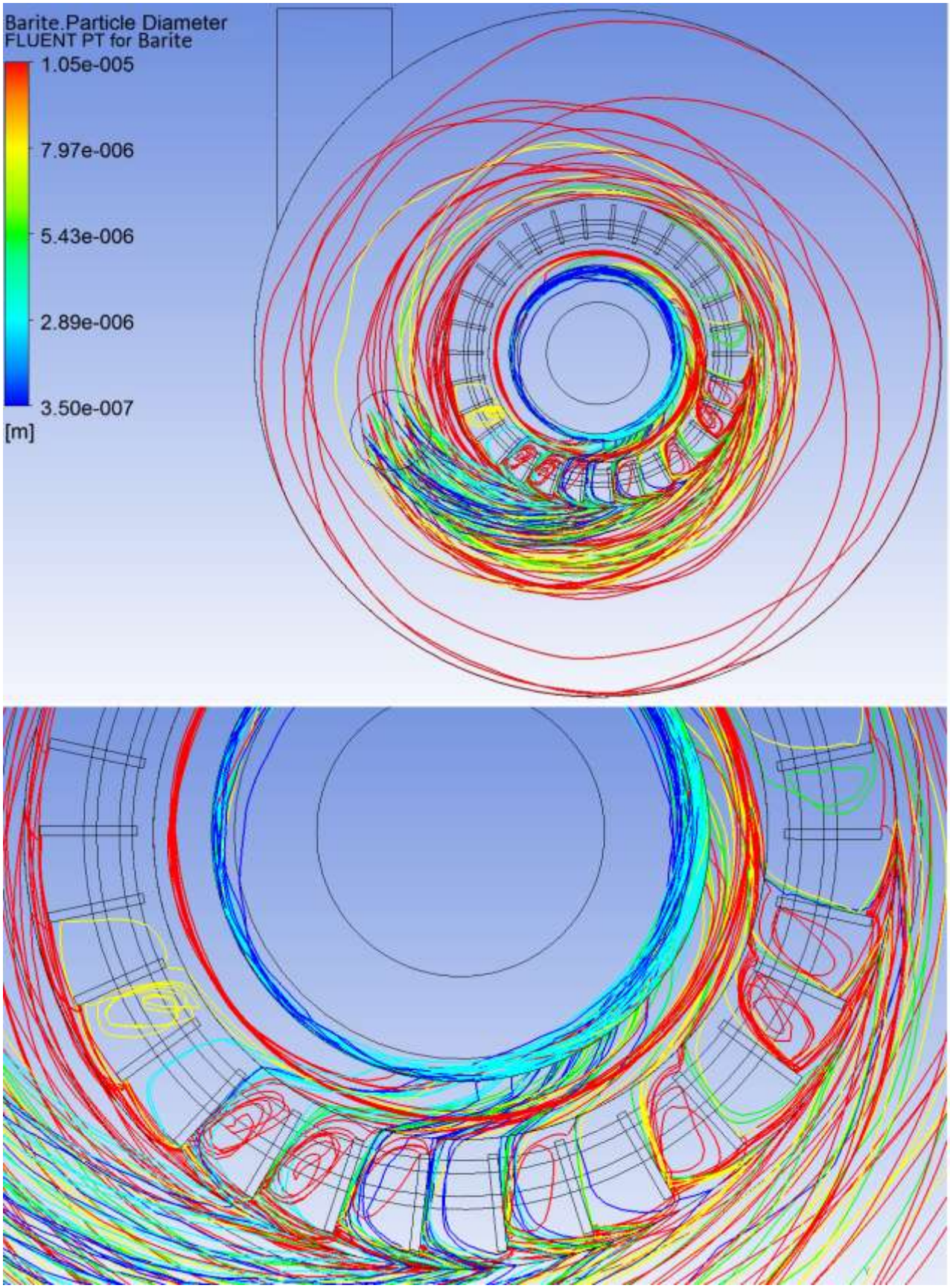

Figure 174 Trajectories of barite particles with 98% passing 12.7 microns for 40F40R

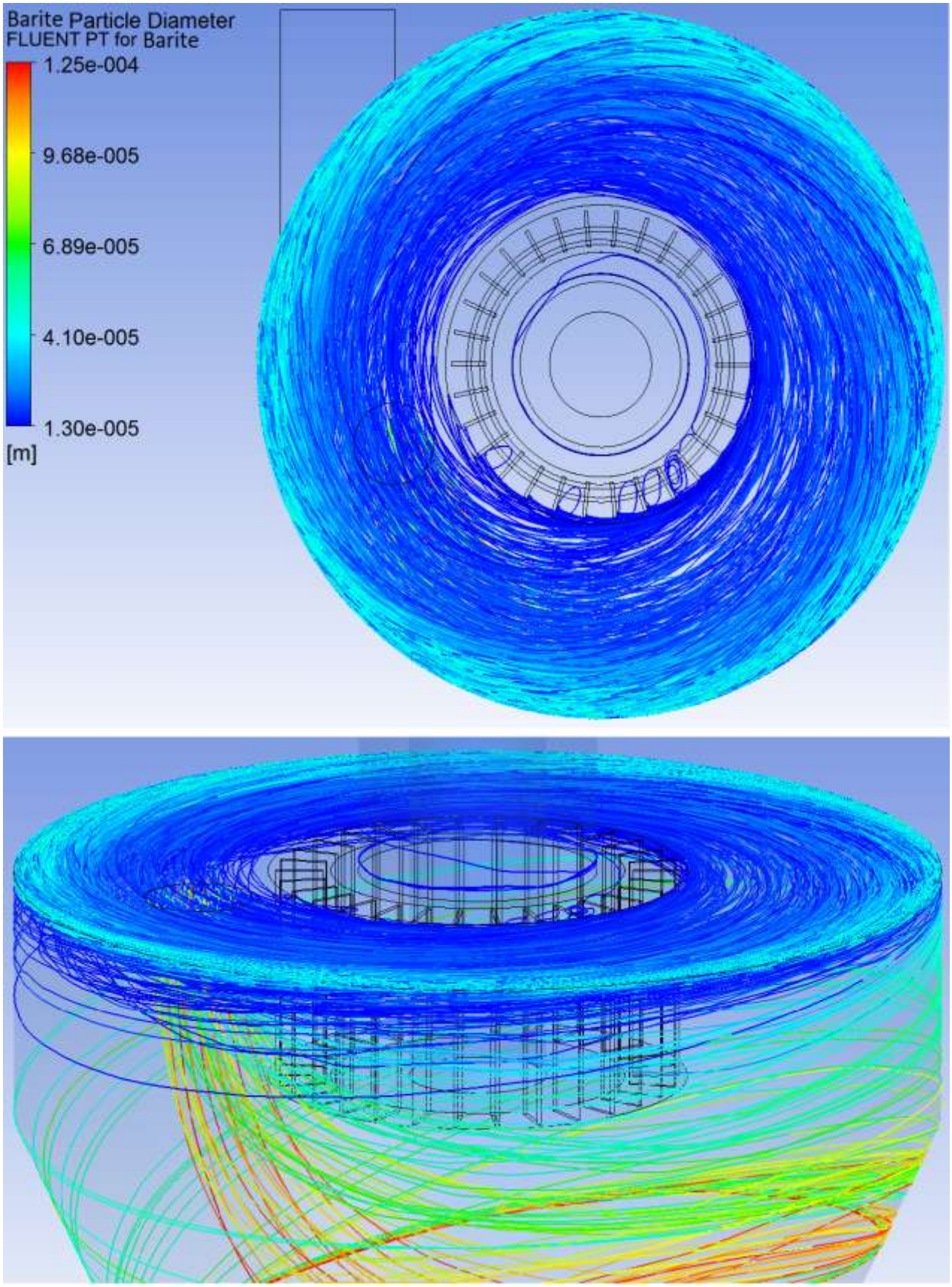

Figure 175 Trajectories of barite particles with size above 12.7 microns for 40F40R

10.3.3 Particle Trajectories for 40F50R Simulation

Particle size distribution analysis of fine fraction obtained from classification trial with given set of parameters established that 95% passing value was 8.31 microns and 98% passing value was 10.6 microns and 50% passing value of 2.4 microns. Just for comparison, red blood cell is 8 microns large across and single bacteria is 2 microns large. For more distinctive trajectory visualization, particles are divided into two groups. The group with fine particles contains 5 particle diameters with sizes ranging from 0.35 microns to 10.5 microns. It can be noticed in Figure 176 and Figure 177 that particles start following swirling trajectory after they enter classifier and they carry out several rotations around the rotor before they reach blade passageway entry point, unlike particles in previous simulations, where the smallest particles entered blade passageway right after they entered the classifier. This is caused by greater rotor speed as radial velocity component in the classifier internal body domain becomes weaker whilst tangential velocity component increases, accelerating even smaller particles towards outer walls of the classifier. From the isometric view it can be noticed that particles of even smallest sizes are more distributed in the classifier as opposed to previous two simulations. Higher rotor speed translates into greater forces acting on the volume of air in the radial direction towards outer walls (principle of centrifugal fan).It can be concluded that for higher rotor speeds, particles become less sensitive to exact entry location within the injection surface. It can be observed that particles enter blade passageways alongside full perimeter area of the rotor where the smallest particles pass through directly whilst 10.5-micron particles carry out several revolutions in the blade passageway due to recirculation area present in this location. Trajectories of particles with sizes above 10.6 microns can be found in Figure 178. Smallest particle in this group is represented by 13-micron particle where none of these particles are able to enter rotor area and be classified as fines. At few occasions these particles entered blade passageway but were later after several revolutions in recirculation area rejected. Largest particles followed similar trajectory patterns as described in previous two simulations.

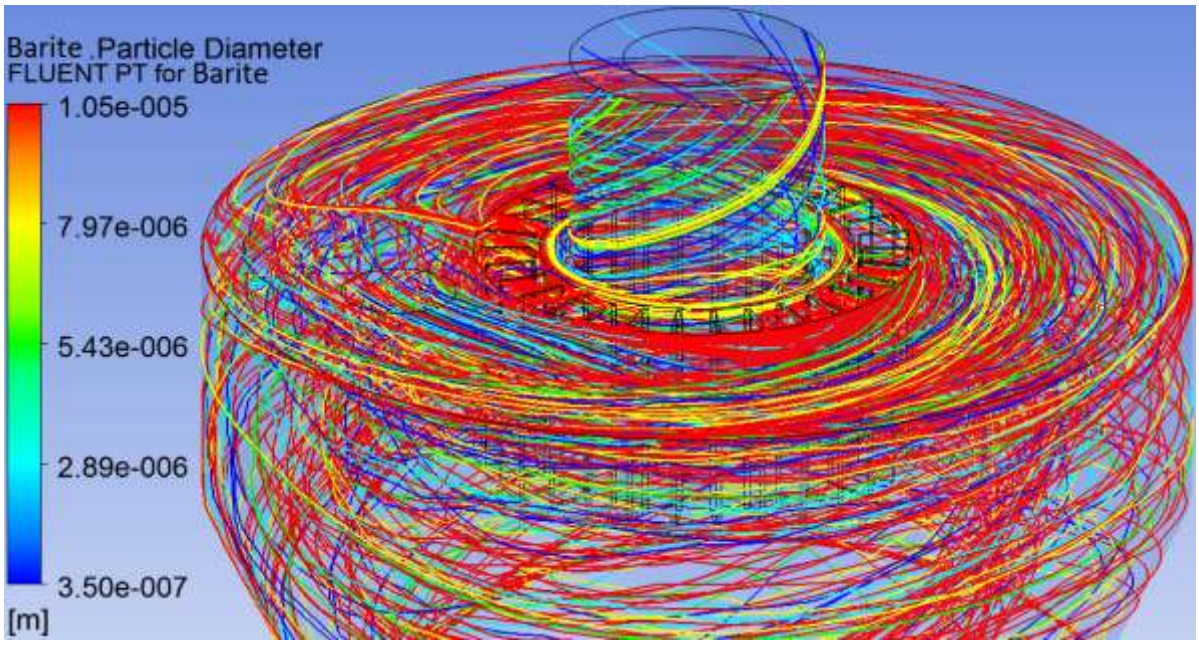

Figure 176 Trajectories of barite particles with 98% passing 10.6 microns for 40F50R isometric view

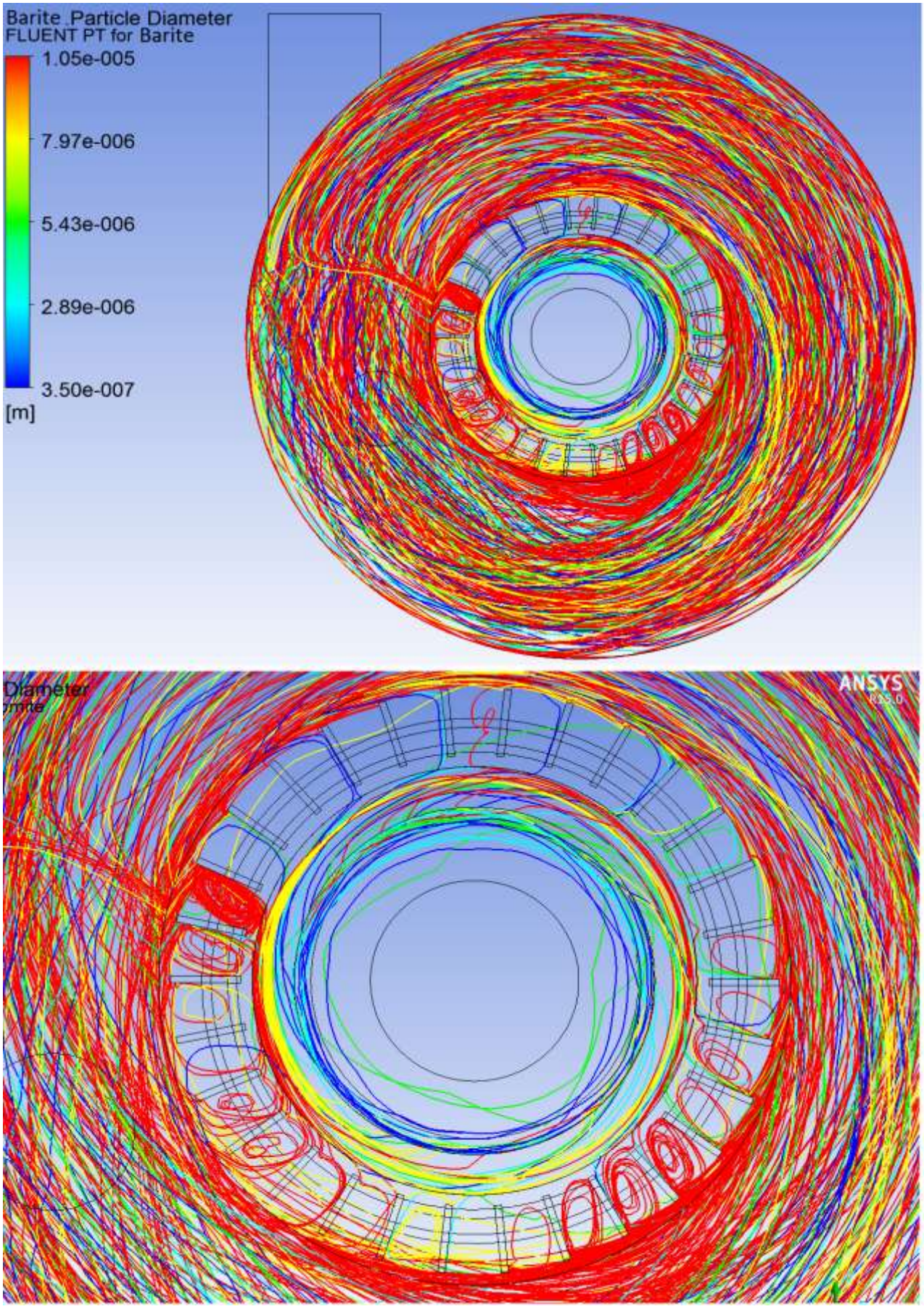

Figure 177 Trajectories of barite particles with 98% passing 10.6 microns for 40F50R

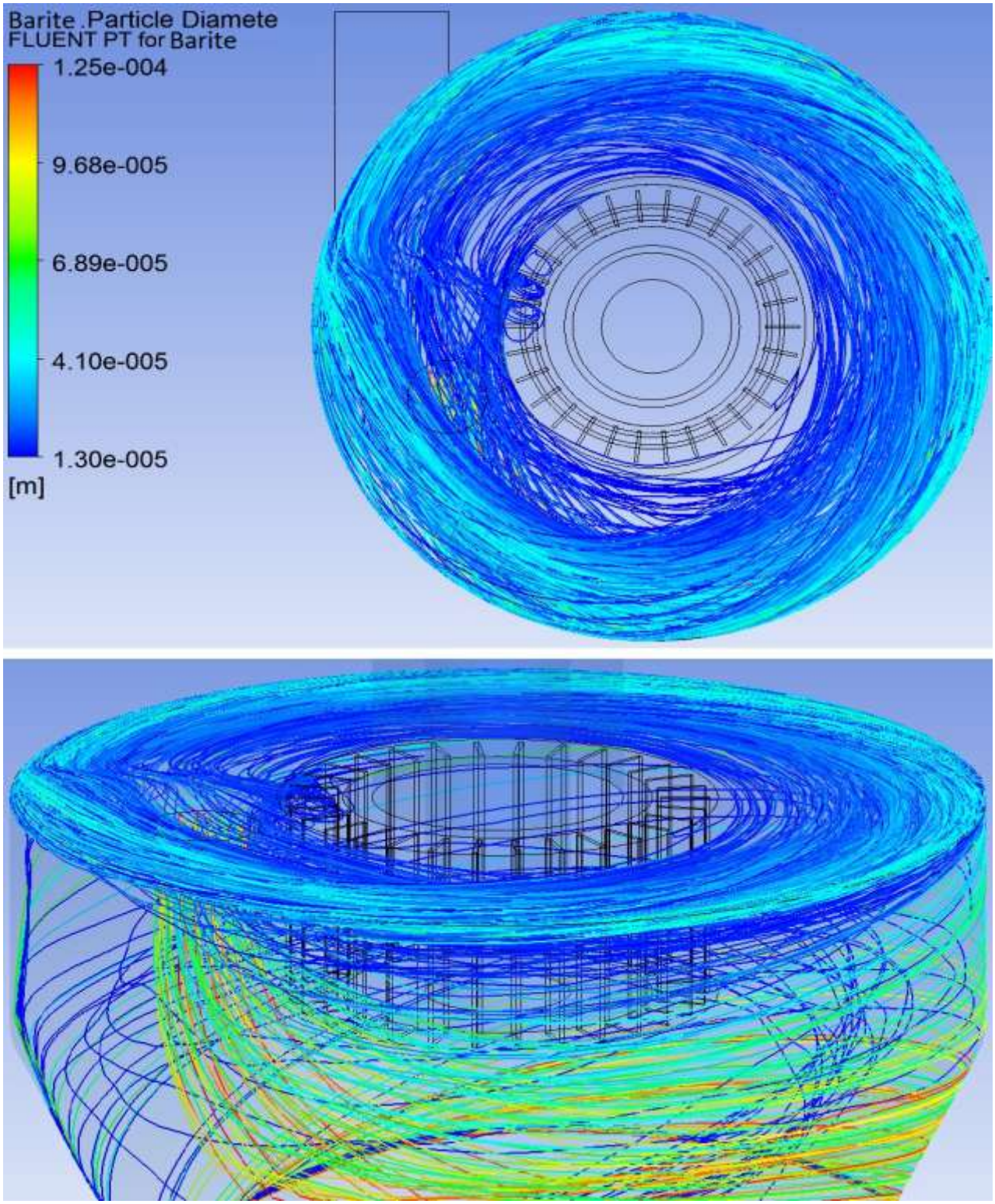

Figure 178 Trajectories of barite particles with size above 10.6 microns for 40F50R

It can be seen in Figure 178 that in one location particles follow slightly out of circle pattern. This can be caused by turbulent flow or transient nature of flow for given settings in the area or by difficulty to find completely converged solution for high rotor speed with used grid mesh. Total number of 2195 particles was tracked whilst 66 particles were terminated as escaped and thus classified into fine fraction.

11 SUMMARY

Increasing requirements on physical properties of particulate materials, like size distribution, consequently increase requirements on methods and devices applied in the process operation of material classification. Air classification method employs action of rotating cage together with purposely distributed flow field to classify particles into fine and coarse fraction by size. This dissertation work focused on study of flow fields and separation zones under varying operating parameters which were at the top limit of capabilities of the air classifier used in experimental section of this work. Based on Reynolds numbers throughout the classifier, flow field inside could be pronounced to be completely turbulent and as such it has major impact on classifier efficiency, its performance and capability to classify particles, even more so as the investigated spectrum of particle sizes lies below 5 microns in diameter.

Theoretical part of this work establishes principles and baseline terms commonly used to describe classification process and it further defines indicators that are used to evaluate performance of classifier like cut size, sharpness of separation, Tromp curve, etc. These indicators are then later used in experimental section to evaluate performance of the classifier. Three generations of air classifiers are presented together with separation zones employed and the operating principle of rotor air classifier being the last generation is explained in detail. Main factors affecting performance of classifier are summarized as rotor tip velocity, air flow velocity, feed rate and geometrical arrangement and structural parameters of the classifier. Researches dealing with cut size and classification efficiency prediction models are summarized from least to most complex models which use numerical models and CFD simulations.

Experimental section firstly describes air classifier unit with all the devices in the loop where these are rotor air classifier, centrifugal fan, rotary feeder, cyclone and control panel. Particular care is taken with centrifugal fan and digital manometer is used for air inlet velocity to classifier measurements. Air classifier can be considered as ineffective centrifugal fan acting against the flow generated by main fan in the system. Thus, different classifier rotor speed generates different pressure resistance and effectively changes resistance and pressure drop across of the system. Volumetric flow rate delivered by main fan and thus inlet velocity is dependent on system resistance. Thirteen values are taken at different locations inside of the air inlet duct for each set of settings for 5 classifier motor settings (30, 35, 40, 45, 50 Hz) at 2 fan motor settings 30 and 40Hz. These values are then averaged and correlated with values of air inlet velocity calculated with respect to fan affinity laws. Final air inlet velocities consist of 10 values for 10 sets of operating parameters and these are later used in velocity inlet boundary condition in numerical CFD simulations.

Rotor blade passageway and its proximity is one of the main areas of interest of this work. It is the area where rotor interacts with flow field and with particles and therefore it has crucial significance in particle classification. Particle image velocimetry (PIV) is an advanced method used for visualization of flow patterns and vector maps and for the actual velocity measurements. Modifications carried out to air classifier in order to implement double laser head and high-speed camera for PIV measurements are introduced briefly. Support stands were designed in specific way to allow for laser and camera alignment and calibration where the laser illuminated horizontal plane intersecting classifier rotor whilst camera was installed at the top of the classifier and was

focused at the blade passageway. System was then seeded with DEHS oil droplets with submicron particles which were used to reflect light from laser beam. Two consequent images with known delta time between them were taken. These were then split into interrogation windows and based on particle shift within the two windows the displacement vector was calculated and transformed into local velocity vector. In order to describe flow variations in the passageway area for varying operating parameters, 1000 image pairs were taken for 10 sets of parameters as described previously. Therefore, a total number of 20 000 images were taken where each image was in RAW format with approximate size of 30MB making the total size of collected data 600 GB. Images were then post processed and presented in comprehensive sets of contours, vector maps and graphs. A formation of forced vortex is observed in the blade passageway area at all ten cases. Intensity of this vortex increases with increasing rotational speed whilst its size decreases. Distribution of radial velocity in the passageway is such that it reaches positive values (inward direction) alongside the trailing blade whilst it reaches negative values (outward direction) alongside the leading blade, effectively forming a forced vortex. Plane intersecting passageway is overlaid by sampling lines equi spaced after 5mm in radial direction and radial velocities profiles are plotted along these lines. Positive radial velocity becomes a major velocity component in the passageway due to two reasons. Rotor blades are arranged in straight radial pattern and thus directing air in radial fashion and secondly the forced vortex confines passageway area and thus due to conservation of mass law, velocity is increased in the unrestricted area.

It was attempted to carry out PIV velocity measurements also with barite as feed material. Vector maps would have showed velocity vectors of particles in a group rather than flow properties. Injection of compressed air was used to help keep the window for camera and laser clean. It however was not sufficient and the particles completely covered both windows within seconds. Also, due to nature of barite particles, the amount of light reflected was creating an excessive amount of noise to be simply filtered out by camera lens filters and software filtration.

In the second half of experimental section, 11 classification trials were carried out with barite feed material. 300 Kg of barite with particle distribution as required for drilling mud had been provided by client from oil industry and approximately 25 Kg of barite was used in each test. In order to establish split ratio and fines recovery, buckets with fine and coarse fractions were weighed after each test, resulting into 22 weight measurements. Particle size analysis was then carried out to establish distribution curves and major % passing values for both fractions. 3 particle size analyses were carried out for each fraction and these were then averaged to give representative distribution. This amounts into 66 particle distribution analysis and these were carried out by Microtrac which uses laser diffraction principle.

3 tests were carried out with constant fan and classifier setting whilst feed rate was increased for each test. This resulted into decreasing particle sizes which is positive but also into decreased fine particles recovery, Table 27 and Table 28. It could be explained by increased particle loading in the classifier leading into increased particle interactions. Particles would start creating agglomerates and thus restricting path for smaller particles to be classified as fines and also trapping them in these agglomerates. Fines recovery for lowest feed rate was 13.56% whilst for the highest it was 7.51%. Smallest recorded 50% passing size from all the trials was for this setting and its value was 1.674 microns.

Operating parameters of the 8 remaining trials were organized in such a way that both influence of rotational speed of classifier rotor and influence of air inlet velocity could have been investigated whilst the feed rate was set to be constant. Three sets of tests were conducted for 30, 40 and 50 Hz centrifugal fan motor settings with 3 trials in each test for 30, 40 and 50 Hz classifier motor setting. Results of all the trials were in good agreement with classification theory and anticipated trends.

Major % passing values that are used to describe size distribution of particulate materials were for a constant classifier and feed rate settings and decreasing fan settings also decreasing. Lesser amount of air delivered into the system leads into smaller air velocity and thus smaller drag force acting on a single particle. PIV measurement confirmed that intensity of the forced vortex, thus radial velocities in blade passageway are reducing as seen in Figure 105 effectively leading into finer cut size of the classifier. This trend was recorded for all the cases with the above mentioned operating parameters. It was observed that for very fine particle classification applications such as this, the actual sensitivity of % passing values of fine fraction on fan settings is very low. Change of fan settings from 50 to 40 and from 40 to 30 Hz only resulted in % passing values decrease in range of 0.5 - 1 microns. This is only a very small particle distribution change for a rather significant fan setting alteration. On the other hand, recovery of fine particles decreased significantly, somewhere in region of 10 %, for fan settings decrease from 50 to 30 Hz, as seen in Table 27.

Major % passing values of particle distribution of fine fraction were decreasing for increasing classifier rotor settings with constant fan and feed rate. Higher classifier rotor tip velocity translates into greater centrifugal force acting on a single particle and also on a volume of fluid. Particles travelling at lower velocity interact with rotor blades which reject and accelerate these particles towards the outer wall of classifier. In the internal body of the classifier, it can be concluded that a higher tip velocity increases tangential velocity and decreases radial velocity of airflow in the classifier body as seen in Figure 168. PIV measurements of flow field in the blade passageway indicate increasing intensity of the forced vortex with increasing rotor speed. This could be explained by increased local mixing of air with both positive and negative radial velocity. Classifier rotor itself can be considered as centrifugal fan and therefore generating airflow against the main fan. Higher rotor speed means greater amount of air flowing in the negative radial direction. Due to conservation of mass flow rate, the intensity of forced vortex is therefore increased. This trend has been observed for all the cases with the above defined operating parameters. It was observed again that for a very fine particle classification as this, the actual sensitivity of % passing values of fine fraction on rotor settings is very low. Alteration of classifier motor settings from 30 to 40 and from 40 to 50 Hz only resulted in % passing values decrease in a range of 1.5 - 2 microns. This is a minor particle distribution change for a significant rotor speed alteration. Similarly, like the previous cases with decreasing fan setting, increasing rotor speed decreased recovery of fine particles and therefore increased by-pass of the classifier. For alteration of motor supply frequency from 30 to 50 Hz, by-pass increased by approximately 10% as seen in Table 27. Tromp curves were plotted for each classification trial and it can be seen that by-pass (the amount of fine particles classified into coarse fraction) increased significantly with decreasing fan setting and increasing rotor setting. The actual values of by-pass varied between 53% and 88% which means that the classification process is very ineffective. For comparison, by-pass values for a more standard application are usually 10%.

Based on the results provided, it can be concluded that for classification of particles with sizes below 10 microns, the actual classification process becomes less and less sensitive to operating parameters like air velocity and rotor tip velocity. The process also becomes very ineffective because of large amounts of fine particles being classified into coarse fraction.

Numerical simulations were carried out using commercially available CFD software Ansys Workbench (Meshing, Fluent and CFD-Post). Air classifier geometry was simplified and modelled up in 3D software Autodesk Inventor. Assembly consisting of four parts was then imported into Ansys Meshing where it was further post processed and meshed with grid of control volumes. Ansys Fluent was then used to solve Reynolds averaged Navier-Stokes partial differential equations together with additional 2 differential equations to include turbulence effects. Ten simulations were carried out for operating parameters as used for PIV measurements. Inlet velocities measured by digital manometer were used for velocity inlet boundary condition together with associated rotor rotational speed and converged solutions for fluid phase (continuum) were found for all the 10 cases. Three particle analysis of barite feed material were realized by laser diffraction method (Microtrac) and averaged in order to obtain representative size distribution curve. This curve was then transformed into Rosin- Rammler distribution to obtain characteristic points and these were then used to specify discrete phase of the simulation. Particles were then tracked for each fluid phase solution and particle trajectories are displayed.

Each numerical simulation correctly predicts formation of forced vortex in blade passageway. Location of positive radial velocity alongside trailing blade and negative radial velocity alongside leading blade is predicted correctly. Blade passageway was mapped by 9 sampling lines located after 5 mm in radial direction. These lines are in the same position as sampling lines used for mapping during PIV measurements. Radial velocity profiles are ten plotted and compared to measured data. Magnitudes of these velocities are slightly over predicted when compared to PIV measurements, they however exhibit correct trend of increasing vortex intensity for increasing rotor tip velocity. It has been observed that the vortex intensity is not uniform in all the blade passageways. This is explained by inner throat lip leakage position (Figure 165) where as consequence the axis of rotation of the swirling flow is not coincident with axis of rotation of classifier rotor, as seen in Figure 170. This leads into a mainly positive radial velocity component in one half of the classifier and mainly negative radial velocity component in the other half, as seen in Figure 163. In the outside proximity of the rotating domain (rotor) and within the same vertical band, increasing rotor speed increases tangential velocity of the flow and decreases radial component of the velocity. This has an important impact on particle classification and is discussed later.

Axial velocity profiles were investigated by cutting classifier by two planes (XZ & YZ) through the centreline as seen in Figure 169 and Figure 171. It can be noticed that after the air flow leaks through the lip, it carries on swirling alongside conical surface of the classifier in the upwards direction. There is a point on the conical surface where the flow separates from the wall and carries on towards classifier rotor. This is an area of classifier with positive axial velocity. In the core of the classifier, axial velocity is negative and forms one large recirculation area which overlaps down to bottom section of classifier where the tangential inlet is located. This again has important consequences for particle classification and is discussed later. The axial velocity decreases with increasing rotor speed. It is explained by increased tangential component of the velocity at the expense of reduced radial and axial component.

Barite particles were tracked in the classifier for 3 solved fluid phase solutions. Operating parameters for these selected cases were 40 Hz fan setting and 30, 40 and 50 Hz classifier setting. Particles with size distribution as per classification trials were injected into the classifier through a surface in the top face of the classifier. In order to add clarity to trajectory visualizations these were filtered by size corresponding to 98% passing diameter. Simulation correctly predicted particle behaviour where particles of different sizes followed different and anticipated trajectories. Smallest particles from the feed were able to enter internal area of the rotor, thus were classified into fine fraction. Particles with larger diameter were not able to enter either due to swirling flow and consequent cyclonic action or due to interaction with rotor blades which rejected those oversized particles. In general, there was a good agreement between predicted maximum particle size able to pass through the rotor and actual measured maximum particle size that passed through the rotor during classification trials. As a reflection of results of predicted particle trajectories and of measured and simulated flow patterns inside of the air classifier, there appear to be negative factors attached to these flow realities which limit performance of the classifier and its capability to classify even smaller particles. These are summarized below:

- Radial velocity component of the swirling flow in the upper part of the classifier, in the area between rotor blades and outer wall, is not always positive (inward oriented). This means that after the particles are injected, there is a portion of even fine particles that is accelerated towards outer wall of the classifier and not towards the rotor. This fact effectively limits chances of these particles to be classified as fines which increases by-pass and thus decreases classification efficiency.
- As the particles follow swirling descending trajectory around inner wall of the classifier and towards throat of the inner cone, they cross an area where the flow separates from the conical section of classifier body towards rotor blades. Increased particle concentration around the wall leads into greater amount of swirling consistent mass with greater momentum. It has been observed that these particles which contain portion of the fines are unable to separate from the wall in the region of the flow separation. This again increases by-pass and decreases classification efficiency.
- Particles that are able to separate from the near wall region and find their way into core may then get trapped in the recirculation area present under the classifier rotor. As an effect, recirculation areas increase particle concentration in the flow which consequently increases chances for particle-particle interactions and possible agglomeration. Axial velocity in the core of the classifier takes negative values and thus accelerates particles towards bottom of the classifier where the coarse fraction outlet is located. Fine particles that enter lower section of the classifier body with tangential air inlet very rarely find their way back up to be classified as fines. This again increases by-pass and decreases classification efficiency.
- Due to non-uniform radial and tangential velocity distribution in the area around the rotor, particles of the same size may be approaching rotor with different velocities. Some of the particles with size close to cut size may then pass through the rotor blades whilst some may not. This reduces sharpness of separation of the classification process.
- Radial velocities in all the blade passageways are even less uniform due to misaligned axis of rotation of the swirling flow. This leads to positive and negative radial velocities in each half of the passageways. This reduces sharpness of separation of classification.

- Forced vortex is formed in the blade passageway area due to nature of straight, radially oriented blades. This vortex acts like recirculation area and it has been observed that some of the particles were trapped in here, whilst some of the fine particles were sucked and accelerated in the negative radial direction. Intensity of this vortex increases with increasing rotor speed which is essential for ultra-fine particle classification. Some portion of fine particles is rejected into coarse fraction due to this and thus increasing by-pass and decreasing classification efficiency. This vortex also increases tangential velocity at the entry point to the blade passageway and therefore excessively accelerating particles towards rotor blades which increases wear rate.
- For lower classifier rotor speeds, smallest particles were immediately escaping classifier body into fine fraction. Increasing rotational speed of rotor (required for ultrafine classification) essentially increases tangential velocity in the area outside of the rotor and decreases radial velocity in this area. This is a positive phenomenon for ultrafine particle classification. However due to this, even the ultrafine particles follow several revolutions around the rotor before they attempted to pass through the rotor blade passageway. Therefore, ultra-fine particle residence time in classifier is increased which increases chances of particle agglomeration in the classifier and thus reduces classification efficiency.

Limits of air classification method for classification of particles below 10 microns in size can be lowered by 2 groups of measures. First group represents operating parameters of the classifier and current technical design possibilities:

- Maximum rotor tip velocity used during experiments was 42 m/s which translate to 2975 RPM. This was the limit of technical possibilities of the classifier. Higher tip velocity increases centrifugal force acting on the particle which leads into finer cut size.
- Minimum tangential inlet air velocity used during experiments was 11.6 m/s. Lower air velocity decreases drag force acting on the particle which leads into finer cut size.
- Higher feed rate of particles into the classifier results into increased particle-particle interaction and agglomeration. These agglomerated groups of particles act as barriers for smaller particles which lead into finer cut size of the classifier. The classification efficiency is however significantly compromised.
- It can be seen in equation 4.4 that cut size depends on air density. Therefore, finer cut size can be achieved by reducing density of the air used in the classification process.

Second group represents structural parameters of the classifier:

- Forced vortex which originates in the blade passageway due to rotor rotation can be minimized by optimized blade design. Inclined or curved blade geometry decreases effects of centrifugal action on volume of air.
- Flow field recirculation areas originate in the classifier due to design and fabrication imperfections. These increase particle residence in the classifier. Recirculation zones can be identified by CFD software simulation and structural parameter optimization.
- Tangential air inlet creates non-uniform swirling flow field which results into non-uniform radial velocity distribution in the blade passageways. Multiple tangential air inlets would increase concentricity of swirling flow and classifier body and thus improve radial velocity distributions

- Increased number of discrete phase feed inlets results into better dispersion of particles around the classifier rotor and thus increasing efficiency of classification process.
- Trajectories and residence time of particles under 2 microns were increased in length and time due to high tangential swirling flow velocities and low radial flow velocities. Ultrafine particle classification is sensitive to structural parameters. Closer position of feed inlets to classifier rotor results into shorter residence time and therefore smaller chance of particle agglomeration.

Combination of all the above-mentioned measures must be applied during classifier design process and operation in order to move limits of air classification method towards submicron particle classification.

In order to achieve targets appointed in the dissertation work, several experimental and numerical methods and techniques were applied during the research. Main experimental measuring methods used were weight readings for coarse and fine fraction splits, pressure readings taken by digital manometer, particle size analysis established by Microtrac and velocity vector map readings realized by particle image velocimetry method (PIV). Limitations of these methods are summarized below:

- Error introduced by inaccuracy of digital scales used for taking weight readings of fine and coarse fraction which were used for Tromp curve plots.
- Error introduced by inaccuracy of dynamic pressure readings taken and converted into air inlet velocity values by digital manometer. Significantly increased accuracy would be achieved by application of PIV method to establish velocity profiles in the air inlet duct for velocity inlet boundary condition in numerical simulations.
- Error introduced by inaccuracy of dry laser diffraction method (Microtrac) which was used to establish particle size distribution curves. Wet process provides more accurate readings for powder materials with particle sizes below 10 microns.
- Error introduced by inaccuracy of particle image velocimetry (PIV). Accuracy of optical assembly was slightly reduced by installation of two windows (camera and laser access) which were required to contain seeding particles inside of the air classifier. Special optical lens (Scheimpflug) was used in order to compensate for angle between camera plane and investigated plane. Constant seeding was required in order to provide enough particles for the measurement. This was caused by the fact that the classifier was separating oil droplets from the flow. These droplets were then trapped by walls. Due to metal construction of classifier, there was an increased amount of reflections and background noise. Simpler calibration method (direct measurement and scaling instead of calibration plate) was used due to limited access to investigated area in the classifier.
- A considerable amount of reflections of laser sheet from metal parts of the classifier, especially rotor blades was responsible for increased background noise.
- 100% alignment of blade passage with field of view of camera and laser sheet was not possible due to manual locking of the assembly and its geometrical realities. This resulted into increased amount of laser sheet reflections from further end of trailing blades.
- Finer control volumes of the mesh and better structuring are required for simulations where completely turbulent flows with high velocities are anticipated.

12 CONCLUSION

This dissertation work analyses current state of knowledge in dynamic air classification field and reviews literature in the area available up to date of the work. The most important operating parameters affecting particle classification are identified and decomposed onto their fundamental effects in theoretical section of the work. Air classifier performance predicting equations and numerical models are summarized.

CFD simulations were carried out to investigate flow field patterns and mechanisms of a dynamic air classifier that limit ultrafine particle classification. Particle trajectories were tracked for barite feed material with particle size distribution as used in the experimental section.

Particle image velocimetry (PIV) state of the art visualization technique was implemented into classifier setup in a challenging environment. The actual velocity profiles, vortex structures and velocity magnitudes in the blade passageway region are measured, visualized and analysed. The results present a unique information dataset and it extends current knowledge of dynamic air classification process and explain dependency of flow structures on operating parameters.

Classification trials with barite were realized for varying operating parameters and fine and coarse fractions were analysed by laser diffraction method. Limit modes of air classification method are described and generalized.

Specific operating parameters for ultrafine classification are established. Structural parameters of the classifier like blade passageway design, body diameter, feed material feeding distribution and dispersion in an air stream play even more important role in particle classification under 10 microns. Ultimate objective is to achieve uniform flow field without vortexes and recirculation zones present. These turbulent structures are diffusive and chaotic and are causing rapid mixing which negatively affects particle classification. All the above mentioned individual tasks with results form a comprehensive analysis and lay a fundamental basis for dynamic air classifier redesign to overcome current limits of the method.

13 LITERATURE

[1] Altun, O., Benzer, H. (2014). *Selection and mathematical modelling of high efficiency air classifiers*. In: Powder Technology, vol. 264, pp. 1-8.

[2] Bakker, A., Haidari, A., H., Oshinowo, L., M. (2001). *Realize greater benefits from CFD*. In: AIChE Journal, vol. 47, pp. 45-53.

[3] Boysan, F., Ayers, W., H., Swithenbank, J. (1982). *A fundamental mathematical modelling approach to cyclone design*. In: Institution of Chemical Engineers, vol. 60, pp. 222-230.

[4] Dijkink, B. H., Speranza, L., Paltsidis, D., Vereijken, J., M. (2007). *Air dispersion of starch-protein mixtures: A predictive tool for air classification performance.* In: Powder Technology, vol. 172, pp. 113-119.

[5] Eswaraiah, C., Kavitha, T., Vidyasagar, S., Narayanan, S., S. (2008). *Classification of metals and plastics from printed circuit boards (PCB) using air classifier*. In: Chemical Engineering and Processing, vol. 47, pp 565-576.

[6] Eswaraiah, C., Narayanan, S., S., Jayanti, S. (2008). *A reduced efficiency approach-based process model for a circulating air classifier*. In: Chemical Engineering and Processing, vol. 47, pp. 1887-1900.

[7] Feng, Y., Liu, J., Liu, S. (2008). *Effects of operating parameters on flow field in a rotor air classifier*. In: Minerals Engineering, vol. 21, pp. 598-604.

[8] Galk, J., Peukert, W., Krahnen, J. (1999). *Industrial classification in a new impeller wheel classifier*. In: Powder Technology, vol. 105, pp. 186-189.

[9] Gao, L., Yu, Y., Liu, J. (2013). *Study on the cut size of a rotor air classifier.* In: Powder Technology, vol. 237, pp. 520-528.

[10] Griffiths, W., D., Boysan, F. (1996). *Computational fluid dynamics (CFD) and empirical modelling of the performance of a number of cyclone samplers.* In: Journal of Aerosol Science, vol. 27, no. 2, pp. 281-304.

[11] Guizani, R., Mokni, I., Mhiri, H., Bournot, P. (2014). *CFD modelling and analysis of the fish-hook effect on the rotor separator's efficiency*. In: Powder Technology, vol. 264, pp. 149-157.

[12] Guo, L., Liu, J., Liu, S., Wang, J. (2007). *Velocity measurements and flow field characteristic analyses in a rotor air classifier*. In: Powder Technology, vol. 178, pp. 10-16.

[13] Hideghéty, A. (2013). *Suspension flow modelling*. Master Thesis, Brno University of Technology, Faculty of Mechanical Engineering, Energy Institute.

[14] Hoekstra, A., J., Derksen, J., J., Van Den Akker, H., E., A. (1999). *An experimental and numerical study of turbulent swirling flow in gas cyclones.* In: Chemical Engineering Science, vol. 54, pp. 2055-2065.

[15] Holdich, R., G. (2002). *Fundamentals of Particle Technology*. Midland Information Technology and Publishing.

[16] Huang, Q., Liu, J., Yu, Y. (2012). *Turbo air classifier guide vane improvement and inner flow field numerical simulation.* In: Powder Technology, vol. 226, pp. 10-15.

[17] Chase, G., G., (2012). Solids notes 11. The University of Akron

[18] Jiao, J., Zheng, Y., Sun, G., Wang, J. (2006). *Study on the separation efficiency and the flow field of a dynamic cyclone*, vol. 49, pp. 157-166.

[19] Johansen, S., T., Silva, S., R. (1996). *Some considerations regarding optimum flow fields for centrifugal air classification.* In: International Journal of Mineral Processing, vol. 44-45, pp. 703-721.

[20] Karunakumari, L., Eswaraiah, C., Jayanti, S., Narayanan, S., S. (2005). *Experimental and numerical study of a rotating wheel air classifier*. In: American Institute of Chemical Engineers Journal, vol. 51, no. 3, pp. 776-790.

[21] Kim, J., C., Lee, K., W. (1990). *Experimental study of particle collection by small cyclones.* In: Aerosol Science and Technology, vol. 12, no. 4, pp. 1003-1015.

[22] Klumpar, I., V., Currier, F., N., Ring, T., A. (1986). *Air Classifiers*. In: Chemical Engineering, pp 77-92.

[23] Kolacz, J. (2002). *Investigating flow conditions in dynamic air classification*. In: Minerals Engineering, vol. 15, pp. 131-138.

[24] Leschonski, K. (1996). *Classification of particles in the submicron range in an impeller wheel air classifier*. In: KONA Powder and Particle Journal, no. 14, pp. 52-60.

[25] Liu, S., Liu, J., Guo, L. (2006). *Study on theoretical cut size of rotor air classifier*. In: Non-Ferrous Mining and Metallurgy, vol. 22, pp. 138-140.

[26] Liu, R., Liu, J., Yu, Y. (2015). *Effects of axial inclined guide vanes on a rotor air classifier*. In: Powder Technology, vol. 280, pp. 1-9.

[27] Powtech 83: *Particle technology* – (The Institute of Chemical Engineers symposium series, ISSN 0307 – 0492, 69).

[28] Shapiro, M., Galperin, V. (2005). *Air classification of solid particles: a review*. In: Chemical Engineering and Processing, vol. 44, pp. 279-285.

[29] Toneva, P., Wirth, K., Peukert, W. (2011). *Grinding in an air classifier mill – part II: Characterisation of the two-phase flow.* In: Powder Technology, vol. 211, pp. 28-37.

[30] Yu, Y., Liu, R., R., Liu, J. (2014). *Correspondence analysis and establishment of evaluation model of classification performance indices for a rotor air classifier*. In: Marerialwissenschaft und Werkstifftechnik, vol. 45, no. 10, pp. 900-911.

[31] Yu, Y., Liu, J., Zhang, K. (2014). *Establishment of a prediction model for the cut size of rotor air classifier.* In: Powder Technology, vol. 254, pp. 274-280.

[32] Wang, Q., Melaaen, M., Silva, S., R. (2001). *Investigation and simulation of a cross-flow air classifier.* In: Powder Technology, vol. 120, pp. 273-280.

[33] Zhang, Y., Tieming, W. (1999). *Study on the critical grading size of pulverizer with vertical axes.* In: Food and Machinery, vol. 5, pp. 40-41.

[34] Adamčík, M. (2010). *Mechatronics of classifying of micro particles by air separation.* University of Technology, Brno.

[35] Kolb, D., A. (1984). *Experiential learning: experience as the source of learning and development*. Pearson Education Inc., Upper Saddler River. New Jersey.

[36] Johansson, R., Evertsson, M. (2012). *CFD simulation of a gravitational air classifier*. In: Minerals Engineering, vol. 3, pp. 20-26.

[37] Wang, Q., Melaaen, M., Chr., Silva, S., R. (2001). *Investigation and simulation of a cross-flow air classifier*. In: Powder Technology, vol. 120, pp. 273-280.

[38] Bernotat, S., Umhauer, H. (1973). *Application of spark tracing method to flow measurements in an air classifier*. In: Opto-electronics, vol. 5, pp. 107-118.

[39] Bomelburg, H., J., Herzog, J., R., Weske, J., R. (1959). *The electric spark method for quantitative measurements in flowing gases*. In: Z. Flugwiss, vol. 7, pp. 322-329.

[40] Yu, Y., Saadat, M., Untaroiu, A., Thomas, B., R., Wood, H., G. (2016). *Prediction of Turbo air classifier cut size based on particle trajectory*. In: ASME Turbo Expo 2016: Turbomachinery Technical Conference and Exposition, vol. 6.

[41] Liu, Z., Zheng, Y., Jia, L., Zhang, Q. (2007). *An experimental method of examining three-dimensional swirling flows in gas cyclones by 2D-PIV*. In: Chemical Engineering Journal, vol. 133, pp. 247-256.

[42] Xing, W., Wang, Y., Zhang, Y., Yamane, Y., Saga, M., Lu, J., Zhang, H., Jin, Y. (2015). *Experimental study on velocity field between two adjacent blades and gas–solid separation of a turbo air classifier*. In: Powder Technology, vol. 286, pp. 240-245.

[43] Miyazaki, K., Chen, G., Yamamoto, F., Ohta, J., Murai, Y., Horri, K. (1999). *PIV measurement of particle motion in spiral gas solid two-phase flow*. In: Experimental thermal and fluid science, vol. 19, pp. 194-203.

[44] Liu, Z., Zheng, Y., Jia, L., Jiao, J., Zhang, Q. (2006). *Stereoscopic PIV studies on the swirling flow structure in a gas cyclone*. In: Chemical Engineering Science, vol. 61, pp. 4252-4261.

[45] Toneva, P., Epple, P., Breuer, M., Peukert, W., Wirth, K. (2011). *Grinding in an air classifier mill – part I: Characterisation of the one-phase flow.* In: Powder Technology, vol. 211, pp. 19-27.

[46] Xia, B., Chen, Y., Chen, B. (2015). *Numerical Simulation Analysis of Ultrafine Powder Centrifugal Classifier*. In: 5th International Conference on Information Engineering for Mechanics and Materials, pp. 216-221.

[47] Wang, X., Ge, X., Zhao, X., Wang, Z. (1998). *A model for performance of the centrifugal counter current air classifier*. In: Powder Technology, vol. 98, pp. 172-176.

[48] Xu, N., Li., G., Huang, Z. (2005). *Numerical simulation of particle motion in turbo classifier.* In: China Particulogy, vol. 3, no. 5, pp. 275-278.

[49] Ren, W., Liu, J., Yu, Y. (2016). *Design of a rotor cage with non-radial arc blades for turbo air classifiers*. In: Powder Technology, vol. 292, pp. 46-53.

[50] Wang, X., Ge, X., Zhao, X., Wang, Z. (1999). *Study on horizontal turbine classification*, vol. 102, pp. 166-170.

[51] Snow, R. H., Allen, T., Ennis, B. J., Litster, J. D. (1984). *Size reduction and size enlargement*. In: Microscope.

[52] Sun, Z., Sun, G., Yang, X., Yuan, Y., Wang, Q., Liu, J. (2017). *Effects of fine particle outlet on performance andflow field of a centrifugal air classifier.* In: Chemical Engineering Research and Design, vol. 117, pp. 139-148.

[53] Buffalo Forge Company, Edited by Robert Jorgensen (1983). *An Engineer's HandbookOn Fans and Their Applications, Eighth Edition.* In: Fan Engineering, Buffalo New York

[54] Abubakar G. Salisu, Yagana B. Abba, Zarah Mohammed (2015). *Environmental and health hazards associated with exploration of barite from Bukkuyum (Zamfara State), Nigeria.* In: Academic Journals, vol. 2(3), pp. 11-15

[55] Microtrac Inc. (2008). *Microtrac Flex Software Operations manual Rev. O,* Images used courtesy of MICROTRAC, Inc.

[56] Moukalled, F., Mangani, L., Darwish, M. (2016). *The Finite Volume Method in Computational Fluid Dynamics,*vol 113

[57] Ansys Inc. (2009), *Ansys Fluent 12.0 Theory guide*, Images used courtesy of ANSYS, Inc.

[58] Versteeg, H.K., Malalasekera, W. (1995). *An Introduction to Computational Fluid Dynamics*

[59] Morsi, S. A., Alexander, A. J., (1972). *An Investigation of Particle Trajectories in Two-Phase Flow Systems.* In: J. Fluid Mech., vol.55, no.2, pp. 193-208.

[60] NASA-Drag of a sphere [Online], [cited 16.06.2017]. Available from: https://www.grc.nasa.gov/www/k-12/airplane/dragsphere.html

[61] Ounis, H., Ahmadi, G., McLaughlin J. B. (1991). *Brownian Diffusion of Submicrometer Particles in the Viscous Sublayer*.In: Journal of Colloid and Interface Science., vol 143(1), pp 266-277
[62] Haide, A., Levenspiel, O. (1989). *Drag Coefficient and Terminal Velocity of Spherical and Nonsherical Particles.*In: Powder Technology., vol 58, pp 63-70
[63] Haldich, R. G. (2002). *Fundamentals of particle technology.*
[64] Dantec - Measurement principles of PIV [Online], [cited 12.07.2017]. Available from: https://www.dantecdynamics.com/measurement-principles-of-piv
[65] LaVision GmbH. (2017). Flow master DaVis 8.4 product manual

Author's publications

- Adamčík, M., Svěrák, Peciar, P.: *Parameters effecting forced vortex formation in blade passageway of dynamic air classifier*. In print: Acta Polytechnica
- Adamčík, M., Svěrák, Raudenský, M.: *Flow structure and particle trajectories in blade passageway of rotor air classifier*. Submitted to Journal: Advanced Powder Technology

Other publications

- Sverak, T., Bulejko, P., Ostrezi, J., Kristof, O., Kalivoda, J., Kejik, P., Mayerova, K. and Adamcik, M.: *Separation of gaseous air pollutants using membrane contactors.* Full text: Proceedings of 1th International conference AEE 2017 VŠB Ostrava, November 2017
- Bulejko, P., Sverak, T., Kalivoda, J., Kristof, O., Kejik, P., Mayerová, K., Adamčík, M.: *Separace partikulárních nanočástic ze vzdušin na dutých symetrických PP membránách.* Proceedings 64. konference chemického a procesního inženýrství CHISA 23.-26. října 2017, wellness hotel Jezerka, přehrada Seč v Železných horách, Abstrakt, V57 ČSCHI a Orgit, Praha, 2017

Active participation in exhibitions & congresses & seminars and consultations

- Active participation in Powtech 2008, Nuremberg, Germany (Powtech is a leading event in the world of powder, granule and bulk solids technologies. It reflects the current state of the art in mechanical processing technologies and instrumentation)
- Active participation in Powtech 2010, Nuremberg, Germany
- Active participation in Powtech 2011, Nuremberg, Germany
- Active participation in Powtech&Partec 2013, Nuremberg, Germany
- Oilfield minerals outlook- propant prospects for Europe 2013, London, United Kingdom
- Active participation in International Engineering Fair 2013, Brno, Czech Republic
- Active participation in Hillhead quarrying & construction & recycling 2014, Buxton, United Kingdom
- Active participation inSalima International Food Fair, Brno, Czech Republic
- Active participation in Powtech 2015, Nuremberg, Germany
- Pneumatic conveying seminar 2016, Institution of Mechanical Engineers, London, United Kingdom
- Active participation in Powtech&Partec 2017, Nuremberg, Germany
- Victor Kaplan Department of Fluid Engineering 2016, Brno University of Technology, Czech Republic
- Wolfson Centre for Bulk Solids Handling 2017, University of Greenwich, London, United Kingdom
- Department of Biomedical Enginering and Mechanics 2017, VirginiaTech University, Blacksburg, United States of America

Bradley
PULVERIZER COMPANY
INCORPORATED WITH LIMITED LIABILITY IN U.S.A.

15 KENNET ROAD
CRAYFORD, GREATER LONDON
DA1 4QN; UNITED KINGDOM

Tel: +44 1322 559106
Fax: +44 1322 528690
mail@bradleypulverizer.co.uk
www.bradleypulverizer.co.uk

INTERSHIP REPORT

Start date: 01.09. 2012
Finish date: 01.02.2014
Duration: 18 months

I would like to hereby confirm that during the above mentioned period I have lived and worked for American Company and Research Facility based in London. There I was working as a member of a team or as a leader on following projects related to subject industry sector.

Air classifier rotor dynamics and vibration study

The aim was to study dynamic behaviour of classifier rotor system. To study steady and transient state rotor responses. To study construction of parts, shafts, effects on bearings, non-linear coupling forces between rotating and static parts for further modal analysis.

Stress analysis and FEM method Ansys/Inventor

The aim was to model up critical parts (shaft, bearing housing, bearings, rotor cage, etc.) of the rotor system of the classifier in 3D. Stress analysis was then carried out on those parts using Finite Element Method. Two software packages (Ansys Workbench / Autodesk Inventor Stress Analysis Environment) were used and the results were compared.

Modal & harmonic frequency analysis (Air Classifier) Ansys/Autodesk

The aim was to study and minimize machine vibrations and acoustics. Objects were realized by modelling various Air Classifiers in 3D environments (Autodesk Inventor – Product Design Suite). Those were afterwards imported into Ansys Workbench where modal and harmonic simulations were carried out to learn about natural frequencies and natural shapes of vibrationsof devices. Based on findings of the simulations and experiments, classifier features have been redesigned to minimize negative effects of vibrations on the equipment.

Fluid flow analysis and CFD method Ansys Fluent

Developing suitable 3D models to simulate flow through the classifier. Simulating fluid flow through the classifier with known boundary conditions by using Ansys Fluent. Injecting particles, tracking and studying trajectories. Creating section views with velocity and pressure profiles. So far without rotating structures, ongoing.

Kinematic and dynamic simulations

Creating functional 3D assemblies of classifiers, mills, mixers and simulating kinematic and dynamic behaviour of new devices. Working in a team to achieve pre-set design parameters by using data obtained from simulations.

Development of new equipment

Requirements for a higher capacity grinding equipment or a more cost effective way of producing fertilizers have arisen. Working as a member of a team on a development of new equipment to meet pre-set process requirements.

Classification tests

Member of a team, carrying out classification tests on powder products of different clients. Tests were carried out on a test plant. Determining correct process settings to achieve parameters required by client.

Particle size analysis and Laser vs. sieve analysis

Working with Microtrac tri-laser diffraction analyzer carrying out particle size analysis. Studying different particle size distribution curves in conjunction with classification tests. Carrying out sieve analysis.

10th of April 2015, London

BRADLEY PULVERIZER COMPANY

Vice President

MARTIN ADAMCIK

Some of the projects realized by the author of this work

P623 - MS20 Classification system

Design, procurement and project management of a closed circuit classification system with capability to separate 3 fractions with automatic control of airflows through different loops of the system realized by actuated dampers. Various product grades from different particle discharge points of the system and corresponding operating parameters were established during commissioning with recipe like settings for easy change over between desired products. Project was realized for European client.

P624 - 82 000 m3/hr Cyclone

Design of a static cyclonic separation device with constrained volumetric air flow rate and particle loading which was implemented into an existing plant. Some of the requirements raised by client were low pressure drop and high collection efficiency for fine particles. Project was realized for Middle Eastern client.

P626 - Vacuum conveying system

Implementation and commissioning of dilute phase conveying system into an existing plant grinding an extremely abrasive catalytic converter to specific fine particle distribution requirements for later purification process. Project was realized in the United Kingdom.

P628 BM20 Grinding circuit

Design and project management of a closed grinding circuit with 22 TPH throughput. Circuit was simultaneously drying and particle distribution was controlled by VBC classifier located on top of the mill. Project was realized for client in Asia.

P629 MS5 Classification system

Responsible for design, procurement and project management of a closed circuit classification system realized as a compact skid mounted version. Project was realized in the United Kingdom.

P630 Complete fertilizer plant

Responsible for design, procurement and project management of key systems of SSP & TSP fertilizer producing plant. These include feed material intake system, grinding circuit, powder and product handling, acid storage and dilution, reactor mixer unit, piping and instrumentation and scrubbing unit. Involved in design and implementation of 3 stage scrubbing unit to reduce emissions of silicon tetrafluoride. Special requirements of particle distribution of ground phosphate were imposed. Greater surface area of powder results into faster and more complete chemical reaction with acid whilst too fine powder results into compromised operation and reduced efficiency of the scrubbing unit. Project was realized in Africa.

P635 MS100 Classification system

Responsible for design, procurement and project management of a closed-circuit classification system with special abrasion resistant lining. Throughput of the plant was 100 TPH of fly ash and the project was realized in Asia.

P638 VBC100 Inline classifier

Responsible for design, procurement and project management of an inline dynamic air classifier which was implemented into an existing operation with limiting operating conditions. Project was realized in Europe.

P639 VBC50 Inline classifier

Responsible for design, procurement and project management of an inline dynamic air classifier which was implemented into an existing operation with limiting operating conditions. Project was realized in Africa.

P640- P642 2xBM20 & BM6 Circuits

Responsible for design, procurement and project management of 3 independent grinding circuits with dynamic air classifiers controlling parameters of particle size distribution of the product. Project was realized in Africa.

P643 BM10 Grinding circuit

Responsible for design, procurement and project management of grinding circuit with dynamic air classifier controlling parameters of product. Air flows through different loops of the system were controlled automatically by actuated dampers for various products and dense phase conveying was used for final product conveying. Project was realized in the United Kingdom.

P645 MS20 Classification system

Responsible for design, implementation and commissioning of a closed circuit classification system into existing operation with special focus on increased classification efficiency and reduced by-pass of the system. Project was realized in the United Kingdom.

P646 3xBM60 Grinding circuit

Responsible for design and implementation of 3 closed grinding and drying grinding circuits. Total throughput of all 3 lines was 400 TPH and parameters of the product were controlled by static air classifiers. Project was realized in Africa.

P651 VBC50 Inline classifier

Responsible for design, procurement and implementation of an inline dynamic air classifier with strict conditions on very fine particle size distribution due to process requirements in oil industry. Project was realized in the United Kingdom.

14 NOMENCLATURE

A	[m2]	cross section area of particle
c	[m/s]	speed of sound in the medium
C_c		Cunningham correction factor to Stokes drag law
C_d& C_D		drag coefficient
C_f		skin friction
D or d	[m]	diameter
$\bar{d}$	[m]	mean diameter
d_{50}&d_{cut}	[m]	cut size
$D_p$ord_p	[m]	particle diameter
du	[m/s]	velocity
dy	[m]	coordinate in direction perpendicular to flow direction
e_n		normal coefficient or restitution and it defines the amount momentum preserved after collision
E_T		deviation
F	[N]	force
f	[Hz]	frequency
f_c		relative frequency of particles size x
$F_c$or F_C	[N]	centrifugal force
f_{cx}		relative frequency of coarse particles of size x
$F_d$or F_D	[N]	drag force
F_{Cor}	[N]	Coriolis force
$F_g$of F_G	[N]	gravitational force
G	[N]	gravitational force
g	[m/s2]	gravitational acceleration
G_k		generation of turbulent kinetic energy due to mean velocity gradient
G_b		generation of turbulent kinetic energy due to buoyancy
G(x)		grade efficiency
k	[J/kg]	turbulent kinetic energy
M	[kg]	mass
M_p	[kg]	particle mass
M_c	[kg]	mass of coarse particles
M_f	[kg]	mass of fine particles
n		spread diameter
N	[RPM]	rotational speed
P	[Pa]	pressure
P_S	[Pa]	static pressure
P_T	[Pa]	total pressure
P_R	[kW]	shaft power
P_M	[kW]	rated power
ρ	[kg/m3]	density
ρ_p	[kg/m3]	density of particles
Q	[m3/s]	air flow rate
r	[m]	rotor radius
r_p	[m]	particle radius
Re		Reynolds number
Re_{SPH}		Reynolds number calculated with diameter of sphere having the same volume

S_d		size selectivity
S		degree of dispersion
t	[s]	time
t	[°C]	temperature
U	[V]	rated voltage
u	[m/s]	velocity
u_P	[m/s]	particle velocity
u_{max}	[m/s]	maximum velocity observed
u_τ	[m/s]	friction velocity
u_e	[m/s]	parallel velocity
V	[m3]	volume
V_p	[%]	volume of particles
v	[m/s]	velocity
v_p	[m/s]	particle velocity
v_{TS}	[m/s]	terminal settling velocity
v_φ	[m/s]	circumferential velocity
v_R or v_{Rel}	[m/s]	relative velocity
v_n	[m/s]	normal component of particle velocity
y	[°]	rotor blade arrangement angle
y	[m]	distance between wall and first centroid
Y_d		represents mass fraction
Y_M		contribution of the fluctuating dilatation in compressible turbulence to the overall
ω	[rad/s]	angular velocity
Ω	[rad/s]	angular velocity
τ_{ij}	[m2/s2]	Reynolds stress tensor
ΔS		size selectivity increment
B		sharpness of separation
δ	[kg/kg]	humidity
η_N		Newton classification efficiency
η		classification sharpness index
μ	[Pa.s]	dynamic/molecular viscosity
τ	[Pa]	shear tensor from viscous stresses
ϕ		flow variable
$\overline{\phi}$		mean value
ϕ'		fluctuating value
μ_t	[m2/s]	turbulent eddy viscosity
δ_{ij}		Kronecker delta
ε	[m2/s3]	dissipation rate
σ_k and σ_ε		turbulent Prandtl numbers
λ		molecular mean free path

15 LIST OF FIGURES

16 LIST OF TABLES

17 ATTACHEMENTS

Tabular data of coarse fraction for classification trial TB1, TB2 and TB3

Size [µm]	TB1		TB2		TB3	
	% Chan	% Pass	% Chan	% Pass	% Chan	% Pass
209.3	0.15	100.00	0.27	100.00	0.35	100.00
176	0.18	99.74	0.39	99.73	0.46	99.55
148	0.21	99.56	0.55	99.34	0.57	99.09
124.5	0.35	99.35	0.68	98.79	0.66	98.52
104.7	0.55	99.00	0.68	98.11	0.73	97.86
88	0.69	98.45	0.61	97.43	0.80	97.13
74	0.87	97.76	0.73	96.82	0.89	96.33
62.23	1.04	96.89	0.88	96.09	1.03	95.44
52.33	1.25	95.85	1.19	95.21	1.24	94.41
44	1.55	94.60	1.70	94.02	1.57	93.17
37	2.04	93.05	2.45	92.32	2.08	91.60
31.11	2.82	91.01	3.41	89.87	2.83	89.52
26.16	4.00	88.19	4.51	86.46	3.86	86.69
22	5.52	84.19	5.69	81.95	5.12	82.83
18.5	7.09	78.67	6.77	76.26	6.39	77.71
15.56	8.14	71.58	7.41	69.49	7.33	71.32
13.08	8.32	63.44	7.48	62.08	7.44	63.99
11	7.70	55.12	7.16	54.60	7.16	56.55
9.25	6.49	47.42	6.27	47.44	6.22	49.39
7.78	5.21	40.93	5.17	41.17	5.11	43.17
6.54	4.10	35.72	4.10	36.00	4.10	38.06
5.5	3.28	31.62	3.25	31.90	3.34	33.96
4.62	2.75	28.34	2.71	28.65	2.88	30.62
3.89	2.52	25.59	2.49	25.94	2.70	27.74
3.27	2.51	23.07	2.51	23.45	2.76	25.04
2.75	2.60	20.56	2.64	20.94	2.93	22.28
2.312	2.63	17.96	2.71	18.30	2.98	19.35
1.945	2.46	15.33	2.54	15.59	2.76	16.37
1.635	2.14	12.87	2.19	13.05	2.34	13.61
1.375	1.85	10.73	1.87	10.86	1.95	11.27
1.156	1.72	8.88	1.72	8.99	1.78	9.32
0.972	1.79	7.16	1.78	7.27	1.85	7.54
0.818	1.92	5.37	1.94	5.49	2.02	5.69
0.688	1.77	3.45	1.81	3.55	1.88	3.67
0.578	1.16	1.68	1.20	1.74	1.24	1.79
0.486	0.52	0.52	0.54	0.54	0.55	0.55

Particle size distribution curve of coarse fraction for classification trial TB1

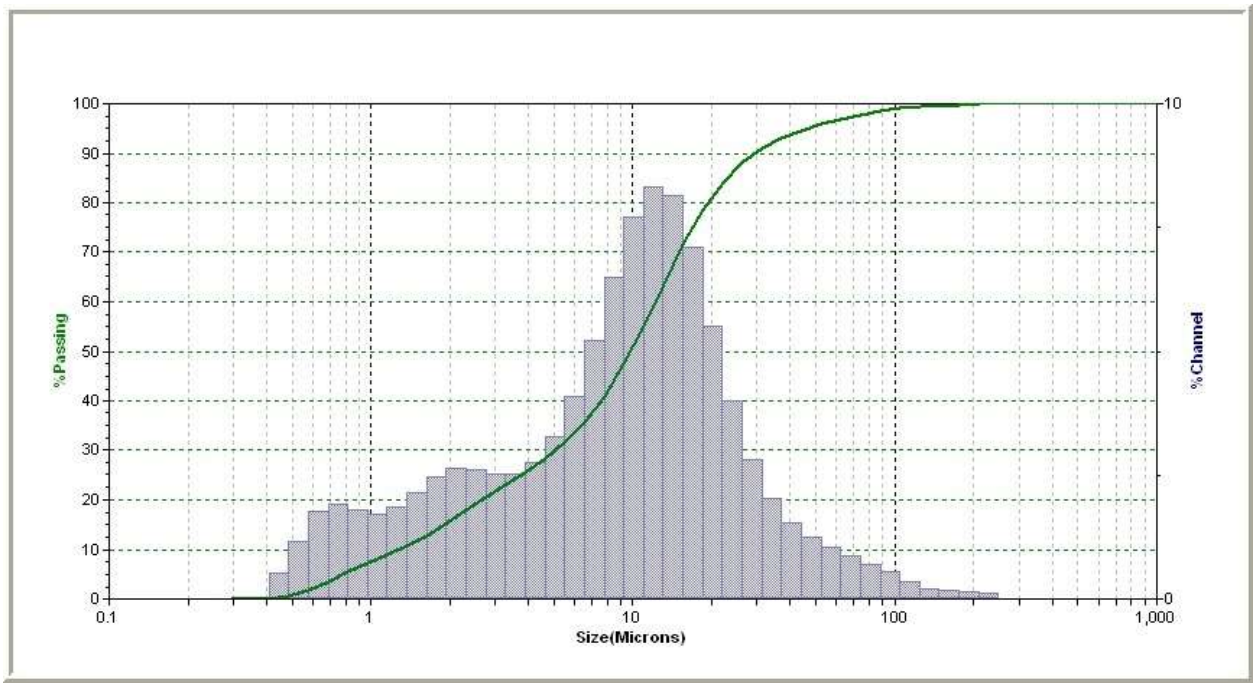

Particle size distribution curve of coarse fraction for classification trial TB2

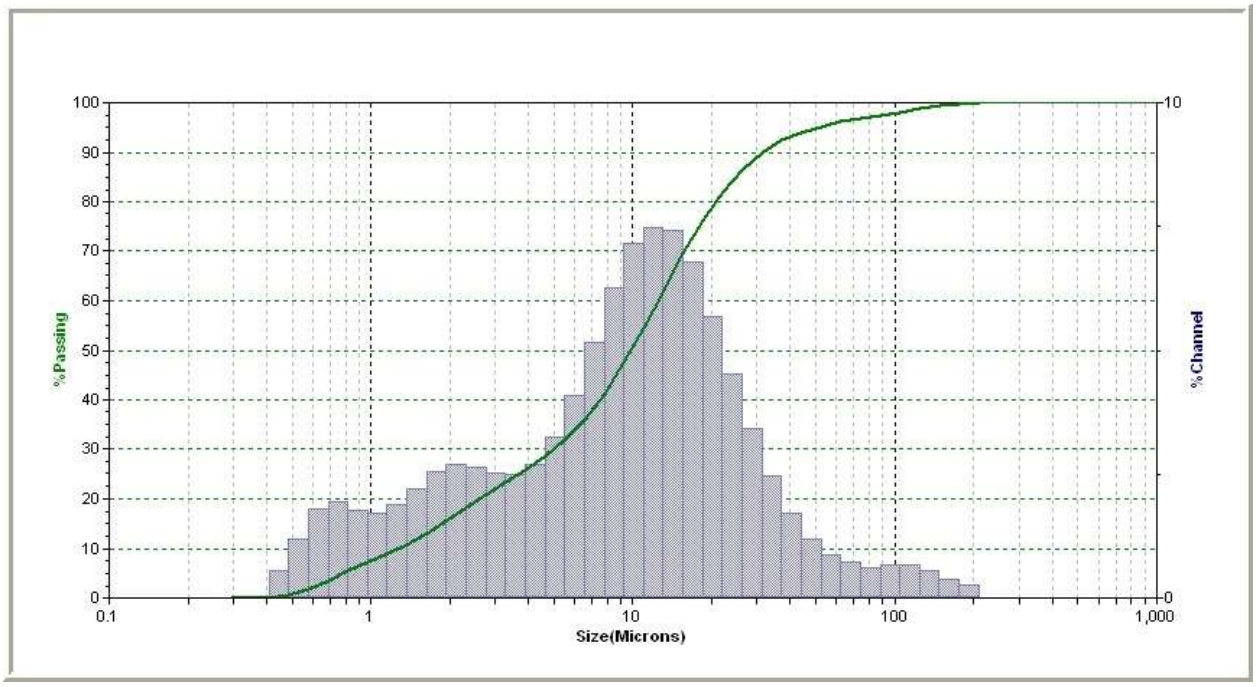

Particle size distribution curve of coarse fraction for classification trial TB3

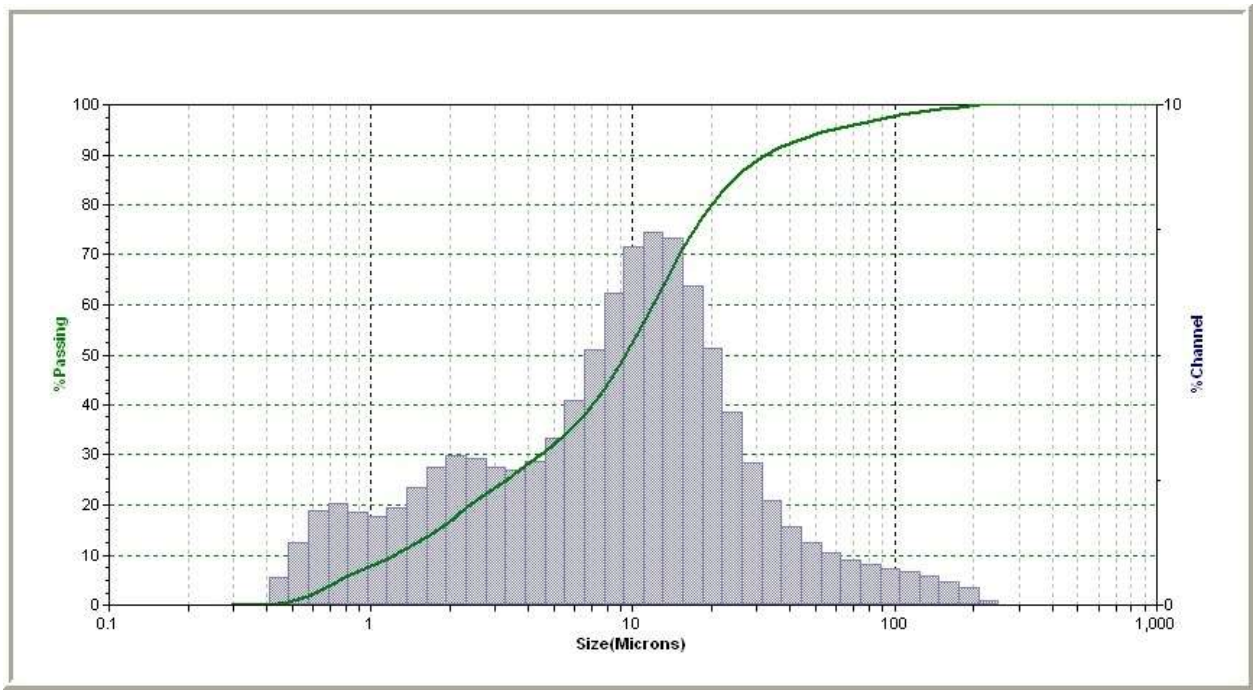

Tabular data for Tromp curve for classification trial TB1

Diameter [µm]	Median	Coarse [%]	Coarse [Kg]	Fines [%]	Fines [Kg]	Feed [Kg]	Tromp	Tromp red.
209.3	166.9	0.00	0.00	0.00	0.0000	0.00	1	1
176		0.18	0.04	0.00	0.0000	0.04		
148		0.21	0.04	0.00	0.0000	0.04		
124.5		0.35	0.07	0.00	0.0000	0.07		
104.7	83.465	0.55	0.12	0.00	0.0000	0.12	1	1
88		0.69	0.15	0.00	0.0000	0.15		
74		0.87	0.18	0.00	0.0000	0.18		
62.23		1.04	0.22	0.00	0.0000	0.22		
52.33	41.72	1.25	0.26	0.00	0.0000	0.26	0.980128	0.933327
44		1.55	0.33	0.00	0.0000	0.33		
37		2.04	0.43	0.38	0.0126	0.44		
31.11		2.82	0.60	0.61	0.0202	0.62		
26.16	20.86	4.00	0.84	0.93	0.0308	0.87	0.966728	0.888368
22		5.52	1.16	1.22	0.0404	1.21		
18.5		7.09	1.50	1.45	0.0480	1.54		
15.56		8.14	1.72	1.83	0.0606	1.78		
13.08	10.43	8.32	1.76	2.65	0.0877	1.84	0.897002	0.654427
11		7.70	1.62	4.17	0.1380	1.76		
9.25		6.49	1.37	6.14	0.2032	1.57		
7.78		5.21	1.10	7.33	0.2426	1.34		
6.54	5.215	4.10	0.87	7.36	0.2436	1.11	0.774861	0.244624
5.5		3.28	0.69	6.27	0.2075	0.90		
4.62		2.75	0.58	5.18	0.1715	0.75		
3.89		2.52	0.53	4.62	0.1529	0.68		
3.27	2.6075	2.51	0.53	4.72	0.1562	0.69	0.737693	0.119921
2.75		2.60	0.55	5.39	0.1784	0.73		
2.312		2.63	0.55	6.28	0.2079	0.76		
1.945		2.46	0.52	6.73	0.2228	0.74		
1.635	1.3035	2.14	0.45	6.31	0.2089	0.66	0.701951	9.03E-07
1.375		1.85	0.39	5.35	0.1771	0.57		
1.156		1.72	0.36	4.54	0.1503	0.51		
0.972		1.79	0.38	4.10	0.1357	0.51		
0.818	0.652	1.92	0.41	3.57	0.1182	0.52	0.841659	0.468742
0.688		1.77	0.37	2.20	0.0728	0.45		
0.578		1.16	0.24	0.67	0.0222	0.27		
0.486		0.52	0.11	0.00	0.0000	0.11		

Tabular data for Tromp curve for classification trial TB2

Diameter [µm]	Median	Coarse [%]	Coarse [Kg]	Fines [%]	Fines [Kg]	Feed [Kg]	Tromp	Tromp red.
209.3	166.9	0.27	0.06	0.00	0.0000	0.06	1	1
176		0.39	0.09	0.00	0.0000	0.09		
148		0.55	0.12	0.00	0.0000	0.12		
124.5		0.68	0.15	0.00	0.0000	0.15		
104.7	83.465	0.68	0.15	0.00	0.0000	0.15	1	1
88		0.61	0.13	0.00	0.0000	0.13		
74		0.73	0.16	0.00	0.0000	0.16		
62.23		0.88	0.19	0.00	0.0000	0.19		
52.33	41.72	1.19	0.26	0.00	0.0000	0.26	0.983136	0.937771
44		1.70	0.37	0.00	0.0000	0.37		
37		2.45	0.54	0.45	0.0117	0.55		
31.11		3.41	0.75	0.82	0.0213	0.77		
26.16	20.86	4.51	0.99	1.29	0.0335	1.03	0.969272	0.886611
22		5.69	1.25	1.63	0.0424	1.29		
18.5		6.77	1.49	1.74	0.0452	1.53		
15.56		7.41	1.63	1.88	0.0489	1.68		
13.08	10.43	7.48	1.65	2.31	0.0601	1.71	0.933581	0.75491
11		7.16	1.58	3.21	0.0835	1.66		
9.25		6.27	1.38	4.52	0.1175	1.50		
7.78		5.17	1.14	5.66	0.1472	1.28		
6.54	5.215	4.10	0.90	5.91	0.1537	1.06	0.844053	0.424551
5.5		3.25	0.72	5.25	0.1365	0.85		
4.62		2.71	0.60	4.41	0.1147	0.71		
3.89		2.49	0.55	4.05	0.1053	0.65		
3.27	2.6075	2.51	0.55	4.43	0.1152	0.67	0.782849	0.198703
2.75		2.64	0.58	5.55	0.1443	0.73		
2.312		2.71	0.60	6.93	0.1802	0.78		
1.945		2.54	0.56	7.50	0.1950	0.75		
1.635	1.3035	2.19	0.48	7.10	0.1846	0.67	0.729832	0.003071
1.375		1.87	0.41	6.04	0.1570	0.57		
1.156		1.72	0.38	5.34	0.1388	0.52		
0.972		1.78	0.39	5.20	0.1352	0.53		
0.818	0.652	1.94	0.43	4.87	0.1266	0.55	0.841039	0.41343
0.688		1.81	0.40	3.05	0.0793	0.48		
0.578		1.20	0.26	0.86	0.0224	0.29		
0.486		0.54	0.12	0.00	0.0000	0.12		

Tabular data for Tromp curve for classification trial TB3

Diameter [µm]	Median	Coarse [%]	Coarse [Kg]	Fines [%]	Fines [Kg]	Feed [Kg]	Tromp	Tromp red.
209.3	166.9	0.35	0.08	0.00	0.0000	0.08	1	1
176		0.46	0.11	0.00	0.0000	0.11		
148		0.57	0.13	0.00	0.0000	0.13		
124.5		0.66	0.15	0.00	0.0000	0.15		
104.7	83.465	0.73	0.17	0.00	0.0000	0.17	1	1
88		0.80	0.19	0.00	0.0000	0.19		
74		0.89	0.21	0.00	0.0000	0.21		
62.23		1.03	0.24	0.00	0.0000	0.24		
52.33	41.72	1.24	0.29	0.00	0.0000	0.29	0.998215	0.992917
44		1.57	0.37	0.00	0.0000	0.37		
37		2.08	0.49	0.00	0.0000	0.49		
31.11		2.83	0.66	0.17	0.0032	0.67		
26.16	20.86	3.86	0.90	0.27	0.0051	0.91	0.995123	0.980649
22		5.12	1.20	0.31	0.0059	1.20		
18.5		6.39	1.50	0.41	0.0078	1.50		
15.56		7.33	1.72	0.38	0.0072	1.72		
13.08	10.43	7.44	1.74	0.39	0.0074	1.75	0.986775	0.94752
11		7.16	1.68	0.66	0.0125	1.69		
9.25		6.22	1.46	1.18	0.0224	1.48		
7.78		5.11	1.20	2.05	0.0390	1.23		
6.54	5.215	4.10	0.96	2.96	0.0562	1.02	0.915084	0.663031
5.5		3.34	0.78	3.57	0.0678	0.85		
4.62		2.88	0.67	3.92	0.0745	0.75		
3.89		2.70	0.63	4.43	0.0842	0.72		
3.27	2.6075	2.76	0.65	5.46	0.1037	0.75	0.821822	0.292945
2.75		2.93	0.69	7.08	0.1345	0.82		
2.312		2.98	0.70	8.69	0.1651	0.86		
1.945		2.76	0.65	9.29	0.1765	0.82		
1.635	1.3035	2.34	0.55	8.75	0.1663	0.71	0.748467	0.001855
1.375		1.95	0.46	7.90	0.1501	0.61		
1.156		1.78	0.42	7.67	0.1457	0.56		
0.972		1.85	0.43	8.46	0.1607	0.59		
0.818	0.652	2.02	0.47	8.82	0.1676	0.64	0.81412	0.262379
0.688		1.88	0.44	5.71	0.1085	0.55		
0.578		1.24	0.29	1.47	0.0279	0.32		
0.486		0.55	0.13	0.00	0.0000	0.13		

Tabular data of coarse fraction for classification trial TB4, TB5 and TB2

Size [µm]	TB4		TB5		TB2	
	% Chan	% Pass	% Chan	% Pass	% Chan	% Pass
209.3	0.33	100.00	0.39	100.00	0.27	100.00
176	0.44	99.67	0.51	99.50	0.39	99.73
148	0.57	99.23	0.65	98.99	0.55	99.34
124.5	0.69	98.66	0.76	98.34	0.68	98.79
104.7	0.81	97.97	0.84	97.58	0.68	98.11
88	0.91	97.16	0.91	96.74	0.61	97.43
74	1.03	96.25	0.99	95.83	0.73	96.82
62.23	1.19	95.22	1.14	94.84	0.88	96.09
52.33	1.44	94.03	1.40	93.70	1.19	95.21
44	1.86	92.59	1.83	92.30	1.70	94.02
37	2.54	90.73	2.52	90.47	2.45	92.32
31.11	3.54	88.19	3.50	87.95	3.41	89.87
26.16	4.83	84.65	4.75	84.45	4.51	86.46
22	6.27	79.82	6.12	79.70	5.69	81.95
18.5	7.54	73.55	7.32	73.58	6.77	76.26
15.56	8.31	66.01	7.89	66.26	7.41	69.49
13.08	8.42	57.70	7.96	58.37	7.48	62.08
11	7.93	49.28	7.27	50.41	7.16	54.60
9.25	6.72	41.35	6.02	43.14	6.27	47.44
7.78	5.27	34.63	4.69	37.12	5.17	41.17
6.54	3.94	29.36	3.57	32.43	4.10	36.00
5.5	2.96	25.42	2.79	28.86	3.25	31.90
4.62	2.37	22.46	2.36	26.07	2.71	28.65
3.89	2.07	20.09	2.20	23.71	2.49	25.94
3.27	2.01	18.02	2.26	21.51	2.51	23.45
2.75	2.04	16.01	2.42	19.25	2.64	20.94
2.312	2.04	13.97	2.50	16.83	2.71	18.30
1.945	1.91	11.93	2.36	14.33	2.54	15.59
1.635	1.67	10.02	2.04	11.97	2.19	13.05
1.375	1.45	8.35	1.73	9.93	1.87	10.86
1.156	1.35	6.90	1.59	8.20	1.72	8.99
0.972	1.38	5.55	1.64	6.61	1.78	7.27
0.818	1.46	4.17	1.75	4.97	1.94	5.49
0.688	1.35	2.71	1.63	3.22	1.81	3.55
0.578	0.92	1.36	1.09	1.59	1.20	1.74
0.486	0.44	0.44	0.50	0.50	0.54	0.54

Particle size distribution curve of coarse fraction for classification trial TB4

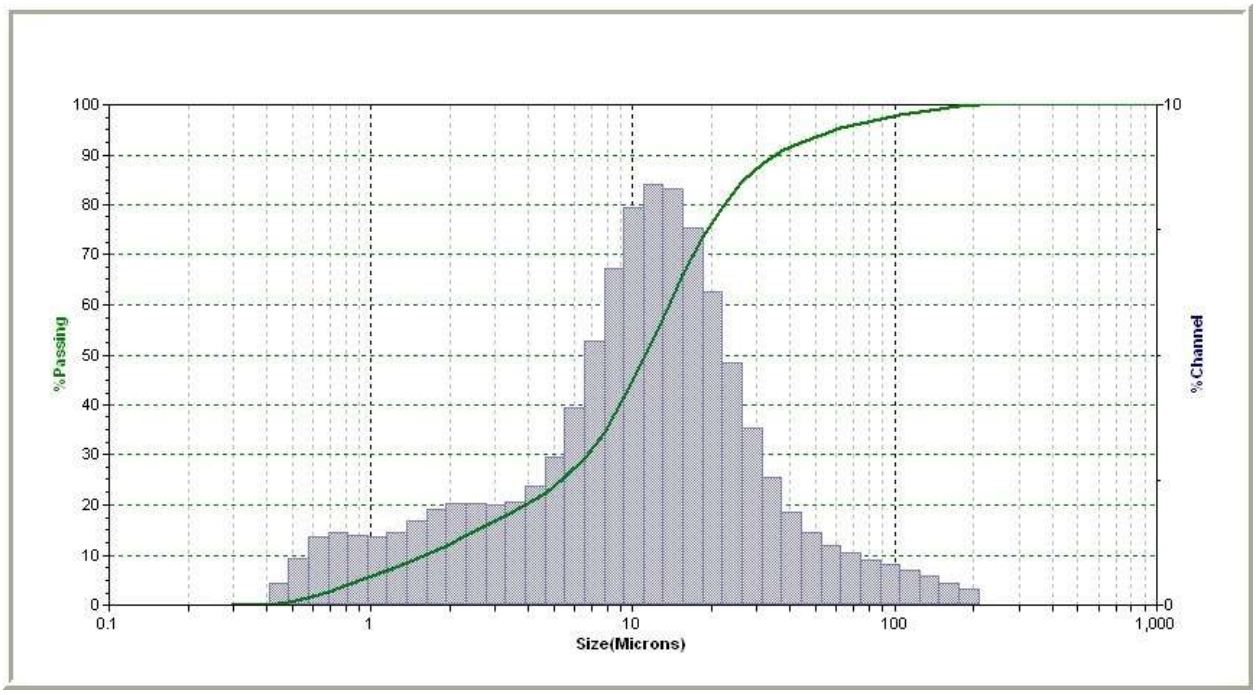

Particle size distribution curve of coarse fraction for classification trial TB5

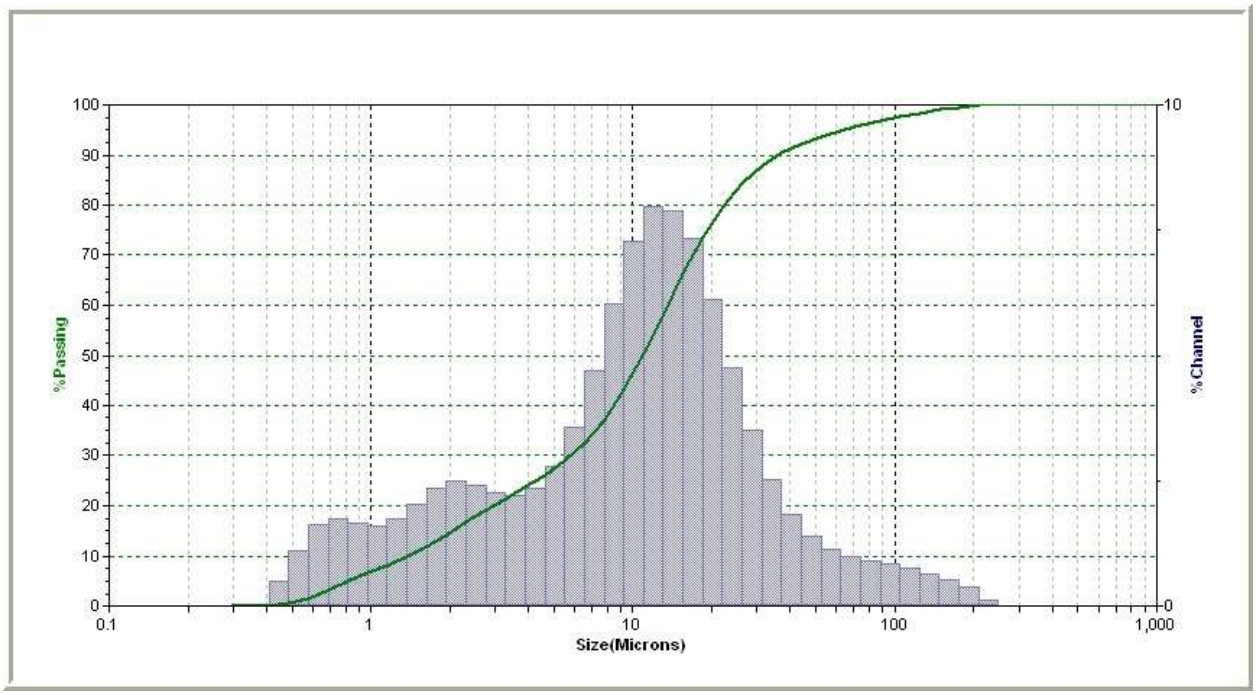

Particle size distribution curve of coarse fraction for classification trial TB2

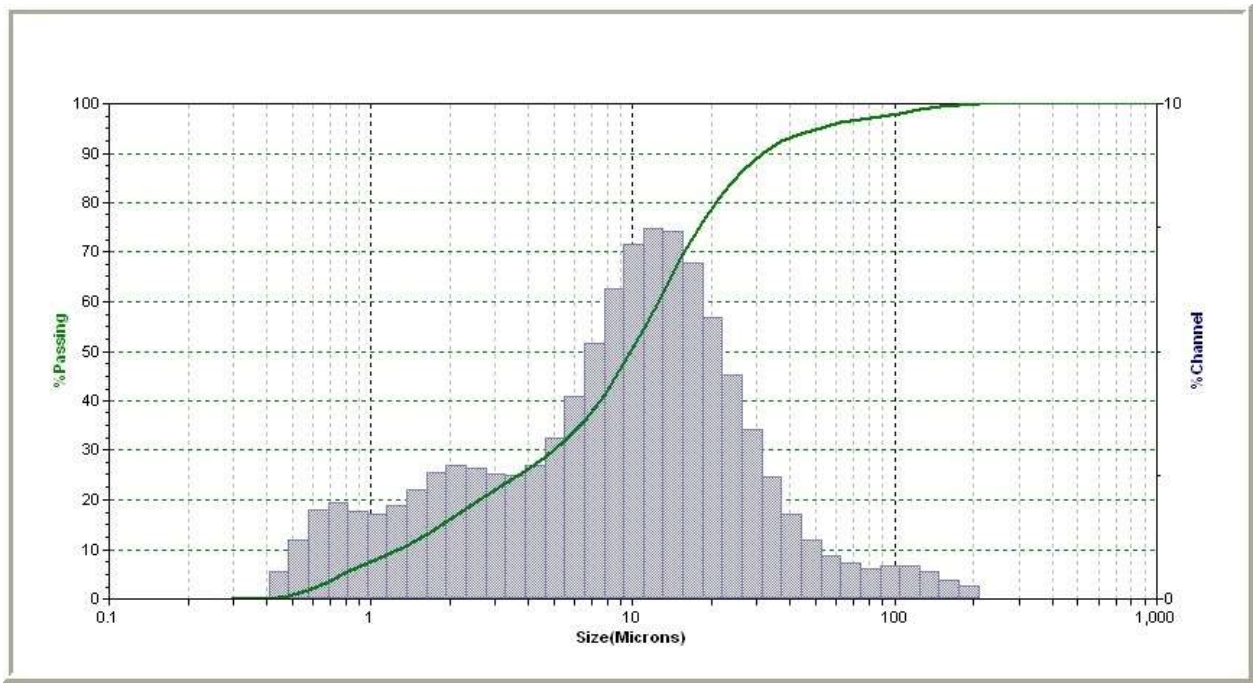

Tabular data for Tromp curve for classification trial TB4

Diameter [µm]	Median	Coarse [%]	Coarse [Kg]	Fines [%]	Fines [Kg]	Feed [Kg]	Tromp	Tromp red.
209.3	166.9	0.33	0.06	0.00	0.0000	0.06	1	1
176		0.44	0.09	0.00	0.0000	0.09		
148		0.57	0.11	0.00	0.0000	0.11		
124.5		0.69	0.14	0.00	0.0000	0.14		
104.7	83.465	0.81	0.16	0.00	0.0000	0.16	1	1
88		0.91	0.18	0.00	0.0000	0.18		
74		1.03	0.20	0.00	0.0000	0.20		
62.23		1.19	0.23	0.00	0.0000	0.23		
52.33	41.72	1.44	0.28	0.00	0.0000	0.28	1	1
44		1.86	0.36	0.00	0.0000	0.36		
37		2.54	0.50	0.00	0.0000	0.50		
31.11		3.54	0.69	0.00	0.0000	0.69		
26.16	20.86	4.83	0.95	0.00	0.0000	0.95	0.972269	0.940414
22		6.27	1.23	0.42	0.0227	1.25		
18.5		7.54	1.48	0.83	0.0448	1.52		
15.56		8.31	1.63	1.54	0.0832	1.71		
13.08	10.43	8.42	1.65	2.79	0.1507	1.80	0.809417	0.590496
11		7.93	1.55	4.83	0.2608	1.82		
9.25		6.72	1.32	7.42	0.4007	1.72		
7.78		5.27	1.03	9.18	0.4957	1.53		
6.54	5.215	3.94	0.77	9.04	0.4882	1.26	0.604494	0.150181
5.5		2.96	0.58	7.39	0.3991	0.98		
4.62		2.37	0.46	5.70	0.3078	0.77		
3.89		2.07	0.41	4.80	0.2592	0.66		
3.27	2.6075	2.01	0.39	4.74	0.2560	0.65	0.563093	0.061223
2.75		2.04	0.40	5.30	0.2862	0.69		
2.312		2.04	0.40	6.07	0.3278	0.73		
1.945		1.91	0.37	6.42	0.3467	0.72		
1.635	1.3035	1.67	0.33	5.97	0.3224	0.65	0.534665	0.00014
1.375		1.45	0.28	4.99	0.2695	0.55		
1.156		1.35	0.26	4.06	0.2192	0.48		
0.972		1.38	0.27	3.46	0.1868	0.46		
0.818	0.652	1.46	0.29	2.85	0.1539	0.44	0.749821	0.462443
0.688		1.35	0.26	1.69	0.0913	0.36		
0.578		0.92	0.18	0.51	0.0275	0.21		
0.486		0.44	0.09	0.00	0.0000	0.09		

Tabular data for Tromp curve for classification trial TB5

Diameter [µm]	Median	Coarse [%]	Coarse [Kg]	Fines [%]	Fines [Kg]	Feed [Kg]	Tromp	Tromp red.
209.3	166.9	0.39	0.08	0.00	0.0000	0.08	1	1
176		0.51	0.10	0.00	0.0000	0.10		
148		0.65	0.13	0.00	0.0000	0.13		
124.5		0.76	0.15	0.00	0.0000	0.15		
104.7	83.465	0.84	0.17	0.00	0.0000	0.17	1	1
88		0.91	0.18	0.00	0.0000	0.18		
74		0.99	0.20	0.00	0.0000	0.20		
62.23		1.14	0.23	0.00	0.0000	0.23		
52.33	41.72	1.40	0.28	0.00	0.0000	0.28	0.993826	0.98112
44		1.83	0.37	0.00	0.0000	0.37		
37		2.52	0.51	0.00	0.0000	0.51		
31.11		3.50	0.70	0.33	0.0116	0.72		
26.16	20.86	4.75	0.95	0.47	0.0165	0.97	0.978634	0.934659
22		6.12	1.23	0.64	0.0224	1.25		
18.5		7.32	1.47	0.88	0.0308	1.50		
15.56		7.89	1.59	1.28	0.0448	1.63		
13.08	10.43	7.96	1.60	2.01	0.0704	1.67	0.897788	0.687425
11		7.27	1.46	3.27	0.1145	1.58		
9.25		6.02	1.21	5.01	0.1754	1.39		
7.78		4.69	0.94	6.67	0.2335	1.18		
6.54	5.215	3.57	0.72	7.32	0.2562	0.97	0.698103	0.076768
5.5		2.79	0.56	7.20	0.2520	0.81		
4.62		2.36	0.47	6.52	0.2282	0.70		
3.89		2.20	0.44	6.08	0.2128	0.66		
3.27	2.6075	2.26	0.45	6.16	0.2156	0.67	0.673001	1.59E-06
2.75		2.42	0.49	6.63	0.2321	0.72		
2.312		2.50	0.50	7.01	0.2454	0.75		
1.945		2.36	0.47	6.82	0.2387	0.71		
1.635	1.3035	2.04	0.41	6.01	0.2104	0.62	0.676085	0.009434
1.375		1.73	0.35	5.01	0.1754	0.52		
1.156		1.59	0.32	4.29	0.1502	0.47		
0.972		1.64	0.33	3.95	0.1383	0.47		
0.818	0.652	1.75	0.35	3.52	0.1232	0.47	0.815905	0.437019
0.688		1.63	0.33	2.22	0.0777	0.41		
0.578		1.09	0.22	0.70	0.0245	0.24		
0.486		0.50	0.10	0.00	0.0000	0.10		

Tabular data of coarse fraction for classification trial TB6, TB7 and TB8

Size [µm]	TB6		TB7		TB8	
	% Chan	% Pass	% Chan	% Pass	% Chan	% Pass
209.3	0.11	100.00	0.10	100.00	0.35	100.00
176	0.38	99.89	0.38	99.90	0.45	99.65
148	0.49	99.51	0.48	99.52	0.56	99.20
124.5	0.60	99.02	0.58	99.04	0.67	98.64
104.7	0.71	98.42	0.67	98.46	0.75	97.97
88	0.79	97.71	0.76	97.79	0.83	97.22
74	0.87	96.92	0.86	97.03	0.92	96.39
62.23	1.00	96.05	1.00	96.17	1.07	95.47
52.33	1.24	95.05	1.20	95.17	1.28	94.40
44	1.67	93.81	1.54	93.97	1.61	93.12
37	2.36	92.14	2.09	92.43	2.14	91.51
31.11	3.33	89.78	2.96	90.34	2.93	89.37
26.16	4.54	86.45	4.14	87.38	4.04	86.44
22	5.87	81.91	5.46	83.24	5.35	82.40
18.5	7.08	76.04	6.64	77.78	6.58	77.05
15.56	7.81	68.96	7.42	71.14	7.37	70.47
13.08	7.80	61.15	7.48	63.72	7.37	63.10
11	7.27	53.35	7.28	56.24	7.10	55.73
9.25	6.11	46.08	6.37	48.96	6.19	48.63
7.78	4.85	39.97	5.19	42.59	5.10	42.44
6.54	3.77	35.12	4.10	37.40	4.08	37.34
5.5	3.01	31.35	3.28	33.30	3.28	33.26
4.62	2.57	28.34	2.79	30.02	2.80	29.98
3.89	2.43	25.77	2.62	27.23	2.62	27.18
3.27	2.52	23.34	2.69	24.61	2.69	24.56
2.75	2.70	20.82	2.86	21.92	2.86	21.87
2.312	2.78	18.12	2.92	19.06	2.92	19.01
1.945	2.59	15.34	2.70	16.14	2.70	16.09
1.635	2.20	12.75	2.29	13.44	2.28	13.39
1.375	1.84	10.55	1.92	11.15	1.91	11.11
1.156	1.68	8.71	1.76	9.23	1.75	9.20
0.972	1.74	7.03	1.83	7.47	1.82	7.45
0.818	1.88	5.29	2.00	5.64	1.99	5.63
0.688	1.74	3.41	1.86	3.64	1.86	3.64
0.578	1.15	1.67	1.23	1.78	1.23	1.78
0.486	0.52	0.52	0.55	0.55	0.55	0.55

Particle size distribution curve of coarse fraction for classification trial TB6

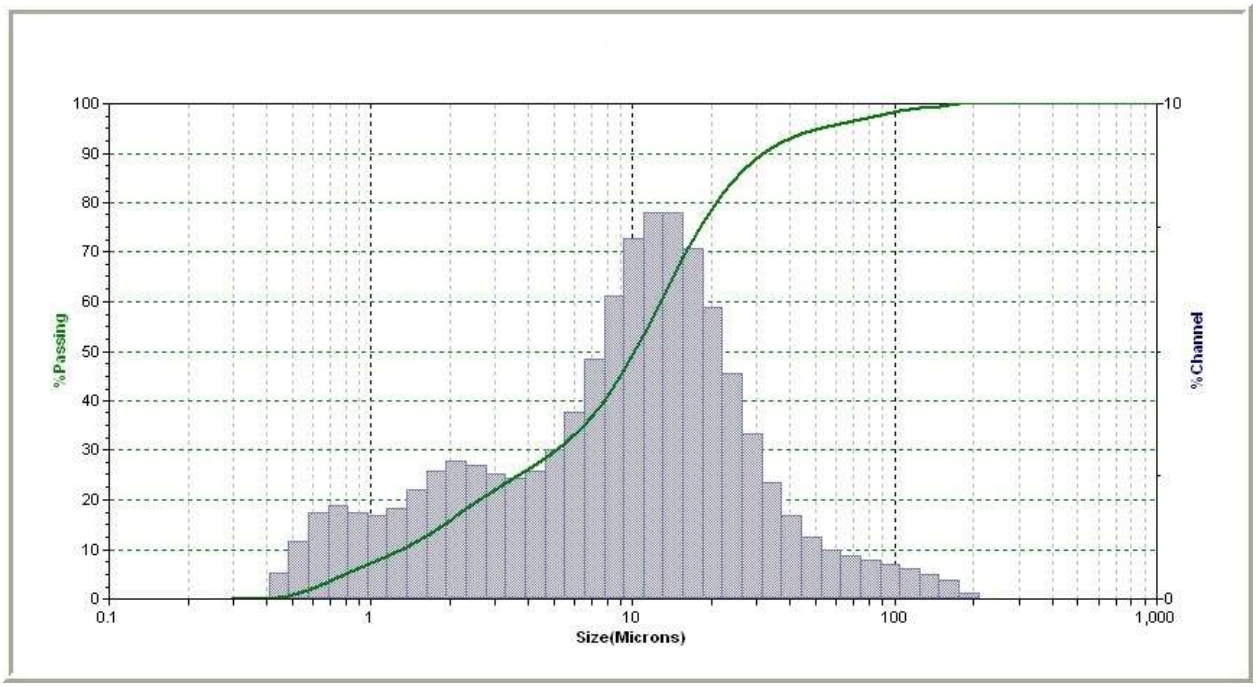

Particle size distribution curve of coarse fraction for classification trial TB7

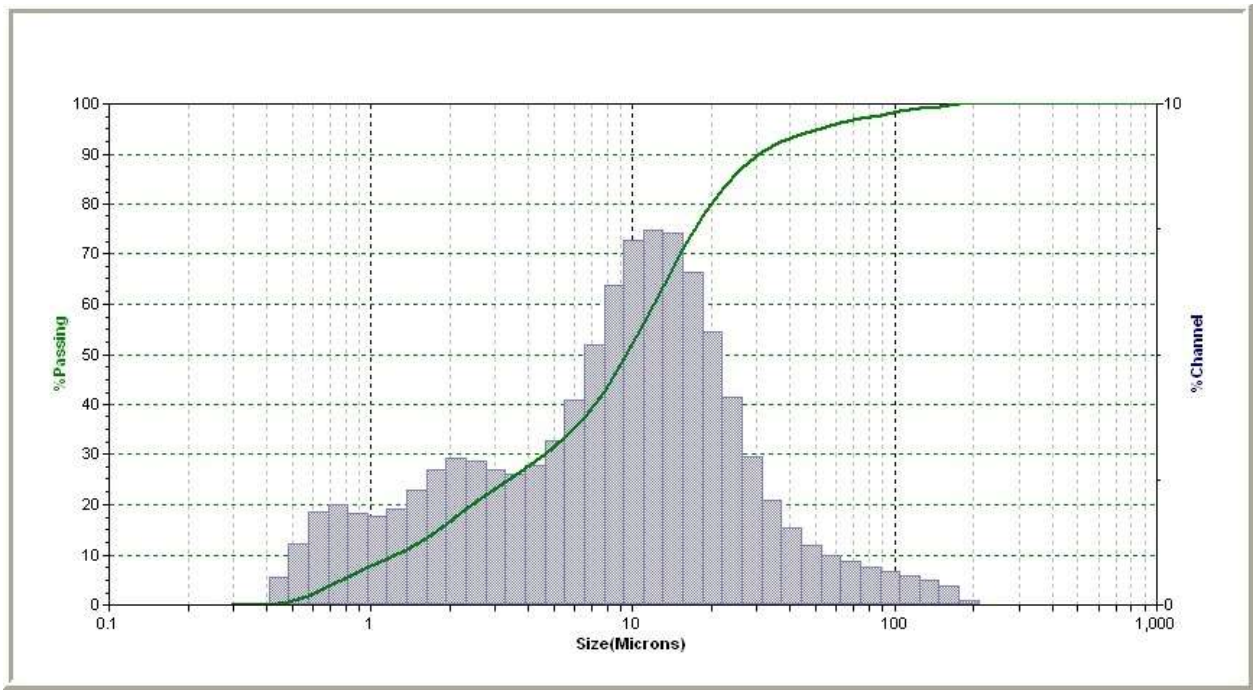

Particle size distribution curve of coarse fraction for classification trial TB8

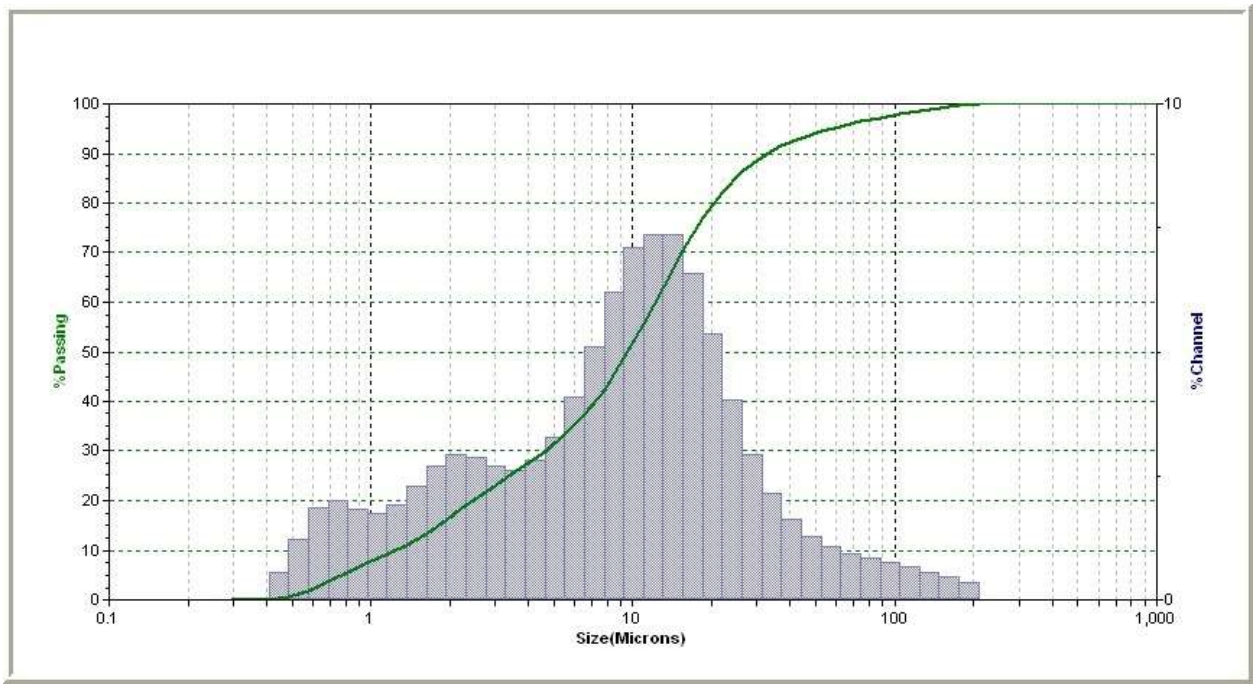

Tabular data for Tromp curve for classification trial TB6

Diameter [µm]	Median	Coarse [%]	Coarse [Kg]	Fines [%]	Fines [Kg]	Feed [Kg]	Tromp	Tromp red.
209.3	166.9	0.11	0.02	0.00	0.0000	0.02	1	1
176		0.38	0.08	0.00	0.0000	0.08		
148		0.49	0.10	0.00	0.0000	0.10		
124.5		0.60	0.12	0.00	0.0000	0.12		
104.7	83.465	0.71	0.14	0.00	0.0000	0.14	1	1
88		0.79	0.16	0.00	0.0000	0.16		
74		0.87	0.18	0.00	0.0000	0.18		
62.23		1.00	0.20	0.00	0.0000	0.20		
52.33	41.72	1.24	0.25	0.00	0.0000	0.25	1	1
44		1.67	0.34	0.00	0.0000	0.34		
37		2.36	0.48	0.00	0.0000	0.48		
31.11		3.33	0.67	0.00	0.0000	0.67		
26.16	20.86	4.54	0.92	0.00	0.0000	0.92	0.979035	0.945403
22		5.87	1.19	0.40	0.0192	1.20		
18.5		7.08	1.43	0.68	0.0326	1.46		
15.56		7.81	1.58	1.20	0.0576	1.64		
13.08	10.43	7.80	1.58	2.19	0.1051	1.68	0.842554	0.589985
11		7.27	1.47	3.90	0.1872	1.66		
9.25		6.11	1.23	6.22	0.2986	1.53		
7.78		4.85	0.98	8.16	0.3917	1.37		
6.54	5.215	3.77	0.76	8.43	0.4046	1.17	0.645546	0.076943
5.5		3.01	0.61	7.47	0.3586	0.97		
4.62		2.57	0.52	6.07	0.2914	0.81		
3.89		2.43	0.49	5.25	0.2520	0.74		
3.27	2.6075	2.52	0.51	5.18	0.2486	0.76	0.651684	0.092928
2.75		2.70	0.55	5.71	0.2741	0.82		
2.312		2.78	0.56	6.37	0.3058	0.87		
1.945		2.59	0.52	6.56	0.3149	0.84		
1.635	1.3035	2.20	0.44	6.01	0.2885	0.73	0.616005	1.23E-05
1.375		1.84	0.37	5.11	0.2453	0.62		
1.156		1.68	0.34	4.39	0.2107	0.55		
0.972		1.74	0.35	4.06	0.1949	0.55		
0.818	0.652	1.88	0.38	3.65	0.1752	0.55	0.770259	0.401716
0.688		1.74	0.35	2.30	0.1104	0.46		
0.578		1.15	0.23	0.69	0.0331	0.27		
0.486		0.52	0.11	0.00	0.0000	0.11		

Tabular data for Tromp curve for classification trial TB7

Diameter [µm]	Median	Coarse [%]	Coarse [Kg]	Fines [%]	Fines [Kg]	Feed [Kg]	Tromp	Tromp red.
209.3	166.9	0.10	0.02	0.00	0.0000	0.02	1	1
176		0.38	0.08	0.00	0.0000	0.08		
148		0.48	0.11	0.00	0.0000	0.11		
124.5		0.58	0.13	0.00	0.0000	0.13		
104.7	83.465	0.67	0.15	0.00	0.0000	0.15	1	1
88		0.76	0.17	0.00	0.0000	0.17		
74		0.86	0.19	0.00	0.0000	0.19		
62.23		1.00	0.22	0.00	0.0000	0.22		
52.33	41.72	1.20	0.27	0.00	0.0000	0.27	1	1
44		1.54	0.34	0.00	0.0000	0.34		
37		2.09	0.46	0.00	0.0000	0.46		
31.11		2.96	0.65	0.00	0.0000	0.65		
26.16	20.86	4.14	0.91	0.00	0.0000	0.91	0.988805	0.960622
22		5.46	1.21	0.39	0.0125	1.22		
18.5		6.64	1.47	0.58	0.0186	1.49		
15.56		7.42	1.64	0.88	0.0282	1.67		
13.08	10.43	7.48	1.65	1.53	0.0490	1.70	0.913326	0.695133
11		7.28	1.61	2.90	0.0928	1.70		
9.25		6.37	1.41	5.22	0.1670	1.57		
7.78		5.19	1.15	7.60	0.2432	1.39		
6.54	5.215	4.10	0.91	8.40	0.2688	1.17	0.761796	0.162138
5.5		3.28	0.72	7.69	0.2461	0.97		
4.62		2.79	0.62	6.26	0.2003	0.82		
3.89		2.62	0.58	5.27	0.1686	0.75		
3.27	2.6075	2.69	0.59	5.10	0.1632	0.76	0.757469	0.14692
2.75		2.86	0.63	5.72	0.1830	0.82		
2.312		2.92	0.65	6.69	0.2141	0.86		
1.945		2.70	0.60	7.19	0.2301	0.83		
1.635	1.3035	2.29	0.51	6.68	0.2138	0.72	0.715781	0.000283
1.375		1.92	0.42	5.59	0.1789	0.60		
1.156		1.76	0.39	4.73	0.1514	0.54		
0.972		1.83	0.40	4.39	0.1405	0.54		
0.818	0.652	2.00	0.44	3.97	0.1270	0.57	0.844174	0.451896
0.688		1.86	0.41	2.49	0.0797	0.49		
0.578		1.23	0.27	0.73	0.0234	0.30		
0.486		0.55	0.12	0.00	0.0000	0.12		

Tabular data for Tromp curve for classification trial TB8

Diameter [µm]	Median	Coarse [%]	Coarse [Kg]	Fines [%]	Fines [Kg]	Feed [Kg]	Tromp	Tromp red.
209.3	166.9	0.35	0.08	0.00	0.0000	0.08	1	1
176		0.45	0.10	0.00	0.0000	0.10		
148		0.56	0.13	0.00	0.0000	0.13		
124.5		0.67	0.15	0.00	0.0000	0.15		
104.7	83.465	0.75	0.17	0.00	0.0000	0.17	1	1
88		0.83	0.19	0.00	0.0000	0.19		
74		0.92	0.21	0.00	0.0000	0.21		
62.23		1.07	0.25	0.00	0.0000	0.25		
52.33	41.72	1.28	0.29	0.00	0.0000	0.29	1	1
44		1.61	0.37	0.00	0.0000	0.37		
37		2.14	0.49	0.00	0.0000	0.49		
31.11		2.93	0.67	0.00	0.0000	0.67		
26.16	20.86	4.04	0.93	0.16	0.0040	0.93	0.994719	0.979126
22		5.35	1.23	0.24	0.0060	1.24		
18.5		6.58	1.51	0.32	0.0080	1.52		
15.56		7.37	1.70	0.42	0.0105	1.71		
13.08	10.43	7.37	1.70	0.68	0.0170	1.71	0.956492	0.828033
11		7.10	1.63	1.49	0.0373	1.67		
9.25		6.19	1.42	3.12	0.0780	1.50		
7.78		5.10	1.17	5.49	0.1373	1.31		
6.54	5.215	4.08	0.94	7.24	0.1810	1.12	0.812067	0.257184
5.5		3.28	0.75	7.39	0.1848	0.94		
4.62		2.80	0.64	6.60	0.1650	0.81		
3.89		2.62	0.60	5.98	0.1495	0.75		
3.27	2.6075	2.69	0.62	6.07	0.1518	0.77	0.781392	0.135937
2.75		2.86	0.66	6.84	0.1710	0.83		
2.312		2.92	0.67	7.79	0.1948	0.87		
1.945		2.70	0.62	8.05	0.2013	0.82		
1.635	1.3035	2.28	0.52	7.49	0.1873	0.71	0.747075	0.000297
1.375		1.91	0.44	6.30	0.1575	0.60		
1.156		1.75	0.40	5.38	0.1345	0.54		
0.972		1.82	0.42	5.00	0.1250	0.54		
0.818	0.652	1.99	0.46	4.49	0.1123	0.57	0.866937	0.474058
0.688		1.86	0.43	2.73	0.0683	0.50		
0.578		1.23	0.28	0.73	0.0183	0.30		
0.486		0.55	0.13	0.00	0.0000	0.13		

Tabular data of coarse fraction for classification trial TB9, TB10 and TB11

Size [µm]	TB9		TB10		TB11	
	% Chan	% Pass	% Chan	% Pass	% Chan	% Pass
209.3	0.24	100.00	0.33	100.00	0.24	100.00
176	0.44	99.76	0.42	99.67	0.42	99.76
148	0.55	99.32	0.52	99.25	0.51	99.34
124.5	0.66	98.77	0.61	98.73	0.58	98.83
104.7	0.75	98.11	0.70	98.12	0.64	98.25
88	0.83	97.36	0.79	97.42	0.72	97.61
74	0.92	96.53	0.90	96.63	0.82	96.89
62.23	1.04	95.61	1.05	95.73	0.97	96.07
52.33	1.23	94.57	1.29	94.68	1.20	95.10
44	1.55	93.34	1.66	93.39	1.55	93.90
37	2.08	91.79	2.24	91.73	2.08	92.35
31.11	2.91	89.71	3.05	89.49	2.87	90.27
26.16	4.11	86.80	4.09	86.44	3.96	87.40
22	5.59	82.69	5.26	82.35	5.29	83.44
18.5	6.99	77.10	6.42	77.09	6.59	78.15
15.56	7.77	70.11	7.33	70.67	7.39	71.56
13.08	7.81	62.34	7.54	63.34	7.50	64.17
11	7.28	54.53	7.25	55.80	7.11	56.67
9.25	6.22	47.25	6.25	48.55	6.17	49.56
7.78	5.02	41.03	5.04	42.30	5.08	43.39
6.54	3.92	36.01	3.95	37.26	4.06	38.31
5.5	3.10	32.09	3.16	33.31	3.27	34.25
4.62	2.62	28.99	2.71	30.15	2.79	30.98
3.89	2.45	26.37	2.56	27.44	2.63	28.19
3.27	2.55	23.92	2.66	24.88	2.73	25.56
2.75	2.77	21.37	2.88	22.22	2.95	22.83
2.312	2.87	18.60	2.98	19.34	3.05	19.88
1.945	2.68	15.73	2.78	16.36	2.83	16.83
1.635	2.26	13.05	2.35	13.58	2.39	14.00
1.375	1.88	10.79	1.95	11.23	2.00	11.61
1.156	1.72	8.91	1.77	9.28	1.83	9.61
0.972	1.78	7.19	1.84	7.51	1.91	7.78
0.818	1.93	5.41	2.00	5.67	2.09	5.87
0.688	1.78	3.48	1.88	3.67	1.95	3.78
0.578	1.18	1.70	1.24	1.79	1.27	1.83
0.486	0.52	0.52	0.55	0.55	0.56	0.56

Particle size distribution curve of coarse fraction for classification trial TB9

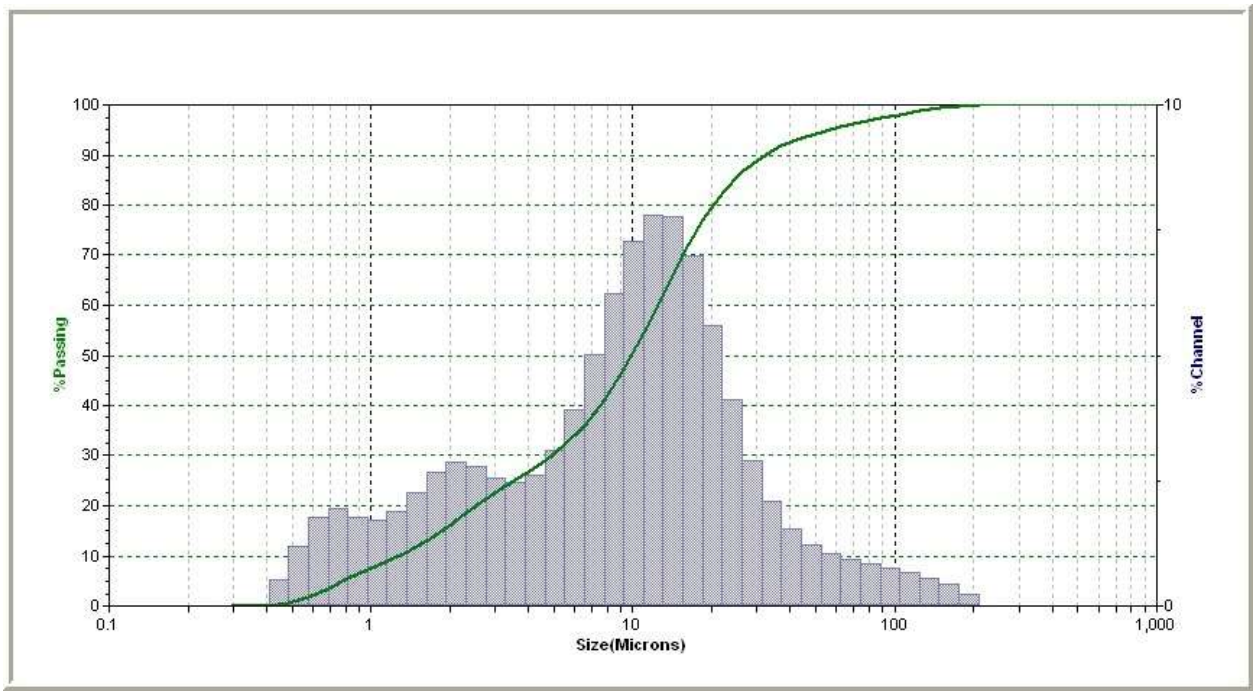

Particle size distribution curve of coarse fraction for classification trial TB10

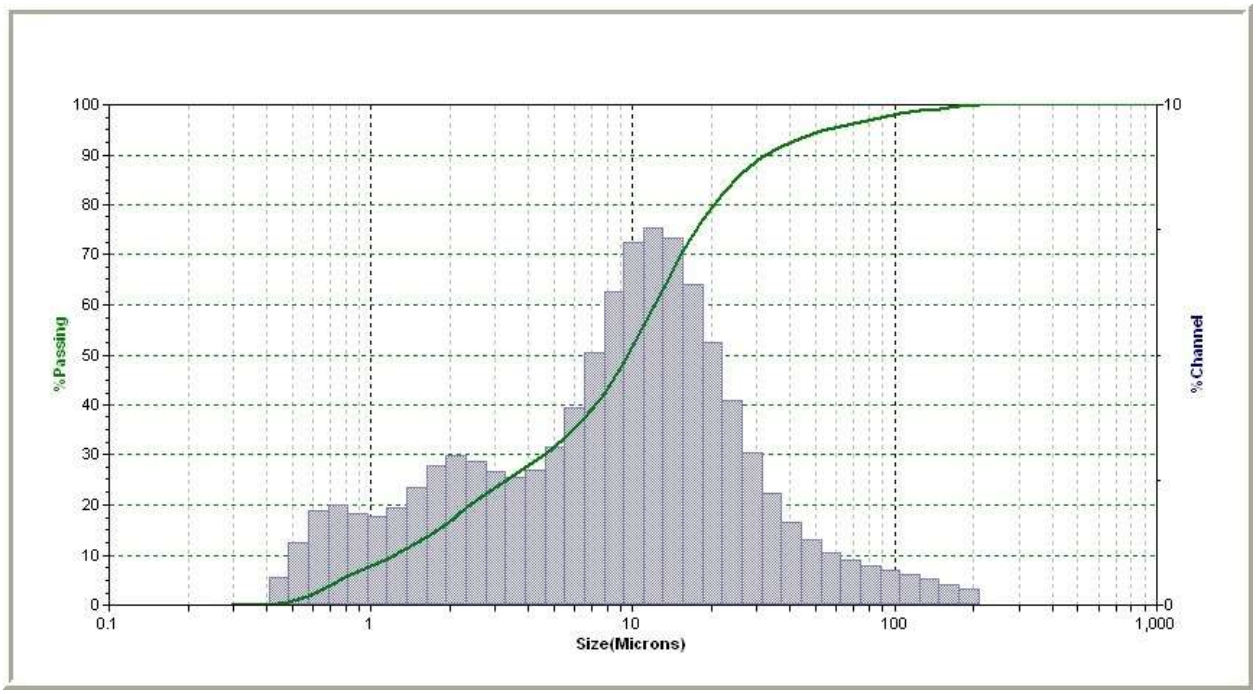

Particle size distribution curve of coarse fraction for classification trial TB11

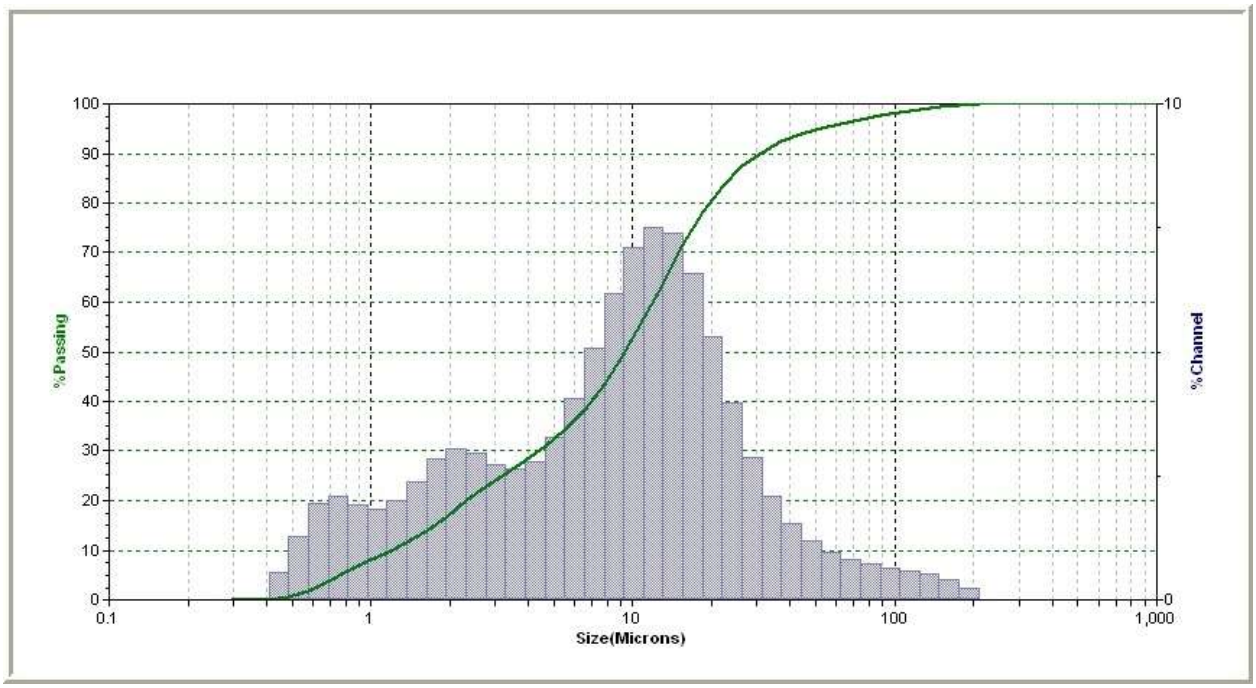

Tabular data for Tromp curve for classification trial TB9

Diameter [µm]	Median	Coarse [%]	Coarse [Kg]	Fines [%]	Fines [Kg]	Feed [Kg]	Tromp	Tromp red.
209.3	166.9	0.24	0.05	0.00	0.0000	0.05	1	1
176		0.44	0.10	0.00	0.0000	0.10		
148		0.55	0.12	0.00	0.0000	0.12		
124.5		0.66	0.15	0.00	0.0000	0.15		
104.7	83.465	0.75	0.17	0.00	0.0000	0.17	1	1
88		0.83	0.18	0.00	0.0000	0.18		
74		0.92	0.20	0.00	0.0000	0.20		
62.23		1.04	0.23	0.00	0.0000	0.23		
52.33	41.72	1.23	0.27	0.00	0.0000	0.27	0.995284	0.983078
44		1.55	0.34	0.00	0.0000	0.34		
37		2.08	0.46	0.11	0.0030	0.46		
31.11		2.91	0.64	0.19	0.0051	0.65		
26.16	20.86	4.11	0.90	0.29	0.0078	0.91	0.987074	0.953619
22		5.59	1.23	0.52	0.0140	1.24		
18.5		6.99	1.54	0.77	0.0208	1.56		
15.56		7.77	1.71	1.03	0.0278	1.74		
13.08	10.43	7.81	1.72	1.56	0.0421	1.76	0.939358	0.782412
11		7.28	1.60	2.58	0.0697	1.67		
9.25		6.22	1.37	4.09	0.1104	1.48		
7.78		5.02	1.10	5.62	0.1517	1.26		
6.54	5.215	3.92	0.86	6.41	0.1731	1.04	0.80985	0.317727
5.5		3.10	0.68	6.19	0.1671	0.85		
4.62		2.62	0.58	5.49	0.1482	0.72		
3.89		2.45	0.54	5.04	0.1361	0.68		
3.27	2.6075	2.55	0.56	5.25	0.1418	0.70	0.768637	0.169851
2.75		2.77	0.61	6.18	0.1669	0.78		
2.312		2.87	0.63	7.39	0.1995	0.83		
1.945		2.68	0.59	7.84	0.2117	0.80		
1.635	1.3035	2.26	0.50	7.31	0.1974	0.69	0.721327	9.67E-05
1.375		1.88	0.41	6.13	0.1655	0.58		
1.156		1.72	0.38	5.35	0.1445	0.52		
0.972		1.78	0.39	5.26	0.1420	0.53		
0.818	0.652	1.93	0.42	5.11	0.1380	0.56	0.824238	0.369351
0.688		1.78	0.39	3.33	0.0899	0.48		
0.578		1.18	0.26	0.96	0.0259	0.29		
0.486		0.52	0.11	0.00	0.0000	0.11		

Tabular data for Tromp curve for classification trial TB10

Diameter [µm]	Median	Coarse [%]	Coarse [Kg]	Fines [%]	Fines [Kg]	Feed [Kg]	Tromp	Tromp red.
209.3	166.9	0.33	0.08	0.00	0.0000	0.08	1	1
176		0.42	0.10	0.00	0.0000	0.10		
148		0.52	0.12	0.00	0.0000	0.12		
124.5		0.61	0.15	0.00	0.0000	0.15		
104.7	83.465	0.70	0.17	0.00	0.0000	0.17	1	1
88		0.79	0.19	0.00	0.0000	0.19		
74		0.90	0.22	0.00	0.0000	0.22		
62.23		1.05	0.25	0.00	0.0000	0.25		
52.33	41.72	1.29	0.31	0.00	0.0000	0.31	0.997892	0.985513
44		1.66	0.40	0.00	0.0000	0.40		
37		2.24	0.54	0.12	0.0016	0.54		
31.11		3.05	0.73	0.20	0.0026	0.73		
26.16	20.86	4.09	0.98	0.30	0.0039	0.98	0.99345	0.954983
22		5.26	1.26	0.57	0.0074	1.26		
18.5		6.42	1.53	0.85	0.0111	1.55		
15.56		7.33	1.75	1.08	0.0140	1.77		
13.08	10.43	7.54	1.80	1.55	0.0202	1.82	0.972733	0.812601
11		7.25	1.73	2.47	0.0321	1.76		
9.25		6.25	1.49	3.94	0.0512	1.54		
7.78		5.04	1.20	5.48	0.0712	1.28		
6.54	5.215	3.95	0.94	6.23	0.0810	1.03	0.910765	0.3867
5.5		3.16	0.76	5.93	0.0771	0.83		
4.62		2.71	0.65	5.24	0.0681	0.72		
3.89		2.56	0.61	4.90	0.0637	0.68		
3.27	2.6075	2.66	0.64	5.24	0.0681	0.70	0.887023	0.223523
2.75		2.88	0.69	6.21	0.0807	0.77		
2.312		2.98	0.71	7.31	0.0950	0.81		
1.945		2.78	0.66	7.70	0.1001	0.76		
1.635	1.3035	2.35	0.56	7.24	0.0941	0.66	0.854559	0.000407
1.375		1.95	0.47	6.31	0.0820	0.55		
1.156		1.77	0.42	5.63	0.0732	0.50		
0.972		1.84	0.44	5.57	0.0724	0.51		
0.818	0.652	2.00	0.48	5.39	0.0701	0.55	0.913025	0.402234
0.688		1.88	0.45	3.53	0.0459	0.50		
0.578		1.24	0.30	1.01	0.0131	0.31		
0.486		0.55	0.13	0.00	0.0000	0.13		

Tabular data for Tromp curve for classification trial TB11

Diameter [µm]	Median	Coarse [%]	Coarse [Kg]	Fines [%]	Fines [Kg]	Feed [Kg]	Tromp	Tromp red.
209.3	166.9	0.24	0.06	0.00	0.0000	0.06	1	1
176		0.42	0.11	0.00	0.0000	0.11		
148		0.51	0.13	0.00	0.0000	0.13		
124.5		0.58	0.15	0.00	0.0000	0.15		
104.7	83.465	0.64	0.16	0.00	0.0000	0.16	1	1
88		0.72	0.18	0.00	0.0000	0.18		
74		0.82	0.21	0.00	0.0000	0.21		
62.23		0.97	0.24	0.00	0.0000	0.24		
52.33	41.72	1.20	0.30	0.00	0.0000	0.30	0.999483	0.995387
44		1.55	0.39	0.00	0.0000	0.39		
37		2.08	0.52	0.00	0.0000	0.52		
31.11		2.87	0.72	0.10	0.0010	0.72		
26.16	20.86	3.96	0.99	0.14	0.0014	1.00	0.997059	0.973763
22		5.29	1.33	0.32	0.0032	1.33		
18.5		6.59	1.65	0.46	0.0046	1.66		
15.56		7.39	1.85	0.80	0.0080	1.86		
13.08	10.43	7.50	1.88	1.33	0.0133	1.90	0.981284	0.833042
11		7.11	1.78	2.27	0.0227	1.81		
9.25		6.17	1.55	3.67	0.0367	1.59		
7.78		5.08	1.28	5.11	0.0511	1.33		
6.54	5.215	4.06	1.02	5.87	0.0587	1.08	0.936691	0.435241
5.5		3.27	0.82	5.70	0.0570	0.88		
4.62		2.79	0.70	5.15	0.0515	0.75		
3.89		2.63	0.66	4.91	0.0491	0.71		
3.27	2.6075	2.73	0.69	5.37	0.0537	0.74	0.911993	0.214923
2.75		2.95	0.74	6.52	0.0652	0.81		
2.312		3.05	0.77	7.85	0.0785	0.84		
1.945		2.83	0.71	8.26	0.0826	0.79		
1.635	1.3035	2.39	0.60	7.69	0.0769	0.68	0.887914	0.000123
1.375		2.00	0.50	6.50	0.0650	0.57		
1.156		1.83	0.46	5.77	0.0577	0.52		
0.972		1.91	0.48	5.80	0.0580	0.54		
0.818	0.652	2.09	0.52	5.71	0.0571	0.58	0.934008	0.411314
0.688		1.95	0.49	3.69	0.0369	0.53		
0.578		1.27	0.32	1.01	0.0101	0.33		
0.486		0.56	0.14	0.00	0.0000	0.14		